Delft University of Technology

Extreme gusts and their role in wind turbine design

Bos, Rene

DOI

Publication date
2017

Document Version
Final published version

Important note
To cite this publication, please use the final published version (if applicable).
Please check the document version above.

Extreme gusts and their role in wind turbine design

Extreme gusts and their role in wind turbine design

Proefschrift

ter verkrijging van de graad van doctor
aan de Technische Universiteit Delft,
op gezag van de Rector Magnificus prof. ir. K. C. A. M. Luyben,
voorzitter van het College voor Promoties,
in het openbaar te verdedigen op dinsdag 4 juli 2017 om 15:00 uur

door

René BOS

Master of Science in Sustainable Energy Technology,
geboren te Nieuwegein, Nederland.

Dit proefschrift is goedgekeurd door de

promotor: Prof. dr. G. J. W. van Bussel
copromotor: Dr. ir. W. A. A. M. Bierbooms

Samenstelling promotiecommissie:

Rector Magnificus	voorzitter
Prof. dr. G. J. W. van Bussel	Technische Universiteit Delft
Dr. ir. W. A. A. M. Bierbooms	Technische Universiteit Delft

Onafhankelijke leden:

Prof. dr. G. A. Bossanyi	University of Bristol/DNV-GL
Prof. dr. P. W. Cheng	Universität Stuttgart
Prof. dr. S. Emeis	Karlsruher Institut für Technologie
Prof. dr. ir. P. H. A. J. M. van Gelder	Technische Universiteit Delft
Prof. dr. M. Muskulus	Norges Teknisk-Naturvetenskapelige Universitet
Prof. dr. S. J. Watson	Technische Universiteit Delft, *reservelid*

Voor Jack

Contents

Summary

Wind energy is already one of the cheapest forms of sustainable energy and is one of the major technologies used to combat climate change. Nevertheless, its widespread success depends greatly on its ability to compete with fossil-fueled power plants. Traditionally, wind turbines try to benefit from economies of scale. They do this by growing towards larger rotor diameters as soon as state-of-the-art technologies are able to support even longer blades; a process that continues to this day. At present, 8–10-MW machines are making their appearance on the market while 10- to 20-MW concepts—with diameters up to 250 m—already lie on the drawing board.

A key issue in upscaling is estimating the long-term loads, most notably the extreme loads, which are the result of decades of turbulent wind. These play an important role in the design, because they determine the required strength for many load-carrying structures. However, designers are faced with a tremendous computational burden when trying to predict extreme loads and often have to settle for a low accuracy. Therefore, any potential gains of a new blade shape or a new control method can be easily outweighed by the sheer uncertainty. This has motivated this research on extreme wind gusts. Extreme wind gusts are some of the most severe events that a turbine can encounter, and understanding them will help to gain insight into important design loads.

Within this research work, the concept of a gust has been extended, from its common perception to a mathematical description of fully three-dimensional velocity fields. The notion that a gust is a three-dimensional phenomenon is very important—especially when the size of turbine blades can outgrow the characteristic turbulent structures in the atmospheric boundary layer. Velocity amplitudes are then no longer a convenient measure of the severity, since small peaks are easily cancelled out over the rotor disk. Instead, wind gusts are treated as concentrations of momentum, which are directly related to the forces transferred to the structure.

The mathematical treatment of gusts has been carried out with spectral models under the assumptions of homogeneity and Gaussian turbulence. These model the statistical properties of turbulence in terms of the scales of motion (or wavelengths), while adhering to the basic physics. The process of translating these properties to the spatial domain can be manipulated to yield conditionally random velocity fields, containing wind gusts with extremely high momentum contents. It was found that, in order to preserve the conservation of mass, the fluid that is displaced in a wind gust has to recirculate. That is why the streamlines around gusts are generally in the shape of vortex-like structures and why velocity peaks cannot extend infinitely in space. Furthermore, the expected Euler

characteristic appeared to be a good representation of the probability of finding such events in a domain, even for very rare cases with long return periods.

Compared to many deterministic gust models, which assume a uniform inflow, these stochastic gusts clearly reveal vulnerable areas in the rotor plane. This was demonstrated with a simplified model of the DTU 10 MW reference turbine with a rotor diameter of 178 m. The rotor is especially susceptible to high bending moments when it is hit in the top half of the disk, around two-thirds of the blade span, and during a blade's downstroke. Still, there are many more situations imaginable where an extreme gust does not trigger any significant load; for example, by landing close to the blade root or simply missing the blades altogether. For this reason, a single N-year gust has little to no contribution to the N-year load. The long-term loads thus have to be found probabilistically, taking into account the variation of all the environmental parameters.

Yet, many of such methods that rely on brute force (e.g., the crude Monte Carlo method) are notoriously inefficient in the early design phases when computational resources are scarcely available. For such cases, importance sampling methods are much more reliable. They are based on the idea that, instead of simulating the entire life of a wind turbine, the long-term extreme loads can be predicted by only evaluating the response to the most severe events. This was demonstrated in this thesis with a simplified model of the DTU 10 MW reference turbine (without control) as well as with the complete NREL 5 MW reference turbine in the FAST v7 aeroelastic code. Several sampling distributions were presented, spanning four-dimensional parameter spaces and taking into account wind speed, gust amplitude, and gust position (lateral and vertical). The most sophisticated method was able to reduce the deviation from the true 50-year blade root bending moment by a factor 10 to 100—the equivalent of roughly a factor 1,000 increase in efficiency—compared to extrapolating the results of a crude Monte Carlo method. Next to manual sampling methods, an automated approach, based on a genetic algorithm, was able to successfully generate extreme gusts that target certain weaknesses of the turbine.

The results of this work can be applied directly to predict the extreme loads of new designs with less uncertainty. Moreover, the events that trigger these loads can now be studied in detail. This allows the designers to work with less conservatism, which will help to further reduce the cost of wind energy.

Samenvatting

Windenergie is één van de goedkoopste vormen van duurzame energie en één van de voornaamste technologieën om klimaatverandering tegen te gaan. Desalniettemin hangt het grootschalige succes sterk af van de concurrentiepositie ten opzichte van fossielgestookte centrales. Traditioneel gezien proberen windturbines te profiteren van een economisch schaalvoordeel. Dit doen ze door te groeien naar grotere rotordiameters naarmate nieuwe technieken beschikbaar komen die nog langere bladen mogelijk maken; een proces wat tot op de dag van vandaag nog doorgaat. Tegenwoordig maken 8 tot 10 MW machines hun opwachting op de markt, terwijl concepten van 10 tot 20 MW — met diameters tot wel 250 m — al op de tekentafel liggen.

Een belangrijke kwestie bij het opschalen van windturbines is het schatten van de langetermijnsbelastingen, voornamelijk de extreme belastingen, die het resultaat zijn van tientallen jaren aan turbulente wind. Deze spelen een belangrijke rol in het ontwerp, want ze bepalen voor een groot deel de sterkte-eisen van veel dragende constructies. Ontwerpers worden echter geconfronteerd met een enorme rekenlast wanneer ze extreme belastingen willen voorspellen. Daardoor moeten zij zich vaak neerleggen bij een lage nauwkeurigheid en worden de eventuele winsten van een nieuwe bladvorm of regelmethode al snel tenietgedaan door de enorme onzekerheid. Dit is de motivatie geweest voor dit onderzoek naar extreme windvlagen. Extreme windvlagen zijn enkele van de zwaarste gebeurtenissen die een windturbine kan tegenkomen, en ze begrijpen helpt om meer inzicht te krijgen in belangrijke ontwerpbelastingen.

Binnen dit onderzoekswerk is het concept van een vlaag uitgebreid, van de alledaagse opvatting naar een wiskundige omschrijving van volledig driedimensionale snelheidsvelden. Het idee dat een vlaag een driedimensionaal fenomeen is, is van groot belang — zeker wanneer het formaat van turbinebladen de karakteristieke turbulente structuren in de atmosferische grenslaag kan overtreffen. Snelheidsamplitudes zijn dan ook niet langer een handige maat voor de zwaarte, omdat deze makkelijk over de rotorschijf uitgemiddeld worden. In plaats daarvan worden windvlagen behandeld als concentraties van impuls, die direct gerelateerd zijn aan de krachten die worden doorgespeeld aan de constructie.

De wiskundige behandeling van vlagen is uitgevoerd met spectrale modellen op aanname van homogeniteit en Gaussische turbulentie. Deze modelleren de statistische eigenschappen van turbulentie in termen van de verschillende bewegingsschalen (of golflengtes), terwijl vastgehouden wordt aan de basisfysica. Het proces, waarin deze eigenschappen worden vertaald naar het ruimtelijke domein, kan gemanipuleerd worden om zo voorwaardelijk willekeurige snelheidsvelden te leveren met daarin windvlagen van extreem hoge impulsgehaltes. Er is onder andere gevonden dat, om het massabehoud

in stand te houden, de lucht die verplaatst wordt in een windvlaag moet recirculeren. Daarom vormen de stroomlijnen rond vlagen in het algemeen een wervelachtige structuur en kunnen snelheidspieken niet tot in het oneindige uitstrekken. Verder bleek de Eulerkarakteristiek een goede voorstelling te zijn van de kans om zulke gebeurtenissen binnen een domein tegen te komen, zelfs voor hele zeldzame gevallen met lange herhalingstijden.

Vergeleken met veel deterministische vlaagmodellen, die een uniforme instroming aannemen, leggen deze stochastische vlagen duidelijk kwetsbare gebieden in het rotorvlak bloot. Dit is gedemonstreerd met een vereenvoudigd model van de DTU 10 MW referentieturbine met een diameter van 178 m. De rotor is met name vatbaar voor hoge buigmomenten wanneer het in de bovenste helft wordt geraakt, rond tweederde van de spanwijdte en gedurende de neergaande slag van een blad. Desondanks zijn er veel meer situaties denkbaar waarin een extreme vlaag geen significante belasting veroorzaakt, bijvoorbeeld wanneer het vlak bij de bladwortel landt of simpelweg de bladen helemaal mist. Om deze reden heeft een enkele N-jaarsvlaag weinig tot geen invloed op de N-jaarsbelasting. Langetermijnsbelastingen moeten daarom op een probabilistische wijze gevonden worden, rekening houdend met de variatie van alle omgevingsparameters.

Toch zijn veel van zulke methoden die vertrouwen op brute kracht (bijv. de grove Monte Carlo methode) behoorlijk inefficiënt in de vroege ontwerpfases wanneer weinig rekenmiddelen voorhanden zijn. In zulke gevallen zijn zogenaamde importance sampling methodes veel betrouwbaarder. Deze zijn gebaseerd op het idee dat, in plaats van de gehele levensduur van een turbine te simuleren, de langetermijnbelastingen kunnen worden voorspeld met alleen de repons op de zwaarste gebeurtenissen. In dit proefschrift is dit gedemonstreerd met een vereenvoudigd model van de DTU 10 MW referentieturbine (zonder regeling) en de complete NREL 5 MW referentieturbine in de FAST v7 aeroelastische code. Verschillende steekproefverdelingen zijn hiervoor gepresenteerd, verspreid over vierdimensionale parameterruimtes, inclusief windsnelheid, vlaagamplitude en vlaagpositie (lateraal en verticaal). De meest geavanceerde methode kon de afwijking tot de ware 50-jaarsbelasting verkleinen met een factor 10 tot 100 — het equivalent van grofweg een factor 1,000 toename in efficiëntie — vergeleken met het extrapoleren van de resultaten van een grove Monte Carlo methode. Naast handmatige steekproefmethodes was ook een automatische aanpak, op basis van een genetisch algoritme, succesvol om extreme vlagen te laten genereren die mikken op bepaalde zwaktes van de turbine.

De resultaten van dit werk kunnen direct worden toegepast om de extreme belastingen van nieuwe ontwerpen te kunnen voorspellen met minder onzekerheid. Daarnaast kunnen de omstandigheden waarin deze belastingen veroorzaakt worden in detail bestudeerd worden. Dit stelt ontwerpers in de gelegenheid om minder conservatief te werken, wat uiteindelijk helpt om de kosten van windenergie verder te verlagen.

Chapter 1

Introduction
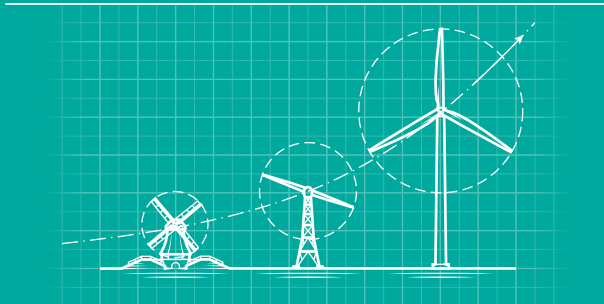
"Anything that can go wrong, will go wrong."

— MURPHY'S LAW

ONE OF THE CHALLENGES in engineering is not to make sure things do not fail, but to have them fail at the right time. This is especially true for wind turbines, of which the cost price directly influences their commerical viability. They spend years in a turbulent wind climate, sometimes in very remote locations, trying to survive storms, waves, and gusts (while preferably producing electricity in the process).

1.1 Wind energy

Climate change is one of the biggest threats to face future generations. Large-scale emissions of greenhouse gases, deforestation, and intensive agriculture since the Industrial Age have led to irreversible damage to the Earth's climate and ecosystem. The scientific proof for this is collected every five to six years in the assessment reports of the Intergovernmental Panel on Climate Change (IPCC):

> "Warming of the climate system is unequivocal, and since the 1950s, many of the observed changes are unprecedented over decades to millennia. The atmosphere and ocean have warmed, the amounts of snow and ice have diminished, sea level has risen, and the concentrations of greenhouse gases have increased."
>
> (IPCC, 2013, p. 4)

The effects of this have become more prominent in recent history. It is likely[1] that that climate change has been the leading cause of the increase in heat waves and heavy precipitation events seen since 1950 (Stocker et al., 2013, p. 110). This is a great threat for the water and food security (not to mention the political instabilities it may cause). For instance, a warmer climate can trigger an advance of alien plant and insect species that may harm crops (Crowl et al., 2008; Diez et al., 2012; Epstein, 2001). Also, the bleaching of coral reefs has a tremendous impact on fish stocks. Over 2016 alone, a 700-km stretch of coral has died in the Great Barrier Reef (ARC Centre of Excellence for Coral Reef Studies, 2016), owing to warming ocean temperatures.

---

[1] "Likely" is the term used by the IPCC to indicate a 66–100% probability.

One of the key points in combating climate change is reshaping the world's energy supply. In 1971, the worldwide energy production amounted to 6,101 Mtoe (71.0 PWh), 86.7% of which came from fossil fuels (i.e., coal, oil, and natural gas). With the growth in population size, this has increased to 13,699 Mtoe (159.3 PWh) in 2014, with fossil fuels still making up 81.1% (IEA, 2016a). However, the production from renewable energy sources has been on a slow but steady rise. In 2014, energy from wind, solar thermal, solar photovoltaic, and geothermal has increased by 11.1%, 7.7%, 35.1%, and 8.3%, respectively (IEA, 2016b).

1.1.1 Historical development and trends

Especially in Europe, wind energy has established itself as one of the most commercially viable renewable energy sources. For 2030, the European Wind Energy Association (EWEA) has estimated that wind energy will supply roughly a quarter of the EU's total electricity demand—533 TWh onshore and 245 TWh offshore (EWEA, 2015). Yet, the *technical potential* (i.e., the total resource that can be harvested with present-day technology) is estimated to be about 45 PWh onshore and another 30 PWh offshore (EEA, 2009).

Together with the ecological argument, the strongest driver for the development of wind energy has been the price and availability of crude oil (see Figure 1.1). Up until the Industrial Revolution, wind was one of the primary sources of energy and was used to mill grain, saw wood, and pump water. After the invention of the steam engine, windmills, watermills, and horse mills were starting to be replaced by fossil-fuel powered machines. These grew more powerful as technology progressed, but could of course also operate independently of the wind conditions. The Netherlands, for instance, housed some 10,000 windmills halfway through the 19th century, of which a little over 1,100 remain today.

During the electrification period, which started in the 1880s, power production became more centralized, as the burning of fossil fuels is most effective in large combustion chambers. Still, there was some interest in wind energy to power farms in rural areas. Some notable examples of this are the machines built by Charles Brush (1849–1929) in 1888 and Poul la Cour (1846–1908) in 1891. At the time of World War I, scientific advancements in propeller technology led to a better understanding of rotor aerodynamics (Van Kuik, 2007). Several full-scale prototypes were built over the course of the following decades, with the most prominent one being the 1.25-MW Smith-Putnam machine in 1942, the largest turbine ever constructed for 37 years to come. It operated for 1,100 hours until a major blade failure, which would have been prevented were it not for the material shortages during World War II. In 1957, Johannes Juul (1887–1969)—who was a student of Poul la Cour—designed a 24-m diameter, 200-kW turbine at Gedser, Denmark. It was a three-bladed, upwind, stall-regulated machine that operated maintenance-free for eleven years. Often called the "Danish design", it formed the basis for modern wind turbines seen today.

Wind energy technology took a big leap during the 1970s and 1980s. This was after Arab oil-producing countries issued an oil embargo in late 1973, in response to the US aid to Israel during the Yom Kippur War, which resulted in a 70% step increase in oil price. Later, a second energy crisis would emerge in 1979, triggered by the Iranian revolution. Therefore, driven by the desire for energy independence, the US government backed a major research and development program at NASA. It focused primarily on large machines that were viable for utility-scale electricity production. The first prototype was the 100-

kW Mod-0, installed in 1975, which had a two-bladed rotor downwind of a lattice tower. Already in 1979, the world's first multi-megawatt machine was installed, being the 61-m diameter, 2-MW Mod-1. The philosophy was that, in order to be cost-effective, wind turbines have to be big enough to benefit from the economies of scale.[2] Several larger units were constructed in the years to follow: the Mod-2 (91 m, 2.5 MW), the WTS-4 (79.2 m, 4 MW), and the Mod-5B (97.5 m, 3.2 MW). Also, a 121.5-m diameter, 7.3-MW machine was on the drawing board, but was never actually built.

Meanwhile in Denmark, students and staff of the Tvind school designed and constructed a 54-m diameter, downwind turbine on a large concrete tower. When it entered operation in 1978, it was the world's largest wind turbine at the time. It had its 40-year anniversary in 2015.

There was also a considerable research effort into vertical-axis wind turbines (VAWTs), primarily at Sandia National Laboratories. These had the advantage that they could operate under any wind direction, thereby eliminating the need for a yaw system, and had the heavy drivetrain located on the bottom instead of up on a tower. Among others, experiments were carried out on a 17-m and a 34-m device, installed in 1977 and 1987, respectively. The designs were eventually translated to a 17-m and 19-m diameter commercial product, of which over 500 were installed up until the mid 1990s (Sutherland, Berg and Ashwill, 2012). The largest VAWT ever to be constructed is the 96-m tall, 64-m diameter, 4-MW machine located in Québec, Canada. Although there is no reason why VAWTs should not be as successful as their horizontal-axis counterparts from a technical perspective, the technology fell from grace due to the cost of the blades and issues with reliability at that time. VAWTs namely suffer from strong torque fluctuations that affect the fatigue life, but also have difficulties to start up in low wind speeds (e.g., see Bos, 2012).

During this era, wind turbines were widely sold as commercial products. In particular in the United States, tax credit schemes for renewable energy together with the high oil price made it very attractive for private developers to invest in wind energy. This led to a proliferation of wind turbines, and about 12 GW of renewable energy capacity was installed in California alone in the 1980s (Shukla and Sawyer, 2012, p. 136). Three giant wind farms—Altamont Pass, Tehachapi, and San Gorgonio—together house more than 13,000 turbines and were responsible for 30% of the world's installed wind power capacity in 1995 (California Energy Commission, 2016). Most turbine designs that found their way into the commercial market were two-bladed, based on the US research programs, and three-bladed, based on the Danish design. Here as well, the trend moved towards larger rotor diameters and higher power ratings. In 1985, about two-thirds of the newly installed capacity comprised of units in the range of 51–100 kW (Rashkin and Goetze van Steyn, 1986, p. 12). Ten years later, in 1995, 46% of new installations were rated over 200 kW (Siebensohn Small, 1997, p. 22).

The development in the United States slowed down in the mid-1990s after the oil price collapse and with the renewable energy schemes ending. At that time, most of the market activity moved to Europe, where the people had ongoing concerns about the environment, strengthened by the Chernobyl disaster of 1986. Especially countries such

---

[2]   Much of the infrastructure costs—think of the grid connection, the foundation, and the installation—are one-time investments that do not scale as rapidly as the price of a bigger machine. Therefore, larger wind turbines can often deliver electricity at a lower kWh-price than smaller ones.
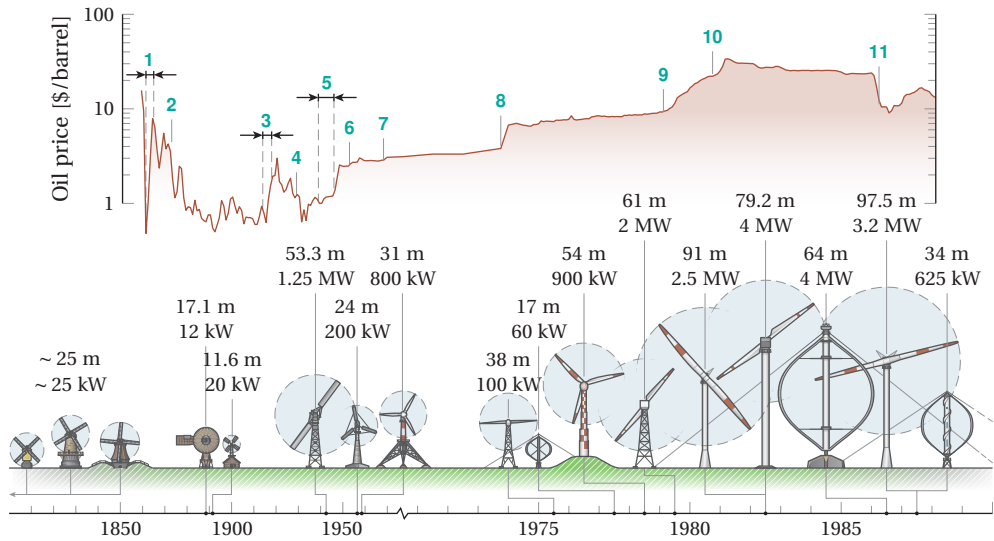
Figure 1.1: Historical development of wind energy and its link to the price of crude oil (US Energy Information Administration, 2016). **1:** *American Civil War* (1861–1865). **2:** *Stock market crash marking the start of the Long Depression* (1873). **3:** *World War I* (1914–1918). **4:** *Stock market crash and beginning of the Great Depression* (1929). **5:** *World War II* (1939–1945). **6:** *Iranian coup d'état* (1953). **7:** *Six-Day War* (1967). **8:** *Yom Kippur (Arab-Israeli) War* (1973). **9:** *Iranian Revolution* (1979). **10:** *Iraqi invasion of Iran* (1979). **11:** *Price collapse of crude oil* (1986).

as Germany, Denmark, and Spain had some very successful policies in place that allowed wind energy to flourish (Shukla and Sawyer, 2012, pp. 26–30).

The 1990s also saw the first offshore wind turbine: a 25-m diameter, 220-kW machine off the coast of Nogersund, Sweden. It was followed by the first offshore farm at Vindeby, Denmark, consisting of eleven 450-kW turbines, located 2 km from shore. In the Netherlands, four 500-kW machines were installed in the IJsselmeer. They ran from 1994 until they were removed in 2016 after meeting their end-of-life.[3] Several pilot projects were commissioned across Europe in the years after, such as a 5-MW farm at Tunø Knob, Denmark in 1995 (ten 500-kW units, 5.5 km offshore) and a 2.75-MW farm in southern Gotland near Burgvik, Sweden in 1997 (five 550-kW units, 5.7 km offshore).

The wind energy industry saw a sharp growth in the 2000s. This was mainly due to increasing concerns about climate change, which materialized in the Kyoto Protocol in 1997, but also because of the volatile oil prices. A rapidly increasing world population, emerging economies such as China, and tensions in the Middle East caused the price for a barrel of crude oil to rise from $21.84, averaged over 2001, to $128.08 in July 2008 (US Energy Information Administration, 2016). Over the same period, the total global installed capacity of wind power increased fourfold, from 23.9 to 120.7 GW (GWEC, 2016). After the 2008 financial crisis, the European and North-American markets stagnated and were

---

[3]   Already the (two-bladed) rotor broke off from one of the machines in late 2014 due to accumulated fatigue damage (NUON, 2016).
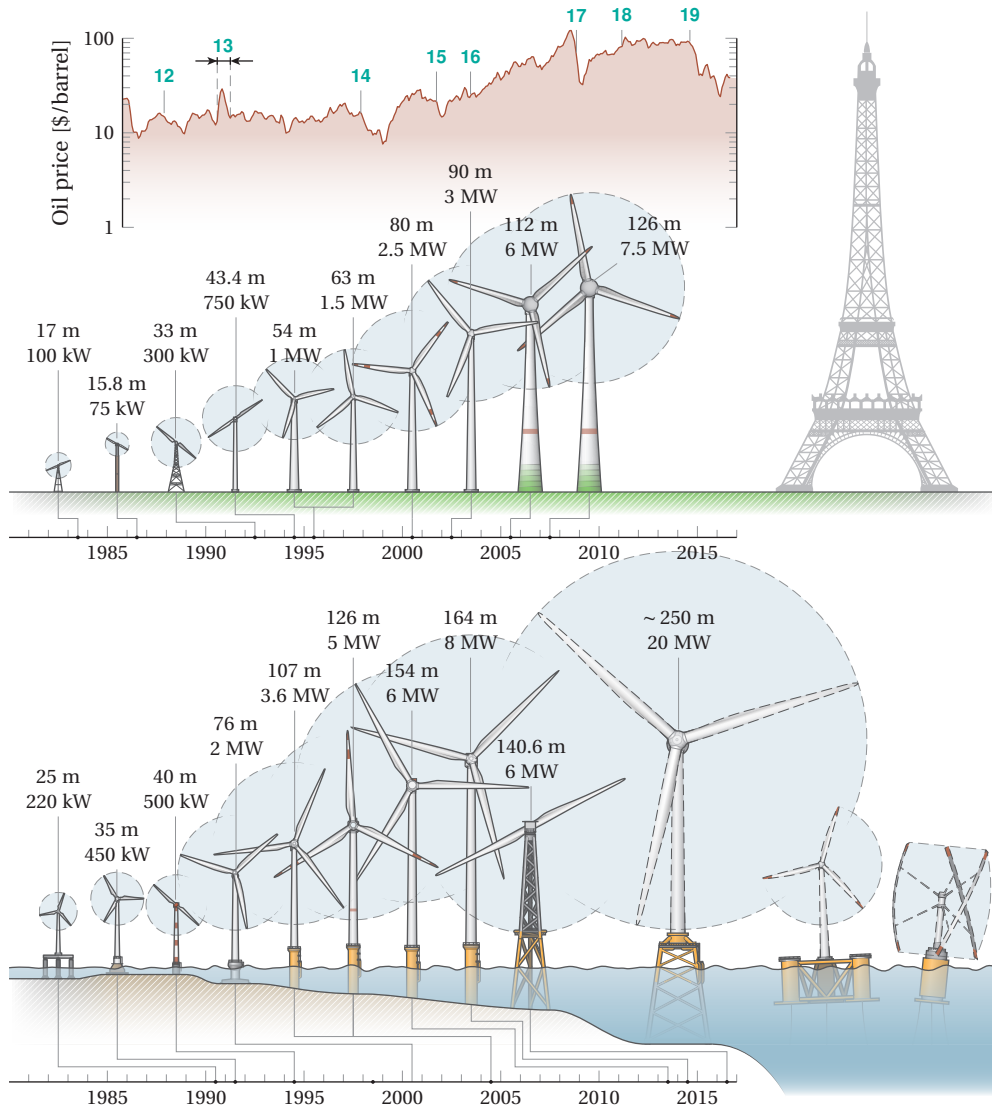
Figure 1.1 (*continued*): Historical development of wind energy and its link to the price of crude oil (US Energy Information Administration, 2016). **12:** *Stock market crash* (1987). **13:** *Gulf War* (1990–1991). **14:** *Stock market crash and start of the Asian financial crisis* (1997). **15:** *11 September terrorist attacks* (2001). **16:** *U.S. invasion of Iraq* (2003). **17:** *Global financial crisis* (2008). **18:** *Arab Spring* (2011). **19:** *Oil price drop* (2014).

overtaken by Asia. This was mainly due to the massive deployment of wind energy in China, where 33.9 GW was installed in 2015 alone, totalling over 145 GW.[4]

---

[4] One notable project is the construction of the onshore wind farm in Gansu, China, which began in 2009 and is planned to output a total of 20 GW in 2020 (Reuters, 2009).

Favored by the economies of scale, wind turbines and their power ratings grew as new materials and control methods became available to support longer blades. In 2000, the largest commercial machine already had a rotor diameter of 80 m and was rated at 2.5 MW. Turbines of 3 MW and up shortly followed in the years after. Most of these were upscales of previous versions, which is a strategy that many manufacturers chose to eliminate part of the risk from the design process. A prototype of a 126-m diameter, 5-MW machine was installed at the end of 2004. It was superseded by a 6-MW (an upgrade of an earlier 4.5-MW version from 2002) and 7.5-MW unit in 2005 and 2007, respectively.

At the same time, with the prospect of higher energy yields, the industry also focused more on offshore development. In 2000, the world's largest offshore wind farm was installed near Copenhagen with twenty 2-MW units. The first true large-scale farm was constructed in Horns Rev, 14–20 km off the coast of Denmark. It features a total of 80 wind turbines—all 80-m diameter, 2-MW machines—and became operational in 2002. In the Netherlands, the first offshore wind farm was commissioned in 2007 with 36 turbines of 3 MW, located 10–18 km off the coast of Egmond aan Zee.

From the late 2000s, offshore wind farm projects have greatly increased in scale. A second wind farm in Horns Rev, Denmark, commissioned in 2009, had the title of world's largest offshore farm with a total of 209 MW installed capacity. It was overtaken by a 300-MW farm in 2010, and ultimately by a 630-MW farm in 2013, both off the coast of Kent in the United Kingdom. In 2014, the oil price greatly dropped after a period of relative stability, which caused much of the investments in the offshore oil and gas industry to stagnate. However, despite the clear negative effect this has on the competitiveness of wind power overall, it also led to lower interest rates, lower steel prices, and cheaper offshore transport (e.g., see ECB, 2016). As of 2016, many projects exceeding 1–2 GW already exist in a proposal stage.

The growth in the offshore wind energy sector also triggered many manufacturers to focus on dedicated offshore turbines. These are tailored to the offshore wind climate, but also aim to reduce some of the cost drivers. Two-bladed machines, of which a 6-MW prototype was installed in 2014, are again interesting because of their lower top mass and the ease of transport and installation. In addition, different foundation designs for deeper waters are being investigated to expand the amount of suitable offshore sites. For very deep waters where fixed-bottom foundations are no longer economical, floating wind turbines may be a valid alternative. This also sparked a renewed interest in vertical-axis wind turbines, which benefit from a low center of mass (e.g., see Paulsen et al., 2015).

1.1.2 Challenges in upscaling

The widespread success of wind energy is tied to its ability to be cost-effective. Especially for offshore plants, the price per kWh of energy is still roughly twice of what is generated onshore and and three to four times the price of brown coal.[5] Most of the capital costs of an offshore wind plant (30–50%) are made up by the wind turbines and, as drawn in Figure 1.2, nearly half of the costs of the wind turbines are due to the tower and rotor blades.

---

[5]   For Germany in 2013, the levelized cost of electricity (LCOE)—which is the average price of a unit of energy that a plant produces compared to its investment costs, operations costs, and fuel costs, but excluding any externalities—was 0.045–0.107 €/kWh for onshore wind, 0.119–0.194 €/kWh for offshore wind, and 0.038–0.053 €/kWh for brown coal (Kost et al., 2013).
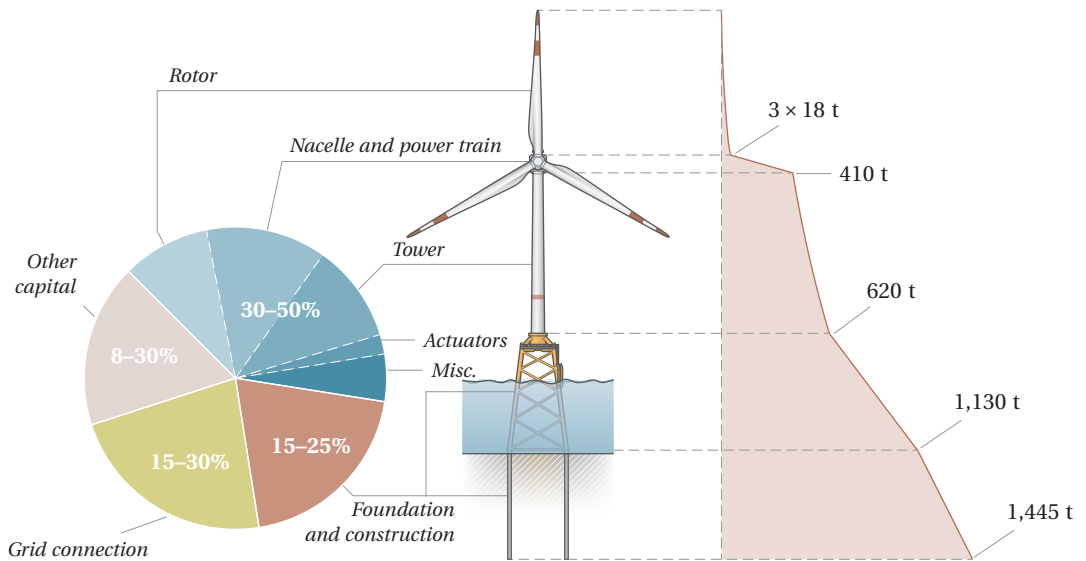
Figure 1.2: Capital cost breakdown (left) and cumulative mass distribution (right) of a representative offshore plant with a 5-MW wind turbine (DOTI, 2015; EWEA, 2007; Seidel, 2007; Taylor et al., 2015).

Whereas many have argued that onshore machines have reached their maximum size because of visual impact and transport limitations, offshore machines still continue to grow. In 2014, the world's largest wind turbine was a 164-m diameter, 8-MW prototype installed in Denmark. A study on the upper limits concluded that even 20-MW units, with a rotor diameter in the order of 250 m, are technically feasible (UpWind, 2011). By upscaling the rotor, the energy yield of a wind turbine increases proportional to the square of the diameter, while many of the capital costs—such as the price of the grid connection—remain roughly the same. However, the volume and masses of many of the structural components increase by the cube of the diameter.[6] This is the effect of the *square-cube law*, of which examples can be found from engineering to biology. For instance, if a human being would be scaled up linearly, he or she would collapse under their own body weight, since the masses outgrow the cross-section of the bones and muscles.[7] It also explains why ants are capable of carrying objects many times their own weight, but whales suffocate if not supported by the buoyancy of seawater.

A wind turbine suffers from the square-cube law for the simple reason that every additional kilogram of mass has to be supported by a structural element, which is supported by another structural element, which all have to be manufactured, transported, and installed on a remote location. This puts an exceptionally high penalty on overdimensioning the blades (i.e., making things stronger and heavier than they need to be), since the extra weight is easily amplified by the tower and the foundation. In Figure 1.2, for

---

[6] Doubling the length of the blades would increase the rotor area, and therefore the energy capture, by a factor 4. Unfortunately, it would also increase their volume and masses by a factor 8.

[7] This is why the bones of elephants are proportionally much thicker than those of a mouse.

example, a 410-ton rotor-nacelle assembly is carried by a 210-ton tower, mounted on a 510-ton jacket structure.

1.1.3 **Probabilistic design and extreme loads**

Over the years, the way for turbines to grow in diameter has been through advances in materials science, structural design, and load reduction. However, this is becoming increasingly difficult as machines push towards the limits of engineering. But apart from finding new ways to cope with the higher loads, another strategy is to design closer to an economical failure rate. This is the *probabilistic design* approach.

Ideally, a wind turbine should be strong enough to survive its design lifetime, but not too strong. Every year of operation, there is a probability of a catastrophic failure, such as a blade snapping off or the tower collapsing. This failure probability can be reduced by increasing the safety limits on the design, thereby making it stronger but heavier. However, at some point, preventing a very rare failure no longer outweighs the cost of a more expensive design.[8] In theory, it is exactly that point where a design is most economical.

Various target failure probabilities exist for various applications, depending on the consequence of failure. For example, unmanned offshore platforms are designed for an annual failure probability of 0.05% (once every 2,000 years), but manned platforms are designed for a 0.003% probability (once every 33,000 years), as set by the ISO (2001). In the Netherlands, the probability that an area of land may flood is set per dike-ring. Based on the number of inhabitants and the economic activity, this number may vary from 0.4% (once every 250 years) to 0.01% (once every 10,000 years) (e.g., see Vergouwe, 2014, p. 12). Other examples are the so-called *life-critical systems*—such as defibrillator machines, aircraft avionics, or car airbags—which are designed for a 0.001% annual failure rate (once every 100,000 years). These target risks are deliberately set by designers or by society. In fact, that such probabilities are not at all unrealistic is proven by the fact that many people are willing to accept a one-in-ten-million chance to win the lottery.

The major structural components of a wind turbine are sized to handle the *long-term loads*, which divide roughly into *fatigue loads* and *extreme loads*. Fatigue damage is caused by cyclic loading, like the blades experiencing alternating low and high wind speeds while rotating. Over a turbine's design lifetime, it will accumulate the damage of well over 100 million of these cycles.

Extreme loads, on the other hand, are more or less coincidental events that are very hard to predict. Because of the computational burden of running complex simulation models, the load belonging to a certain target probability is often estimated by extrapolating the short-term load peaks. This process is sketched in Figure 1.3. A designer will run a limited number of simulation cases from which the highest loads are extracted. Out of ten extreme loads, for example, the five highest loads will determine the level that belongs to a 50% probability of exceedance. Subsequently, the highest of ten loads sets the 10% level. As long as these peaks are representative of one type of extreme load behavior, this trend can be followed towards very low probabilities to find some N-year extreme load. However, one can imagine that another randomized sample of loads would have produced

---

[8]   For example, one would readily accept an additional 0.1% chance of a turbine collapsing every year if it would half the investment costs.
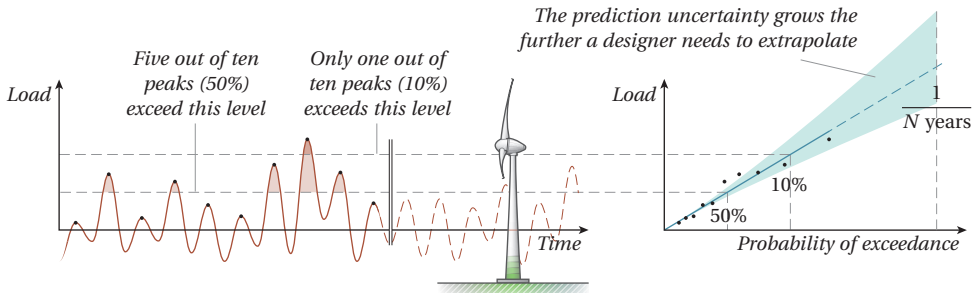
Figure 1.3: Prediction of extreme load behavior after simulating only a fraction of the turbine's design lifetime. Load peaks are extracted from a time series and sorted. With enough data available, a trend becomes visible that can be matched to a distribution function and extrapolated to very low probabilities.

a different trend and a different N-year load. As a result, extreme load predictions are clouded by uncertainty the further one needs to extrapolate.

Reducing this uncertainty is an important issue in wind turbine design. High uncertainty means high risk, which will have to be accounted for by safety factors and may lead to gross overdimensioning. Obtaining good extreme load predictions are particularly difficult to obtain in the conceptual design phase. At that stage, the computational budget for simulations has to be shared between several concepts and multiple design iterations. Any gains made by gradual changes to a design can be easily outweighed by the uncertainty. Therefore, it is hard to evaluate whether certain solutions are able to achieve actual weight reductions.

1.2 Why study gusts?

Within the context of wind energy, this research on wind gusts is motivated by three main objectives. The first reason is to better predict the extreme load behavior of wind turbine components with less effort. One can imagine that extreme load peaks are highly correlated to the gusts that are spawned within the wind field. When a designer has the ability to directly model such interactions, in theory, the computational budget can be used much more efficiently and the uncertainty surrounding ultimate design loads can be tremendously reduced. This may mean lower safety factors and therefore weight reductions, which in turn means lower capital costs and, ultimately, cheaper energy.

Secondly, wind turbine rotors have grown—and are still growing—to unprecedented sizes. Whereas a strong gust could completely envelop a machine in the 1980s, the same gust now only affects a fraction of a modern-day rotor blade. Some widely used gust models that still assume a uniform inflow are outdated and need to be replaced by a more physical model.

Finally, wind gusts form an interesting scientific topic. Although many have some kind of idea of the concept of a gust, they remain rather abstract phenomena. In fact, understanding gusts is one of the long-term research challenges that lie in the field of wind energy (Van Kuik et al., 2016). This thesis work aims to make a significant contribution to this.

3 A mathematical treatment of gusts
What do the velocity fields around extreme gusts look like in space, and how often do they occur?
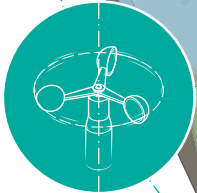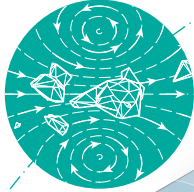
2 The nature of wind gusts
A gust is a familiar concept to many, but what is it exactly?

1 Introduction
Where does this research fit into the total picture?

4 Gust loads on rotor blades

How do gusts affect rotor blades? Are certain parts more vulnerable to high gust loads?

5 Predicting extreme gust loads

What are the highest loads over the long run? How can they be accurately predicted early in the design phase?

6 Conclusions

What are the major findings? What does the outcome of this research mean for the field?
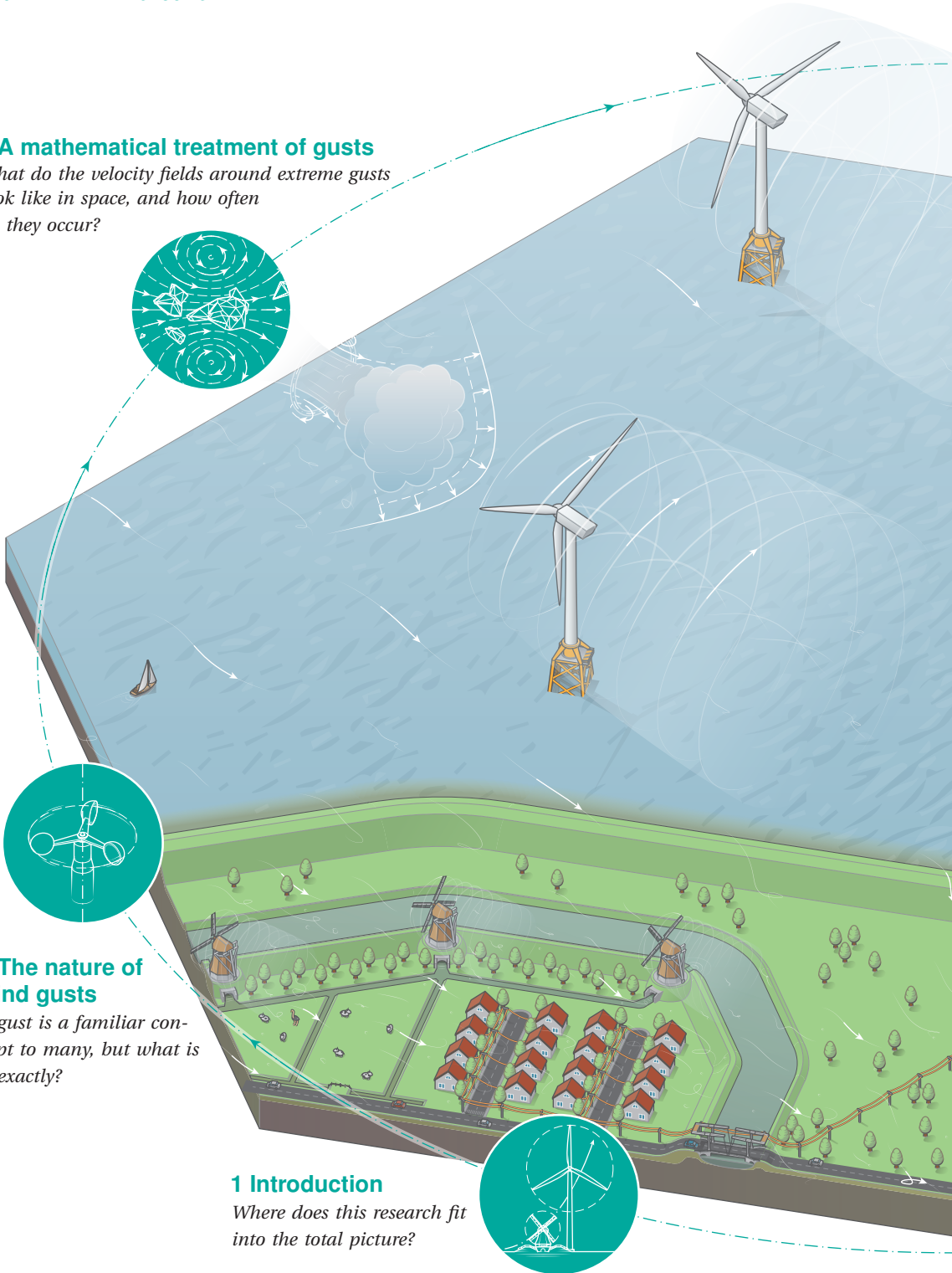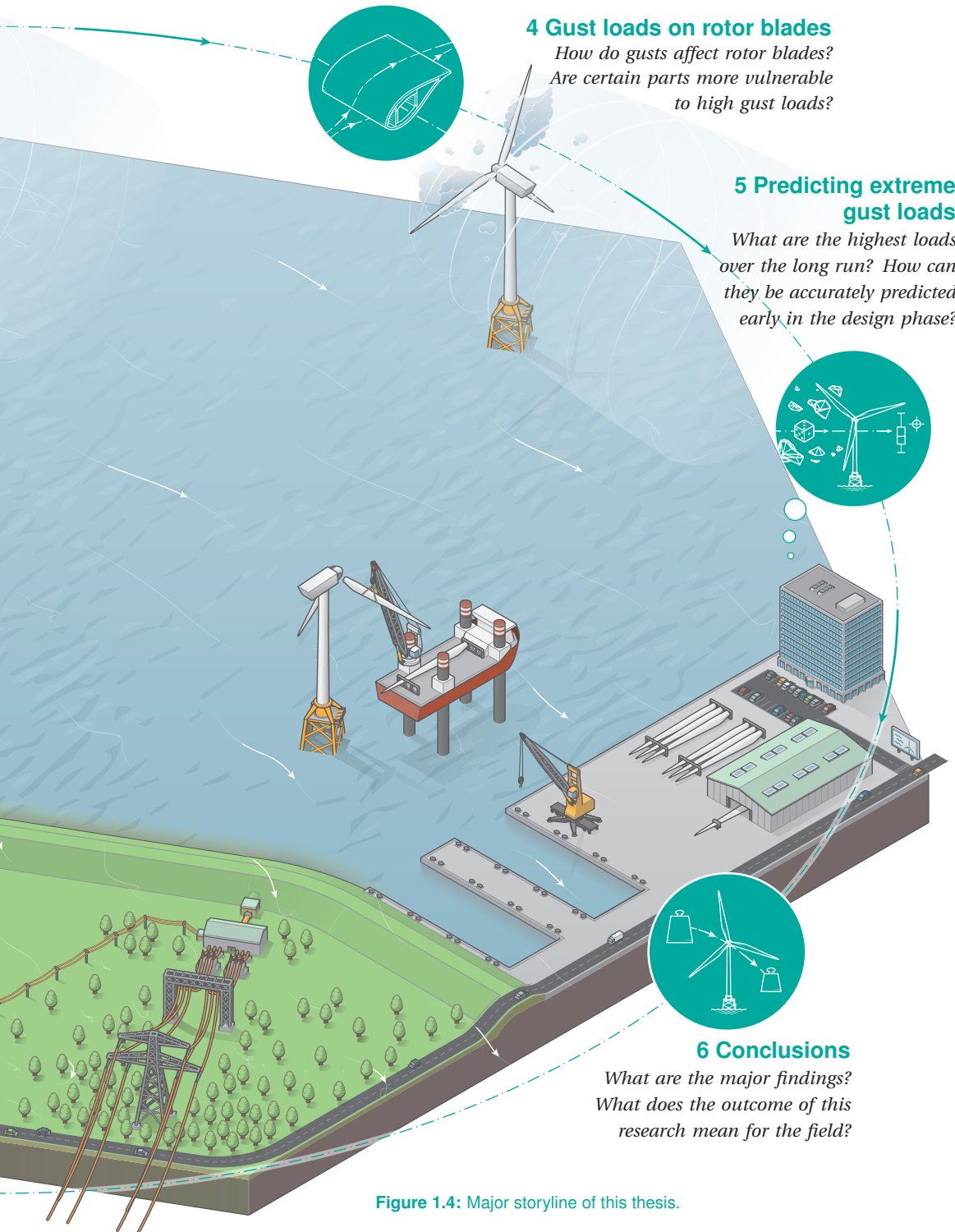
Figure 1.4: Major storyline of this thesis.

1.3 **Thesis outline**

In this thesis, the work is divided into four core chapters that can, more or less, be read independently. Nevertheless, they are part of a bigger storyline, illustrated by Figure 1.4.

First, Chapter 2 will focus on gaining a better understanding of gusts and some of the driving mechanisms. It is written to be accessible to a somewhat wider audience, as it touches several fields of engineering. Furthermore, it also motivates the direction that is taken in Chapter 3, which presents a mathematical description of a wind gust in a three-dimensional velocity field. In addition, these events will be connected to a probability to make them suitable for design exercises. Using this model, Chapter 4 will start to explore some of the consequences of dealing with gusts that are finite in space. That the understanding of extreme gusts indeed leads to better extreme load predictions is proven by Chapter 5. Several methods are presented there to replace brute force Monte Carlo methods that are able to achieve considerable reductions in uncertainty. Finally, Chapter 6 will wrap up the most important findings and will hand out some recommendations for future research.

Chapter 2
The nature of wind gusts

"Windmills, which are used in the great plains of Holland and North Germany to supply the want of falling water, afford another instance of the action of velocity. The sails are driven by air in motion – by wind."

— HERMANN VON HELMHOLTZ, *1847*

THE WIND is, of course, where it all starts. This first core chapter deals with wind and gusts in a more general sense. Its purpose is to make certain concepts tangible before diving into the hard mathematics of Chapter 3. The discussion will be somewhat limited to our current understanding of gusts, but will also address some of the areas where it falls short. By doing to, it will open a direction that the rest of this thesis work will follow.

First, Section 2.1 takes off with a general introduction of the wind climate in the atmospheric boundary layer. Then, Section 2.2 focuses on the question "what is a gust?" by approaching it from several perspectives. These different ways of looking at gusts has also led to the development of different gust models for engineering problems, of which a couple of examples are discussed in Section 2.3. Finally, Section 2.4 will treat the statistics of real-life gusts measured offshore.

2.1 The atmospheric boundary layer

Wind is one of nature's ways to restore balance. On a global scale, an imbalance exists because the Equator receives more solar energy than the areas around the poles, while the Earth rotates and only one side is heated at a time. The result is that quantities such as heat, momentum, and moisture are carried by the wind and redistributed over the Earth's surface, steered by our planet's rotation and the high and low pressure systems. Close to the ground lies the *atmospheric boundary layer*, which is the lowest part—say, the first 100 to 3,000 m (Stull, 1988, p. 4)—of the troposphere that is directly influenced by the presence of the Earth's surface. It is also the realm where almost all of human life is situated (except for the people in airplanes and a handful of astronauts). Buildings, wind turbines, and ground vehicles all have to be engineered to withstand anything that can happen inside this layer. This includes storms, but also years of being exposed to the everyday conditions.
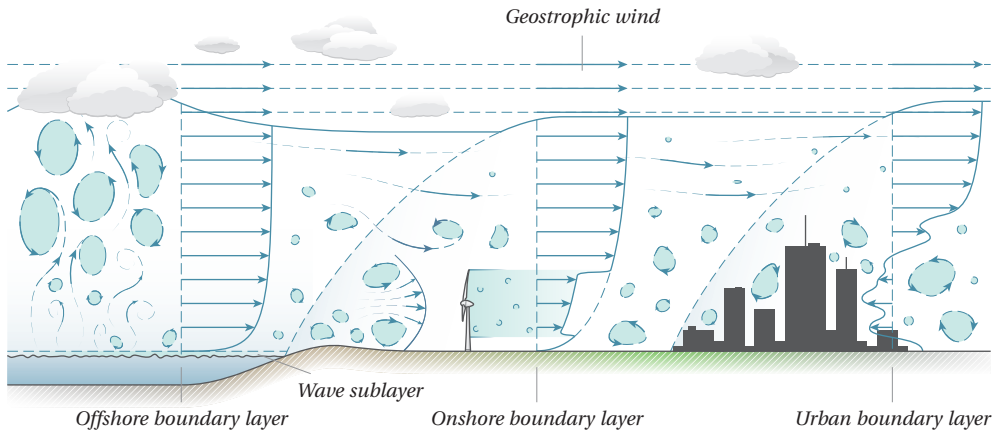
Figure 2.1: Sketch of the atmospheric boundary layer.

The wind speed in the atmospheric boundary layer varies from approximately zero, very close to the ground, to that of the geostrophic wind.[1] The way in which it varies with height is called *wind shear*. Naturally, a rough surface with a lot of obstacles slows the wind down more than a clean, flat surface (see Figure 2.1). This can get very complex when moving offshore. There, pressure differences surrounding the waves give rise to a sublayer extending up to five times the wave height (Emeis, 2011). Stronger winds produce higher waves that, in turn, increase the roughness of the sea surface.

Wind shear also depends greatly on the *atmospheric stability*, which is the tendency for air parcels to rise and mix with their surroundings. For example, during a hot summer's day with lots of evaporation, air at the surface wants to leave its position and rise to higher altitudes. This is an *unstable* atmosphere, in which the boundary layer is well-mixed with a full velocity profile (i.e., weak wind shear). On the other hand, *stable* conditions are found during periods with almost no vertical transport (e.g., at night). In such cases, the boundary layer is characterized by weak mixing and a strong shear profile. A situation where vertical motions are neither encouraged or discouraged is called a *neutral* atmosphere.

The conditions over offshore sites are again somewhat different from what is found onshore. Partly, this is due to the large thermal capacity of water compared to the land surface. The ocean temperature hardly knows a diurnal cycle and, compared to the air temperature, lags behind the annual cycle by one or two months. In addition, the wind over seas is influenced by a strong upward flux of humidity that forms a significant part of the total buoyancy flux (Emeis, 2011). As a result, the offshore wind shear profiles can look very different from onshore profiles (Holtslag, 2016). Likewise, the wind conditions also vary from urban to rural areas. Flow that is separated from buildings and channeled through streets leads to a very complex and unpredictable wind climate. The effects on the atmospheric stability can be noticeable even at higher altitudes, owing to the heat that is contained and released by buildings.

---

[1]   The geostrophic wind is the (theoretical) wind that would exist when the pressure and Coriolis forces are in perfect balance.

Locally, the flow is dominated by *turbulence*. Turbulence is characterized by a highly chaotic flow where vortex-like structures, called *eddies*,[2] move in seemingly random[3] patterns while they mix the fluid properties at the smallest scales. As they are transported (advected) by the mean wind, eddies will interact with other eddies, causing them to stretch and tilt until they finally break down and become part of new eddies. The result is that the wind speed fluctuates heavily, both in space and time, and over a wide range of scales.

2.2 What is a gust?

Wind gusts, although being a familiar concept to many, are remarkably complex phenomena. Not necessarily because it is hard to grasp how and why the wind speed can change abruptly, but because a gust is more of a symptom that can be related to many different mechanisms.

A gust is commonly described as a brief increase in wind speed. Many English dictionaries, for instance, define it similar to

> "A sudden brief rush of wind"
>
> (Merriam-Webster Online, 2016)

Alternatively, the same phenomenon could be called a *blast* of wind, a *flurry*, a *whiff*, or a *puff*. All these words more or less match the common perception of a gust – being something of a jet, much like the air exiting one's mouth when blowing out a candle.

2.2.1 From a statistical perspective

The way that gusts are commonly described has to do with how the wind speed is measured, namely by small anemometers. These output a fluctuating signal that behaves like any other random process for which statistical tools are readily available. From the viewpoint of such a point observer—only able to perceive the velocity in a very small part of the total flow field—a gust is reduced to a perturbation from the *mean wind speed*.

The mean wind speed is traditionally determined over an interval of ten minutes,[4] corresponding to the spectral gap in the *Van der Hoven spectrum* (after Van der Hoven, 1957), sketched in Figure 2.2. This spectrum shows how much kinetic energy is stored in wind speed variations of a certain frequency. Obvious periodical effects are due to the seasons, the day-night cycle, and the movement of high and low pressure systems. On an hourly scale, though, there is often not that much variation during regular conditions. Therefore, the period of ten minutes up to several hours is commonly labeled the *spectral gap*. All the scales of motion that are lower in frequency are then assumed to shape the

---

[2] Although the terms *eddy* and *vortex* are often used interchangeably to denote a swirling motion of fluid, they are not always equal. In this work, a vortex is said to be a rather stable structure where the vorticity is concentrated along one single axis, whereas an eddy can have distributed properties within any closed streamline. Moreover, eddies have a viscous origin and are considered to be an integral part of the turbulent cascade (see Subsection 3.2.1). An idealized vortex, on the other hand, can exist in inviscid flow.

[3] "Random" is the word readily used for processes that are too intricate to fully grasp.

[4] Averages over longer time intervals—e.g., an hour or a day—are also common in climatology, for instance. In aviation, on the other hand, shorter intervals are often used in order to correctly represent the conditions during take-off and landing maneuvers.

mean wind speed, which tends to follow a *Weibull distribution* with varying shape and scale factors throughout the year.

On the smallest scales, on the other side of the spectral gap, is *turbulence*. This is a locally generated process and is often treated as something that is simply superimposed on the bulk wind speed. Separating turbulence from the mean flow is called the *Reynolds decomposition*, after Osborne Reynolds (1842–1912).[5] Mathematically, it is stated as

$$\underbrace{\mathbf{u}(\mathbf{x}, t)}_{\textit{Total velocity}} = \overbrace{\bar{\mathbf{u}}(\mathbf{x})}^{\textit{Mean flow}} + \underbrace{\mathbf{u}'(\mathbf{x}, t)}_{\substack{\textit{Unsteady} \\ \textit{component}}}. \tag{2.1}$$

where $\mathbf{u} = [u, v, w]^{\mathsf{T}}$ is the wind speed vector, with u pointing in the streamwise direction, w pointing vertically upwards to the zenith, and v given by the right-hand rule. The bar, $\bar{\square}$, is used to denote the mean (time-averaged) component and the prime, $\square'$, is used for the unsteady component. Moreover, $\mathbf{x} = [x, y, z]^{\mathsf{T}}$ is the position vector (where x matches the direction of u, etc.) and t is the time.

When turbulence is seen as a random process with countless eddies of different sizes moving in chaotic patterns, the *central limit theorem* is often used to argue that turbulent velocity fluctuations are normally (Gaussian) distributed. Each unsteady velocity component is then described by a zero mean and a variance, σ^2, which can be derived from a time series such as the one shown in Figure 2.3. The variances of the three velocity components added together yield the *turbulence kinetic energy* (TKE):

$$k \equiv \tfrac{1}{2}\left(\sigma_u^2 + \sigma_v^2 + \sigma_w^2\right). \tag{2.2}$$

The turbulence kinetic energy is a quantity that—as the name might imply—describes how much kinetic energy is carried by the turbulent eddies. Its definition states that energetic field of turbulence is described by a wide probability distribution where high velocities are common.
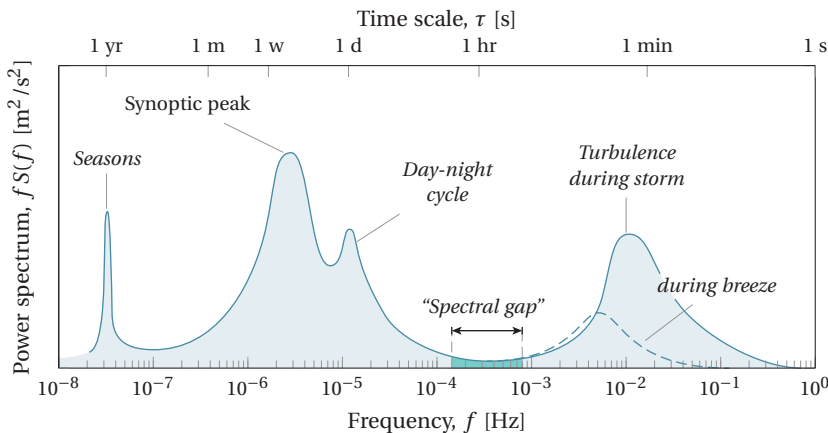
Figure 2.2: Van der Hoven spectrum (1957) as drawn by Alan Davenport (Isyumov, 2012).

---

[5]   Though, the same concept was already mentioned by Leonardo da Vinci (1452–1519), who recognized that turbulent structures are carried by the bulk flow.

Cup anemometer records a one-dimensional signal as it samples the wind field
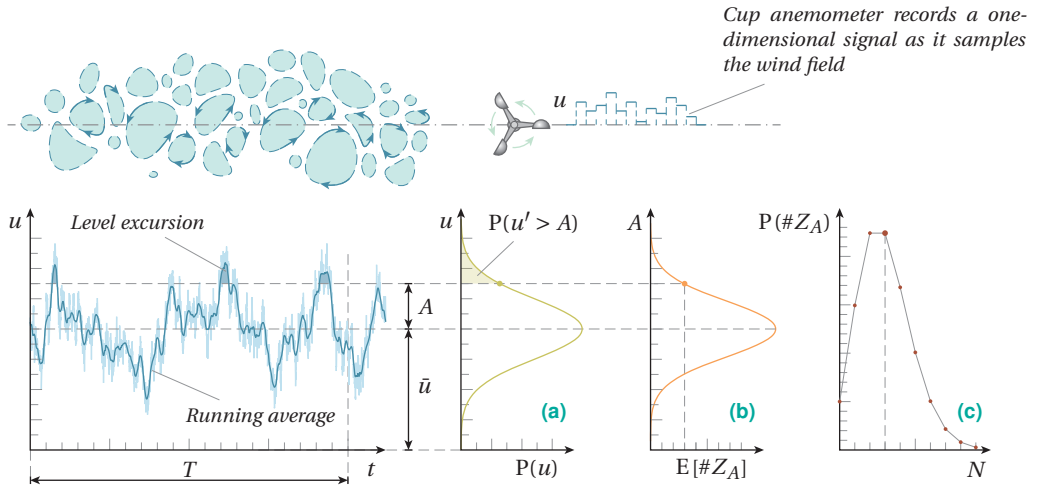
Figure 2.3: Different from the physical approach, statistics is not necessarily interested in how gusts are exactly formed. Strong gusts appear naturally as the extremes of a random process, which can be predicted as long as the statistical parameters of the process are known (e.g., see Kristensen et al., 1991). In meteorology, gusts are commonly recorded from a 3-second running average (Beljaars, 1987a,b). The bulk of these velocity fluctuations are Gaussian and can be fitted to a *normal distribution* **(a)**. The mean (expected) number of peaks that pass a certain threshold level, A, during a time period, T, is predicted by *Rice's formula* **(b)**. Given that mean, the probability of N of such peaks actually occurring is given by the *Poisson distribution* **(c)**.

The same variance is also contained under the turbulent part of the spectrum and can be found by integrating the spectral density, $S(f)$, over that frequency range.[6] Specifically for the u-component, this is expressed as:

$$\sigma_u^2 = \int S_{uu}(f)\,\mathrm{d}f, \tag{2.3}$$

which is the *zeroth-order spectral moment*. In addition, the spectrum also contains higher-order statistics. The *second-order spectral moment*, in particular, describes the frequency (or the steepness) with which the wind speed moves up and down.[7] This can be expressed as the variance of the first derivative and is obtained from the spectral density by

$$\sigma_{\dot{u}}^2 = \int (2\pi f)^2 S_{uu}(f)\,\mathrm{d}f, \tag{2.4}$$

where the single dot is used to denote the first time derivative. Together, the zeroth- and second-order spectral moments completely define the gustiness of the wind by setting both the amplitudes and frequencies of the velocity fluctuations. Under the strict

---

[6] Here, $S(f)$ is used to specifically denote the spectral density as a function of temporal frequency. In the following chapters, the focus is more the wave number spectra, $E(\kappa)$ and $\mathbf{\Phi}(\kappa)$.

[7] For example, think of a low- and a high-frequency sine wave of the same amplitude. The variance of the two signals is the same, but the amount of level crossings is not. This difference is described by the second-order spectal moment.

assumption that turbulence is Gaussian, *Rice's formula* (1944) expresses the expected number of isolated events where the velocity amplitude exceeds a certain level:

$$\mathrm{E}\,[\#Z_A] = \frac{T}{2\pi}\sqrt{\frac{\sigma_{\dot{u}}}{\sigma_u}}\,\mathrm{e}^{-\frac{A^2}{2\sigma_u^2}}, \tag{2.5}$$

where T is a given time period, A the threshold level, and where Z_A is used to denote the set of threshold exceedances.

These high amplitudes are called *gusts*, which usually last for a couple of seconds before they drop back below the threshold level. In meteorology in particular, gusts are usually defined as peaks of the "instantaneous" wind speed, which is a running three-second average:

> "**WIND GUST** is the maximum 3-second wind speed (in knots) forecast to occur within a 2-minute interval at a height of 10 meters. Wind gust forecasts are valid at the top of the indicated hour."
>
> (National Weather Service, 2016)

This three-second average is used to negate the effects of the anemometer's response time and the rest of the (digital) measurement chain, but also to restrict gusts to events that are relevant for large structures (Beljaars, 1987a,b).

Peaks where the velocity exceeds very high amplitudes (e.g., several standard deviations above the mean) are *extreme gusts*. The expected number of such events can be used to formulate the probability of finding N gusts in the same time period. This requires the *Poisson distribution*, expressed as

$$\mathrm{P}\,(\#Z_A = N) = \frac{(\mathrm{E}\,[\#Z_A])^N}{N!}\mathrm{e}^{-\mathrm{E}[\#Z_A]}. \tag{2.6}$$

It leads to the perhaps somewhat confusing result that, if an event occurs once every hour on average, it is not guaranteed to happen every hour. In fact, the probability of it occurring in any hour-long period is about 37% and the probability of it not occurring at all is also 37%. Still, the Poisson distribution is successful in modeling all kinds of events, ranging from the amount of callers waiting in line at a helpdesk to the number of Prussian army men accidentally kicked to death by horses (Von Bortkewitsch, 1898, pp. 23–25). An example of the Poisson distribution for $\mathrm{E}\,[\#Z_A] = 3$ can be found in Figure 2.3.

2.2.2 From a physical perspective

Clearly, looking at Figure 2.3, the statistical perspective is limited to the information that wind speed sensors can offer. These sensors are generally close to single-point observers that fail to grasp the spatial structure of the flow. In fact, several flow structures in the atmospheric boundary layer can leave a velocity signature that qualifies as a gust. Figure 2.4, for example, shows an overview of the scales of motion found within the Earth's atmosphere. This diagram appears in different forms in many textbooks on meteorology, but always shows that the length scale of flow structures is roughly proportional to the time scale at which they pass the observer. Gust events, with a time scale in the order of several to tens of seconds, would therefore classify as micro-scale structures that fit
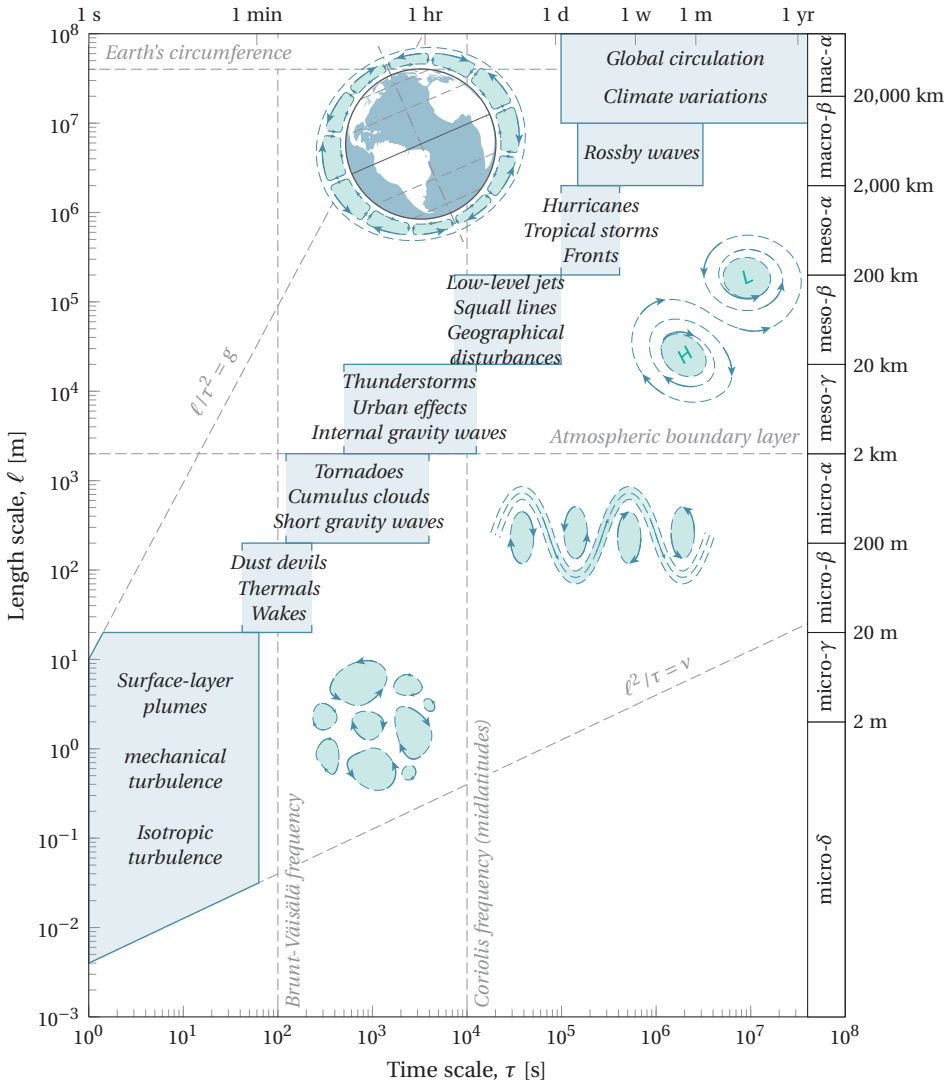
Figure 2.4: Meteorological scales of motion, compiled from the works of Orlanski (1975), Steyn et al. (1981), and Stull (2011). Here, ν and g are used to denote the kinematic viscosity and the acceleration due to gravity, respectively.

within the atmospheric boundary layer. Indeed, although different definitions for gusts exist for different fields of study, they are most commonly linked to turbulent eddies and the outflow of downbursts.

Looking at turbulence specifically, a gust is an air parcel that moves around as the flow is being rearranged (see Figure 2.5a). The more violent this rearrangement process is (i.e., the higher the turbulence kinetic energy), the stronger are the gusts. This means that gusty wind can be expected close to the ground and in the wake of objects. When
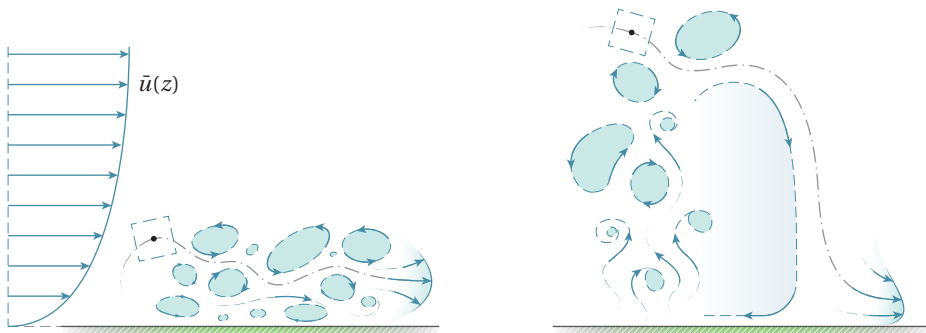
(a): An air parcel moving around in locally generated turbulence.

(b): An air parcel dropping from a higher altitude after overcoming the buoyancy flux.

Figure 2.5: Gusts can spawn from locally generated turbulence or, as hypothesized by Brasseur (2001), from turbulence at higher altitudes.
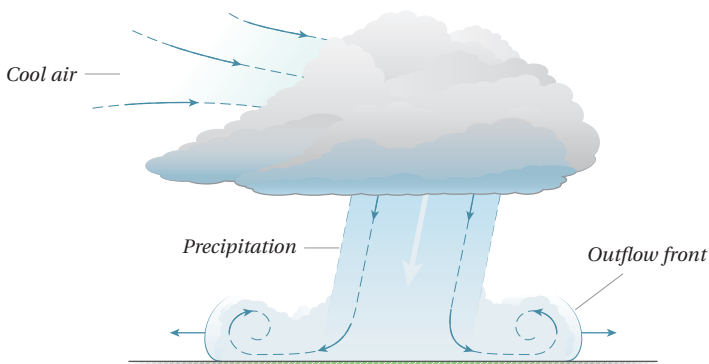
Figure 2.6: Sketch of a downburst.

buoyancy effects are taken into account, gusts can also be linked to vertical displacements of air. A popular method for gust forecasting, for instance, is the method of Brasseur (2001). It predicts that gusts can originate from turbulence at higher altitudes and drop down to ground level when their kinetic energy content is high enough to overcome the buoyancy flux (see Figure 2.5b). This could lead to events that cannot be predicted from local conditions, as they are spawned from a different TKE budget.

In addition, there are events on the gust time scale that are spawned outside the regular turbulence process. *Downdrafts*, for example, are caused by air that is being dragged down during a thunderstorm by the combination of precipitation and local cooling (see Figure 2.6). After this air column hits the ground, it spreads out radially from the point of impact and covers the area with high wind speeds and high turbulence levels. Downbursts are an example of *straight-line winds*, which are called that way to distinguish them from tornadoes.

However, the velocity signature from these events are no longer called gusts but *squalls*:

> "A sudden increase of wind speed of at least eight metres per second (16 knots), the speed rising to 11 metres per second (22 knots) or more and lasting for at least one minute;"
>
> (WMO, 1995, p. I.1-A–13)

These cases are also where the usual statistical approach fails. During a thunderstorm, the driving low pressure system can be very unstationary and can overlap the spectral gap in the Van der Hoven spectrum (Beljaars, 1987b, pp. 10–11). Turbulence is then no longer only generated locally, but is also strongly influenced by what happens on the mesoscale. This means that the turbulent scales of motion can no longer be separated correctly from the mean flow using simple ten-minute averages.

2.2.3 Extreme events

A particular case where the statistical and physical perspectives meet is the explanation of the *Draupner rogue wave*. This was a freak event that occurred on 1 January 1995 where a 26-m high ocean wave (crest to trough) hit the Draupner platform, located 160 km off the coast of Norway (see Figure 2.7a). Although the wave height on its own was, with a return period of 100 years, nothing extraordinary (Haver, 2004), it was very rare for the sea state at that time with a significant wave height[8] of 12 m (see Figure 2.7b).

Rogue waves have been a part of seafaring history for quite some time, but have usually been dismissed as tall tales. However, with the current modern ships, more and more people actually live to tell about their encounter with rogue waves. And especially with the coming of camera-equipped phones, video evidence is starting to pile up. Also, actual scientific evidence in the form of wave records is now becoming available—of

(a): Time series (Haver, 2004).

(b): Wave height distribution, where H_s is the significant wave height.
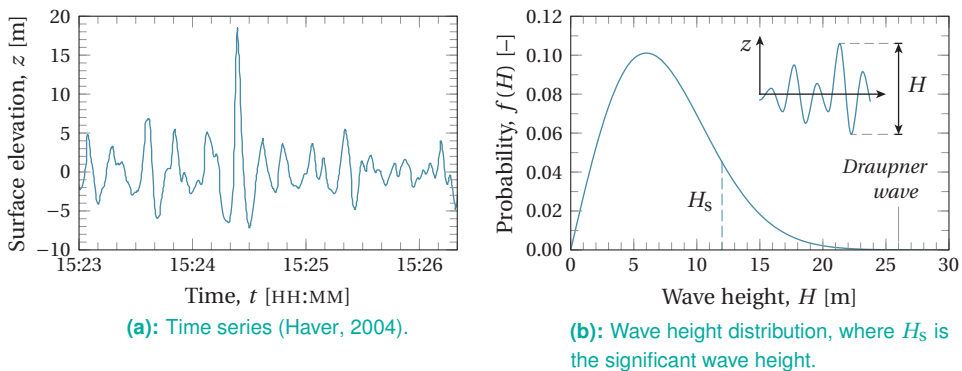
Figure 2.7: The Draupner rogue wave was an almost mythical event that occurred on 1 January 1995 in the North Sea.

---

8   The significant wave height is defined as the average wave height of the one-third highest waves. It also acts as the scale parameter for the Rayleigh distribution, which describes the probability density of the wave heights.

(a): NewWave (Tromans, Anaturk and Hagemeijer, 1991).

(b): NewGust (Bierbooms, Cheng et al., 2001).
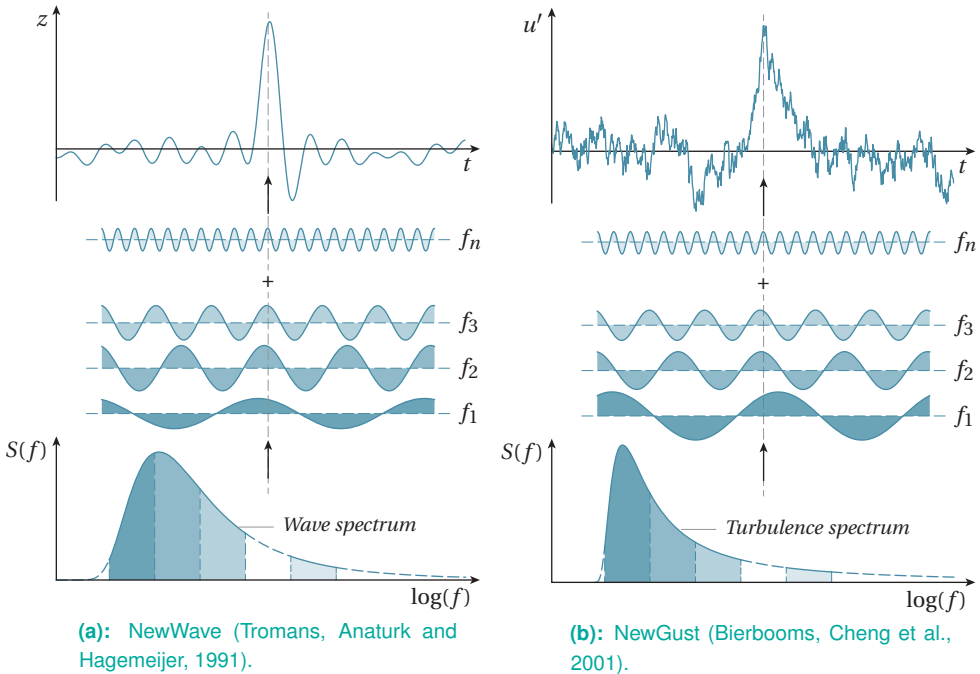
Figure 2.8: Principle of the *NewWave* and *NewGust* methods. Extreme events are synthesized through a summation of waves, each with a variance that covers part of the spectrum. The phases of the waves, however, are constrained in order to yield a prescribed amplitude.

which the Draupner wave was the first—which have shown that rogue waves are actually more common than previously thought (Smith, 2007).

There are multiple explanations for the existence of rogue waves. Arguments based on physics often point to nonlinear effects such as the Benjamin-Feir instability, where small waves travel slower than large waves and get swallowed up into one big front (Adcock and Taylor, 2014). Other authors point to sharp changes in water depth (Janssen and Herbers, 2009), special wind-wave interactions (Onorato and Proment, 2012), or crossing sea states (Ruban, 2010).

On the other hand, the statistical argument is that waves like this can simply be expected from regular conditions. A very high wave can arise from the interference of wave modes, where the crests of several waves of different lengths coincide to produce a peak. In fact, based on the theory of Lindgren (1970), rogue waves can be reproduced from the wave spectrum and synthesized through a Fourier series. This design practice, which is sketched in Figure 2.8a, is known as *NewWave* (Tromans, Anaturk and Hagemeijer, 1991).

The same principle can also be applied to gusts, since, as discussed earlier, many statistical properties of turbulence can be covered by a spectrum (see Figure 2.8b). Indeed, a similar process exists to recreate the shape of extreme gusts, aptly named *NewGust* (Bierbooms, Cheng et al., 2001). Although it is debatable whether sinusoids are a good representation of turbulent fluctuations, the gust shapes produced by this method come

very close to the actual measurements (Bierbooms, Dragt and Cleijne, 1999). Moreover, the NewGust method has been successfully implemented in wind turbine design exercises (Bierbooms, 2009) to replace brute force calculation methods.[9]

It is likely that these extreme waves and extreme gusts will become more common, simply because the worldwide data coverage is increasing. Considering the number of offshore platforms and scientific instruments in the North Sea, the Draupner wave was bound to happen somewhere sooner or later. This is a consequence of the *law of truly large numbers*:

> "*The Law of Truly Large Numbers.* Succinctly put, the law of truly large numbers states: With a large enough sample, any outrageous thing is likely to happen. The point is that truly rare events, say events that occur only once in a million [as the mathematician Littlewood (1953) required for an event to be surprising] are bound to be plentiful in a population of 250 million people. If a coincidence occurs to one person in a million each day, then we expect 250 occurrences a day and close to 100,000 such occurrences a year."
>
> (Diaconis and Mosteller, 1989)

A nice practical example of this is the maximum gust velocity measured at the data stations of the Royal Dutch Meteorological Institute (KNMI), plotted in Figure 2.9. Since the 1950's, the number of active stations in the Netherlands recording gusts has increased from 1 to 48. This has resulted into more extremes being logged, which might give the impression
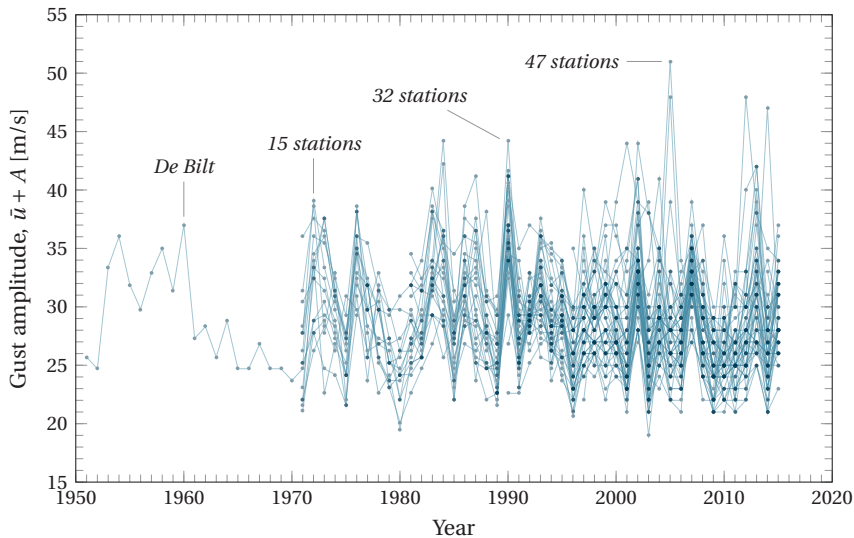

Figure 2.9: Annual extreme wind gusts measured at KNMI data stations from 1951 to 2015. The more data is being logged, the more common high-amplitude gusts appear to be.

---

[9] Though, with the growth in turbine diameter, the issue of extreme gusts becomes a three-dimensional problem. This will be the primary focus of Chapter 3.

that the wind climate is shifting towards stronger gusts.[10] However, although this gives some food for sensational news articles, this is not necessarily what happens in real life.[11]

2.2.4 From the perspective of a moving observer

How exactly wind gusts are experienced depends strongly on the observer's perspective. Traditionally, wind gusts have always been defined from the *Eulerian perspective*, which is the way a fluid is observed from an Earth-fixed reference frame. This should not come as a surprise, seeing as most wind speed sensors (anemometers) are mounted on towers or masts. From the Eulerian perspective, any stationary observer slices through the wind field much like a rock in a flowing river. If an approaching wind field, $\mathbf{u}(\mathbf{x})$, is imagined as a wave front that is being advected by a mean velocity $\bar{\mathbf{u}}$ (see Figure 2.10a), the turbulent eddies contained within that field approach the observer at fixed rate. The observed (sampled) wind speed at a point $\mathbf{x}_{obs}$ is then

$$\mathbf{u}_{obs}(t) = \mathbf{u}(\mathbf{x}_{obs}, t), \tag{2.7}$$

where $\mathbf{x} = \left[x, y, z\right]^{\mathsf{T}}$ is a position vector, $\mathbf{u} = [u, v, w]^{\mathsf{T}}$ a velocity vector, and t the time. In this case, an observer would experience a mean wind speed of $\bar{\mathbf{u}}$, and all the velocities that deviate are perceived as gusts.

Another way to observe the wind is from a *Lagrangian perspective* that moves along with the fluid's advection velocity, much like a leaf being carried by the wind. If an observer is released in the flow at a position $\mathbf{x}_{obs}(0)$ at $t = 0$, it would experience a velocity of

$$\mathbf{u}_{obs}(t) = \mathbf{u}(\mathbf{x}_{obs}(0) + \bar{\mathbf{u}}t, t). \tag{2.8}$$

Consequently, a Lagrangian observer does not sample the eddies along a forced path. What can possibly be perceived as gusts is merely caused by the turbulent mixing within the wave front itself. In fact, if the wave front is completely frozen in time, it would experience no gusts at all.

Gusts can also be measured from the *perspective of a moving observer*. For example, a cyclist riding at 10 km/h in the direction of a 15-km/h wind will experience a 5-km/h tailwind. Though, if the cyclist would accelerate to, say, 20 km/h, this changes to a 5-km/h headwind and the cyclist would no longer feel to be pushed by the wind, but would experience drag from it instead. Logically, this also changes the way turbulence is perceived:

$$\mathbf{u}_{obs}(t) = \mathbf{u}(\mathbf{x}_{obs}(t), t) - \dot{\mathbf{x}}_{obs}. \tag{2.9}$$

As drawn in Figures 2.10b and c, a moving observer can experience the same flow in different ways. A cyclist riding towards the wind will experience shorter and steeper bursts,[12] superimposed on a higher mean wind speed. A cyclist riding in the direction of

---

[10] Following the same train of thought, the growth of installed wind power capacity should also lead to more encounters with extreme gusts. In addition, the probability for a single machine to encounter an extreme gust increases with its swept area, since a larger volume of air is sampled.

[11] So far, there is no definite proof whether climate change is causing stronger gusts. There is some speculation that higher levels of moisture in the atmosphere can cause downbursts to occur more frequently(KNMI, 2009, p. 22). On the other hand, the *mean* wind speed has been gradually decreasing over the Netherlands, mainly due to an increase in building density (KNMI, 2015, p. 16).

[12] An observer moving towards the wind will sample more eddies than a stationary observer, which increases the chance of encountering stronger gusts.
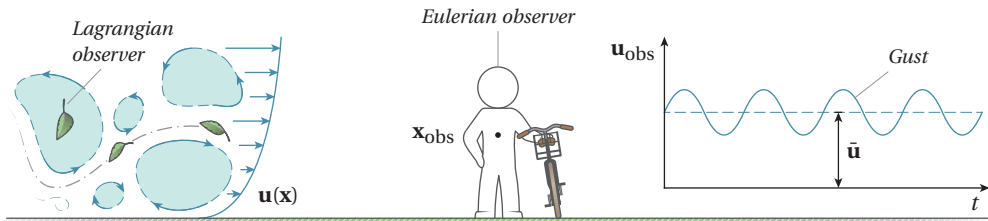
(a): For an Eulerian observer, the rate at which eddies are sampled is determined by the advection velocity, $\bar{\mathbf{u}}$. A Lagrangian observer, moving with the wind field, would only perceive the velocity gradients that result from turbulent mixing within the wave front.
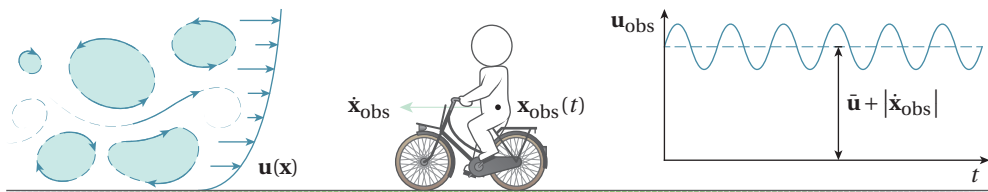
(b): An observer moving upwind will experience a higher mean wind speed with shorter, steeper gusts.
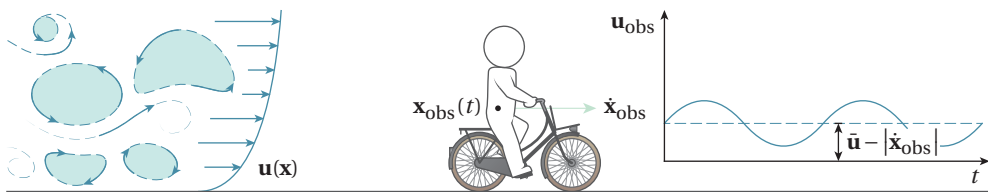
(c): An observer moving downwind will experience a lower mean wind speed with longer, more gradual gusts.

Figure 2.10: A cyclist sampling turbulent eddies transported by a wave front.

the wind, on the other hand, will perceive a much calmer wind climate where the gusts are stretched out over time, maybe even up to the point where they are no longer relevant.

The interplay between an observer and a wind field can be very complicated, and what is exactly perceived as a gust is very situation-dependent. For example, a kite flying crosswind will sample eddies along a certain flight path in a plane perpendicular to the wind, rather than only in the streamwise direction (see Figure 2.11a). In addition, it already experiences changing velocities that result from turning and diving. Another example is a rocket flying through a steady stream, as drawn in Figure 2.11b. Even though the wind speed is constant in time, the rocket will experience a sudden burst in crosswind that results in something best described as gust loading. Similar situations arise when ground vehicles pass through the wake of their surroundings, such as a car driving past an opening in a sound barrier.

2.2.5 **From the perspective of a large structure**

Up until now, gusts have been loosely defined as fluctuations of wind speed, which is also how they are measured in practice. The Royal Dutch Meteorological Instutute (KNMI), for instance, will give out a warning for very severe gusts if their velocities are expected to exceed 100 km/h. Other synonyms for a gust, such as *wind blast* or the Dutch "windstoot" (thrust of wind), also give the impression that they can be treated as one-dimensional. This more or less matches our own perception of a gust, being something that is much larger than the average person, and how large exactly is not really relevant.
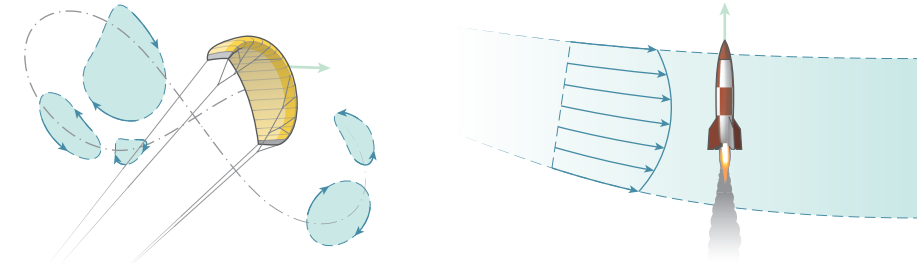
(a): A kite flying crosswind samples turbulent eddies in the plane perpendicular to the wind.

(b): A rocket flying through a steady stream will perceive gust loading, even though the stream itself is generally not classified as a gust.

Figure 2.11: Moving observers perceive a turbulent wind field very differently from an Eulerian (stationary) observer.

Figure 2.12: For very large structures, it can no longer be assumed that gusts extend infinitely in space. Instead, they have to be treated as volumes.

However, there are plenty of cases imaginable where just a velocity is not enough information. Take a bridge spanning a river, for example (see Figure 2.12). Hopefully, the engineers who designed the bridge have made sure it can withstand any wind gust it could encounter within its lifetime. At the same time, they cannot reasonably expect a 100-km/h gust ever being able to engulf an entire bridge, maybe spanning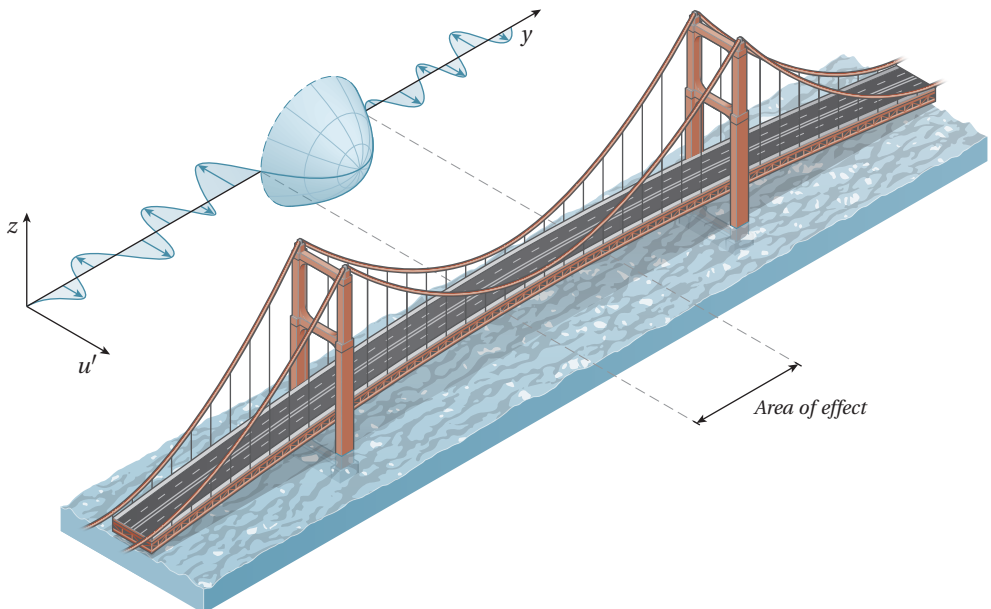 hundreds of meters. Clearly, for such a bridge, and for many other types of structures, a designer needs to know much more than just a velocity amplitude.

Gusts are relevant for many branches of engineering because they push and pull objects; that is, they apply a force, F. From basic aerodynamics, it is known that

$$F \propto \tfrac{1}{2}\rho u^2 S, \tag{2.10}$$

where ρ is the air density and S the object's frontal surface. The first parameters grouped together make the *dynamic pressure*, $\tfrac{1}{2}\rho u^2$. In aerospace engineering, most notably in rocketry, the point in a flight trajectory where a vehicle experiences the maximum dynamic pressure is called "max Q". Passing max Q is a critical point for the launch of spacecraft, since it is the moment at which the structure is expected to undergo the highest loads.

This concept works for rockets, at least, since the majority of the incoming velocity, u, is made up from their own forward motion and is relatively uniform over S. In the case of the bridge, however, the maximum dynamic pressure might be stored in a localized peak that is much smaller than the bridge itself. Integrated over the volume of this peak, V, it yields the *kinetic energy*:

$$K = \tfrac{1}{2}\rho \int_V \|\mathbf{u}(\mathbf{x})\|^2 \, \mathrm{d}\mathbf{x}. \tag{2.11}$$

The amount of kinetic energy stored in a gust determines the damage it can potentially inflict by deforming and ultimately breaking a structure (see Figure 2.13). However, for a designer, energy is not a convenient measure for the strength of a gust. This is because it has no direction and does not separate well from the mean wind.

Instead, when a designer is interested in impulse loads and stress levels, the quantity that is directly relevant is *momentum*. Momentum is defined as mass multiplied by
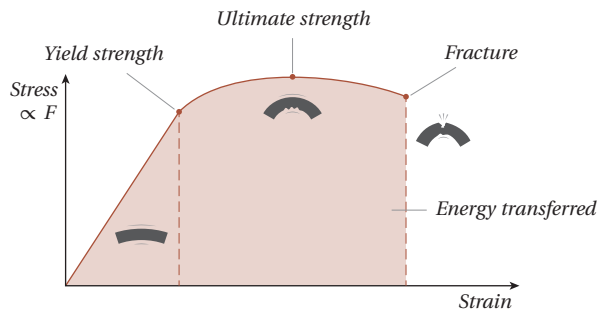
Figure 2.13: A generic stress-strain curve. While under the yield strength, a material deforms elastically. Above it, a material enters the plastic region, where the material undergoes permanent deformation until it fractures. The total energy that is transferred to the structure is given by the area under the curve.
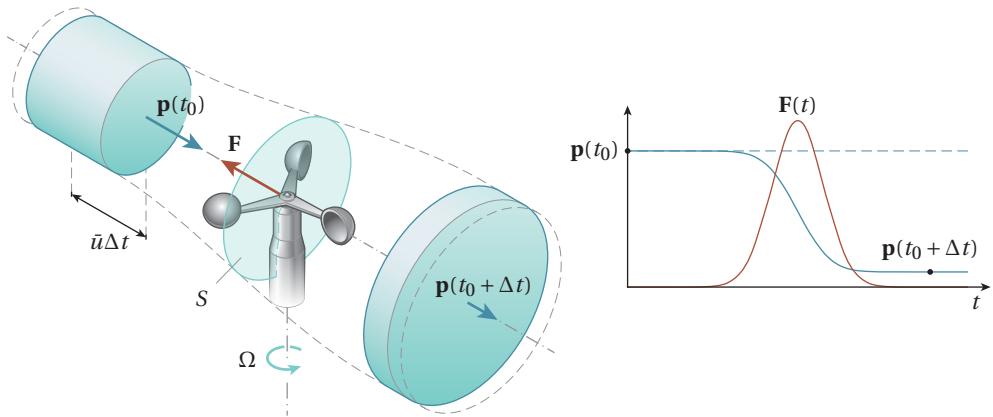
Figure 2.14: An air parcel interacting with a cup anemometer over an effective surface, S, and a sampling period, Δt. The parcel loses momentum as the anemometer pushes back on the flow with a force, **F**.

velocity and can be found by integrating the velocity over the gust's volume, V:[13]

$$\mathbf{p} = \rho \int_V \mathbf{u}(\mathbf{x})\,d\mathbf{x}. \tag{2.12}$$

When a gust interacts with an object, it can transfer some of its momentum through the *impulse-momentum* relation. The force, **F**, transmitted to an object equals the change in momentum, **p**, of a gust:

$$\mathbf{F}(t) = -\frac{d\mathbf{p}}{dt}. \tag{2.13}$$

In reaction, the object pushes back on the flow. Over a time period Δt, this weakens the gust according to

$$\mathbf{p}(t_0) - \mathbf{p}(t_0 + \Delta t) = \int_{t_0}^{t_0 + \Delta t} \mathbf{F}(t)\,dt. \tag{2.14}$$

Even in the case of a cup anemometer—which is close to a single-point observer—the rate at which it speeds up is determined by the amount of momentum a gust can transfer during its time of passing.[14] To a large extent, this is determined by the size of the device. Like a horizontal-axis wind turbine, a cup anemometer has a certain frontal area, which means that it "sees" the flow through a small streamtube rather than over a line. Therefore, as sketched in Figure 2.14, the information that an anemometer can provide is limited to what happens in this streamtube. Gusts much smaller than S may pass through unnoticed, but gusts much larger than S are not fully appreciated.[15]

---

[13] The notation $\int d\mathbf{x}$ is used to denote the volume integral $\iiint dx\,dy\,dz$.

[14] For a cup anemometer, the number of revolutions it makes during a sample period is what is translated into a wind speed measurement.

[15] This also raises the question how relevant such gust measurements are for the structural loads on bridges or wind turbines.

Over the course of one sampling period, Δt, the anemometer comes into contact with a total momentum content, $\mathbf{p}(t_0)$. Part of it will be converted into the angular momentum that makes the rotor spin and the remaining momentum, $\mathbf{p}(t_0 + \Delta t)$, is left in the wake. The difference between the two is the rotor *thrust*, $\mathbf{F}$, which is a force that is transferred through the bearings and, ultimately, to the structure on which it is mounted. *Severe gusts* are those that can transfer a lot of momentum in a very short time period, thereby producing a high peak force. The dynamics of this interaction can be very complicated and is not something that can be answered in this section (this will be the focus on Chapter 4). Still, based on Figure 2.14, it is possible to identify the *severity* as the gust's initial momentum, $\mathbf{p}(t_0)$.

2.2.6 A general definition of a gust

This section will conclude by answering the question in its title to provide a gust definition for the remaining chapters. A good definition should

- include cases where the observer is either steady or moving;

- be representative of the driving physical mechanisms;

- allow a proper statistical treatment;

- relate to how gusts are experienced (i.e., forces or loads).

Something that seems fitting is

> The projection of a turbulent momentum concentration onto an observer.

It restricts gusts to events that are generated locally by turbulence. Events such as downbursts are assumed to be fundamentally different processes and are placed outside of the scope of this thesis. Moreover, the focus lies on momentum, since velocity amplitudes alone are not enough to assess the impact that gusts have on a design. As will become clear in the next chapter, this also enables the full statistical treatment of three-dimensional gusts.

2.3 Gusts in design problems

Although statistical descriptions for gusts have been around for quite some time, deterministic models are still widely used in many branches of engineering.

2.3.1 Deterministic gust models

Structures that spend their lifetime in a turbulent wind field have to withstand encounters with severe gusts. Therefore, for a designer to make something "gust-proof", he or she will have to rely on an appropriate *gust model*. Many of such gust models can be classified as "engineering models" – models that sacrifice accuracy for speed and simplicity. These are valued because they provide a clear design objective, which is why they have often found their way into engineering standards.

In the past, many deterministic gust shapes have been used to assess wind loading on aircraft. Many of these classical problems are posed by employing certain wave functions

of which the response, in some cases, could be solved analytically. Some famous examples are given in the works of Wagner (1925), Theodorsen (1935), and Von Kármán (1938). Küssner's problem (1936), shown in Figure 2.15a, describes how an airfoil section travels through a step in vertical wind speed:

$$w'(x) = \begin{cases} A, & \text{for } x \le \bar{u}t/c, \\ 0, & \text{for } x > \bar{u}t/c, \end{cases} \tag{2.15}$$

where A is the gust amplitude and c the airfoil's chord length. The response function, later obtained by Von Kármán (1938) through thin airfoil theory, shows how the lift coefficient reacts:

$$C_l(t) = 2\pi \frac{A}{\bar{u}} K(s), \tag{2.16}$$

where $K(s)$ is known as *Küssner's function*, with $s = x/(c/2)$ being the number of semi-chords traveled. Another common example of a deterministic gust is the *1–cos gust*, sketched in Figure 2.15b, which is part of the Federal Aviation Administration (FAA) regulations (see Code of Federal Regulations, 2006; title 14, sec. 23.333):

$$w'(x) = \begin{cases} \dfrac{A}{2}\left[1 - \cos\left(\dfrac{2\pi x}{25c}\right)\right], & \text{for } 0 \le x \le c, \\ 0, & \text{otherwise,} \end{cases} \tag{2.17}$$

where c is the mean geometric chord length.

Step functions are, of course, highly idealized, but could be appropriate in cases where a vehicle is covering a large distance in a short time. During the Apollo and Space Shuttle programs, for example, NASA employed a 9-m/s quasi square-wave gust with wavelengths ranging from 60 to 300 m (see Figure 2.15c) to assess the performance of launch vehicles (NASA, 2000, p. 2-84–89). In addition, a simple sine wave model was used to model turbulent fluctuations over the flight path. This had to be added to a mean wind speed profile, for which seasonal variations were taken into account.

Ground vehicles, such as trains, buses, and cars, suffer from wind loads as well. Though, what is often being modeled are not gusts per se, but variations in crosswind caused by the wakes of obstacles next to the road. These leave gradients in the mean wind speed that, when picked up by a moving vehicle, are experienced as gusts. Such velocity changes have been modeled as sinusoids (Theissen, 2012) or as steps (Hucho and Emmelmann, 1973), as sketched in Figure 2.15d.

Other waveforms can be thought of that specifically trigger some kind of structural response for certification purposes. The International Electrotechnical Commission (IEC), for example, prescribes that wind turbines have to withstand a fully coherent *extreme operating gust* (often called the "Mexican hat") that is notoriously difficult for control systems to handle (IEC, 2005a):

$$u'(t) = \begin{cases} -0.37 A \sin\left(\dfrac{3\pi t}{\tau}\right)\left[1 - \cos\left(\dfrac{2\pi t}{\tau}\right)\right], & \text{for } 0 \le t \le \tau, \\ 0, & \text{otherwise,} \end{cases} \tag{2.18}$$
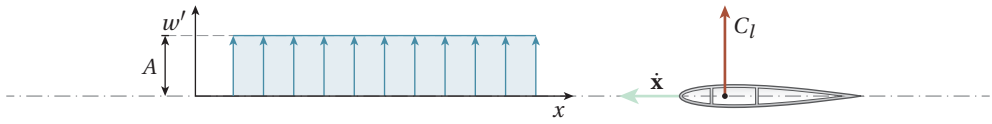
(a): Küssner's problem (1936).
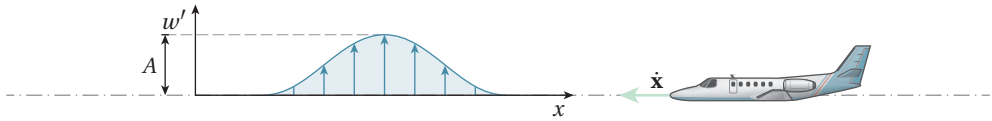
(b): The 1–cos gust from the FAA regulations 2006; title 14, sec. 23.333).
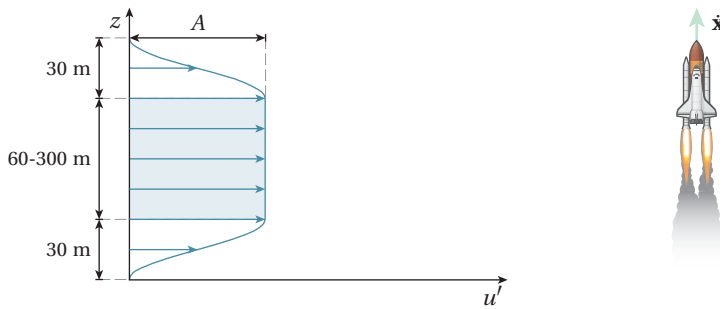
(c): NASA used a simple quasi square-wave to model gusts during the launch of the Apollo and Space Shuttle programs (NASA, 2000, p. 2-84–85).
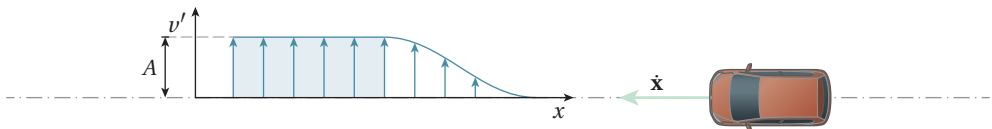
(d): Gust models are also used to model the effects of crosswind on ground vehicles. This example shows a step function with a smooth ramp (Hucho and Emmelmann, 1973).
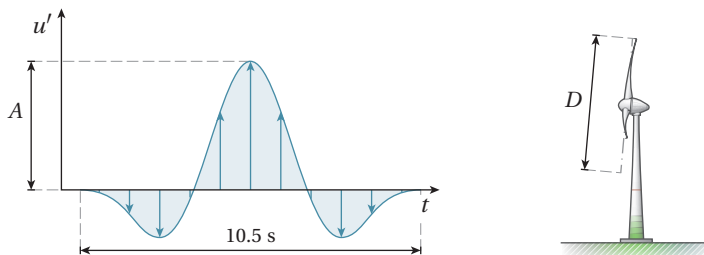
(e): The IEC extreme operating gust prescribed used for wind turbine certification is based on a common wavelet function and is completely coherent over the rotor disk (IEC, 2005a).

Figure 2.15: Examples of deterministic gust models used in engineering.

where the time scale, τ, is taken as 10.5 seconds. However, this model has become less and less physical as turbine diameters have grown in size over the past decades. Although the amplitude, A, decreases with increasing rotor diameter, D, the velocity profile is still completely uniform over the yz-plane. This means that it behaves more like a shockwave (i.e., without conservation of mass) than a realistic turbulent structure.

2.3.2 Extreme events and extreme loads

The pitfall with many of these engineering models is that they are sometimes directly linked to the long-term design loads. They can give the illusion that "if a structure can withstand the most extreme event happening in its design lifetime, it should also be able to survive its design lifetime without failing." However, this mixes up *extreme events* and *extreme loads*, which are not always related. The term "extreme" merely implies that an event is rare, but not necessarily harmful.

A good example to distinguish the two is of a wind turbine operating in a steady mean wind speed. Depending on its distribution, the highest mean wind speed to occur in a twenty-year design lifetime might be well over 40 m/s. However, most turbines are put in a parked state beyond 25 m/s (e.g., see Figure 4.3), since it is not economically viable to operate in those conditions. The blades are then pitched to feather in order to generate zero lift, which leads to considerably lower loads than when the turbine would be operating at maximum thrust. Instead, the highest loads in the design lifetime are often found at and around a turbine's *rated wind speed*, which it encounters regularly.

The same argument holds for gust events. Especially in the design of wind turbine controllers, a lot of attention is sometimes given to the Mexican hat gust because it plays such a major role in certification. This is also because estimating the long-term extreme loads during normal operation is a tedious process with plenty of room for error, therefore hard to integrate in a design loop. However, by doing so, one easily overlooks the many everyday gusts that have a high probability of someday landing on a very vulnerable spot in the rotor.
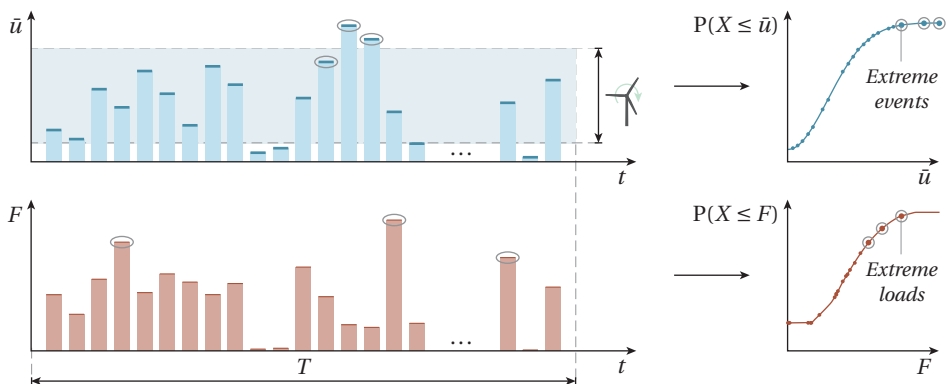
Figure 2.16: Sketch of a load series derived from a set of wind speeds. It shows that the long-term extreme loads do not always follow from the extreme events, which are by definition rare but not necessarily harmful.

2.4 **Gusts measured offshore**

Finally, this chapter is concluded with a look at real-life gust events and the conditions from which they are spawned.

2.4.1 **The OWEZ met mast**

The Netherlands' first offshore wind farm was built between 2005 and 2007, 10–18 km off the coast of Egmond aan Zee. It consists of 36 turbines, each with a rated power of 3 MW, spaced out over an area of 27 km^2.

Prior to construction, a 116-m high met mast was installed at 52° 36' 22.9" N, 4° 23' 22.7" E (see Figure 2.17). Meteorological data in the form of 10-min mean values, spanning from July 2005 to December 2010, is publicly available online from the website of NoordzeeWind.[16] In addition, high-frequency (4 Hz) time series are available from May 2007 to December 2008.

The mast is a triangular lattice tower mounted on a monopile foundation in a 20-m deep seabed. As drawn in Figure 2.18, it has three measurement stations at 21 m, 70 m, and 116 m. Each of them has three booms equipped with a cup anemometer and a wind vane. Furthermore, each of the northwest booms has a sonic anemometer installed and each of the south booms has a thermometer and a humidity sensor. A pressure sensor is found at 20 m and two accelerometers (north-south and east-west) are located on the tower top. Finally, another thermometer is located at –3.8 m to measure seawater temperature and a Doppler profiler is positioned at –17 m to measure the current speed.
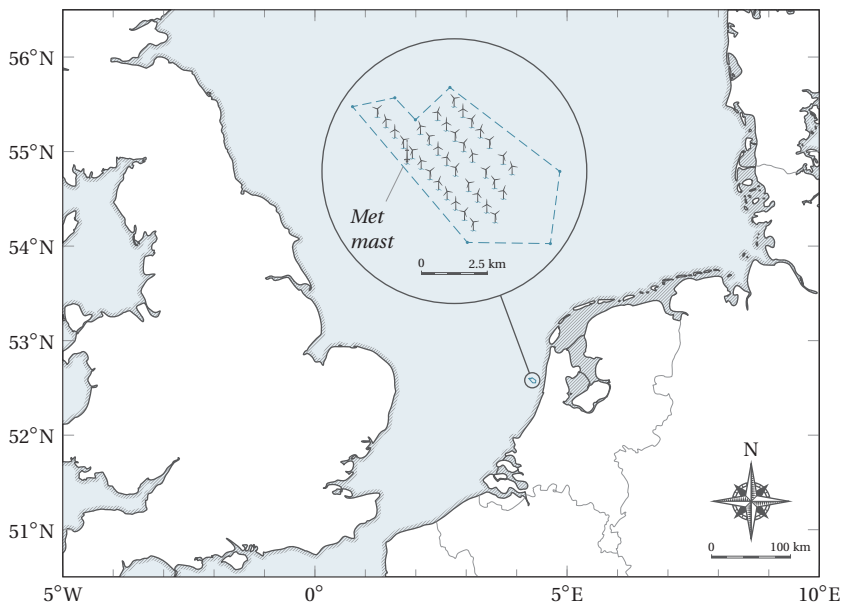
Figure 2.17: The Offshore Windpark Egmond aan Zee (OWEZ) is located in the Dutch North Sea, between 10 and 18 km off the coast.

---

[16] See www.noordzeewind.nl/kennis/rapporten-data/.
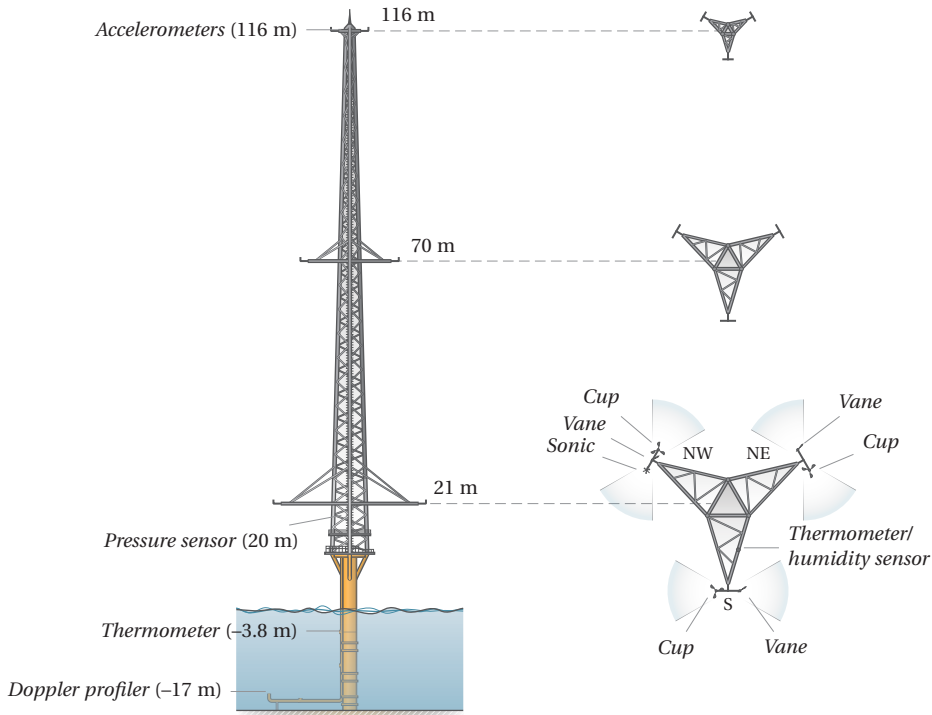
Figure 2.18: Geometry of the OWEZ met mast with the measurement stations at 21, 70, and 116 m (Kouwenhoven, 2007). The instrument layout is the same at every station.
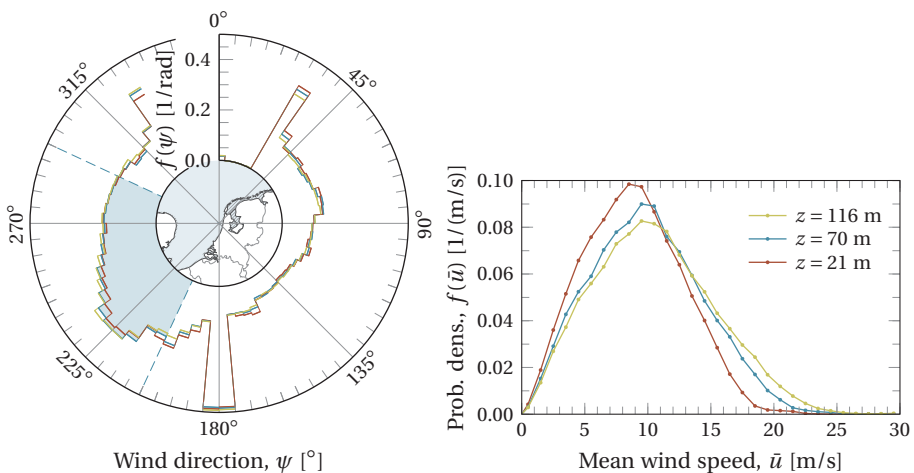
(a): Wind rose, where the shaded sector marks the undisturbed wind directions.

(b): Mean wind speed distribution for the undisturbed wind directions.

Figure 2.19: Distributions of the 10-min mean wind direction and mean wind speed from July 2005 to December 2010.

2.4.2 **Data coverage**

Unfortunately, data is not always available and, when it is, not always of good quality. Since the park was already operating during the measurement campaign, the met mast is located in the wake of the neighboring turbines for the wind directions between 315 and 135°(Kouwenhoven, 2007). In practice, however, already significantly higher turbulence intensities were noted for 295 to 155°(Wagenaar and Eecen, 2010, pp. 11–15) and it is recommended to filter the data for those sectors. The data set can be further reduced by only limiting the conditions to what is representative for far offshore. In that case, only including the wind directions between 205 to 25°ensures that the fetch is at least 200 km. This means that the undisturbed wind directions range from 205 to 295°(see Figure 2.19).

For the sonic anemometer, in particular, there are mast effects. Being only installed on the northwest boom, the sonic measurements are distorted by the tower wake for wind directions between 90 to 150°(Wagenaar and Eecen, 2010, p. 11). This does not apply to the vanes and the cup anemometers, since there is always one of the three measuring an undisturbed flow. For these sensors, the data source can be chosen according to the method of Eecen (2008), who divided the wind directions into six 60°sections. The "true" wind direction is found iteratively, by taking averages of two vanes, until the boom is found that is approximately perpendicular to the incoming wind. The cup anemometer mounted on that boom is then assumed to be undisturbed.

Still, for turbulence measurements, the sonic anemometer is generally superior to the cup anemometer. This is because it is able to measure each of the three velocity components and because it does not suffer from inertia. Its drawback is that it has a lower technical availability, which leaves gaps in the data. Especially at the 116-m station, the availability is merely 67.2% (see Figure 2.20). When only the wind directions between 205 and 295°are included, just 25.7% of the data remains.

(a): At $z = 116$ m.

(b): At $z = 70$ m.

(c): At $z = 21$ m.
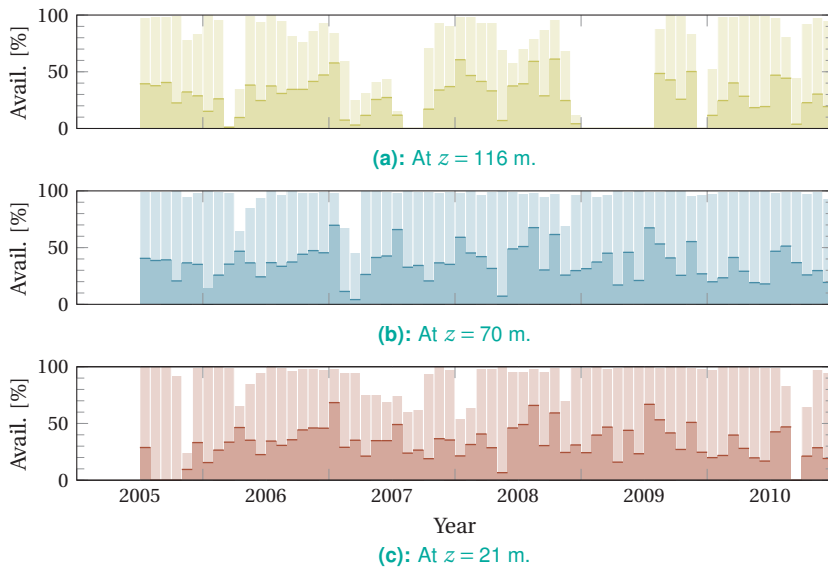
Figure 2.20: Availability of the sonic anemometers from July 2005 to December 2010. Indicated with light bars are the amount of existing ten-minute records per month. The darker bars represent the entries limited to $205 \leq \psi \leq 295°$.

2.4.3 **Turbulence levels**

In general, there are two main mechanisms responsible for the generation of turbulence. One is the mechanical friction generated by the sea surface, the other is the vertical transport of heat; both have an effect on the longitudinal *turbulence intensity*:

$$I_u = \frac{\sigma_u}{\bar{u}}, \qquad (2.19)$$

where σ_u is the standard deviation of the longitudinal (i.e., along-wind) velocity component.

First, Figure 2.21 shows how the turbulence intensity varies with mean wind speed. It starts off relatively high at low wind speeds. On the one hand, this is simply because the denominator in Equation (2.19) is smaller. On the other hand, the low wind speeds also contain periods of fair weather with lots of evaporation and high turbulence. Another characteristic property of offshore turbulence is that it tends to become more intense at higher wind speeds. Stronger winds cause waves to grow, leading to a higher surface friction and an increasing mechanical production of turbulence. Of course, this effect is stronger close to the sea surface, which is clearly shown by the differences between Figures 2.21a and 2.21b.

The second aspect is the vertical transport of heat, which is linked to the stability of the atmosphere. Here, atmospheric stability is determined—as in Holtslag (2016)—through the *bulk Richardson number*:

$$\mathrm{Ri} = \frac{g \dfrac{\Delta \bar{\Theta}_\mathrm{v}}{\Delta z}}{\bar{\Theta}_\mathrm{v} \left(\dfrac{\Delta \bar{u}}{\Delta z} \right)^2}, \qquad (2.20)$$

where g is the acceleration due to gravity and $\bar{\Theta}_\mathrm{v}$ the *virtual potential temperature*, which is derived by following the work of Hutschemaekers (2014). The gradients $\Delta \bar{\Theta}_\mathrm{v}/\Delta z$ and $\Delta \bar{u}/\Delta z$ are determined between $z = 0$ and $z = 21$ m, assuming $\bar{u} = 0$ m/s and a 100%

(a): At $z = 21$ m.   **(b):** At $z = 116$ m.
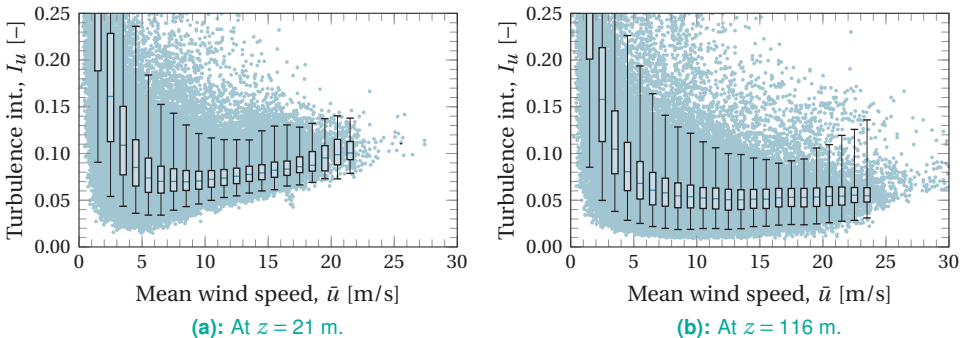
Figure 2.21: Dependency of the turbulence intensity on mean wind speed (filtered for the wind directions $205 \leq \psi \leq 295°$). The thick line in the box plot represents the median; the edges of the box are located at the first and third quartile; and the ends of the whiskers mark the 2.5th and 97.5th percentiles (i.e., the 95% range).

Table 2.1: Atmospheric stability classes defined by Gryning et al. (2007).

Stability class	Obukhov length
Very stable (vs)	$10 \leq L_{\mathrm{O}} \leq 50$ m
Stable (s)	$50 \leq L_{\mathrm{O}} \leq 200$ m
Near-neutral stable (nns)	$200 \leq L_{\mathrm{O}} \leq 500$ m
Neutral (n)	$\left| L_{\mathrm{O}} \right| \geq 500$ m
Near-neutral unstable (nnu)	$-500 \leq L_{\mathrm{O}} \leq -200$ m
Unstable (u)	$-200 \leq L_{\mathrm{O}} \leq -100$ m
Very unstable (vu)	$-100 \leq L_{\mathrm{O}} \leq -50$ m

relative humidity at the sea surface, and assuming that the seawater temperature at a depth of –3.8 m is representative of the sea surface temperature. The atmospheric stability is then classified using the *Obukhov length, L_{O}*, obtained from the empirical relationship from Grachev and Fairall (1997):

$$\frac{z}{L_{\mathrm{O}}} \approx \begin{cases} 10\,\mathrm{Ri}, & \text{for } \mathrm{Ri} \leq 0, \\[2ex] \dfrac{10\,\mathrm{Ri}}{1 - 5\,\mathrm{Ri}}, & \text{for } \mathrm{Ri} > 0. \end{cases} \tag{2.21}$$

The stability classes are listed in Table 2.1.

Figure 2.22a shows that the turbulence intensity is generally higher in unstable conditions (strong buoyant production) than in stable conditions (weak buoyant production). This has a pronounced seasonal variation at offshore sites (see Figure 2.22c). Water takes longer to heat up and cool down than air, causing it to lag behind the air temperature over the seasonal cycle. In autumn, for example, the sea is still warm while the air is starting to cool down. The air that is heated up by the warmer sea surface is tempted to convect, resulting in an unstable atmosphere with high turbulence levels. Vice versa, a colder sea surface has the tendency to stabilize the atmosphere, which is what may happen in early spring.

Another thing to look at is the vertical homogeneity of the boundary layer, which is heavily relied upon in the next chapters. It implies that the statistical properties of turbulence are the same in every direction. Figure 2.23 shows this a rough assumption at best, especially for large vertical separations. Partly, this is because much of the turbulence production takes place near the surface. When the boundary layer is poorly mixed—for example, during stable atmospheric conditions—differences in turbulence intensities are not well evened out. This might also explain why turbulence seems to be more homogeneous at lower wind speeds, which is where a lot of periods with unstable atmospheric conditions are binned (see Figure 2.22b). Comparing Figure 2.23a to Figure 2.23b, the standard deviation of the longitudinal wind speed is more uniform at higher altitudes. Though, whether this is still the case for future 10–20 MW turbines is hard to tell with the OWEZ met mast.

2.4.4 Gust measurements

Spanning a total of 20 months, the high-frequency data set contains tens of thousands of gusts. These one-dimensional events can be analyzed with the available statistical tools, explained in Subsection 2.2.1. Figure 2.24 shows the number of velocity peaks exceeding a normalized level, $A/\sqrt{\Lambda_0}$, where Λ_0 is the zeroth-order spectral moment (i.e., the variance). In the theorical case, for homogeneous Gaussian turbulence, this should approach Rice's formula. However, real-life gusts start to deviate from Gaussian behavior already for amplitudes of 3 to 4 times the standard deviation. It results in heavy distribution tails, a property called *kurtosis*. The underlying reason is that kinetic energy is not evenly distributed throughout a turbulent velocity field. Instead, it may be concentrated in the eddy centers, causing the statistics to vary locally (Castaing, Gagne and Hopfinger, 1990). This is reflected in the tails of Figure 2.24a, where non-Gaussian behavior exists especially at the smallest scales.
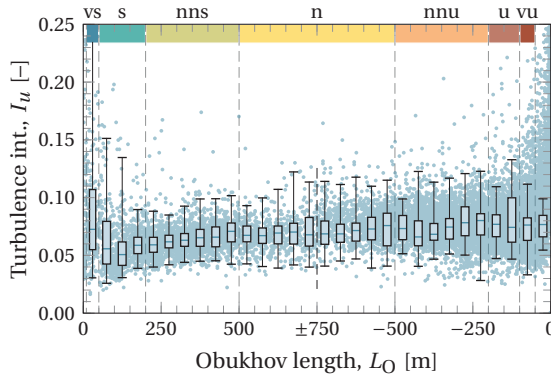
(a): Dependency of the turbulence intensity on atmospheric stability (filtered for the wind directions $205 \leq \psi \leq 295°$). The thick line in the box plot represents the median; the edges of the box are located at the first and third quartile; and the ends of the whiskers mark the 2.5th and 97.5th percentiles (i.e., the 95% range).
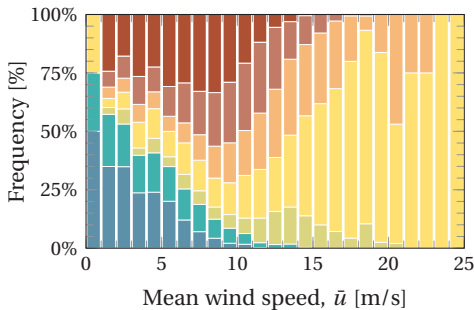
(b): Effect of the mean wind speed on atmospheric stability.
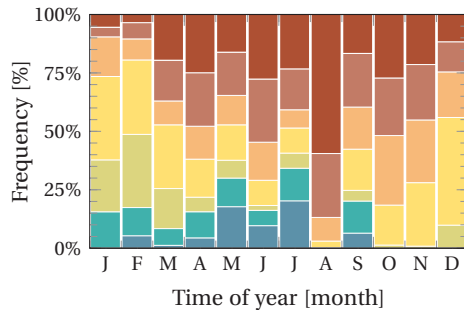
(c): Seasonal variation of atmospheric stability.

Figure 2.22: Stability effects at $z = 21$ m.

Yet, when the mean wind speed increases, the curves start to converge back Rice's formula. One reason for this could be that, when eddies are advected at a higher rate, measurement points logged at a fixed sampling frequency are spaced further apart:

$$\Delta x \approx \bar{u} \Delta t. \tag{2.22}$$

Consequently, this affects the smallest measurable length scales. It does not mean that non-Gaussian behavior simply disappears at higher wind speeds, but only that it can no longer be picked up by the anemometer.

A similar effect is achieved when the velocity peaks are smoothed out over a short time period, τ, as is common practice in meteorology:

$$A = \max \left[u'(t) * g(\tau) \right], \tag{2.23}$$

where $u'(t) * g(\tau)$ denotes convolution with a three-second window. In that case, the non-Gaussian fluctuations are lumped together with neighboring data points and averaged. This is shown in Figures 2.24c and e for time periods of $\tau = 3$ and 10 s. The process of averaging is a low-pass filtering operation that eliminates the small scales. As a result, such smoothed velocity peaks seem to obey Gaussian statistics.

Moreover, Figures 2.24b, d, and f show the return level plots for the ten-minute velocity maxima, which are constructed by sorting and assigning a probability (see Section 5.1). Here, a similar thing happens: data from the higher wind speed bins and longer averaging periods show a more consistent extreme value behavior. Of course, it is merely speculation whether the same holds in three-dimensional space, but it has all the appearances.[17]

Looking at each gust individually, they appear to be completely random. However, gather enough of them together and they start to show a similar velocity signature. As

(a): Ratio of 21 to 70 m.

(b): Ratio of 70 to 116 m.
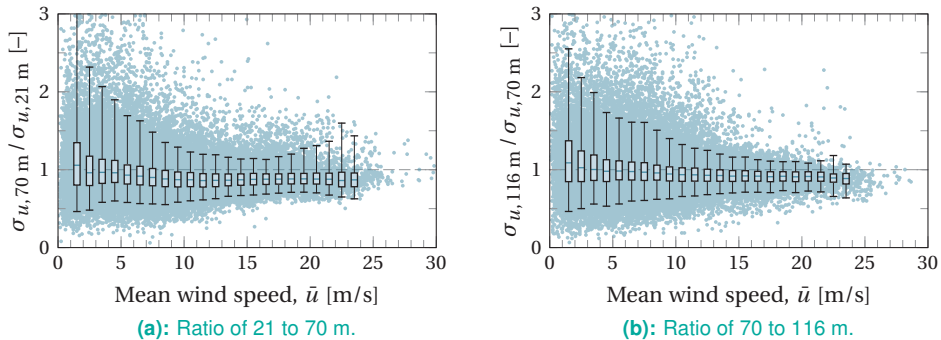
Figure 2.23: Ratio of the standard deviations of the longitudinal wind speed at two heights, as a function of the mean wind speed at $z = 70$ m (filtered for the wind directions $205 \leq \psi \leq 295°$), where homogeneous turbulence has a value equal to 1. The thick line in the box plot represents the median; the edges of the box are located at the first and third quartile; and the ends of the whiskers mark the 2.5th and 97.5th percentiles (i.e., the 95% range).

---

[17] The effect that non-Gaussian turbulence has on wind turbine loads has been studied by Berg et al. (2016), who modified velocity fields generated by a Large Eddy Simulation (LES) in order to match Gaussian statistics. When these ten-minute wind fields, together with the original fields, were fed to a wind turbine model, no significant differences in fatigue or extreme loads were found among 240 realizations. Though, the question remains if this is still true after, say, one million realizations.

(a): Excursion frequency ($\tau = 0$ s).

(b): Return level plot for the (normalized) ten-minute extremes ($\tau = 0$ s).

(c): Excursion frequency ($\tau = 3$ s).

(d): Return level plot for the (normalized) ten-minute extremes ($\tau = 3$ s).

(e): Excursion frequency ($\tau = 10$ s).

(f): Return level plot for the (normalized) ten-minute extremes ($\tau = 10$ s).

Figure 2.24: Statistics of velocity peaks, measured by the sonic anemometer at $z = 116$ m (filtered for the wind directions $205 \leq \psi \leq 295°$). The peaks are extracted after smoothening over a window of $\tau = 0$, 3, and 10 s. The parameter Λ_0 is the zeroth-order spectral moment (i.e., the variance) after smoothening.
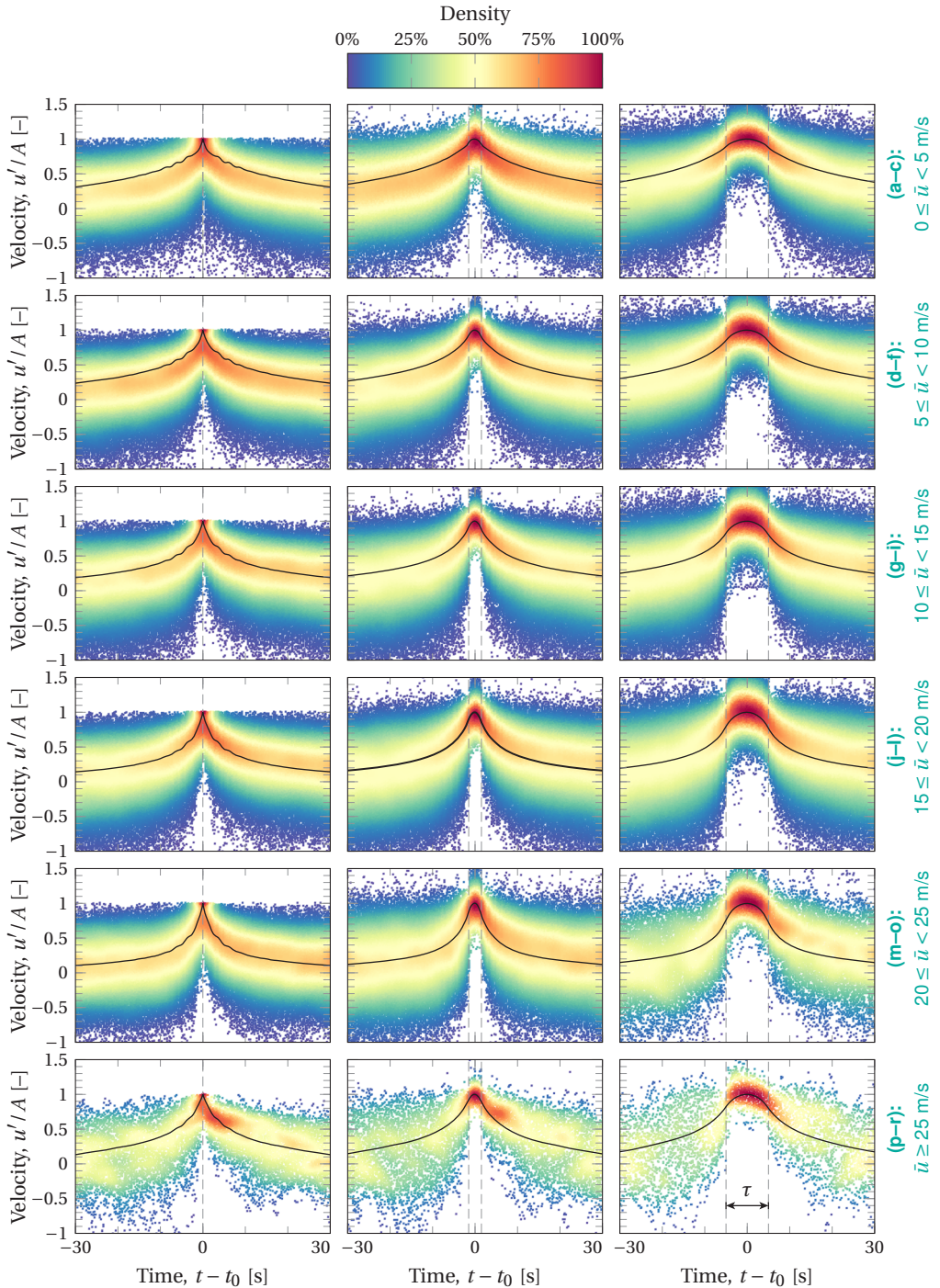
Figure 2.25: Time series around velocity peaks, measured by the sonic anemometer at $z = 116$ m (filtered for the wind directions $205 \leq \psi \leq 295°$). Gusts are selected by amplitude, A, smoothed over a window of $\tau = 0$, 3, and 10 s. The black line is the (smoothed) autocorrelation function.

shown by Bierbooms, Dragt and Cleijne (1999), this *mean gust shape* is given by the autocorrelation function:

$$\mathrm{E}\left[\hat{u}(t)\right] = \mathrm{E}\left[u(t')u(t'+t)\right], \tag{2.24}$$

which can be obtained through an inverse Fourier transform of the turbulence spectrum, $S_u(f)$. To illustrate, Figure 2.25 shows up to 1,000 time series of individual velocity peaks at once, each centered around the amplitude. Before selection, each velocity time series was treated with a band-stop filter to remove a dominant 0.4-Hz harmonic, which could be linked to the met mast's eigenfrequency (Eecen and Branlard, 2008). Overlaying data points are then colored, such that a common shape becomes visible. Clearly, the resemblance to the theoretical mean gust shape is very close. It is only slightly off for the low wind speed bins, likely due to large mutual differences in advection velocity and spectrum shape. In addition, the theory still holds up when the peaks are selected by their smoothed amplitudes, in which case they also look like the smoothed autocorrelation function.
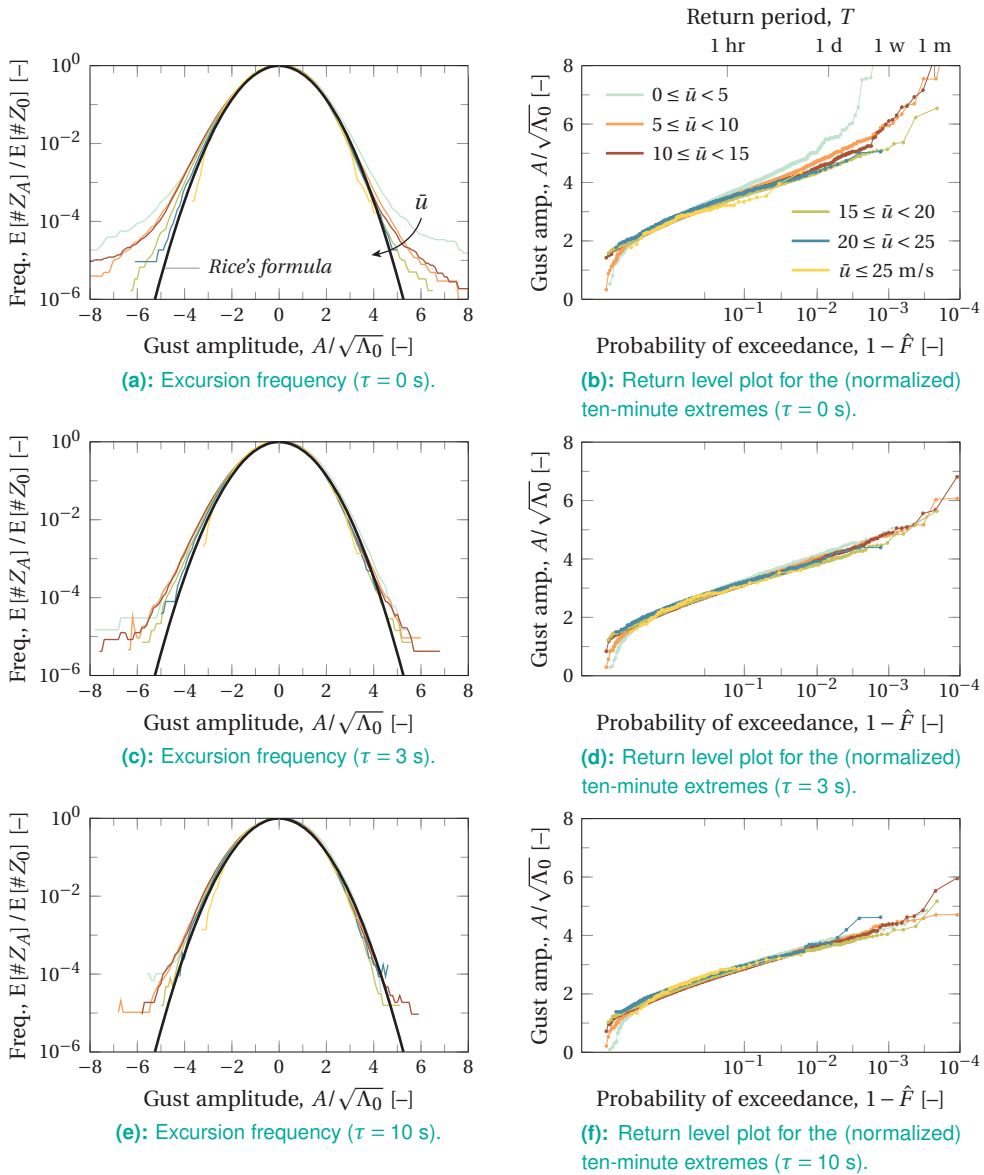
2.4.5 Tower top accelerations

Unfortunately, because the sonic anemometer returns a point measurement, it does not provide much useful information about how damaging the gusts actually are. One possible way to still get some data on the severity of the wind conditions is to rely on the tower itself. As drawn in Figure 2.18, two accelerometers (north-south and east-west) are mounted on the tower top, of which the standard deviations and ten-minute maxima are available. The magnitude of the two component standard deviations should be representative of the forces acting on the tower (i.e., the violence with which it is rocked back and forth):[18]

$$\sigma_{\ddot{x}} = \sqrt{\sigma_{\ddot{x},\text{N-S}}^2 + \sigma_{\ddot{x},\text{E-W}}^2}. \tag{2.25}$$

Although the available data does not allow a direct comparison between the gusts and the tower motions, it is possible to take a look in which conditions the tower experiences the highest fluctuating loads. First, Figure 2.26a gives an overview of the seasonal variations. It shows that the highest values for $\sigma_{\ddot{x}}$ are found during severe storms that occur primarily from late autumn to early spring. The heaviest one on record is "Kyrill", which was one of the heaviest storms in the last few decades that wreaked havoc across Europe in January 2007. Such storms often bring southwesterly winds with high turbulence levels as they travel over the North Sea (see Figure 2.26b).

The data can also be binned by the Richardson number and the atmospheric pressure (see Figure 2.26c). It shows that the highest fluctuating loads are often found near neutral atmospheric conditions. Unsurprisingly, this is also where the highest wind speeds and strongest gusts are found (Suomi et al., 2015a).

Finally, zooming in on a five-day period surrounding the maximum $\sigma_{\ddot{x}}$, some interesting things are happening (see Figure 2.27). The highest fluctuating loads occurred in the period 14:10–14:20, when the atmospheric pressure was at its lowest point. The same time period also contains the highest velocity peak. Recorded at 21-m height, it reached an amplitude of 38.4 m/s ($\approx 4.0\sigma_u$).

---

[18] Ideally, the maximum tower top accelerations should be compared to the velocity time series at all three measurement stations. However, this was too much work to incorporate in the present study.

The storm also brought a flurry of even more extreme peaks, sometimes exceeding $5\sigma_u$. Like with the physical explanations of rogue waves (see Subsection 2.2.3), one explanation is that extreme gusts are generated by some nonlinear mechanism. However, these events, together with those occurring over the next three days, can also be linked to rapidly changing mean wind speeds. A more plausible explanation is therefore that it was wrong to apply the Reynolds decomposition on the basis of a ten-minute spectral gap. This makes it hard to define a mean wind speed and also complicates the definition of gusts.

The following chapters will not deal with storm conditions. Instead, the discussion is limited to extreme gusts spawned from stationary, homogeneous turbulence, which lends itself to a proper statistical treatment. The modeling of turbulence and gusts in storms is a possible next step, as part of future research.
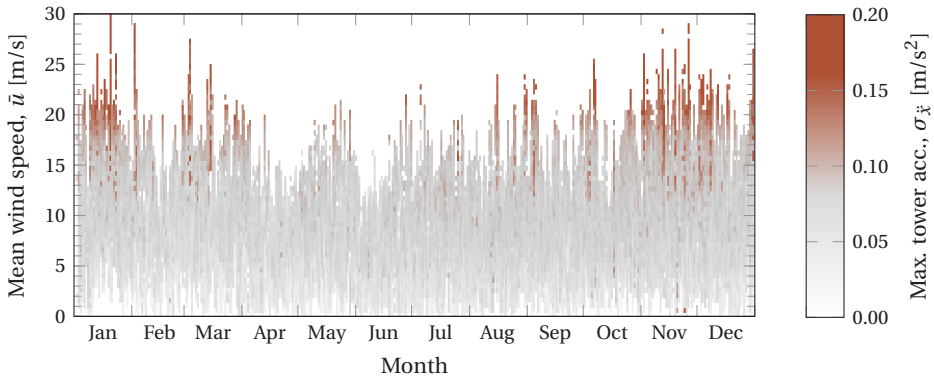
(a): Most violent tower top accelerations found over the year, where the most severe conditions are found on 18 January 2007 during the passing of the storm Kyrill.
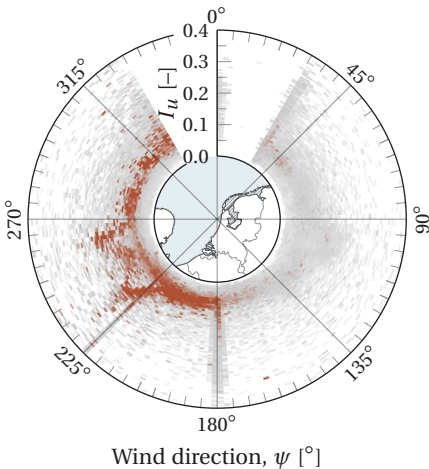
(b): Most violent tower top accelerations for different wind directions and turbulence intensities.
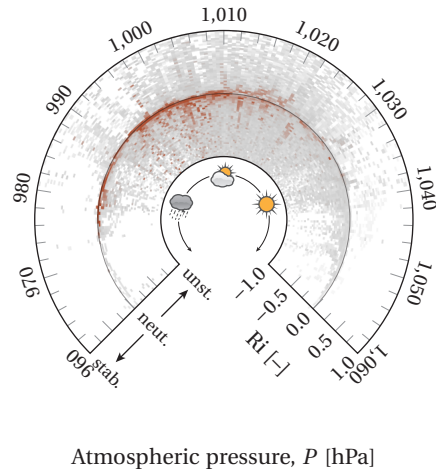
(c): Most violent tower top accelerations at different atmospheric pressures and Richardson numbers.

Figure 2.26: Severe wind conditions measured at the OWEZ site from July 2005 to December 2010.
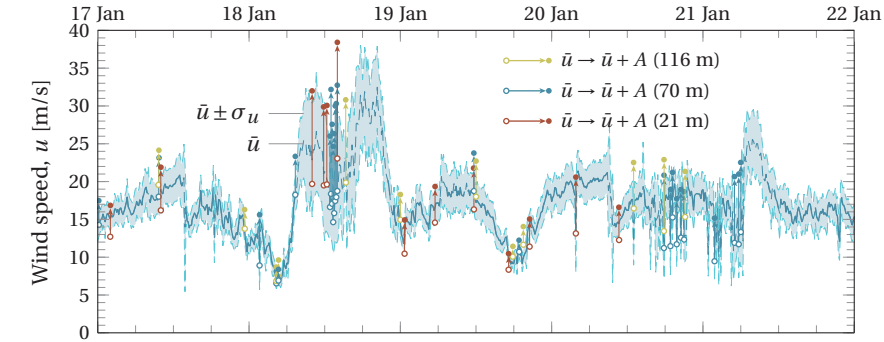
(a): Wind speed (cup) and standard deviations at $z = 70$ m, and gusts $(A > 4\sigma_u)$ at all heights.
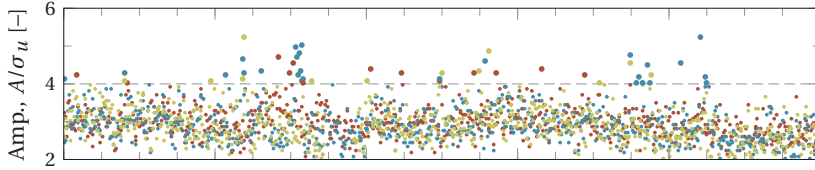
(b): Normalized ten-minute extreme gust amplitudes at $z = 21$, 70, and 116 m.
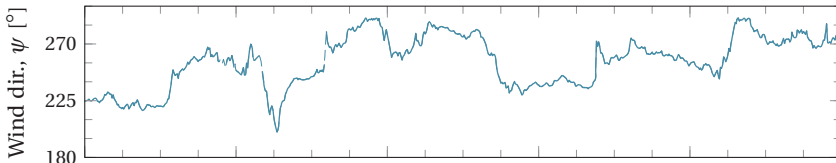
(c): Wind direction.
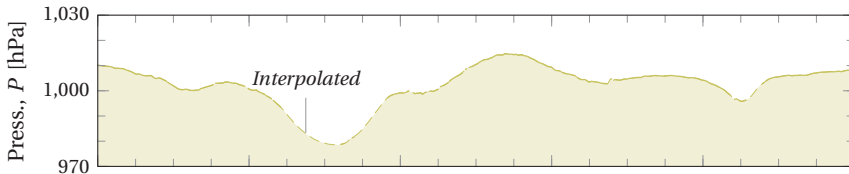
(d): Atmospheric pressure.
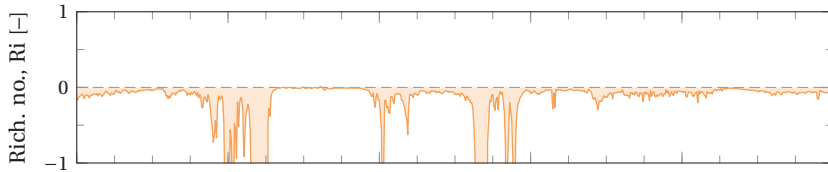
(e): Richardson number.
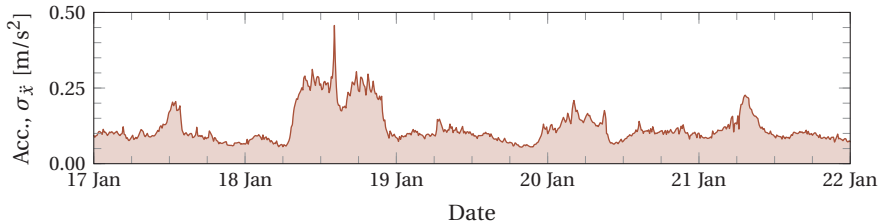
(f): Violence of tower top accelerations, $\sigma_{\ddot{x}}$.

Figure 2.27: Ten-minute data recorded around the passing of the storm Kyrill in January 2007.

Chapter 3
A mathematical treatment of gusts

This chapter features work from the following publications:

Bos, R., W. A. A. M. Bierbooms, and G. J. W. van Bussel (2013). "Extreme gust loads for novel wind turbines." *9th EAWE PhD Seminar on Wind Energy in Europe*. 22–25 September. Visby, Sweden.

Bos, R., W. A. A. M. Bierbooms, and G. J. W. van Bussel (2014). "3D stochastic gusts as an alternative to the Mexican hat wavelet." *10th EAWE PhD Seminar on Wind Energy in Europe*. 28–31 October. Orléans, France.

Bos, R., W. A. A. M. Bierbooms, and G. J. W. van Bussel. "The spatial structure of severe wind gusts." *Manuscript submitted for publication*.

W IND GUSTS are a symptom of turbulent momentum transport and can come in different shapes, sizes, and amplitudes. The goal of this chapter is to derive a mathematical formulation of such events that takes into account all possible manifestations in a probabilistic fashion. The focus is mainly on homogeneous Gaussian turbulence in three-dimensional domains.

First, the discussion starts in Section 3.1 from the physical perspective. After that, Section 3.2 will switch to the statistical perspective by explaining the principles of stochastic turbulence modeling. Then follows the heart of this chapter and of the entire thesis: the derivation of the three-dimensional velocity fields around gusts in Section 3.3 and their statistics in Section 3.4. Finally, Section 3.5 concludes this chapter with a bit of speculation about how gusts could evolve in time.

3.1 Causes of unsteadiness

In order to understand gusts, one needs to understand turbulence. Although the equations of fluid motion cannot be solved directly (or at least not yet), they do tell which processes play a role on the gust time scale.

3.1.1 The Navier-Stokes equations

The physics of turbulence is governed by the *Navier-Stokes equations*. For an incompressible fluid with a constant density and viscosity (i.e., $\nabla \cdot \mathbf{u} = 0$), a momentum balance

dictates that

$$\underbrace{\frac{D\mathbf{u}}{Dt}}_{Inertia} = \overbrace{-\frac{1}{\rho}\nabla P}^{\substack{Pressure\\gradient}} + \underbrace{\nu\nabla^2\mathbf{u}}_{Shear\ stress} + \overbrace{\frac{1}{\rho}\sum\mathbf{f}}^{\substack{(External)\\body\ forces}}, \tag{3.1}$$

where ρ is the (air) density, P is the pressure, ν is the kinematic viscosity, and $\sum\mathbf{f}$ is the collection of body forces. For atmospheric flows in particular, this can be extended as

$$\underbrace{\frac{\partial\mathbf{u}}{\partial t}}_{\substack{Eulerian\\acceleration}} = \overbrace{-\mathbf{u}\cdot\nabla\mathbf{u}}^{Advection} - \underbrace{\frac{1}{\rho}\nabla P}_{\substack{Atmospheric\\pressure\ gradient}} + \overbrace{\nu\nabla^2\mathbf{u}}^{Shear\ stress} - \underbrace{\nabla\left(gz\right)}_{Gravity} - \overbrace{2\mathbf{\Omega}_{\mathrm{E}}\times\mathbf{u}}^{Coriolis\ effect}, \tag{3.2}$$

where the centrifugal force due to the Earth's rotation has been included in the total scalar gravity field, $-\nabla(gz)$. Furthermore, g is the acceleration due to gravity and $\|\mathbf{\Omega}_{\mathrm{E}}\| = 7.29\cdot10^{-5}$ rad/s is the angular velocity of Earth's rotation.

A gust is commonly seen as a deviation from the mean flow, following from the *Reynolds decomposition*:

$$\underbrace{\mathbf{u}(\mathbf{x},t)}_{Total\ velocity} = \overbrace{\bar{\mathbf{u}}(\mathbf{x})}^{Mean\ flow} + \underbrace{\mathbf{u}'(\mathbf{x},t)}_{\substack{Unsteady\\component}}. \tag{3.3}$$

The *mean flow* is defined such that it is constant in time and the unsteady component is completely stationary:

$$\bar{\mathbf{u}}(\mathbf{x}) \equiv \lim_{T\to\infty}\frac{1}{T}\int_0^T\mathbf{u}(\mathbf{x},t)\,dt, \tag{3.4}$$

where T is the averaging period. An interesting result now follows from the *principle of continuity*. Since it must hold that $\nabla\cdot\mathbf{u} = 0$ and $\overline{\nabla\cdot\mathbf{u}} = 0$, it can be shown that the continuity equation applies to both the steady and unsteady component of the velocity:

$$\nabla\cdot\mathbf{u} = \nabla\cdot\left(\bar{\mathbf{u}}+\mathbf{u}'\right),$$
$$= \nabla\cdot\bar{\mathbf{u}} + \nabla\cdot\mathbf{u}'; \tag{3.5a}$$
$$\overline{\nabla\cdot\mathbf{u}} = \overline{\nabla\cdot\bar{\mathbf{u}}} + \overline{\nabla\cdot\mathbf{u}'},$$
$$= \nabla\cdot\bar{\mathbf{u}}; \tag{3.5b}$$

which implies that $\nabla\cdot\bar{\mathbf{u}} = 0$ and $\nabla\cdot\mathbf{u}' = 0$. Applying the Reynolds decomposition to Equation (3.2) then yields

$$\frac{\partial}{\partial t}\left(\bar{\mathbf{u}}+\mathbf{u}'\right) = -\left(\bar{\mathbf{u}}+\mathbf{u}'\right)\cdot\nabla\left(\bar{\mathbf{u}}+\mathbf{u}'\right) - \frac{1}{\rho}\nabla(\bar{P}+P') + \nu\nabla^2\left(\bar{\mathbf{u}}+\mathbf{u}'\right) - \nabla\left(gz\right) - 2\mathbf{\Omega}_{\mathrm{E}}\times\left(\bar{\mathbf{u}}+\mathbf{u}'\right). \tag{3.6}$$

Now, even though the fluid is formally considered as incompressible, density variations due to temperature are usually allowed to exist in the buoyancy term (e.g., see Stull,

1988, p. 84). This is the *Boussinesq approximation*, which leads to

$$\bar{\rho} + \rho' \approx \bar{\rho}, \tag{3.7a}$$

$$\left(\bar{\rho} + \rho'\right)g \approx \bar{\rho}g - \frac{\Theta_v'}{\Theta_v}\bar{\rho}g, \tag{3.7b}$$

where Θ_v is the *virtual potential temperature*. Moreover, it is convenient to split the mean pressure term into a horizontal and vertical component:

$$\frac{1}{\bar{\rho}}\nabla\bar{P} = \frac{1}{\bar{\rho}}\nabla\bar{P}_{xy} + \frac{1}{\bar{\rho}}\nabla\bar{P}_z. \tag{3.8}$$

Under the assumption of a hydrostatic balance, the vertical component then cancels out with gravity:

$$\frac{1}{\bar{\rho}}\nabla\bar{P}_z + \nabla(gz) = 0. \tag{3.9}$$

After expanding the advection term, the final result is:

$$\underbrace{\frac{\partial \mathbf{u}'}{\partial t}}_{\substack{\text{Eulerian} \\ \text{acceleration}}} = -\overbrace{\bar{\mathbf{u}}\cdot\nabla\bar{\mathbf{u}}}^{\substack{\text{Mean} \\ \text{transport}}} - \underbrace{\bar{\mathbf{u}}\cdot\nabla\mathbf{u}'}_{\substack{\text{Turbulence} \\ \text{advection by} \\ \text{mean flow}}} - \overbrace{\mathbf{u}'\cdot\nabla\bar{\mathbf{u}}}^{\text{Shear distortion}} - \underbrace{\mathbf{u}'\cdot\nabla\mathbf{u}'}_{\substack{\text{Turbulent} \\ \text{transport}}} - \overbrace{\frac{1}{\bar{\rho}}\nabla\bar{P}_{xy}}^{\substack{\text{Horizontal pressure} \\ \text{gradient}}} - \underbrace{\frac{1}{\bar{\rho}}\nabla P'}_{\text{Pressure fluctuations}} + \overbrace{\nu\nabla^2(\bar{\mathbf{u}} + \mathbf{u}')}^{\text{Viscous dissipation}}$$

$$\cdots + \underbrace{\nabla\left(gz\frac{\Theta_v'}{\Theta_v}\right)}_{\text{Atmospheric stability}} - \overbrace{2\boldsymbol{\Omega}_E \times (\bar{\mathbf{u}} + \mathbf{u}')}^{\text{Coriolis effect}}. \tag{3.10}$$

For the remainder of this chapter, the overbar will be left out from the density term ($\rho = \bar{\rho}$).

3.1.2 Scale analysis

In order to recognize the relevant terms in Equation (3.10), it is convenient to do a scale analysis. Each term is then compared to the advection term, $\mathbf{u}\cdot\nabla\mathbf{u}$ in terms of a length scale, ℓ, and a velocity scale U. Nondimensionalizing the Navier-Stokes equations yields the following dimensionless quantities:

$$\frac{\left\|\frac{1}{\rho}\nabla\bar{P}_{xy}\right\|}{\|\mathbf{u}\cdot\nabla\mathbf{u}\|} \propto \frac{\Delta\bar{P}_{xy}}{\rho U^2} = \text{Eu}$$

is the *Euler number*, representing the ratio of the pressure forces to the inertial forces. The Euler number can be used to characterize how fluid is put into motion as response to a certain pressure field. When the flow field is assumed to be influenced solely by local pressure gradients, one speaks of *Eulerian wind*. It is also used to typify the pressure drop in pipe flows, where Eu = 1 indicates

an ideal frictionless flow.

$$\frac{\left\|\nabla\left(gz\frac{\Theta_v'}{\bar\Theta_v}\right)\right\|}{\|\mathbf{u}\cdot\nabla\mathbf{u}\|} \propto \frac{g\ell}{U^2}\frac{\Theta_v'}{\bar\Theta_v} = \mathrm{Ri}$$

is the *Richardson number* and is the ratio of potential to kinetic energy. Values of Ri > 0 and Ri < 0 represent a stable and unstable atmosphere, respectively. For Ri = 0, the atmosphere is said to be neutral. When the Richardson number is above a certain critical value (often taken as 0.25), the stabilizing buoyancy force dominates over the inertial force and the flow tends to be laminar.

$$\frac{\left\|\nu\nabla^2\mathbf{u}\right\|}{\|\mathbf{u}\cdot\nabla\mathbf{u}\|} \propto \frac{\nu}{U\ell} = \frac{1}{\mathrm{Re}}$$

reveals the *Reynolds number*. The Reynolds number represents the ratio of the inertial and viscous forces and can be an indicator for the degree of turbulence. The term $\mathbf{u}\cdot\nabla\mathbf{u}$ can be said to generate turbulence, while $\nu\nabla^2\mathbf{u}$ destroys it through viscous dissipation. For Re $\ll$ 1, turbulence is highly damped and the flow is completely laminar, leading to *Stokes flow* or *creeping flow*.

$$\frac{\left\|2\mathbf{\Omega}_E\times\mathbf{u}\right\|}{\|\mathbf{u}\cdot\nabla\mathbf{u}\|} \propto \frac{f_C\ell}{U} = \frac{1}{\mathrm{Ro}}$$

where Ro is the *Rossby number*. Here, $f_C = 2\|\mathbf{\Omega}_E\|\sin\varphi$ is the Coriolis frequency with φ denoting latitude. The Rossby number represents the ratio of inertial forces and Coriolis forces. Low values indicate that a system is strongly governed by Coriolis forces, while high values would suggest that a system is primarily controlled by inertial and centrifugal forces. The Rossby and Reynolds numbers together form the Ekman number, Ek $= \sqrt{\mathrm{Ro}/\mathrm{Re}}$, which shows to what extend disturbances at the top of the atmospheric boundary layer are propagated to the surface and also defines the height of the Ekman layer.

The magnitude of these parameters at moderate latitudes can be found rather straightforwardly (e.g., see Holton, 2004) by noting that

- $\rho \sim 10^0$ kg/m^3,

- $\mathrm{d}\bar P_{xy}/\mathrm{d}x \sim 10^{-3}$ Pa/m,

- $g \sim 10^1$ m/s^2,

- $\Theta_v'/\bar\Theta_v \sim 10^{-2}$,

- $\nu \sim 10^{-5}$ m^2/s,

- $f_C \sim 10^{-4}$ rad/s.

Drawing the dimensionless numbers as a function of a length and a velocity scale then results in Figure 3.1. A term is considered insignificant if it is more than one order
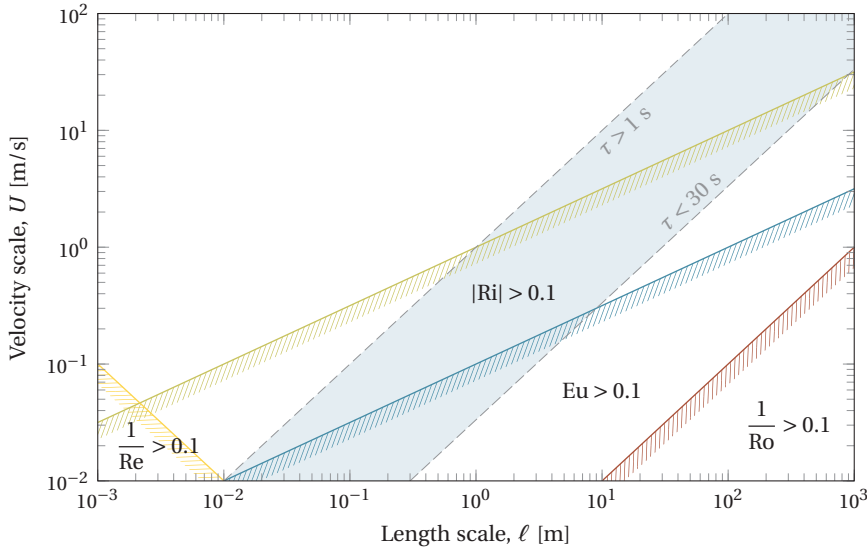
Figure 3.1: Length and velocity scales where the different Navier-Stokes terms become significant compared to the inertial term. The shaded area bounds the region where the Lagrangian time scale matches that of a gust; i.e., between 1 and 30 seconds.

of magnitude smaller than the inertial term. Based on this, it can be said that the atmospheric pressure gradient and the Coriolis force (Eu and Ro^{-1}, respectively) both operate on a too large scale for them to have a significant impact on gusts. On the other end of the spectrum, viscosity (Re^{-1}) is clearly negligble unless for very small length scales. The only term that remains is buoyancy (Ri). However, the role of buoyancy diminishes for $U > 10$, which implies neutral atmospheric conditions.[1]

What would be left of the Navier-Stokes equations are then the advection terms and the pressure fluctuations. However, if $\bar{v} = \bar{w} = 0$, the mean transport term can also be eliminated, because the longitudinal mean wind speed gradient is, according to Equation (3.4), non-existing. This would reduce Equation (3.10) to

$$\frac{\partial \mathbf{u}'}{\partial t} = -\bar{\mathbf{u}} \cdot \nabla \mathbf{u}' - \mathbf{u}' \cdot \nabla \bar{\mathbf{u}} - \mathbf{u}' \cdot \nabla \mathbf{u}' - \frac{1}{\rho} \nabla P'. \tag{3.11}$$

3.1.3 Taylor's hypothesis

As discussed in Section 2.2, the way gusts are perceived are a consequence of the observer's perspective. A stationary observer will describe a velocity, $\mathbf{u} = [u, v, w]^{\mathsf{T}}$, at each fixed point in space and time (e.g., see Figure 3.2). This yields a relation in the shape of

$$\mathbf{u} = f(\mathbf{x}, t), \tag{3.12}$$

where $\mathbf{x} = [x, y, z]^{\mathsf{T}}$ is the position vector and t denotes the time. In this case, the fluid motion is said to be viewed from an *Eulerian perspective*. On the other hand, one could

---

[1]   Indeed, the strongest wind speeds and gusts are often found at neutral and near-neutral conditions (e.g., see Suomi et al., 2015b).
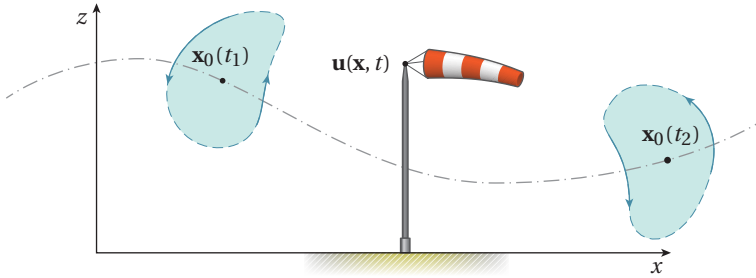
Figure 3.2: An air parcel traveling past a stationary observer.

follow an individual air parcel as it moves with the fluid:

$$\mathbf{x}_0 = f(t), \tag{3.13}$$

where $\mathbf{x}_0$ usually is taken as the parcel's center of mass. This is the *Lagrangian perspective*, which is more concerned with the transport of properties such as mass, temperature, and vorticity. The two frames of reference are connected by the *material derivative*:

$$\underbrace{\frac{\mathrm{D}}{\mathrm{D}t}}_{\substack{\text{Lagrangian}\\\text{acceleration}}} = \overbrace{\frac{\partial}{\partial t}}^{\text{Eulerian acceleration}} + \underbrace{\mathbf{u}\cdot\nabla}_{\text{Advection}}.$$

    A popular shortcut between the two perspectives is *Taylor's hypothesis*, which assumes that the eddies are "frozen" in time. In his 1938 paper, Taylor proposed the following:

> "If the velocity of the air stream which carries the eddies is very much greater than the turbulent velocity, one may assume that the sequence of changes in u at the fixed point are simply due to the passage of an unchanging pattern of turbulent motion over the point, i.e. one may assume that
>
> $$u = \phi(t) = \phi\left(\frac{x}{\bar{u}}\right),$$
>
> where x is measured upstream at time $t = 0$ from the fixed point where u is measured."
>
> (Taylor, 1938)

Formally, it implies that the material derivative is zero ($\mathrm{D}/\mathrm{D}t \approx 0$) and that the Eulerian acceleration is solely driven by (bulk) advection. The major assumption is that, in between two measurements at $t = t_1$ and $t = t_2$, an eddy retains its shape, velocity, and direction. This is often the case for large turbulent structures, since those are known to be particularly long lived (e.g., see Higgins et al., 2012).

    Under Taylor's hypothesis, a stationary observer would be able to deduce the spatial structure of turbulence along a certain path. An eddy measured over a time period, τ, is

then straightforwardly connected to a length scale, ℓ, by

$$\ell \approx \bar{u}\tau, \tag{3.14}$$

where $\bar{u}$ is the speed of advection. Vice versa, an eddy with a length scale ℓ can be expected to pass by in a time $\tau = \ell / \bar{u}$. Adopting Taylor's hypothesis simplifies matters considerably; Equation (3.11) would lose all of its terms apart from the advection by the mean wind:

$$\frac{\partial \mathbf{u}'}{\partial t} = -\bar{\mathbf{u}} \cdot \nabla \mathbf{u}'. \tag{3.15}$$

This is the *linear advection equation*, which has solutions in the form of

$$\mathbf{u}'(\mathbf{x}, t) = \mathbf{u}'(\mathbf{x} - \bar{\mathbf{u}}(t - t_0), t_0), \tag{3.16}$$

which implies that an initial velocity field, $\mathbf{u}'(\mathbf{x}, t_0)$, is simply shifted towards the direction of the mean wind speed at a rate $\bar{\mathbf{u}}$. Section 3.5 will continue with this, but in wave number space.

3.2 Stochastic turbulence modeling

The full Navier-Stokes equations—and even the reduced ones—are unwieldy for practical load calculations. Therefore, statistical methods have been proposed that do not necessarily deal with how velocity fields look like in any moment of time, but rather try to capture the statistics. What follows in this section is a continuation of Subsection 2.2.1.

3.2.1 The energy cascade

Turbulence can be viewed as a process where the energy of some disturbance in the flow is eventually converted into heat. This energy is supplied by the largest scales (the *injective range*) and is transported through the intermediate scales (the *inertial range*), down to the molecular level (the *dissipative range*). An *energy spectrum*, $E(\kappa)$, describes quantitatively how energy is distributed over each wave number, κ, where the wave number is used to represent the scales of motion (see Figures 3.3a and b):

$$\kappa \approx \frac{2\pi}{\ell}. \tag{3.17}$$

A Fourier transform is then used to switch between physical space and wave number space.[2]

The eddies in the injective range draw their energy directly from the mean flow, and their size is set by the scale of the problem. In a wind tunnel, for example, the largest possible length scales are determined by the tunnel diameter. For atmospheric boundary layer flows, the largest eddies are generally limited by the height of the boundary layer ($\sim 10^3$ m).[3]

---

[2] Though, turbulence is composed of eddies, which are discrete coherent structures with finite dimensions and energy. This sort of goes against the nature of the Fourier transform, which turns a single wave number into an infinitely long wave. Instead, it may be appealing to think of a single eddy as more of a wave packet.

[3] In complicated situations like a storm, a downburst, or a squall, the largest structures can well exceed the boundary layer height. This makes the definition a little fuzzy as there may not even be a real distinction between turbulence and the mean flow.

(a): In physical space.   **(b):** In wave number space.
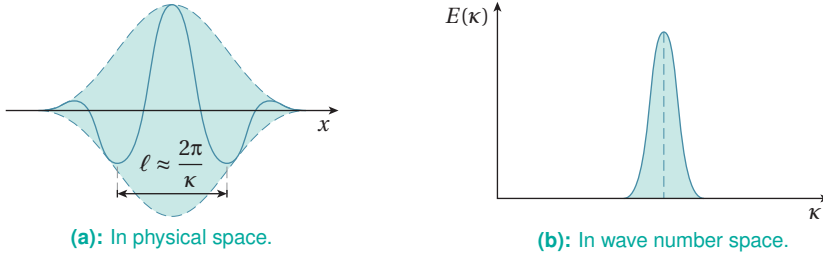
Figure 3.3: An eddy with a length scale $\ell \approx 2\pi/\kappa$ represented as a wave number κ (after Tennekes and Lumley, 1972, p. 259).

Under Richardson's view of turbulence (1922), the inertial range is fully comprised of a hierarchy of eddies. Stretching and tilting cause the larger eddies to break up into smaller eddies, which in turn are broken up into even smaller ones (see Figure 3.4). In 1941, Kolmogorov deduced that, under an average rate of dissipation ϵ, the energy spectrum should scale according to

$$E(\kappa) \propto \epsilon^{2/3} \kappa^{-5/3}, \tag{3.18}$$

classifying turbulence at high wave numbers as *pink noise*. It means that a high degree of self-similarity can be found across the inertial range—if the length scales are halved, the motion would still look the same statistically—which shows some resemblance to fractals (e.g., see Mandelbrot, 1975). This subject is continued in Section 3.4.

In reality, however, this fractal behavior does not continue ad infinitum. The smallest possible scales are defined by the *Kolmogorov microscales*, which Kolmogorov (1941a,b) derived through dimensional analysis:

$$\ell_\mu = \left(\frac{\nu^3}{\epsilon} \right)^{1/4}, \tag{3.19a}$$

$$\tau_\mu = \left(\frac{\nu}{\epsilon} \right)^{1/2}, \tag{3.19b}$$

$$U_\mu = (\nu\epsilon)^{1/4}, \tag{3.19c}$$

where ℓ_μ, τ_μ, and U_μ are a length, time, and velocity scale, respectively. These scales are usually irrelevant for any practical applications and most analytical turbulence spectra will anyway fall to the $-\frac{5}{3}$ law at high wave numbers.

3.2.2 Statistical properties of turbulent flows

Stochastic turbulence models usually assume that the flow shows one or several types of symmetries:

- *Homogeneity* implies that the flow properties are constant throughout the flow field and remain constant under spatial translations: $\mathbf{u}(\mathbf{x}, t) \leftrightarrow \mathbf{u}(\mathbf{x} + \Delta\mathbf{x}, t)$.

- *Isotropy* means that the statistics are unchanged under rotations and reflections: $\mathbf{u}(\mathbf{x}, t) \leftrightarrow \mathbf{u}(\mathbf{x}e^{i\theta}, t)$.
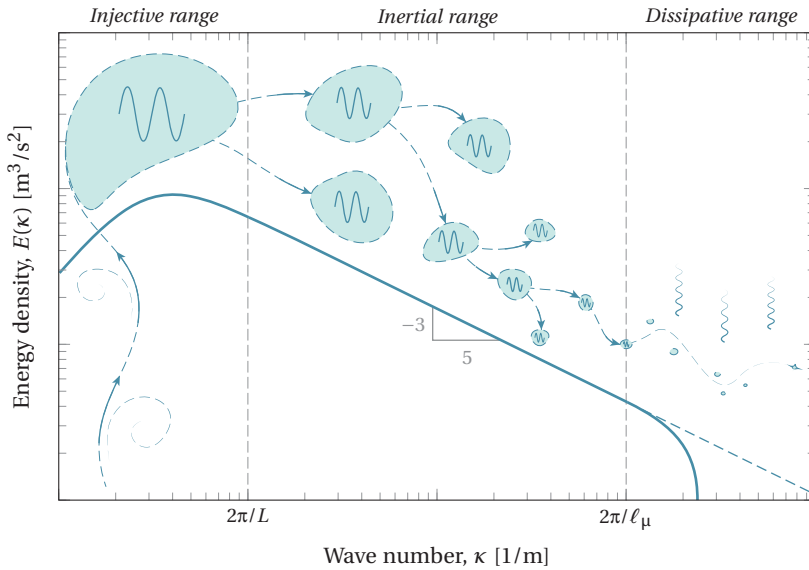
Figure 3.4: Sketch of a turbulence spectrum with the three (sub)ranges, showing how kinetic energy is transported from the largest scales down to the Kolmogorov microscales ($\sim \ell_\mu$) where it is dissipated into heat. The scale of the turbulent flow is set by the turbulence length scale, L.

- *Reflective* turbulence is symmetric with respect to a certain plane: $\mathbf{u}(\mathbf{x}, t) \leftrightarrow \mathbf{u}(-\mathbf{x}, t)$.

- *Stationarity* implies that properties remain invariant in time: $\mathbf{u}(\mathbf{x}, t) \leftrightarrow \mathbf{u}(\mathbf{x}, t + \Delta t)$.

- *Galilean invariance* states that the properties of turbulence remain the same for all inertial frames of reference: $\mathbf{u} \leftrightarrow \mathbf{u}(\mathbf{x}, t) + \Delta \mathbf{u}(\mathbf{x}, t)$.

- *Self-similarity* means that turbulent structures look the same on all scales.

All of these properties are violated in real life up to a certain extent. The effects of buoyancy and shear, for example, quickly destroy isotropy and homogeneity since they contain a directional preference. Also, stationarity can never be fully guaranteed in practice, since many large-scale features exist that can significantly affect what is defined as the mean flow. Furthermore, Galilean invariance is formally violated for large-scale atmospheric flows, because Coriolis forces will start to play a role. And finally, self-similarity can only be preserved in the absence of scale-dependent production and dissipation terms.

3.2.3 Fundamentals of spectral models

The basis of spectral turbulence models lies with the stochastic *Fourier-Stieltjes integral*, which represents a homogeneous velocity field as a stochastic process $d\mathbf{Z}(\boldsymbol{\kappa}, t)$:

$$\mathbf{u}(\mathbf{x}, t) = \bar{\mathbf{u}}(\mathbf{x}) + \int_{\boldsymbol{\kappa}} e^{i\boldsymbol{\kappa}\cdot\mathbf{x}} \, d\mathbf{Z}(\boldsymbol{\kappa}, t), \qquad (3.20)$$

where $\boldsymbol{\kappa} = \left[\kappa_x, \kappa_y, \kappa_z\right]^\mathsf{T}$ is the *wave number vector,* of which the direction and inverse magnitude can be seen as a representation of the orientation and the size of turbulent eddies, respectively. The orthogonal process $\mathrm{d}\mathbf{Z}(\boldsymbol{\kappa}, t)$ is related to the *spectral tensor,* $\boldsymbol{\Phi}(\boldsymbol{\kappa}, t)$, by

$$\overline{\mathrm{d}\mathbf{Z}(\boldsymbol{\kappa}; t)\, \mathrm{d}\mathbf{Z}^*(\boldsymbol{\kappa}'; t)} = \begin{cases} \boldsymbol{\Phi}(\boldsymbol{\kappa}, t)\,\mathrm{d}\boldsymbol{\kappa}, & \text{for } \boldsymbol{\kappa} = \boldsymbol{\kappa}', \\ 0, & \text{for } \boldsymbol{\kappa} \neq \boldsymbol{\kappa}', \end{cases} \tag{3.21}$$

with $\square^*$ denoting a conjugate transpose and $\overline{\square}$ an average.[4] The spectral tensor is the Fourier transform of the covariance tensor:

$$\boldsymbol{\Phi}(\boldsymbol{\kappa}, t) = \frac{1}{(2\pi)^3} \int\limits_{\mathbb{R}^3} \mathbf{R}(\mathbf{r}, t)\mathrm{e}^{-\mathrm{i}\boldsymbol{\kappa}\cdot\mathbf{r}}\,\mathrm{d}\mathbf{r}, \tag{3.22}$$

where the covariance tensor is defined as

$$\mathbf{R}(\mathbf{r}, t) = \overline{\mathbf{u}'(\mathbf{x}; t)\mathbf{u}'^\mathsf{T}(\mathbf{x}+\mathbf{r}; t)}. \tag{3.23}$$

From (3.22) and (3.23) it follows that

$$\overline{\mathbf{u}'\mathbf{u}'^\mathsf{T}}(t) = \int\limits_{\boldsymbol{\kappa}} \boldsymbol{\Phi}(\boldsymbol{\kappa}, t)\,\mathrm{d}\boldsymbol{\kappa}, \tag{3.24}$$

where

$$\overline{\mathbf{u}'\mathbf{u}'^\mathsf{T}} = \begin{bmatrix} \overline{u'^2} & \overline{u'v'} & \overline{u'w'} \\ \overline{u'v'} & \overline{v'^2} & \overline{v'w'} \\ \overline{u'w'} & \overline{v'w'} & \overline{w'^2} \end{bmatrix}. \tag{3.25}$$

Equation (3.24) is *Parseval's theorem* in three dimensions, stating that the energy content in the physical space is completely translated in wave number space. The spectral tensor then describes how this energy is distributed over the wave numbers or eddy scales. The kinetic energy that is carried by turbulence, the *turbulence kinetic energy* (TKE), is defined as the matrix trace of (3.25):

$$k \equiv \tfrac{1}{2}\,\mathrm{tr}\left[\overline{\mathbf{u}'\mathbf{u}'^\mathsf{T}}\right], \tag{3.26}$$

or

$$k \equiv \tfrac{1}{2}\left(\overline{u'^2} + \overline{v'^2} + \overline{w'^2}\right), \tag{3.27}$$

where $\mathrm{tr}\,[\square]$ denotes the matrix trace.[5] This is then linked to the spectral tensor by

$$k(t) = \tfrac{1}{2}\,\mathrm{tr}\left[\int\limits_{\boldsymbol{\kappa}} \boldsymbol{\Phi}(\boldsymbol{\kappa}, t)\,\mathrm{d}\boldsymbol{\kappa}\right]. \tag{3.28}$$

---

[4]   In the left-hand side, t is treated as a parameter rather than a variable to emphasize that the averaging is only applied to $\boldsymbol{\kappa}$.

[5]   Here, $\overline{u'^2}$, $\overline{v'^2}$, and $\overline{w'^2}$ are different ways of writing σ_u^2, σ_v^2, and σ_w^2, which is used in the previous chapter in Equation (2.2).

Under the condition of isotropy (i.e., $\overline{u'^2} = \overline{v'^2} = \overline{w'^2}$), an *energy spectrum* follows from the spectral tensor according to

$$E(\kappa, t) = 2\pi\kappa^2 \, \mathrm{tr}\left[\mathbf{\Phi}(\mathbf{\kappa}, t)\right], \tag{3.29}$$

such that

$$k(t) = \int_\kappa E(\kappa, t) \, \mathrm{d}\kappa, \tag{3.30}$$

where the integration is carried out over a sphere in wave number space with radius $\kappa = \|\mathbf{\kappa}\| = \sqrt{\kappa_x^2 + \kappa_y^2 + \kappa_z^2}$. Vice versa, an isotropic spectral tensor can be constructed from the energy spectrum as given by Batchelor (1953, p. 49):

$$\mathbf{\Phi}(\mathbf{\kappa}, t) = \frac{E(\kappa, t)}{4\pi\kappa^2} \left(\mathbf{I} - \frac{\mathbf{\kappa}\mathbf{\kappa}^\mathsf{T}}{\|\mathbf{\kappa}\|^2} \right), \tag{3.31}$$

with $\mathbf{I}$ denoting the (in this case 3×3) identity matrix. A common spectrum, used for the remaining of this chapter, is the isotropic energy spectrum by Von Kármán (1948):

$$E(\kappa) = \frac{4\Gamma\left(\frac{17}{6}\right)}{\sqrt{\pi}\Gamma\left(\frac{1}{3}\right)} \frac{\sigma_{\mathrm{iso}}^2 \kappa^4 L^5}{\left(1 + \kappa^2 L^2\right)^{17/6}}, \tag{3.32}$$

where $\Gamma(\square)$ is the Gamma function, σ_{iso}^2 the isotropic variance,[6] and L is the turbulence length scale. Alternatively, the above is sometimes expressed as

$$E(\kappa) = \alpha \epsilon^{2/3} L^{5/3} \frac{\kappa^4 L^4}{\left(1 + \kappa^2 L^2\right)^{17/6}}, \tag{3.33}$$

where $\alpha = 1.7$ is the Kolmogorov constant and ϵ is the average rate of dissipation.

3.2.4 Effects of shear

Isotropy, however, is a bold assumption to make in the atmospheric boundary layer. A spectral model that also takes the effects of shear into account is the *uniform shear model*, commonly known as the *Mann model* (after Mann, 1994). It is based on *rapid distortion theory*, which models the statistics of turbulence after a sudden change (e.g., see Subsection 3.5.2). When applied to an initial state $\mathrm{d}\mathbf{Z}(\mathbf{\kappa}(t_0), t_0)$, the distorted field follows from a linear transformation:

$$\mathrm{d}\mathbf{Z}(\mathbf{\kappa}(t), t) = \mathbf{T}\left(\mathbf{\kappa}(t), t; \frac{\mathrm{d}\bar{u}}{\mathrm{d}z}\right) \mathrm{d}\mathbf{Z}(\mathbf{\kappa}(t_0), t_0), \tag{3.34}$$

where $\mathbf{T}$ is a transformation matrix based on a uniform mean wind speed gradient, $\mathrm{d}\bar{u}/\mathrm{d}z$.

Naturally, as time progresses, the field produced by Equation (3.34) grows more anisotropic, even beyond the point at which eddies are expected to break up under too much stretching. To solve this problem, Mann introduced an *eddy lifetime*, $\tau(\kappa)$, to arrive at a stationary field $\mathrm{d}\mathbf{Z}(\mathbf{\kappa}, \tau) \approx \mathrm{d}\mathbf{Z}(\mathbf{\kappa})$. The assumption is that eddies of a size κ^{-1} are

---

6   The isotropic variance follows from $\sigma_{\mathrm{iso}}^2 = \sigma_u^2 = \sigma_v^2 = \sigma_w^2$.

primarily destroyed by smaller structures with a characteristic velocity of $[\int_\kappa^\infty E(\kappa')\,d\kappa']^{1/2}$. Then, based on dimensional grounds, it is deduced that

$$\tau(\kappa) \propto \kappa^{-1} \left[\int_\kappa^\infty E(\kappa')\,d\kappa' \right]^{-1/2},$$

$$\propto \kappa^{-2/3} \left[{}_2F_1\left(\tfrac{1}{3}, \tfrac{17}{6}, \tfrac{4}{3}, -(\kappa L)^{-2}\right) \right]^{-1/2},$$

where ${}_2F_1(\square)$ is the hypergeometric function. The full expression is then given by

$$\tau(\kappa) = \Gamma \left(\frac{\partial \bar{u}}{\partial z}\right)^{-1} (\kappa L)^{-2/3} \left[{}_2F_1\left(\tfrac{1}{3}, \tfrac{17}{6}, \tfrac{4}{3}, -(\kappa L)^{-2}\right) \right]^{-1/2}, \tag{3.35}$$

where Γ is a shear parameter and L is again the turbulence length scale. This results in a spectral tensor with the components

$$\Phi_{uu}(\mathbf{\kappa}) = \frac{E(\kappa_0)}{4\pi\kappa_0^4} \left[\kappa_0^2 - \kappa_x^2 - 2\kappa_x\kappa_{z,0}\zeta_1 + \left(\kappa_x^2 + \kappa_y^2\right)\zeta_1^2 \right], \tag{3.36a}$$

$$\Phi_{vv}(\mathbf{\kappa}) = \frac{E(\kappa_0)}{4\pi\kappa_0^4} \left[\kappa_0^2 - \kappa_y^2 - 2\kappa_y\kappa_{z,0}\zeta_2 + \left(\kappa_x^2 + \kappa_y^2\right)\zeta_2^2 \right], \tag{3.36b}$$

$$\Phi_{ww}(\mathbf{\kappa}) = \frac{E(\kappa_0)}{4\pi\kappa^4} \left[\kappa_x^2 + \kappa_y^2 \right], \tag{3.36c}$$

$$\Phi_{uv}(\mathbf{\kappa}) = \frac{E(\kappa_0)}{4\pi\kappa_0^4} \left[-\kappa_x\kappa_y - \kappa_x\kappa_{z,0}\zeta_2 - \kappa_y\kappa_{z,0}\zeta_1 + \left(\kappa_x^2 + \kappa_y^2\right)\zeta_1\zeta_2 \right], \tag{3.36d}$$

$$\Phi_{uw}(\mathbf{\kappa}) = \frac{E(\kappa_0)}{4\pi\kappa_0^2\kappa^2} \left[-\kappa_x\kappa_{z,0} + \left(\kappa_x^2 + \kappa_y^2\right)\zeta_1 \right], \tag{3.36e}$$

$$\Phi_{vw}(\mathbf{\kappa}) = \frac{E(\kappa_0)}{4\pi\kappa_0^2\kappa^2} \left[-\kappa_y\kappa_{z,0} + \left(\kappa_x^2 + \kappa_y^2\right)\zeta_2 \right], \tag{3.36f}$$

and the remaining ones given by Hermitian symmetry ($\Phi_{ij} = \Phi_{ji}^*$). The wave number $\mathbf{\kappa}_0 = \mathbf{\kappa}(t_0) = \left[\kappa_x, \kappa_y, \kappa_{z,0}\right]^\mathsf{T}$ with $\kappa_{z,0} = \kappa_z(t_0) = \kappa_z + \beta\kappa_x$ is used to describe the initial, unsheared velocity field with

$$\beta = \frac{\partial \bar{u}}{\partial z}\tau \tag{3.37}$$

as a non-dimensional distortion time. Moreover, the parameters ζ_1 and ζ_2 are given by

$$\zeta_1 = \left(C_1 - \frac{\kappa_y}{\kappa_x}C_2 \right), \tag{3.38a}$$

$$\zeta_2 = \left(C_2 + \frac{\kappa_y}{\kappa_x}C_1 \right), \tag{3.38b}$$

with

$$C_1 = \frac{\beta\kappa_x^2 \left(\kappa_0^2 - 2\kappa_{z,0}^2 + \beta\kappa_x\kappa_{z,0}\right)}{\kappa^2 \left(\kappa_x^2 + \kappa_y^2\right)}, \tag{3.39a}$$

$$C_2 = \frac{\kappa_y\kappa_0^2}{\left(\kappa_x^2 + \kappa_y^2\right)^{3/2}} \arctan\left(\frac{\beta\kappa_x\sqrt{\kappa_x^2 + \kappa_y^2}}{\kappa_0^2 - \kappa_{z,0}\kappa_x\beta} \right). \tag{3.39b}$$

In total, the Mann model describes the statistics of sheared turbulence with 3 parameters: a length scale, L, a viscous dissipation rate, $\alpha\epsilon^{2/3}$ (or σ_{iso}, depending on whether Equation (3.32) or (3.33) is used for the isotropic energy spectrum), and a shear parameter, Γ.

3.2.5 Synthesis of Gaussian random fields

In practice, velocity fields are generated by computers on a discretized space. Usually, this is a rectangular box with size $L_x \times L_y \times L_z$ containing a $N_x \times N_y \times N_z$ grid (see Figure 3.5), where the positions are equally spaced according to

$$x = i\Delta x, \quad \text{for } i = 0,\ldots,N_x - 1, \tag{3.40a}$$

$$y = j\Delta y, \quad \text{for } j = 0,\ldots,N_y - 1, \tag{3.40b}$$

$$z = k\Delta z, \quad \text{for } k = 0,\ldots,N_z - 1, \tag{3.40c}$$

with a step size $\Delta x = L_x/N_x$. Instead of a continuous Fourier transform, a spectrum is then translated to the physical space using a *discrete Fourier transform* (DFT). This means Equation (3.20) is approximated by

$$\int_{\kappa} e^{i\kappa \cdot x} d\mathbf{Z}(\kappa, t) \approx \sum_{\kappa} e^{i\kappa \cdot x} \Delta \mathbf{Z}(\kappa, t), \tag{3.41}$$

with

$$\overline{\Delta \mathbf{Z}(\kappa; t)\Delta \mathbf{Z}^*(\kappa; t)} = \int_{\Delta\kappa} \Phi(\kappa - \kappa', t)\, d\kappa', \tag{3.42}$$

where the integral is carried out over the volume $\Delta\kappa = \Delta\kappa_x \Delta\kappa_y \Delta\kappa_z$. Based on a rectangular box with dimensions $L_x \times L_y \times L_z$, the wave numbers for a two-sided spectrum[7] can be
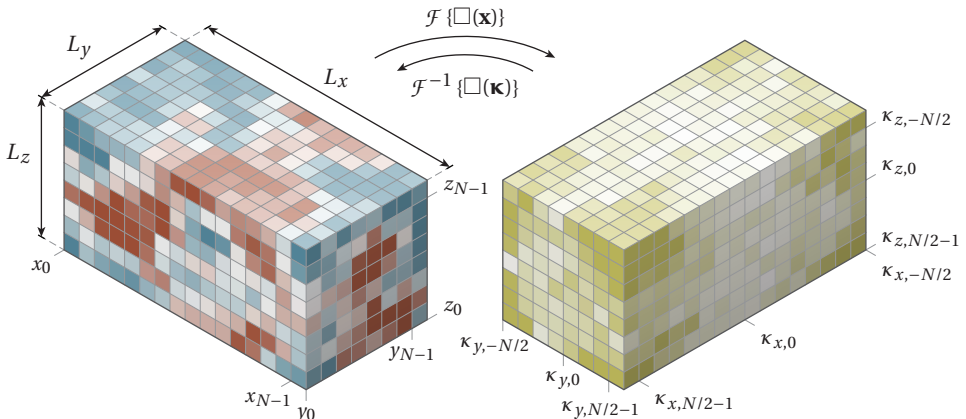
Figure 3.5: The discrete Fourier transform (DFT) is used to translate a $N_x \times N_y \times N_z$ physical domain (left) to the wave number domain (right).

---

[7] In a two-sided spectrum, the variance is equally divided between the positive and negative wave numbers. Since the spectral tensor is Hermitian, it follows that $\Phi(\kappa) = \Phi^*(-\kappa)$.
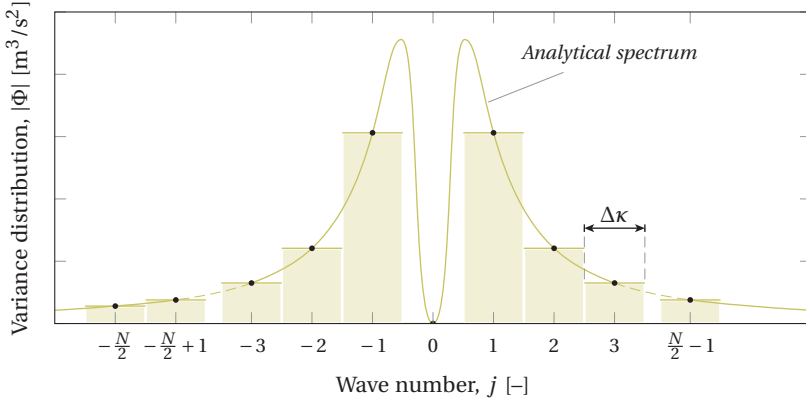
Figure 3.6: In a discretized spectrum, part of the variance is lost below the fundamental frequency ($|j| < 1$) and above the Nyquist frequency ($|j| > N/2$).

discretized according to

$$\kappa_x = i\Delta\kappa_x, \quad \text{for } i = -N_x/2,\ldots,N_x/2-1, \tag{3.43a}$$

$$\kappa_y = j\Delta\kappa_y, \quad \text{for } j = -N_y/2,\ldots,N_y/2-1, \tag{3.43b}$$

$$\kappa_z = k\Delta\kappa_z, \quad \text{for } k = -N_z/2,\ldots,N_z/2-1, \tag{3.43c}$$

with $\Delta\kappa_x = 2\pi/L_x$. Therefore, the length scales that are covered range from the first nonzero wave number, $2\pi/L_x$ (i.e., the fundamental frequency), up to the Nyquist frequency, $N_x\pi/L_x$. This has an effect on the variance that can be translated from and to the wave number space. Parseval's theorem, given by Equation (3.24), now states that

$$\frac{1}{N_x N_y N_z} \sum_{i=0}^{N_x-1} \sum_{j=0}^{N_y-1} \sum_{k=0}^{N_z-1} \mathbf{u}'(x_i, y_j, z_k, t)\mathbf{u}'^{\mathsf{T}}(x_i, y_j, z_k, t)$$

$$= \sum_{i=-N_x/2}^{N_x/2-1} \sum_{j=-N_y/2}^{N_y/2-1} \sum_{k=-N_z/2}^{N_z/2-1} \mathbf{\Phi}(\kappa_{x,i}, \kappa_{y,j}, \kappa_{z,k}, t)\Delta\kappa_x \Delta\kappa_y \Delta\kappa_z. \tag{3.44}$$

As sketched in Figure 3.6, the variance below the fundamental frequency and above the Nyquist frequency is lost in the discrete spectrum. This loss can be minimized by, on the one hand, making the domain large enough and, on the other hand, decreasing the grid spacing.

With spectral models, the randomness is often generated using white noise. The stochastic process, $\Delta\mathbf{Z}$, is then represented as a matrix of coefficients, $\mathbf{C}$, multiplied with a complex white noise vector, $\mathbf{n}$:

$$\Delta\mathbf{Z}(\boldsymbol{\kappa}, t) = \mathbf{C}(\boldsymbol{\kappa}, t)\mathbf{n}(\boldsymbol{\kappa}, t). \tag{3.45}$$

The matrix $\mathbf{C}$ follows from the spectral tensor according to Equation (3.45):

$$\mathbf{C}(\boldsymbol{\kappa}, t)\mathbf{C}^*(\boldsymbol{\kappa}, t) = \int_{\Delta\boldsymbol{\kappa}} \mathbf{\Phi}(\boldsymbol{\kappa} - \boldsymbol{\kappa}', t)\,\mathrm{d}\boldsymbol{\kappa}', \tag{3.46}$$
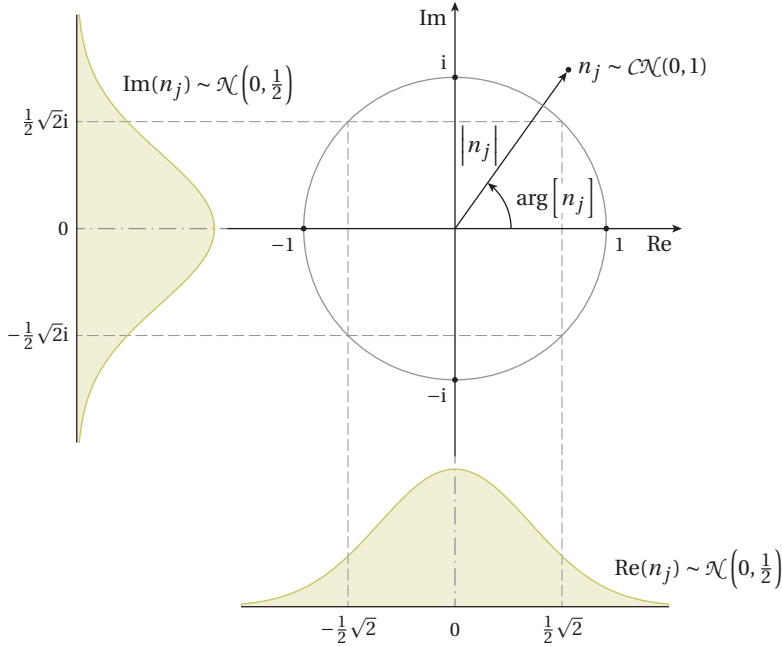
Figure 3.7: The circularly symmetric complex normal distribution for the jth element of the white noise vector $\mathbf{n}$. The complex magnitude, $|n_j|$, is Rayleigh-distributed, whereas the complex argument, $\arg[n_j]$, is uniformly distributed on $[0, 2\pi]$.

which, under the assumption that the domain is much larger than the turbulence length scale, L (Mann, 1998), can be approximated by

$$\mathbf{C}(\boldsymbol{\kappa}, t)\mathbf{C}^*(\boldsymbol{\kappa}, t) \approx \boldsymbol{\Phi}(\boldsymbol{\kappa}, t)\Delta\kappa_x\Delta\kappa_y\Delta\kappa_z. \tag{3.47}$$

The role of the white noise vector, $\mathbf{n}$, is to randomize the harmonics. It is distributed according to a circularly symmetric complex normal distribution, $\mathcal{CN}(0, \mathbf{I})$, which implies that

$$\begin{bmatrix} \text{Re}(\mathbf{n}) \\ \text{Im}(\mathbf{n}) \end{bmatrix} \sim \mathcal{N}\left(\begin{bmatrix} 0 \\ 0 \end{bmatrix}, \frac{1}{2}\begin{bmatrix} \mathbf{I} & 0 \\ 0 & \mathbf{I} \end{bmatrix} \right), \tag{3.48}$$

where $\mathbf{I}$ is the 3×3 identity matrix (e.g., see Figure 3.7). Multiplying with $\mathbf{n}$ causes each of the Fourier coefficients to get a random amplitude and a uniformly distributed phase shift. Based on Equation (3.41), a velocity field is then constructed from

$$\mathbf{u}(\mathbf{x}, t) \approx \bar{\mathbf{u}}(\mathbf{x}) + \sum_{\boldsymbol{\kappa}} \mathbf{C}(\boldsymbol{\kappa}, t)\mathbf{n}(\boldsymbol{\kappa}, t)e^{i\boldsymbol{\kappa}\cdot\mathbf{x}}, \tag{3.49}$$

where $\sum_{\boldsymbol{\kappa}}$ is used to denote the triple sum:

$$\sum_{\boldsymbol{\kappa}}(\boldsymbol{\kappa}) = \sum_{i=-N_x/2}^{N_x/2-1} \sum_{j=-N_y/2}^{N_y/2-1} \sum_{k=-N_z/2}^{N_z/2-1} (\kappa_{x,i}, \kappa_{y,j}, \kappa_{z,k}). \tag{3.50}$$

The zero mode is, in fact, the constant mean wind speed. It is usually not covered by the spectrum, but added separately as $\bar{\mathbf{u}}(\mathbf{x})$. The random vector, $\mathbf{n}$, has an important role, since it ensures that each realization of Equation (3.49) produces a fully randomized, but statistically similar, turbulent velocity field.

As an alternative to using a summation, the Fourier series can also be represented as a linear combination:

$$\mathbf{u}(\mathbf{x}, t) = \bar{\mathbf{u}}(\mathbf{x}) + \boldsymbol{\Psi}(\mathbf{x}, t)\mathbf{n}(t), \tag{3.51}$$

where

$$\boldsymbol{\Psi}(\mathbf{x}, t)\mathbf{n}(t) = \left[\ldots, \mathbf{C}(\boldsymbol{\kappa}_j, t)e^{i\boldsymbol{\kappa}_j \cdot \mathbf{x}}, \mathbf{C}(\boldsymbol{\kappa}_{j+1}, t)e^{i\boldsymbol{\kappa}_{j+1} \cdot \mathbf{x}}, \ldots\right] \begin{bmatrix} \vdots \\ \mathbf{n}(\boldsymbol{\kappa}_j, t) \\ \mathbf{n}(\boldsymbol{\kappa}_{j+1}, t) \\ \vdots \end{bmatrix}. \tag{3.52}$$

The matrix $\boldsymbol{\Psi}$ has three rows, corresponding to the three velocity components:

$$\boldsymbol{\Psi}_u(\mathbf{x}, t) = \left[\ldots, \left[C_{uu}(\boldsymbol{\kappa}_j, t), C_{uv}(\boldsymbol{\kappa}_j, t), C_{uw}(\boldsymbol{\kappa}_j, t)\right]e^{i\boldsymbol{\kappa}_j \cdot \mathbf{x}}, \ldots\right], \tag{3.53a}$$

$$\boldsymbol{\Psi}_v(\mathbf{x}, t) = \left[\ldots, \left[C_{vu}(\boldsymbol{\kappa}_j, t), C_{vv}(\boldsymbol{\kappa}_j, t), C_{vw}(\boldsymbol{\kappa}_j, t)\right]e^{i\boldsymbol{\kappa}_j \cdot \mathbf{x}}, \ldots\right], \tag{3.53b}$$

$$\boldsymbol{\Psi}_w(\mathbf{x}, t) = \left[\ldots, \left[C_{wu}(\boldsymbol{\kappa}_j, t), C_{wv}(\boldsymbol{\kappa}_j, t), C_{ww}(\boldsymbol{\kappa}_j, t)\right]e^{i\boldsymbol{\kappa}_j \cdot \mathbf{x}}, \ldots\right]. \tag{3.53c}$$

The linear combination (3.51) is sometimes a more convenient way of formulating the Fourier series, since a lot of operations involving summations reduce to matrix algebra.

3.3 The spatial structure of wind gusts

In essence, Equation (3.49) describes the set of all possible velocity fields that adhere to the statistics of the spectral tensor. This also includes extreme gusts, although with a very low probability of occurrence.

3.3.1 A wind gust as a momentum concentration

As covered by Subsection 2.2.5, an effective measure of the severity of a gust is its momentum. Just as throwing five billiard balls is potentially more harmful than just throwing one, a gust can be considered more severe if more air particles are involved. For example, the momentum of the collection of air particles sketched in Figure 3.8 is

$$\mathbf{p}(\mathbf{x}_0, t; V) = m \sum_{i \in V} \mathbf{u}(\mathbf{x}_0 + \mathbf{r}_i, t), \tag{3.54}$$

where m is the mass of each particle and V is the volume enclosing them. It shows that, as long as they are heading in the same direction, more particles means that the gust has a higher momentum.

The same can be applied to a continuous velocity field. When the volume, V, is represented as a kernel, g, centered around a position, $\mathbf{x}_0$, the momentum follows from a
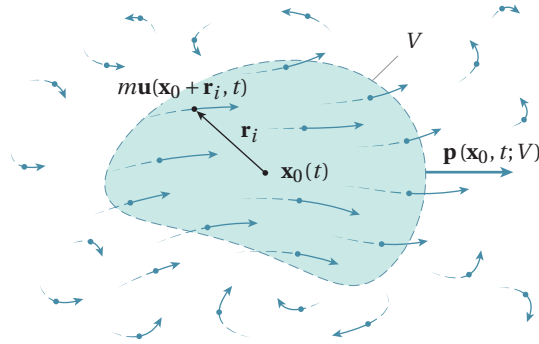
Figure 3.8: A gust represented as a collection of air particles within a volume V, centered around $\mathbf{x}_0$, having a total momentum $\mathbf{p}$.

convolution integral, $\mathbf{u}(\mathbf{x}_0, t) * g$:

$$\mathbf{p}(\mathbf{x}_0, t; V) = \rho \, \mathrm{vol}(V) \int_{\mathbb{R}^3} \mathbf{u}(\mathbf{x}_0 + \mathbf{r}, t) g(\mathbf{r}) \, \mathrm{d}\mathbf{r}, \tag{3.55}$$

where ρ is the air density, $\mathrm{vol}(V)$ is the volume of V, and where the kernel function is

$$g(\mathbf{r}) = \begin{cases} \dfrac{1}{\mathrm{vol}(V)}, & \text{for } \mathbf{r} \in V, \\ 0, & \text{for } \mathbf{r} \notin V. \end{cases} \tag{3.56}$$

Basically, a gust's momentum is equal to the air mass within the volume, V, times the average velocity of that volume. For a severe gust, this velocity should be significantly higher than what is found in the surrounding air (e.g., see Figure 3.9). Therefore, it is often more intuitive to apply the Reynolds decomposition:

$$\begin{aligned}
\mathbf{p}(\mathbf{x}_0, t; V) &= \rho \, \mathrm{vol}(V) \int_{\mathbb{R}^3} \left[\bar{\mathbf{u}}(\mathbf{x}_0 + \mathbf{r}) + \mathbf{u}'(\mathbf{x}_0 + \mathbf{r}, t) \right] g(\mathbf{r}) \, \mathrm{d}\mathbf{r}, \\
&= \rho \, \mathrm{vol}(V) \left[\int_{\mathbb{R}^3} \bar{\mathbf{u}}(\mathbf{x}_0 + \mathbf{r}) g(\mathbf{r}) \, \mathrm{d}\mathbf{r} + \int_{\mathbb{R}^3} \mathbf{u}'(\mathbf{x}_0 + \mathbf{r}, t) g(\mathbf{r}) \, \mathrm{d}\mathbf{r} \right], \\
&= \bar{\mathbf{p}}(\mathbf{x}_0; V) + \mathbf{p}'(\mathbf{x}_0, t; V). \tag{3.57}
\end{aligned}$$

The momentum of a gust is then simply added to the momentum resulting from advection, much like the case of a ball being thrown from a moving car.

If V is symmetric with respect to the xy-plane and the mean wind speed gradient is relatively linear over the volume, a reasonable assumption is that $\bar{\mathbf{u}}(\mathbf{x}_0) * g \approx \bar{\mathbf{u}}(\mathbf{x}_0)$, which leads to

$$\bar{\mathbf{p}}(\mathbf{x}_0; V) = \rho \, \mathrm{vol}(V) \bar{\mathbf{u}}(\mathbf{x}_0). \tag{3.58}$$
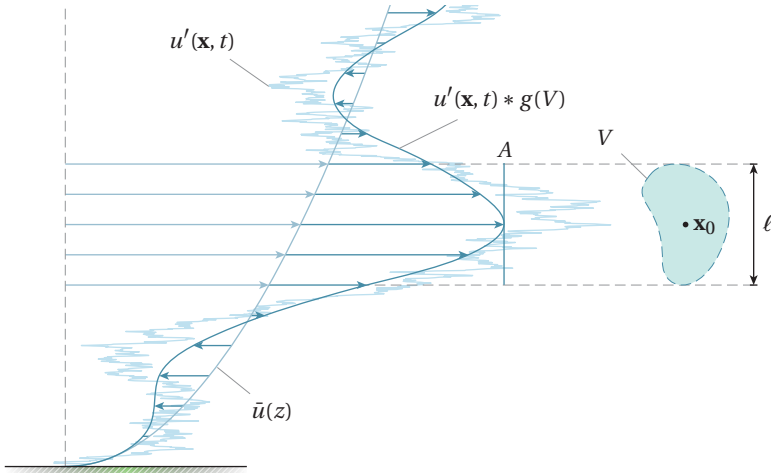
Figure 3.9: A streamwise gust with a length scale, ℓ, having an average velocity of A within the volume, V. Shown are the mean wind speed, $\bar{u}(z)$, the unsteady wind speed, $u'(\mathbf{x}, t)$, and the unsteady wind speed convoluted with the gust volume, $u'(\mathbf{x}, t) * g(V)$.

Moreover, by relying on the *convolution theorem*, the gust momentum is easily translated to wave number space:

$$\mathbf{p}'(\mathbf{x}_0, t; V) = \rho \,\mathrm{vol}(V) \int_{\boldsymbol{\kappa}} G(\boldsymbol{\kappa}) e^{i\boldsymbol{\kappa} \cdot \mathbf{x}_0} \, d\mathbf{Z}(\boldsymbol{\kappa}, t), \tag{3.59}$$

where $G(\boldsymbol{\kappa}) = \mathcal{F}\{g(\mathbf{r})\}$ is now a low-pass filter. This states that a momentum field can be directly obtained from the turbulent velocity spectrum by eliminating the higher wave numbers.

3.3.2 The velocity field around a concentration of momentum

From now on, a gust will be treated as a concentration of momentum in the streamwise direction, denoted by p'. This means that gusts are spawned from the scalar field $u'(\mathbf{x}, t)$, which is assumed to be homogeneous to allow it to be represented by the Fourier series (3.49). Furthermore, the turbulence field is considered at a fixed time t_0, far upstream of any obstacle.

If the gust's (streamwise) velocity amplitude is denoted by A (see Figure 3.9), its momentum is given by

$$p'(\mathbf{x}_0, t_0; V) = \rho \,\mathrm{vol}(V) A. \tag{3.60a}$$

Moreover, if the gust is of any significance, its momentum should at least be a local maximum (or a local mininum):

$$\nabla p'(\mathbf{x}_0, t_0; V) = [0, 0, 0]^{\mathsf{T}}, \tag{3.60b}$$

$$\left| \mathbf{H}_{p'}(\mathbf{x}_0) \right| < 0, \tag{3.60c}$$

where $\left| \mathbf{H}_{p'}(\mathbf{x}_0) \right|$ is the determinant of the Hessian matrix, evaluated at $\mathbf{x}_0$. However, since the interest is in high amplitudes, the point $\mathbf{x}_0$ is most likely not a saddle point anyway, allowing requirement (3.60c) to be dropped. This leads to the following conditional velocity field surrounding a gust:

$$\hat{\mathbf{u}}'(\mathbf{x}, t_0; V) = \left\{ \mathbf{u}'(\mathbf{x}, t_0) \mid p'(\mathbf{x}_0; t_0, V) = \rho \operatorname{vol}(V) A, \ \nabla p'(\mathbf{x}_0, t_0; V) = 0 \right\}. \qquad (3.61)$$

The two requirements can be expressed as a set of linear constraints. From Equation (3.59) it follows that the streamwise momentum can be obtained from filtering the first row of the Fourier transform matrix, $\mathbf{\Psi}$ (3.53a):

$$\begin{bmatrix} p'(\mathbf{x}_0, t_0; V) \\ \nabla p'(\mathbf{x}_0, t_0; V) \end{bmatrix} = \rho \operatorname{vol}(V) \mathbf{Yn}, \qquad (3.62)$$

with

$$\mathbf{Yn} = \begin{bmatrix} \ldots, & G(\boldsymbol{\kappa}_j) \left[C_{uu}(\boldsymbol{\kappa}_j), C_{uv}(\boldsymbol{\kappa}_j), C_{uw}(\boldsymbol{\kappa}_j) \right] e^{i\boldsymbol{\kappa}_j \cdot \mathbf{x}_0}, \ \ldots \\ \ldots, & i\kappa_{x,j} G(\boldsymbol{\kappa}_j) \left[C_{uu}(\boldsymbol{\kappa}_j), C_{uv}(\boldsymbol{\kappa}_j), C_{uw}(\boldsymbol{\kappa}_j) \right] e^{i\boldsymbol{\kappa}_j \cdot \mathbf{x}_0}, \ \ldots \\ \ldots, & i\kappa_{y,j} G(\boldsymbol{\kappa}_j) \left[C_{uu}(\boldsymbol{\kappa}_j), C_{uv}(\boldsymbol{\kappa}_j), C_{uw}(\boldsymbol{\kappa}_j) \right] e^{i\boldsymbol{\kappa}_j \cdot \mathbf{x}_0}, \ \ldots \\ \ldots, & i\kappa_{z,j} G(\boldsymbol{\kappa}_j) \left[C_{uu}(\boldsymbol{\kappa}_j), C_{uv}(\boldsymbol{\kappa}_j), C_{uw}(\boldsymbol{\kappa}_j) \right] e^{i\boldsymbol{\kappa}_j \cdot \mathbf{x}_0}, \ \ldots \end{bmatrix} \begin{bmatrix} \vdots \\ \mathbf{n}(\boldsymbol{\kappa}_j) \\ \vdots \end{bmatrix}. \qquad (3.63)$$

The conditional field (3.10) can then be expressed as

$$\hat{\mathbf{u}}'(\mathbf{x}, t_0; V) = \mathbf{\Psi} \left\{ \mathbf{n} \mid \mathbf{Yn} = \mathbf{b} \right\}, \qquad (3.64)$$

where

$$\mathbf{b} = \begin{bmatrix} A \\ 0 \\ 0 \\ 0 \end{bmatrix} \qquad (3.65)$$

is a vector of constraints. The random vector obeying the constraints $\mathbf{n} \mid \mathbf{Yn} = \mathbf{b}$ can be found through conditional sampling:

$$\hat{\mathbf{n}} = \mathbf{n} + \mathbf{Y}^* \left(\mathbf{YY}^* \right)^{-1} (\mathbf{b} - \mathbf{Yn}), \qquad (3.66)$$

where $\hat{\mathbf{n}}$ is the *conditional white noise vector*. The turbulent velocity field, $\hat{\mathbf{u}}'(\mathbf{x})$, is then obtained from the Fourier series (3.49).

Equation (3.66), in combination with Equations (3.63) and (3.70), is probably the most practically significant result of this thesis. It allows one to directly sample from a collection of severe gusts, while adhering to the statistics of the turbulence spectrum. In other words: it allows designers to produce wind fields that are embedded with gusts, which would otherwise occur naturally in very long time series. How this can be used to the designer's advantage will be demonstrated in the next chapters.

The rest of this section will be used to dive somewhat deeper into this result. Formally, Equation (3.64) describes the set of all possible velocity fields surrounding a streamwise gust. The statistics of this set follow from the joint distribution

$$
\begin{bmatrix} \mathbf{n} \\ \mathbf{Yn} \end{bmatrix} \sim \mathcal{N}\left(\begin{bmatrix} \mathrm{E}\,[\mathbf{n}] \\ \mathrm{E}\,[\mathbf{Yn}] \end{bmatrix}, \begin{bmatrix} \mathrm{E}\,[\mathbf{nn}^*] & \mathrm{E}\,[\mathbf{n(Yn)}^*] \\ \mathrm{E}\,[\mathbf{(Yn)n}^*] & \mathrm{E}\,[\mathbf{(Yn)(Yn)}^*] \end{bmatrix} \right),
\tag{3.67}
$$

which leads to

$$
\mathbf{n}|\mathbf{Yn} = \mathbf{b} \sim \mathcal{N}\left(\mathbf{Y}^*\left(\mathbf{YY}^*\right)^{-1}\mathbf{b}, \mathbf{I} - \mathbf{Y}^*\left(\mathbf{YY}^*\right)^{-1}\mathbf{Y} \right),
\tag{3.68}
$$

implying that

$$
\mathrm{E}\,[\mathbf{n}\,|\,\mathbf{Yn} = \mathbf{b}] = \mathbf{Y}^*\left(\mathbf{YY}^*\right)^{-1}\mathbf{b},
\tag{3.69a}
$$

$$
\mathrm{var}\,[\mathbf{n}\,|\,\mathbf{Yn} = \mathbf{b}] = \mathbf{I} - \mathbf{Y}^*\left(\mathbf{YY}^*\right)^{-1}\mathbf{Y}.
\tag{3.69b}
$$

From this, it can be said that the velocity field in general is built up from a mean gust, $\mathbf{\Psi}\mathrm{E}\,[\mathbf{n}\,|\,\mathbf{Yn} = \mathbf{b}]$, and a Gaussian residual process, $\mathbf{\Delta}(\mathbf{x})$:

$$
\mathbf{\hat{u}}'(\mathbf{x}) = \mathbf{\Psi}\mathrm{E}\,[\mathbf{n}\,|\,\mathbf{Yn} = \mathbf{b}] + \mathbf{\Delta}(\mathbf{x}),
\tag{3.70}
$$

with $\mathrm{var}\,[\mathbf{\Delta}(\mathbf{x})] = \mathbf{\Psi}\mathrm{var}\,[\mathbf{n}\,|\,\mathbf{Yn} = \mathbf{b}]\,\mathbf{\Psi}^*$.

The mean gust shape is deterministic in nature and has an analytical expression. First, writing out the term $\mathbf{YY}^*$ yields

$$
\mathbf{YY}^* = \sum_{\boldsymbol{\kappa}} \begin{bmatrix} 1 & -i\kappa_x & -i\kappa_y & -i\kappa_z \\ i\kappa_x & \kappa_x^2 & \kappa_x\kappa_y & \kappa_x\kappa_z \\ i\kappa_y & \kappa_x\kappa_y & \kappa_y^2 & \kappa_y\kappa_z \\ i\kappa_z & \kappa_x\kappa_z & \kappa_y\kappa_z & \kappa_z^2 \end{bmatrix} G^2(\boldsymbol{\kappa})\big(C_{uu}(\boldsymbol{\kappa})C_{uu}^*(\boldsymbol{\kappa})
$$

$$
\cdots + C_{uv}(\boldsymbol{\kappa})C_{uv}^*(\boldsymbol{\kappa}) + C_{uw}(\boldsymbol{\kappa})C_{uw}^*(\boldsymbol{\kappa})\big).
\tag{3.71}
$$

Following equation (3.47), the uu-component of the spectral tensor can be written as

$$
\Phi_{uu}(\boldsymbol{\kappa})\Delta\kappa_x\Delta\kappa_y\Delta\kappa_z \approx C_{uu}(\boldsymbol{\kappa})C_{uu}^*(\boldsymbol{\kappa}) + C_{uv}(\boldsymbol{\kappa})C_{uv}^*(\boldsymbol{\kappa}) + C_{uw}(\boldsymbol{\kappa})C_{uw}^*(\boldsymbol{\kappa}).
\tag{3.72}
$$

which leads to

$$
\mathbf{YY}^* = \sum_{\boldsymbol{\kappa}} \begin{bmatrix} 1 & -i\kappa_x & -i\kappa_y & -i\kappa_z \\ i\kappa_x & \kappa_x^2 & \kappa_x\kappa_y & \kappa_x\kappa_z \\ i\kappa_y & \kappa_x\kappa_y & \kappa_y^2 & \kappa_y\kappa_z \\ i\kappa_z & \kappa_x\kappa_z & \kappa_y\kappa_z & \kappa_z^2 \end{bmatrix} G^2(\boldsymbol{\kappa})\Phi_{uu}(\boldsymbol{\kappa})\Delta\kappa_x\Delta\kappa_y\Delta\kappa_z.
\tag{3.73}
$$

Moreover, since $\Phi_{uu}(\boldsymbol{\kappa}) = \Phi_{uu}(-\boldsymbol{\kappa})$ and $G^2(\boldsymbol{\kappa}) = G^2(-\boldsymbol{\kappa})$, it follows that

$$
\sum_{\boldsymbol{\kappa}} i\kappa_x G^2(\boldsymbol{\kappa})\Phi_{uu}(\boldsymbol{\kappa}) = 0,
\tag{3.74}
$$

which gets rid of the complex entries in the matrix. In the limit of $\Delta\kappa_x\Delta\kappa_y\Delta\kappa_z \to 0$, this then results in

$$\mathbf{Y}\mathbf{Y}^* = \begin{bmatrix} \Lambda_0 & 0 \\ 0 & \Lambda_2 \end{bmatrix}, \tag{3.75}$$

where Λ_0 and Λ_2 are the zeroth- and second-order spectral moments of the filtered spectrum:

$$\Lambda_0 = \int_{\boldsymbol{\kappa}} G^2(\boldsymbol{\kappa})\Phi_{uu}(\boldsymbol{\kappa})\,\mathrm{d}\boldsymbol{\kappa}, \tag{3.76}$$

$$\Lambda_2 = \int_{\boldsymbol{\kappa}} \boldsymbol{\kappa}\boldsymbol{\kappa}^{\mathsf{T}} G^2(\boldsymbol{\kappa})\Phi_{uu}(\boldsymbol{\kappa})\,\mathrm{d}\boldsymbol{\kappa}. \tag{3.77}$$

Fortunately, being a block matrix makes $\mathbf{Y}\mathbf{Y}^*$ easily invertible:

$$\left(\mathbf{Y}\mathbf{Y}^*\right)^{-1} = \begin{bmatrix} \Lambda_0^{-1} & 0 \\ 0 & \Lambda_2^{-1} \end{bmatrix}. \tag{3.78}$$

The next part is writing out the matrix product $\boldsymbol{\Psi}\mathbf{Y}^*$:

$$\boldsymbol{\Psi}\mathbf{Y}^* = \begin{bmatrix} \ldots, & \begin{bmatrix} C_{uu}(\boldsymbol{\kappa}_j) & C_{uv}(\boldsymbol{\kappa}_j) & C_{uw}(\boldsymbol{\kappa}_j) \\ C_{vu}(\boldsymbol{\kappa}_j) & C_{vv}(\boldsymbol{\kappa}_j) & C_{vw}(\boldsymbol{\kappa}_j) \\ C_{wu}(\boldsymbol{\kappa}_j) & C_{wv}(\boldsymbol{\kappa}_j) & C_{ww}(\boldsymbol{\kappa}_j) \end{bmatrix} e^{\mathrm{i}\boldsymbol{\kappa}_j\cdot\mathbf{x}}, \ldots \end{bmatrix}$$

$$\cdots \begin{bmatrix} \vdots \\ \begin{bmatrix} C_{uu}^*(\boldsymbol{\kappa}_j) & -\mathrm{i}\kappa_x C_{uu}^*(\boldsymbol{\kappa}_j) & -\mathrm{i}\kappa_y C_{uu}^*(\boldsymbol{\kappa}_j) & -\mathrm{i}\kappa_z C_{uu}^*(\boldsymbol{\kappa}_j) \\ C_{uv}^*(\boldsymbol{\kappa}_j) & -\mathrm{i}\kappa_x C_{uv}^*(\boldsymbol{\kappa}_j) & -\mathrm{i}\kappa_y C_{uv}^*(\boldsymbol{\kappa}_j) & -\mathrm{i}\kappa_z C_{uv}^*(\boldsymbol{\kappa}_j) \\ C_{uw}^*(\boldsymbol{\kappa}_j) & -\mathrm{i}\kappa_x C_{uw}^*(\boldsymbol{\kappa}_j) & -\mathrm{i}\kappa_y C_{uw}^*(\boldsymbol{\kappa}_j) & -\mathrm{i}\kappa_z C_{uw}^*(\boldsymbol{\kappa}_j) \end{bmatrix} G(\boldsymbol{\kappa}_j)e^{-\mathrm{i}\boldsymbol{\kappa}_j\cdot\mathbf{x}_0} \\ \vdots \end{bmatrix},$$

leading to

$$\boldsymbol{\Psi}\mathbf{Y}^* = \sum_{\boldsymbol{\kappa}} \begin{bmatrix} C_{uu}(\boldsymbol{\kappa})C_{uu}^*(\boldsymbol{\kappa}) + C_{uv}(\boldsymbol{\kappa})C_{uv}^*(\boldsymbol{\kappa}) + C_{uw}(\boldsymbol{\kappa})C_{uw}^*(\boldsymbol{\kappa}) \\ C_{vu}(\boldsymbol{\kappa})C_{uu}^*(\boldsymbol{\kappa}) + C_{vv}(\boldsymbol{\kappa})C_{uv}^*(\boldsymbol{\kappa}) + C_{vw}(\boldsymbol{\kappa})C_{uw}^*(\boldsymbol{\kappa}) \\ C_{wu}(\boldsymbol{\kappa})C_{uu}^*(\boldsymbol{\kappa}) + C_{wv}(\boldsymbol{\kappa})C_{uv}^*(\boldsymbol{\kappa}) + C_{ww}(\boldsymbol{\kappa})C_{uw}^*(\boldsymbol{\kappa}) \end{bmatrix} \begin{bmatrix} 1, & -\nabla^{\mathsf{T}} \end{bmatrix} G(\boldsymbol{\kappa})e^{\mathrm{i}\boldsymbol{\kappa}\cdot(\mathbf{x}-\mathbf{x}_0)},$$

$$= \sum_{\boldsymbol{\kappa}} \begin{bmatrix} \Phi_{uu}(\boldsymbol{\kappa}) \\ \Phi_{vu}(\boldsymbol{\kappa}) \\ \Phi_{wu}(\boldsymbol{\kappa}) \end{bmatrix} \begin{bmatrix} 1, & -\nabla^{\mathsf{T}} \end{bmatrix} G(\boldsymbol{\kappa})e^{\mathrm{i}\boldsymbol{\kappa}\cdot(\mathbf{x}-\mathbf{x}_0)}\Delta\kappa_x\Delta\kappa_y\Delta\kappa_z. \tag{3.79}$$

As $\Delta\kappa_x\Delta\kappa_y\Delta\kappa_z \to 0$, the sum $\sum_{\boldsymbol{\kappa}}$ can again be replaced by an integral:

$$
\begin{aligned}
\boldsymbol{\Psi}\mathbf{Y}^* &= \left\{ \int_{\boldsymbol{\kappa}} \begin{bmatrix} \Phi_{uu}(\boldsymbol{\kappa}) \\ \Phi_{vu}(\boldsymbol{\kappa}) \\ \Phi_{wu}(\boldsymbol{\kappa}) \end{bmatrix} G(\boldsymbol{\kappa}) e^{i\boldsymbol{\kappa}\cdot(\mathbf{x}-\mathbf{x}_0)}\, d\boldsymbol{\kappa} \right\} \left[1, -\nabla^{\mathsf{T}} \right], \\[2ex]
&= \begin{bmatrix} R_{uu}(\mathbf{x}-\mathbf{x}_0)*g \\ R_{vu}(\mathbf{x}-\mathbf{x}_0)*g \\ R_{wu}(\mathbf{x}-\mathbf{x}_0)*g \end{bmatrix} \left[1, -\nabla^{\mathsf{T}} \right], \\[2ex]
&= \left[\begin{bmatrix} R_{uu}(\mathbf{x}-\mathbf{x}_0)*g \\ R_{vu}(\mathbf{x}-\mathbf{x}_0)*g \\ R_{wu}(\mathbf{x}-\mathbf{x}_0)*g \end{bmatrix}, -\nabla \begin{bmatrix} R_{uu}(\mathbf{x}-\mathbf{x}_0)*g \\ R_{vu}(\mathbf{x}-\mathbf{x}_0)*g \\ R_{wu}(\mathbf{x}-\mathbf{x}_0)*g \end{bmatrix} \right],
\end{aligned}
\tag{3.80}
$$

where $R_{ij}*g$ are the elements of the covariance tensor, given by Equation (3.23), convoluted with the gust volume; i.e.,

$$
R_{ij}(\mathbf{x})*g = \int_{\mathbb{R}^3} R_{ij}(\mathbf{x}+\mathbf{r})g(\mathbf{r})\, d\mathbf{r}.
\tag{3.81}
$$

Substitituting Equations (3.65), (3.78), and (3.80) in Equation (3.69a) gives the expression for the mean gust in wave number space:

$$
\begin{aligned}
\mathrm{E}\left[\hat{\mathbf{u}}'(\mathbf{x})\right] &= \boldsymbol{\Psi}\mathrm{E}\left[\mathbf{n}\,|\,\mathbf{Yn}=\mathbf{b}\right], \\[1ex]
&= \boldsymbol{\Psi}\mathbf{Y}^*\left(\mathbf{Y}\mathbf{Y}^*\right)^{-1}\mathbf{b}, \\[1ex]
&= \frac{A}{\Lambda_0}\int_{\boldsymbol{\kappa}} \begin{bmatrix} \Phi_{uu}(\boldsymbol{\kappa}) \\ \Phi_{vu}(\boldsymbol{\kappa}) \\ \Phi_{wu}(\boldsymbol{\kappa}) \end{bmatrix} G(\boldsymbol{\kappa}) e^{i\boldsymbol{\kappa}\cdot(\mathbf{x}-\mathbf{x}_0)}\, d\boldsymbol{\kappa},
\end{aligned}
\tag{3.82}
$$

and in physical space:

$$
\mathrm{E}\left[\hat{\mathbf{u}}'(\mathbf{x})\right] = \frac{A}{\Lambda_0} \begin{bmatrix} R_{uu}(\mathbf{x}-\mathbf{x}_0)*g \\ R_{vu}(\mathbf{x}-\mathbf{x}_0)*g \\ R_{wu}(\mathbf{x}-\mathbf{x}_0)*g \end{bmatrix}.
\tag{3.83}
$$

Additionally, the variance of the residual process, $\boldsymbol{\Delta}(\mathbf{x})$, is given by

$$\text{var}\left[\mathbf{\Delta}(\mathbf{x})\right] = \mathbf{\Psi}\,\text{var}\left[\mathbf{n}\,|\,\mathbf{Yn} = \mathbf{b}\right]\mathbf{\Psi}^{*},$$

$$= \mathbf{\Psi}\mathbf{\Psi}^{*} - \mathbf{\Psi}\mathbf{Y}^{*}\left(\mathbf{YY}^{*}\right)^{-1}\mathbf{Y}\mathbf{\Psi}^{*},$$

$$= \mathbf{R}(0) - \frac{1}{\Lambda_0}\begin{bmatrix} R_{uu}(\mathbf{x}-\mathbf{x}_0) * g \\ R_{vu}(\mathbf{x}-\mathbf{x}_0) * g \\ R_{wu}(\mathbf{x}-\mathbf{x}_0) * g \end{bmatrix}\begin{bmatrix} R_{uu}(\mathbf{x}-\mathbf{x}_0) * g \\ R_{vu}(\mathbf{x}-\mathbf{x}_0) * g \\ R_{wu}(\mathbf{x}-\mathbf{x}_0) * g \end{bmatrix}^{\mathsf{T}}$$

$$\cdots - \left(\nabla\begin{bmatrix} R_{uu}(\mathbf{x}-\mathbf{x}_0) * g \\ R_{vu}(\mathbf{x}-\mathbf{x}_0) * g \\ R_{wu}(\mathbf{x}-\mathbf{x}_0) * g \end{bmatrix}\right)\mathbf{\Lambda}_2^{-1}\left(\nabla\begin{bmatrix} R_{uu}(\mathbf{x}-\mathbf{x}_0) * g \\ R_{vu}(\mathbf{x}-\mathbf{x}_0) * g \\ R_{wu}(\mathbf{x}-\mathbf{x}_0) * g \end{bmatrix}\right)^{\mathsf{T}}. \tag{3.84}$$

Finally, Equations (3.70) and (3.83) together give the full expression for the velocity field around a wind gust:

$$\hat{\mathbf{u}}'(\mathbf{x}, t_0; V) = \underbrace{\frac{A}{\Lambda_0}\begin{bmatrix} R_{uu}(\mathbf{x}-\mathbf{x}_0; t_0) * g \\ R_{vu}(\mathbf{x}-\mathbf{x}_0; t_0) * g \\ R_{wu}(\mathbf{x}-\mathbf{x}_0; t_0) * g \end{bmatrix}}_{\substack{\text{Deterministic part} \\ \text{(i.e., the ``mean gust'')}}} + \underbrace{\mathbf{\Delta}(\mathbf{x}, t_0)}_{\substack{\text{Stochastic} \\ \text{part}}}. \tag{3.85}$$

This separates the velocity field into a deterministic and a stochastic part (see Figure 3.10). The deterministic part contains all the momentum inside the volume, V, and describes at the same time the most likely, or expected, velocity field around A. Any wave numbers higher than what is cut off by the low-pass filter, $G(\boldsymbol{\kappa})$, do not add any momentum and should therefore have no impact on the overall severity of the gust. If the momentum is
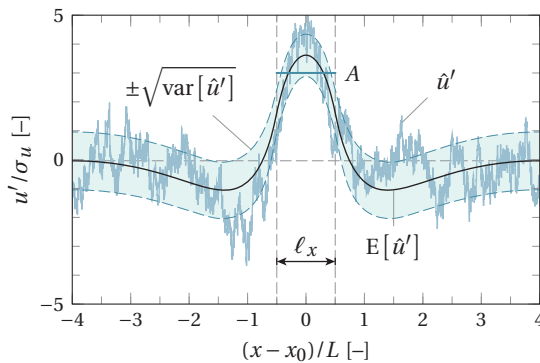

Figure 3.10: The deterministic and stochastic components of a gust, generated from one-dimensional isotropic turbulence with $A = 3\sigma_u$ and where V is a window with a width of $\ell_x = L$. The field $\hat{u}'(x)$ is just one of countless realizations containing the same magnitude event.

spread out over a larger volume, the cut-off wave number decreases and the velocity peak becomes blunter. Another interesting aspect is that the higher the amplitude, the more the deterministic part will start to dominate over the stochastic part. Extreme gusts thus have the tendency to look like the (smoothed) covariance tensor, a result that was also found experimentally in Subsection 2.4.4.

The same holds for three-dimensional domains. For example, consider an ellipsoidal volume given by

$$g(\mathbf{r}) = \begin{cases} \dfrac{6}{\pi \ell_x \ell_y \ell_z}, & \text{for } \dfrac{4x^2}{\ell_x^2} + \dfrac{4y^2}{\ell_y^2} + \dfrac{4z^2}{\ell_z^2} \leq 1; \\[2ex] 0, & \text{for } \dfrac{4x^2}{\ell_x^2} + \dfrac{4y^2}{\ell_y^2} + \dfrac{4z^2}{\ell_z^2} > 1; \end{cases} \tag{3.86}$$

where ℓ_x, ℓ_y, and ℓ_z denote the length, width, and height of the ellipsoid. The corresponding filter is given by its Fourier transformation (e.g., see Koay, Sarlls and Özarslan, 2007):

$$G(\boldsymbol{\kappa}) = \frac{3}{\kappa'^3} \left[\sin(\kappa') - \kappa' \cos(\kappa') \right], \tag{3.87}$$

with

$$\kappa' = \tfrac{1}{2} \sqrt{(\kappa_x \ell_x)^2 + (\kappa_y \ell_y)^2 + (\kappa_z \ell_z)^2}. \tag{3.88}$$

For simplicity, it is assumed that turbulence is homogeneous and isotropic, with the spectral tensor and energy spectrum given by equations (3.31) and (3.32).

Figure 3.11 shows three cases evaluated with Equations (3.83) and (3.85) for spherical volumes ($\ell_x = \ell_y = \ell_z = \ell$). Evidently, the velocity fields are shaped much like circular vortex rings. This is perhaps not surprising, since the flow has to recirculate to preserve continuity within the domain. In fact, it can be shown analytically that the continuity equation is satisfied (i.e., the velocity field is divergence-free) for any shape of V by substituting the isotropic spectral tensor (3.31) in equation (3.82):

$$\nabla \cdot \mathrm{E}\left[\hat{\mathbf{u}}'(\mathbf{x})\right] = \frac{A}{\Lambda_0} \int_{\boldsymbol{\kappa}} \left(\mathrm{i}\kappa_x \Phi_{uu}(\boldsymbol{\kappa}) + \mathrm{i}\kappa_y \Phi_{vu}(\boldsymbol{\kappa}) + \mathrm{i}\kappa_x \Phi_{wu}(\boldsymbol{\kappa}) \right) G(\boldsymbol{\kappa}) \mathrm{e}^{\mathrm{i}\boldsymbol{\kappa}\cdot(\mathbf{x}-\mathbf{x}_0)} \, \mathrm{d}\boldsymbol{\kappa},$$

$$= \frac{A}{\Lambda_0} \int_{\boldsymbol{\kappa}} \frac{E(\kappa)}{4\pi\kappa^4} \left(\mathrm{i}\kappa_x(\kappa_y^2 + \kappa_z^2) - \mathrm{i}\kappa_x\kappa_y^2 - \mathrm{i}\kappa_x\kappa_z^2 \right) G(\boldsymbol{\kappa}) \mathrm{e}^{\mathrm{i}\boldsymbol{\kappa}\cdot(\mathbf{x}-\mathbf{x}_0)} \, \mathrm{d}\boldsymbol{\kappa},$$

$$= 0,$$

where $\kappa = \|\boldsymbol{\kappa}\|$.

Furthermore, as may be expected from Equation (3.83), doubling the amplitude has no effect on the mean streamlines. However, it will cause the deterministic part to start dominating over the stochastic part, which can be seen when comparing Figures 3.11c and d to Figures 3.11a and b. Enlarging the volume, but keeping the amplitude, A, constant, causes the streamlines to spread out. This is due to the low-pass filter that excludes the wave numbers higher than $\kappa = 2\pi/\ell$ from adding to the total momentum content. Instead, the mean shape of the gust is made up from the lower wave numbers, producing a blunter velocity peak.

The size of these gusts is somewhat limited by how much energy is available in the spectrum at the lowest wave numbers, which is prescribed by the turbulent length scale, L.
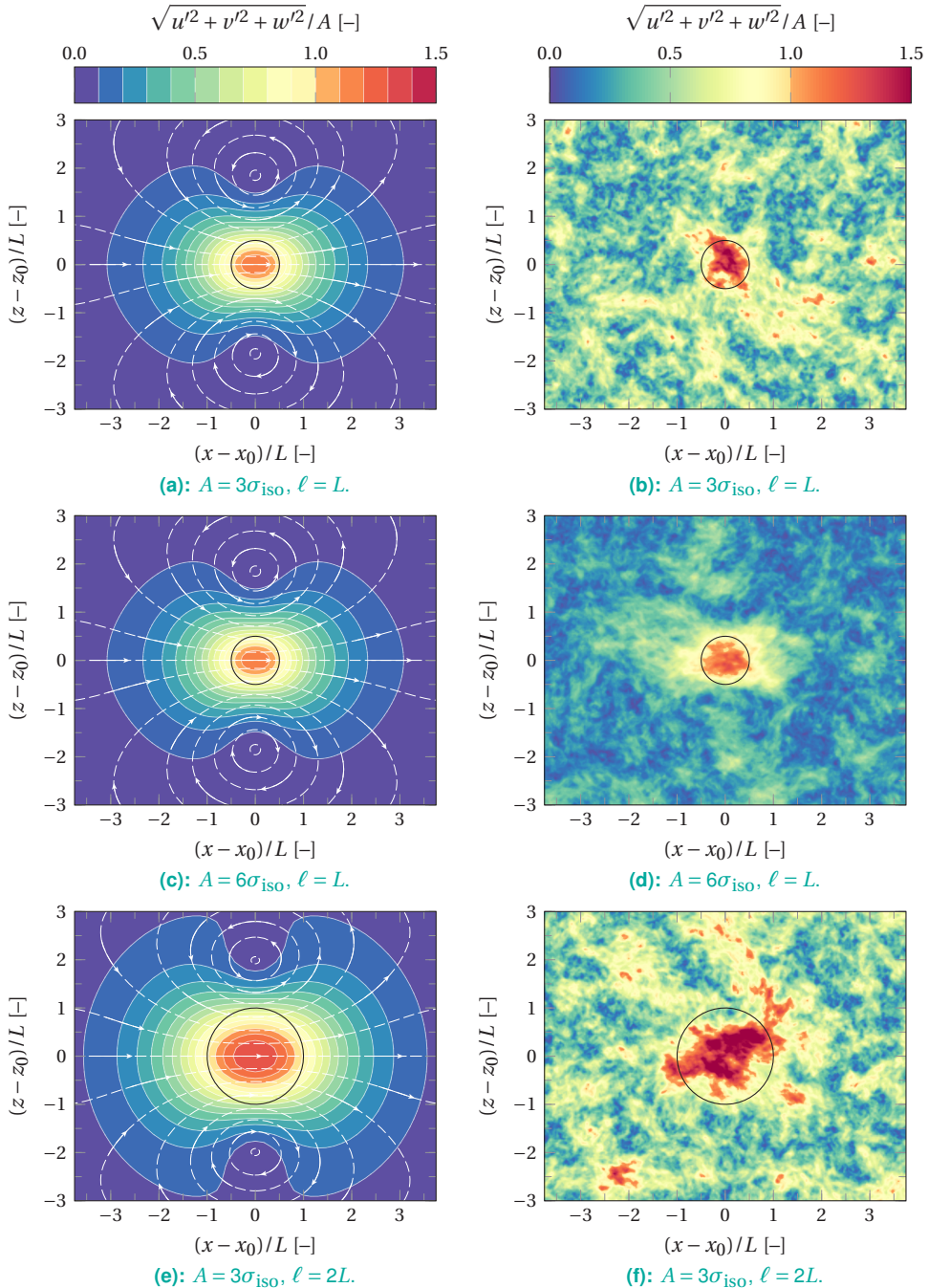
(a): $A = 3\sigma_{\mathrm{iso}}$, $\ell = L$.

(b): $A = 3\sigma_{\mathrm{iso}}$, $\ell = L$.

(c): $A = 6\sigma_{\mathrm{iso}}$, $\ell = L$.

(d): $A = 6\sigma_{\mathrm{iso}}$, $\ell = L$.

(e): $A = 3\sigma_{\mathrm{iso}}$, $\ell = 2L$.

(f): $A = 3\sigma_{\mathrm{iso}}$, $\ell = 2L$.

Figure 3.11: Velocity fields at $y = y_0$ around spherical concentrations of horizontal momentum $(\ell_x = \ell_y = \ell_z = \ell)$ in homogeneous, isotropic turbulence with a domain size of $[0, 8L]^3$. Shown in the left column are the expectations, $\mathrm{E}\left[\hat{\mathbf{u}}'(\mathbf{x})\right]$, with the theoretical streamlines. Shown in the right column are realizations of complete turbulent velocity fields, $\hat{\mathbf{u}}'(\mathbf{x})$.
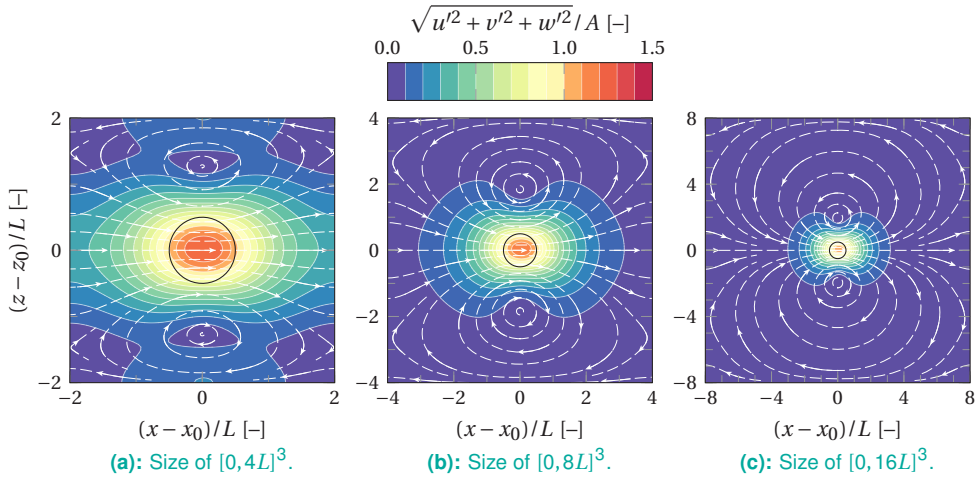
(a): Size of $[0,4L]^3$.   **(b):** Size of $[0,8L]^3$.   **(c):** Size of $[0,16L]^3$.

Figure 3.12: Streamlines around a spherical concentration of horizontal momentum ($\ell = L$) in homogeneous, isotropic turbulence, but generated in different domain sizes.

However, when generating gusts through a Fourier transform, the domain has to be large enough for these wave numbers to exist at all. This is why Mann (1998) recommends a minimum box size of $8L$ in each direction to ensure that the variance under the spectrum is correctly translated to the spatial domain. The effect this has on the gust shape is illustrated in Figure 3.12. Clearly, the gust in this example has trouble fitting in a $[0, 4L]^3$ domain. The variance that should have been provided by wave numbers lower than $2\pi/(4L)$ is now compensated by the higher wave numbers, causing the velocity field to be deformed. On the other hand, a domain that is twice as large in every direction as the $[0, 8L]^3$ minimum still produces roughly the same shape.

In addition, it is interesting to speculate how gusts would look under different atmospheric conditions. The expected velocity fields are obtained from the Mann's spectral tensor (see Section 3.2.4) with the parameter fits from Sathe et al. (2013).[8] The conditions range from stable to unstable at a mean wind speed of 10 m/s and the volume V is taken as a 25-m diameter sphere. The results, shown in Figure 3.13, indicate that gusts become larger and overall more severe as the atmosphere grows unstable. This should come as no surprise, seeing as how the vertical momentum fluxes in unstable conditions promote turbulence and large-scale structures.

Although not visible in Figure 3.13, the shear parameter, Γ, has a pronounced effect on the vertical (w) velocity component as well. This is probably best illustrated in a three-dimensional streamline plot, as shown in Figure 3.14). The dominant features found in the expected velocity field are two counter-rotating vortices that serve to retain the continuity within the domain. These are deformed under shear, which induces an additional downward velocity component in addition to the streamwise amplitude.[9]

---

[8]   Formally, the Mann model only applies to a neutral atmosphere since buoyancy effects are neglected in the rapid distortion equations.

[9]   However, it should be noted that this shape is only valid under very idealized conditions (perfect homogeneity and linear shear), which are unlikely to be found in real life for large turbulent structures.
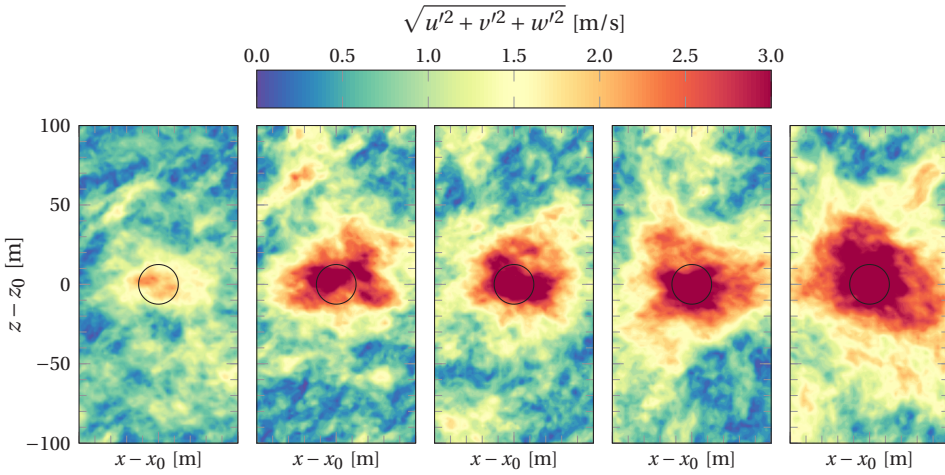
(a) Stable   **(b)** Near-neutral stable   **(c)** Neutral   **(d)** Near-neutral unstable   **(e)** Unstable

Figure 3.13: Velocity fields at $y = y_0$ around spherical concentrations of horizontal momentum ($\ell = 25$ m) in various atmospheric conditions, based on fits of the Mann model by Sathe et al. (2013) at a mean wind speed of 10 m/s. Shown are 50-year extreme gusts through a 100×100 square in a stable ($\alpha\epsilon^{2/3} = 0.041$ m$^{4/3}$/s^2, $L = 16$ m, $\Gamma = 2.7$), near-neutral stable ($\alpha\epsilon^{2/3} = 0.056$ m$^{4/3}$/s^2, $L = 33$ m, $\Gamma = 3.1$), neutral ($\alpha\epsilon^{2/3} = 0.055$ m$^{4/3}$/s^2, $L = 49$ m, $\Gamma = 3.1$), near-neutral unstable ($\alpha\epsilon^{2/3} = 0.043$ m$^{4/3}$/s^2, $L = 89$ m, $\Gamma = 2.8$), and very unstable atmosphere ($\alpha\epsilon^{2/3} = 0.040$ m$^{4/3}$/s^2, $L = 107$ m, $\Gamma = 2.3$). See Table 2.1 for the definition of the stability classes.
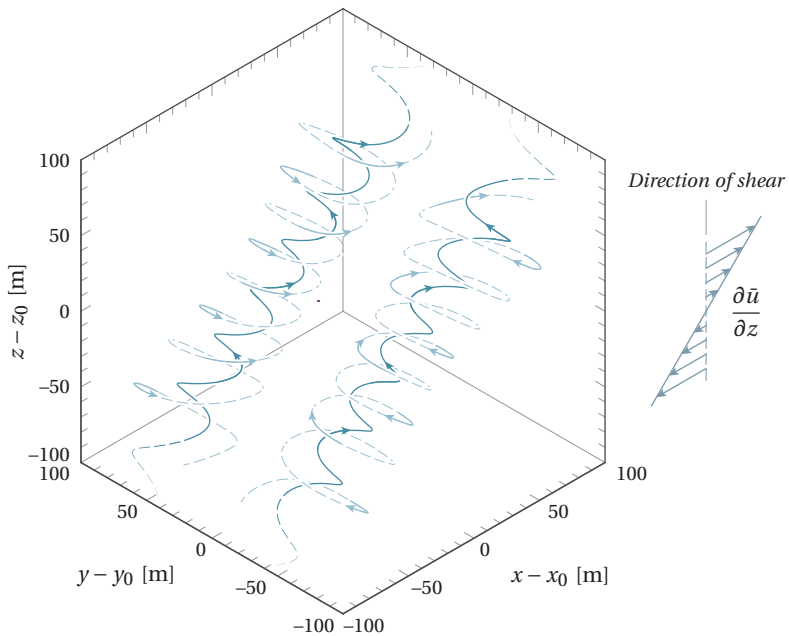

Figure 3.14: Streamlines of the dominant features found in the expected velocity field around a gust ($\ell = 25$ m) in neutral atmospheric conditions ($\alpha\epsilon^{2/3} = 0.055$ m$^{4/3}$/s^2, $L = 49$ m, $\Gamma = 3.1$).

3.4 **The probability of gusts in a 3D domain**

In order to have any idea about the rarity of a gust, its amplitude needs to be coupled to a probability of occurrence. However, this is not so straightforward as turbulence is strongly self-similar at high wave numbers.

3.4.1 **The fractal nature of turbulence**

This self-similarity, expressed by $E(\kappa) \propto \kappa^{-5/3}$, is found across the inertial range and is often assumed to extend up to $\kappa = \infty$ (see Subsection 3.2.1). It brings up the same issue raised by Richardson already in 1926. In the inertial range, the variance of the fluctuations (e.g., $u'(x)$), given by the zeroth-order spectral moment, is finite:[10]

$$\overline{u'u'} = \int E(\kappa)\,\mathrm{d}\kappa,$$
$$\propto \int \kappa^{-5/3}\,\mathrm{d}\kappa < \infty. \tag{3.89}$$

However, the variance of the first derivatives, given by the second-order spectral moment, is infinite:

$$\overline{\frac{\mathrm{d}u'}{\mathrm{d}x}\frac{\mathrm{d}u'}{\mathrm{d}x}} = \int \kappa^2 E(\kappa)\,\mathrm{d}\kappa,$$
$$\propto \int \kappa^{1/3}\,\mathrm{d}\kappa = \infty. \tag{3.90}$$

The diverging integral means that velocity fluctuations become more abundant when moving to smaller scales. Consequently, towards infinitely small scales, a velocity field would also contain an infinite number of gusts.

A nice way of visualizing this is through a *wavelet transform*, which results from a convolution of a signal, $u(t)$, with a certain wavelet function, $\psi(t)$:

$$\mathcal{W}[u(t)] = \frac{1}{\sqrt{|s|}} \int_{-\infty}^{\infty} u(t')\psi^*\left(\frac{t-t'}{s}\right)\mathrm{d}t', \tag{3.91}$$
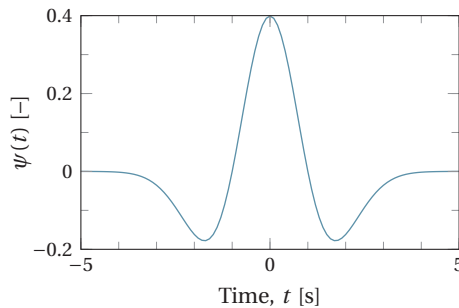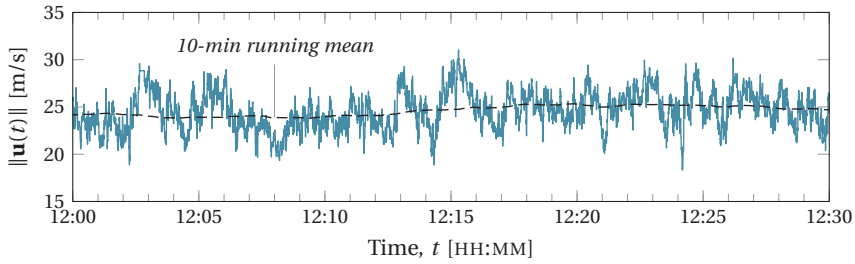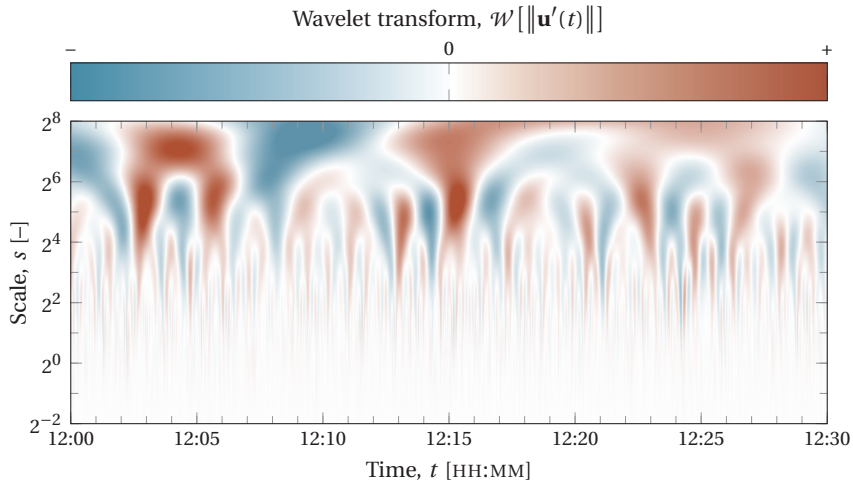

Figure 3.15: The Mexican hat wavelet.

---

[10] In his example, Richardson describes the motion of an air particle with the Weierstrass function, but the same reasoning works with Kolmogorov's 1941 theory too.

(a): Wind speed measured at 116-m height during the passing of a storm over the offshore wind farm Egmond aan Zee in the Dutch North Sea on 12 March 2008.

(b): Wavelet scalogram of the unsteady wind speed, $\|\mathbf{u}'(t)\|$, using the Mexican hat wavelet.
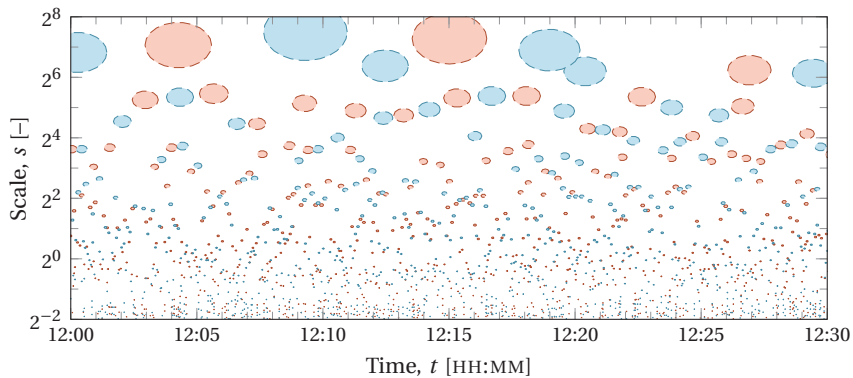
(c): The local minima and maxima in the scalogram show the approximate locations and scales of passing eddies.

Figure 3.16: A wavelet transform can be a nice way to visualize the fractal nature of turbulence.

with $\square^*$ denoting a complex conjugate. The wavelet transform is done for various scales by expanding or contracting the wavelet by a scale factor, s. This results in a *scalogram*, which indicates at which time and scale the signal correlates best with the function $\psi(t)$. In this context, it makes sense to choose a wavelet that resembles a simple gust, for instance a *Mexican hat* (or Ricker wavelet):

$$\psi(t) = \frac{1}{\sqrt{2\pi}} e^{-t^2/2} \left(1 - t^2\right), \tag{3.92}$$

plotted in Figure 3.15. Figure 3.16b then shows the scalogram resulting from a wavelet transform of the time series in Figure 3.16a. If each eddy emits a velocity signature $\psi(t/s)$, the local minima and maxima in the scalogram can be used to decompose the time series into eddies of different scales (see Figure 3.16c). This again shows that, when moving to the smallest scales, gusts are numerous.

An interesting analogy exists between wind gusts and a later research by Richardson (1961), where he studied the length of coastlines. Coastlines, also being fractal in nature, have no well-defined length. In theory, one could wrap a measurement tape around all the infinitesimally small features, leading to an infinite length. However, in practice, one would rather use a ruler or walk a pair of divider calipers. This *coastline paradox* was later picked up by Mandelbrot (1967), who expanded on the idea that the length of a coastline depends on the length of the ruler used to measure it. The practical solution is therefore to settle for a minimum feature size to define what scales are relevant.

The same idea can also be applied to wind gusts, considering that, in Section 3.3, Mandelbrot's ruler has already appeared in the form of a low-pass filter, $G(\mathbf{\kappa})$. Therefore, scales smaller than a cut-off wave number are automatically neglected. This also imposes an upper limit on the integral in Equation (3.90), leading to finite second-order spectral moments. In meteorology, for example, it is common to use a three-second averaging period when dealing with wind gusts in time series. This corresponds to a *wind run*—the gust duration multiplied with the average velocity—in the order of 100 m (Beljaars, 1987b).

### 3.4.2 The Euler characteristic as the number of gusts

The statistics of gusts are complicated because they are spawned from a continuous velocity field instead of being truly discrete events. However, for high enough amplitudes, the events inside a domain, B, that match the requirements (3.60a), (3.60b), and (3.60c) closely match the members of the *excursion set*, Z_A:

$$Z_A = \left\{\mathbf{x} \in B : p'(\mathbf{x}, t_0; V) \geq \rho \, \mathrm{vol}(V) A\right\}. \tag{3.93}$$

The excursion set is the collection of regions that remains in the field p' after subtracting a threshold $\rho \, \mathrm{vol}(V) A$. The number of gusts with a streamwise momentum of at least $\rho \, \mathrm{vol}(V) A$ is then equal to the cardinality of the excursion set, denoted as $\#Z_A$.

Visualizing a level excursion is quite straightforward as long as the domain is one- or two-dimensional. Everything that remains above a certain level is a discrete number of isolated regions that is easily counted, similar to how islands appear in a landscape when the sea level is raised (see Figure 3.17).
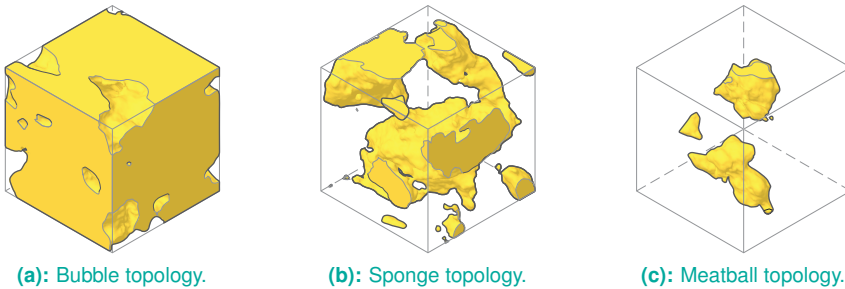
However, when the domain is three-dimensional, these regions are much harder to define. For negative threshold values, first the negative gusts would disappear from
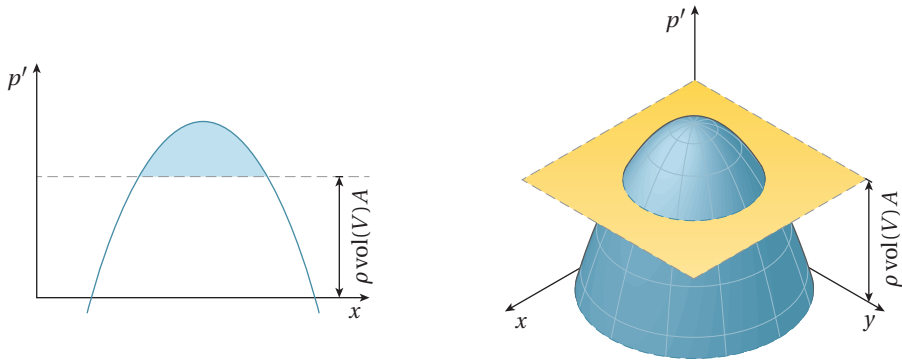
(a): A level excursion in 1D.

(b): A level excursion in 2D.

Figure 3.17: Level excursions are still easy to define and visualize when dealing with just one or two dimensions.

(a): Bubble topology.   **(b):** Sponge topology.   **(c):** Meatball topology.

Figure 3.18: In a three-dimensional domain, the boundaries of the level excursions can look very complicated, making it hard to distinguish between individual structures. Depending on the threshold level, the excursion set will tend to a bubble, sponge, or meatball topology.

the excursion set. This leaves a volume with a lot of holes, called a *bubble* topology (see Figure 3.18a), which looks similar to a Swiss cheese.[11] For threshold levels around zero, individual gusts are still not clearly distuingishable, since high amplitude regions are connected by a network of bridges or *handles*. This is often called a *sponge* topology (see Figure 3.18b). Finally, if the threshold level is high enough, what is left are mainly disconnected regions with a small number of holes, called a *meatball* topology (see Figure 3.18c).

Although there are no analyical expressions to derive the number of isolated high-amplitude regions directly, the *Euler characteristic* of the excursion set is a good approximation (Adler, 1976). The Euler characteristic is a number that describes a topological space and is loosely defined as the number of connected components in Z_A, minus the number of handles, plus the number of holes. As an example, Figure 3.19 shows three topologically distinct objects. First, the ball (a) is a solid object and therefore has an Euler characteristic of $\chi = 1$. A torus (b) is a single connected component minus a handle: $\chi = 0$. Finally, a hollow sphere (c) has a shell plus a cavity: $\chi = 2$.

---

[11] Yes, the color scheme in Figure 3.18 was on purpose.

For high enough threshold levels, the holes and handles disappear from the excursion set, Z_A, leaving only the connected components (i.e., the gusts). This is the basis for the *Euler characteristic heuristic*, which states that

$$\mathrm{E}\,[\#Z_A] \approx \mathrm{E}\left[\chi(Z_A)\right], \tag{3.94}$$

of which an example is shown in Figure 3.20. A generalized expression for $\mathrm{E}\left[\chi(Z_A)\right]$ that applies to N-dimensional domains has been derived by Adler and Taylor (2007):

$$\mathrm{E}\left[\chi(Z_A)\right] = \mathrm{e}^{-\frac{A^2}{2\Lambda_0}} \sum_{k=0}^{N} \sum_{J \in O_k} \frac{\mathrm{vol}(J)\sqrt{|\Lambda_2(J)|}}{(2\pi)^{(k+1)/2}\Lambda_0^{k/2}} H_{k-1}\left(\frac{A}{\sqrt{\Lambda_0}}\right), \tag{3.95}$$

where

$$H_n(x) = \begin{cases} n!\sum_{j=0}^{\lfloor n/2 \rfloor} \dfrac{(-1)^j x^{n-2j}}{j!(n-2j)!2^j}, & n \geq 0, \\[2ex] \sqrt{2\pi}\Psi(x)\mathrm{e}^{x^2/2}, & n = -1, \end{cases} \tag{3.96}$$

(a): A ball ($\chi = 1$).   **(b):** A solid torus ($\chi = 0$).   **(c):** A hollow sphere ($\chi = 2$).
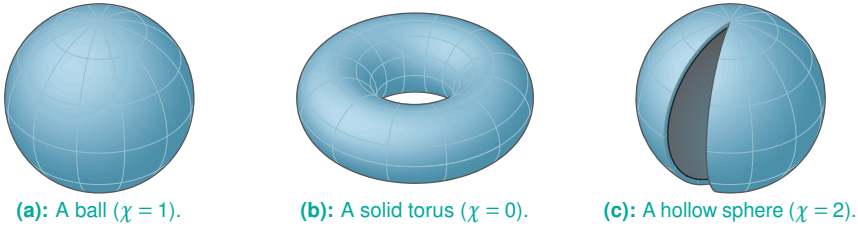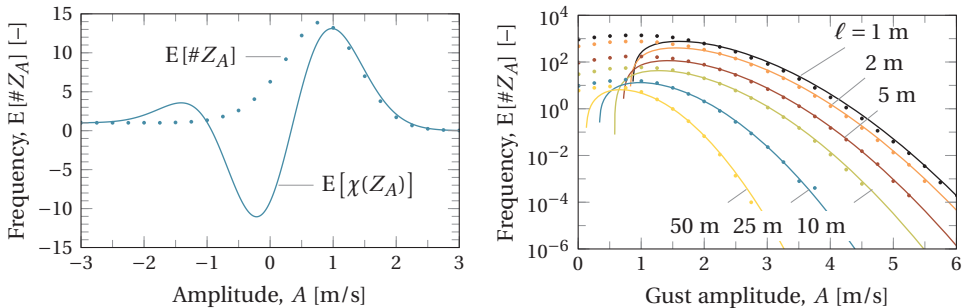
Figure 3.19: Euler characteristics of various objects.

(a): For $\ell = 25$ m ($\sqrt{\Lambda_0} = 0.62$ m/s).   **(b):** For several diameters.

Figure 3.20: Level excursions (dots) averaged over 10,000 velocity fields with homogeneous, isotropic turbulence ($\sigma_{\mathrm{iso}} = 1$ m/s, $L = 25$ m), generated in a cubic domain of $100 \times 100 \times 100$ m (unpadded: $L_x = L_y = L_z = 200$ m, $N_x = N_y = N_z = 2^8$), compared to the Euler characteristic (lines). The velocity field was filtered using a spherical kernel with a diameter, ℓ.
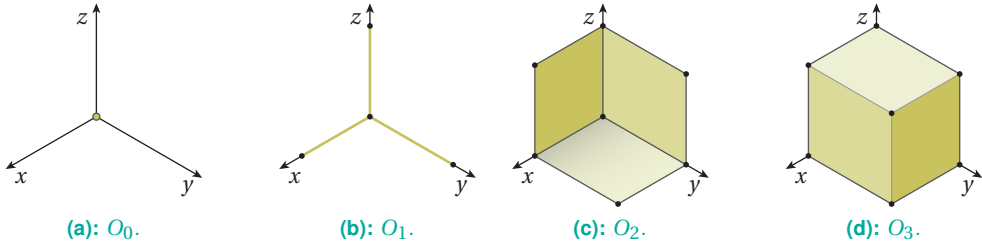
(a): O_0.   **(b):** O_1.   **(c):** O_2.   **(d):** O_3.

Figure 3.21: The sets O_k consist of the k-dimensional faces of the domain B that contain the origin.

is the nth Hermite polynomial and $\Psi(x)$ represents the tail of the Gaussian distribution:[12]

$$\Psi(x) = 1 - \frac{1}{\sqrt{2\pi}} \int_{-\infty}^{x} e^{-v^2/2}\, dv. \tag{3.97}$$

The variance, or zeroth-order spectral moment, of the filtered velocity field is obtained from Equation (3.76). Moreover, $\sum_{J \in O_k}$ denotes summing over the $\binom{N}{k}$ k-dimensional faces of B that contain the origin; $\mathrm{vol}(J)$ is the N-dimensional volume (or Lebesgue measure) of J; and $|\Lambda_2(J)|$ is the determinant of the matrix of second-order spectral moments belonging to J.

When the domain, B, is a three-dimensional rectangular box with sides $L_x \times L_y \times L_z$, O_0 contains the single vertex at the origin; O_1 the three ribs along the x-, y-, and z-axes; O_2 the xyO-, Oyz-, and xOz-planes; and O_3 the volume of the box B (see Figure 3.21). Then, Equation (3.95) can be written as

$$\mathrm{E}\left[\chi(Z_A)\right] = \Psi\left(\frac{A}{\sqrt{\Lambda_0}}\right) + e^{-\frac{A^2}{2\Lambda_0}}\left[c_1 + c_2 \frac{A}{\sqrt{\Lambda_0}} + c_3\left(\frac{A^2}{\Lambda_0} - 1\right)\right], \tag{3.98}$$

with the coefficients

$$c_1 = \frac{1}{2\pi\sqrt{\Lambda_0}}\left(L_x\sqrt{\Lambda_{2,xx}} + L_y\sqrt{\Lambda_{2,yy}} + L_z\sqrt{\Lambda_{2,zz}}\right), \tag{3.99a}$$

$$c_2 = \frac{1}{(2\pi)^{3/2}\Lambda_0}\left(L_xL_y\sqrt{\left|\begin{matrix}\Lambda_{2,xx} & \Lambda_{2,xy} \\ \Lambda_{2,yx} & \Lambda_{2,yy}\end{matrix}\right|} + L_xL_z\sqrt{\left|\begin{matrix}\Lambda_{2,xx} & \Lambda_{2,xz} \\ \Lambda_{2,zx} & \Lambda_{2,zz}\end{matrix}\right|}\right.$$
$$\left.\cdots + L_yL_z\sqrt{\left|\begin{matrix}\Lambda_{2,yy} & \Lambda_{2,yz} \\ \Lambda_{2,zy} & \Lambda_{2,zz}\end{matrix}\right|}\right), \tag{3.99b}$$

$$c_3 = \frac{L_xL_yL_z}{(2\pi)^2\Lambda_0^{3/2}}\sqrt{\left|\begin{matrix}\Lambda_{2,xx} & \Lambda_{2,xy} & \Lambda_{2,xz} \\ \Lambda_{2,yx} & \Lambda_{2,yy} & \Lambda_{2,yz} \\ \Lambda_{2,zx} & \Lambda_{2,zy} & \Lambda_{2,zz}\end{matrix}\right|}, \tag{3.99c}$$

---

[12] The role of $\Psi(A/\sqrt{\Lambda_0})$ is clear in the limit $A \to -\infty$; the point where the entire field is connected and forms a single maximum.

where $\Lambda_{2,ij}$ are the components of the matrix of second-order spectral moments (obtained from Equation (3.77)). In the limit case where $L_y, L_z \to 0$ (i.e., B becomes one-dimensional), the above naturally returns to Rice's formula (Rice, 1944)—which has been treated in Subsection 2.2.1—and the expected Euler characteristic is exactly the number of level crossings:

$$E\left[\chi(Z_A)\right] = \frac{L_x}{2\pi}\sqrt{\frac{\Lambda_{2,xx}}{\Lambda_0}}\, e^{-\frac{A^2}{2\Lambda_0}}. \tag{3.100}$$

3.4.3 The probability of extreme wind gusts

With the result of the previous subsection, it is now possible to express a probability of a gust event happening in a certain domain. By using the Euler characteristic as a measure for the number of local maxima, the occurrence probability of extreme gusts can be derived through the *Poisson limit*. For high amplitudes, a binomial distribution with N successes can be approximated by

$$P(\#Z_A = N) = \frac{(E\left[\#Z_A\right])^N}{N!} e^{-E[\#Z_A]}, \tag{3.101}$$

which gives the probability that there are N independent gusts in a domain B—or equivalently, there are N elements in the excursion set Z_A—where $p'(\mathbf{x}, t_0; V) \geq \rho\,\mathrm{vol}(V)\,A$. The expected number of events in the domain, $E\left[\#Z_A\right]$, functions as the *Poisson parameter* that defines the shape of the distribution.

More appropriate, perhaps, is to represent the problem as a *Poisson point process* where gusts are treated as independent points that originate from the stochastic turbulence process. The Poisson parameter, λ_A, then denotes the average number of gusts per unit volume:

$$\lambda_A = \frac{E\left[\#Z_A\right]}{\mathrm{vol}(B)}. \tag{3.102}$$

The domain B would span at least several minutes and it often holds that $L_x \gg L_y, L_z$. For large enough amplitudes, this allows Equation (3.98) to be simplified to

$$E\left[\chi(Z_A)\right] \approx L_x L_y L_z \frac{\sqrt{|\mathbf{\Lambda_2}|}}{4\pi^2 \Lambda_0^{3/2}} e^{-\frac{A^2}{2\Lambda_0}}\left(\frac{A^2}{\Lambda_0} - 1\right). \tag{3.103}$$

resulting in an earlier expression given by Adler (1976). In essence, this neglects the edges of the domain, which perhaps agrees more with intuition; a domain that is twice as large contains twice as many gusts. Based on the Euler characteristic heuristic, the Poisson parameter is then given by

$$\lambda_A \approx \frac{\sqrt{|\mathbf{\Lambda_2}|}}{4\pi^2 \Lambda_0^{3/2}} e^{-\frac{A^2}{2\Lambda_0}}\left(\frac{A^2}{\Lambda_0} - 1\right), \tag{3.104}$$

and the Poisson distribution becomes

$$P(\#Z_A = N) = \frac{(\lambda_A \mathrm{vol}(B))^N}{N!} e^{-\lambda_A \mathrm{vol}(B)}. \tag{3.105}$$
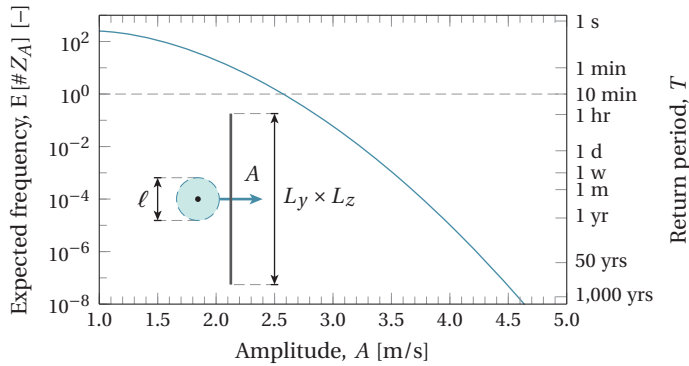
Figure 3.22: Expected number of gusts in a ten-minute period, defined as spherical momentum concentrations ($\ell = L$) in homogeneous, isotropic turbulence ($\sigma_{\text{iso}} = 1$ m/s, $L = 25$ m), advecting though a 100×100 m plane with a constant mean wind speed of $\bar{u} = 10$ m/s.

Concerning extreme gusts, the question is often what kind of amplitude matches a certain *return period* (i.e., the average time period for an event to repeat itself). The return period entails that the probability of encountering an event with a return period, T, is $1/T$ and the expected number of these events over a time period T is, of course, exactly 1. The definition of this T-*gust* requires a reference surface perpendicular to the flow, S, to provide finite values for L_y and L_z. Under Taylor's hypothesis, the domain length and time period are then connected through

$$L_x \approx \bar{u}T, \tag{3.106}$$

where $\bar{u}$ is the advection velocity, often taken as equal to the mean wind speed. The T-gust can be found in several ways. First, the rarest or most extreme deviation relative to the local conditions is found by finding the amplitude, A, for which the "local" Poisson parameter, λ_A, matches a $1/T$ probability (e.g., see Figure 3.22). If the conditions depend on a number of variables, $\boldsymbol{\theta} = [\bar{u}, L, \dots]^{\mathsf{T}}$, the return period simply follows from

$$T = \frac{1}{L_y L_z \bar{u} \lambda_A(\boldsymbol{\theta})}, \tag{3.107}$$

where $L_y L_z \bar{u} \lambda_A(\boldsymbol{\theta})$ can be identified as a *mean gust rate* through a rectangular surface with sides $L_y \times L_z$. Though, this does not lead to a single well-defined event, but instead implies that the T-gust can manifest itself in numerous ways—at different mean wind speeds and from various turbulence spectra, if applicable.

A second way is by finding the amplitude that, considering the entire range of conditions, matches the required return period. The number of gusts that have traveled through S during a time period, T, is then found by a weighted average:

$$\mathrm{E}\,[\#Z_A] = L_y L_z T \int \bar{u} \lambda_A(\boldsymbol{\theta}) f(\boldsymbol{\theta}) \, \mathrm{d}\boldsymbol{\theta}, \tag{3.108}$$

where $f(\boldsymbol{\theta})$ is the probability density function of $\boldsymbol{\theta}$. One way of visualizing this is by dividing the time period, T, into N domains, as sketched in Figure 3.23. Each of these
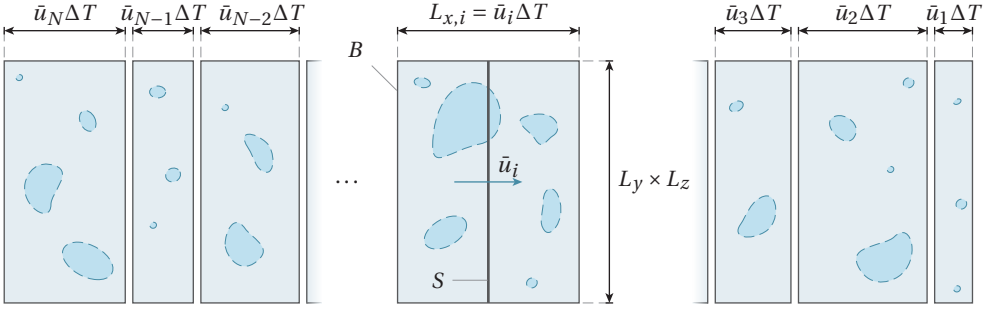
Figure 3.23: A series of domains with an equal time period, ΔT, advecting through a square surface, S, with a mean wind speed $\bar{u}$. Sketched inside the domains are the members of the excursion set $Z_A = \left\{ \mathbf{x} \in B : p'(\mathbf{x}, t_0; V) \geq \rho \operatorname{vol}(V) A \right\}$.

domains spans a fixed time length, ΔT, and has local conditions governed by $f(\boldsymbol{\theta})$. Then, marking every region above a certain threshold level gives the total number of gust events:

$$\sum_{i=1}^{N} \# Z_{A,i} = \sum_{i=1}^{N} L_y L_z \bar{u}_i \Delta T \, \lambda_A(\boldsymbol{\theta}_i), \tag{3.109}$$

The mean number of gusts found in a time period, T, is thus given by

$$\frac{1}{N} \sum_{i=1}^{N} \# Z_{A,i} = \frac{L_y L_z T}{N} \sum_{i=1}^{N} \bar{u}_i \lambda_A(\boldsymbol{\theta}_i), \tag{3.110}$$

which is the same as saying that

$$\mathrm{E}\,[\# Z_A] = L_y L_z T \, \mathrm{E}\,[\bar{u}\lambda_A]. \tag{3.111}$$

In that case, the return period is the reciprocal of the mean gust rate:

$$T = \frac{1}{L_y L_z \mathrm{E}\,[\bar{u}\lambda_A]}. \tag{3.112}$$

However, this yields a rather inconvenient result when the amplitude is added to the mean wind speed: the T-gust may be a ridiculously severe event at low $\bar{u}$ and a negligible one at high $\bar{u}$.

Therefore, a third way is by considering the total amplitude; i.e., the turbulent velocity deviation added to the mean wind speed. The number of gusts then has to be found by modifying Equation (3.104) for the excursion set

$$Z_{A^* = \bar{u}+A} = \left\{ \mathbf{x} \in B : p(\mathbf{x}, t_0; V) \geq \rho \operatorname{vol}(V)(\bar{u} + A) \right\}, \tag{3.113}$$

where $\bar{u}$ is a stochastic mean wind speed with a probability density function, $f(\bar{u})$. After making the substitution $A^* = \bar{u} + A$, it follows that

$$\mathrm{E}\,[\bar{u}\lambda_{A^*}] \approx \int \bar{u} \, \frac{\sqrt{|\boldsymbol{\Lambda}_2|}}{4\pi^2 \Lambda_0^{3/2}} \mathrm{e}^{-\frac{(A^* - \bar{u})^2}{2\Lambda_0}} \left(\frac{(A^* - \bar{u})^2}{\Lambda_0} - 1 \right) f(\bar{u}) \, \mathrm{d}\bar{u}, \tag{3.114}$$

and the return period follows as before from Equation (3.112). The result is a single event that is undeniably the T-gust.[13] Nevertheless, when dealing with practical problems, keeping the event relative to local conditions might be much wiser. The reason is that the response to such events can be very dependent on the surrounding conditions. This is especially the case for wind turbines, which operate under different control regimes for different mean wind speeds.

3.5 Time evolution of wind gusts

The gusts derived in Section 3.3 are spawned from free-stream turbulence, far upstream of any disturbance. However, the spatial structure changes in time due to dissipation, turbulent advection, and external forces acting on the flow. This is an important issue for lidar-assisted control systems used in wind turbines—a subject that will be revisited in Section 4.4—which can measure a gust up to several hundred meters upwind. Such applications require a quick model that can provide a good estimate of how the wind evolves over a period in the order of ten seconds.

3.5.1 Fourier-transformed Navier-Stokes equations

The Navier-Stokes equations, discussed in Subsection 3.1.1, can also be solved in wave number space, where the focus is on the evolution of the Fourier modes. When writing a
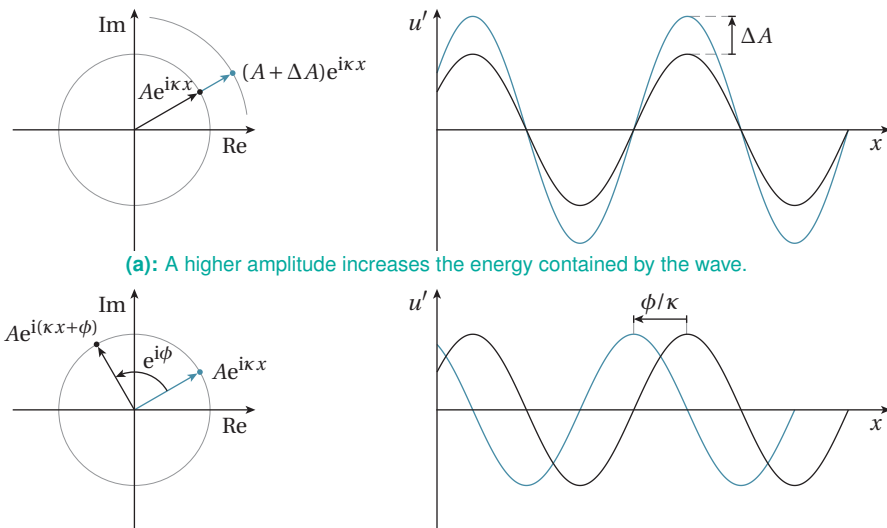
(a): A higher amplitude increases the energy contained by the wave.

(b): A positive (counterclockwise) phase shift will displace the wave in the negative direction without affecting the variance.
Figure 3.24: Each Fourier mode has two degrees of freedom: amplitude and phase, here sketched for a single dimension.

---

[13] However, even more complicated expressions will have to be used when the mean wind speed is not uniform, but varies with height.

scalar process, dZ, in polar form,

$$dZ(\kappa) = A(\kappa)e^{i\phi(\kappa)}, \tag{3.115}$$

each mode has two degrees of freedom: the amplitude, A, and the phase, ϕ (see Figures 3.24a and b). The energy is completely determined by the amplitude:

$$\overline{dZ\,dZ^*} = \overline{\left(Ae^{i\phi}\right)\left(Ae^{-i\phi}\right)} = A^2.$$

The phases, on the other hand, more or less determine the shape of the velocity field in the spatial domain. This is clearly demonstrated by the simple advection equation:

$$\frac{\partial\,dZ}{\partial t} = -i\kappa_x \bar{u}\,dZ, \tag{3.116}$$

with the solution

$$dZ(\kappa, t) = dZ(\kappa, t_0)e^{-i\kappa_x \bar{u}(t-t_0)}. \tag{3.117}$$

Unsurprisingly, it implies that the wave front is being displaced in the streamwise direction by a distance $\bar{u}$ every second (the same result found in Subsection 3.1.3).

For the remainder of this section, a gust is assumed to behave as a locally homogeneous group of waves, centered around $\mathbf{x}_0$ and traveling with the mean wind speed:

$$\dot{\mathbf{x}}_0 = \bar{\mathbf{u}}(\mathbf{x}_0). \tag{3.118}$$

On a time scale in the order of ten seconds, the evolution is governed by Equation (3.11), which was obtained after eliminating the irrelevant terms from the Navier-Stokes equations. The evolution of the process $d\mathbf{Z}$ is then described by a Fourier transform:[14]

$$\frac{\partial\,d\mathbf{Z}}{\partial t} = -\underbrace{(\nabla\bar{\mathbf{u}})\,d\mathbf{Z}}_{\text{Shear distortion}} - \underbrace{i\sum_{\boldsymbol{\kappa}_1+\boldsymbol{\kappa}_2=\boldsymbol{\kappa}}[d\mathbf{Z}(\boldsymbol{\kappa}_1)\cdot\boldsymbol{\kappa}_2]\,d\mathbf{Z}(\boldsymbol{\kappa}_2)}^{\text{Turbulent transport}} - \underbrace{\frac{1}{\rho}i\boldsymbol{\kappa}\,dW}_{\text{Pressure fluctuations}} \tag{3.119}$$

where

$$\mathbf{u}'(\mathbf{x}, t) = \int_{\boldsymbol{\kappa}} e^{i\boldsymbol{\kappa}\cdot(\mathbf{x}_0(t)+\mathbf{r})}\,d\mathbf{Z}(\boldsymbol{\kappa}, t), \tag{3.120a}$$

$$P'(\mathbf{x}, t) = \int_{\boldsymbol{\kappa}} e^{i\boldsymbol{\kappa}\cdot(\mathbf{x}_0(t)+\mathbf{r})}\,dW(\boldsymbol{\kappa}, t), \tag{3.120b}$$

are the Fourier-Stieltjes representations of the unsteady velocity and pressure, respectively. Additionally, the distortion of the wave numbers is described by

$$\frac{\partial\boldsymbol{\kappa}}{\partial t} = -\boldsymbol{\kappa}\cdot\nabla\bar{\mathbf{u}}, \tag{3.121}$$

---

[14] At this point, it is convenient to switch to a Lagrangian perspective where the observer moves with the advection speed. This means the term $\bar{\mathbf{u}}\cdot\nabla\mathbf{u}'$ also drops out of Equation (3.11).

with the solution

$$\boldsymbol{\kappa}(t) = e^{-(t-t_0)\nabla\bar{\mathbf{u}}}\boldsymbol{\kappa}(t_0), \tag{3.122}$$

where

$$e^{-(t-t_0)\nabla\bar{\mathbf{u}}} = \sum_{n=0}^{\infty}[-(t-t_0)\nabla\bar{\mathbf{u}}]^n \tag{3.123}$$

is the matrix exponential. In wave number space, the pressure fluctuations can be written as a function of the unsteady velocity through the Poisson equation and the principle of continuity:

$$\frac{1}{\rho}\|\boldsymbol{\kappa}\|^2\,dW = 2i\boldsymbol{\kappa}\cdot(\nabla\bar{\mathbf{u}})\,d\mathbf{Z} - \boldsymbol{\kappa}\cdot\sum_{\boldsymbol{\kappa}_1+\boldsymbol{\kappa}_2=\boldsymbol{\kappa}}[d\mathbf{Z}(\boldsymbol{\kappa}_1)\cdot\boldsymbol{\kappa}_2]\,d\mathbf{Z}(\boldsymbol{\kappa}_2). \tag{3.124}$$

After substituting this back into Equation (3.119), it can be grouped with the turbulent transport term, yielding

$$\frac{\partial\,d\mathbf{Z}}{\partial t} = -\left(\mathbf{I} - 2\frac{\boldsymbol{\kappa}\boldsymbol{\kappa}^\mathsf{T}}{\|\boldsymbol{\kappa}\|^2}\right)(\nabla\bar{\mathbf{u}})\,d\mathbf{Z} - i\left(\mathbf{I} - \frac{\boldsymbol{\kappa}\boldsymbol{\kappa}^\mathsf{T}}{\|\boldsymbol{\kappa}\|^2}\right)\sum_{\boldsymbol{\kappa}_1+\boldsymbol{\kappa}_2=\boldsymbol{\kappa}}[d\mathbf{Z}(\boldsymbol{\kappa}_1)\cdot\boldsymbol{\kappa}_2]\,d\mathbf{Z}(\boldsymbol{\kappa}_2). \tag{3.125}$$

3.5.2 Dealing with the nonlinear term

Equation (3.125) contains a nonlinear term that describes how kinetic energy is passed on from the wave number pair $\boldsymbol{\kappa}_1$ and $\boldsymbol{\kappa}_2$ to a higher wave number $\boldsymbol{\kappa} = \boldsymbol{\kappa}_1 + \boldsymbol{\kappa}_2$ in a triad interaction (e.g., see Figure 3.25). This process does not affect the total energy contained by a group of waves, but rather redistributes it internally. However, modeling these wave number interactions is unfeasible in practice. That is why most analyical approaches to the Navier-Stokes equations start with either modifying or neglecting the nonlinear term completely.

One such approach is *rapid distortion theory* (Batchelor and Proudman, 1954), which is based on the assumption that the velocity field is distorted so quickly that the slower inertial terms have no effect. Dropping the nonlinear terms from Equation (3.125) then
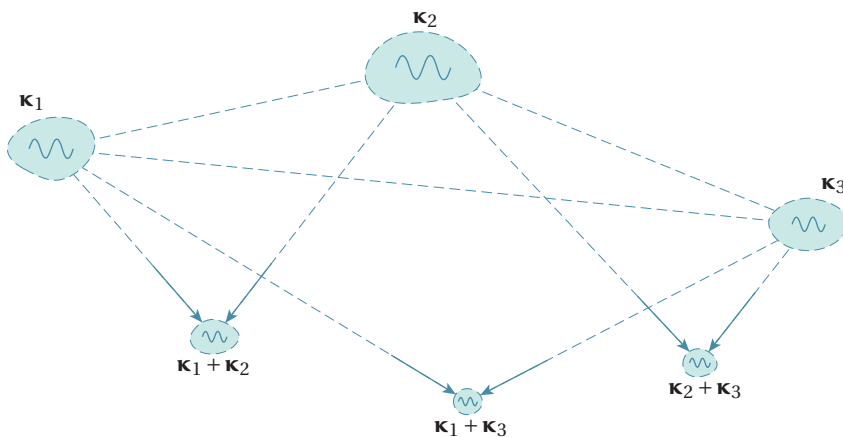

Figure 3.25: In wave number space, kinetic energy is passed on to smaller scales through triad interactions.
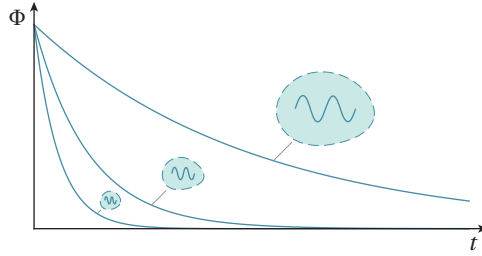
Figure 3.26: Due to viscosity, the variance contained by a wave number is expected to dissipate exponentially, where high wave numbers decay faster than low wave numbers.

leads to

$$\frac{\partial\, d\mathbf{Z}}{\partial t} = -\left(\mathbf{I} - 2\frac{\boldsymbol{\kappa}\boldsymbol{\kappa}^{\mathsf{T}}}{\|\boldsymbol{\kappa}\|^2}\right)(\nabla\bar{\mathbf{u}})\, d\mathbf{Z}, \tag{3.126}$$

which, together with Equation (3.121), are the *rapid distortion equations.* Since all the remaining terms are linear, the solution takes the shape of a linear transformation:

$$d\mathbf{Z}(\boldsymbol{\kappa}, t) = \mathbf{T}(\boldsymbol{\kappa})\, d\mathbf{Z}(\boldsymbol{\kappa}_0, t_0), \tag{3.127}$$

where $\mathbf{T}$ is a transformation matrix and $\boldsymbol{\kappa}_0 = \boldsymbol{\kappa}(t_0)$ is the initial, undisturbed wave number vector. Rapid distortion theory can be applied to flows that undergo a sudden shearing, stretching, or rotation, or any combination thereof (Townsend, 1980).

One way to deal with distortions that are rapid, but not rapid enough, is to rely on an *eddy viscosity*, ν_{T} (Pearson, 1959; Townsend, 1970). The underlying assumption for this is that the transfer process, sketched in Figure 3.25, is approximately uniform for the large eddies and can be taken into account by adding a term $-\nu_{\mathrm{T}}\|\boldsymbol{\kappa}\|^2\, d\mathbf{Z}$. The effect of viscosity can be shown through the linear diffusion equation:

$$\frac{\partial\, d\mathbf{Z}}{\partial t} = -\nu_{\mathrm{T}}\|\boldsymbol{\kappa}\|^2\, d\mathbf{Z}. \tag{3.128}$$

The solution is an exponential decay function:

$$d\mathbf{Z}(\boldsymbol{\kappa}, t) = d\mathbf{Z}(\boldsymbol{\kappa}, t_0)\mathrm{e}^{-\nu_{\mathrm{T}}\|\boldsymbol{\kappa}\|^2(t-t_0)}, \tag{3.129}$$

which is the same as found by Batchelor (1953, p. 93). From this, it also follows that

$$\boldsymbol{\Phi}(\boldsymbol{\kappa}, t) = \boldsymbol{\Phi}(\boldsymbol{\kappa}, t_0)\mathrm{e}^{-2\nu_{\mathrm{T}}\|\boldsymbol{\kappa}\|^2(t-t_0)}, \tag{3.130}$$

implying that the variance is lost faster by the high wave numbers than by the low wave numbers (see Figure 3.26).

Another possible solution is to use a wave number-dependent *eddy lifetime* or *eddy turnover time*, $\tau(\kappa)$, originally proposed by Ropelewski, Tennekes and Panofsky (1973). This can be used to express the probability of an eddy not decaying in a time period Δt (Kristensen, 1979):

$$\mathrm{P} \sim \mathrm{e}^{-\Delta t/\tau(\kappa)}. \tag{3.131}$$

Such an approach has been used by Bossanyi (2012) in a very simple but effective way: by letting one wind field evolve into another. Bossanyi applies this to the phase of the
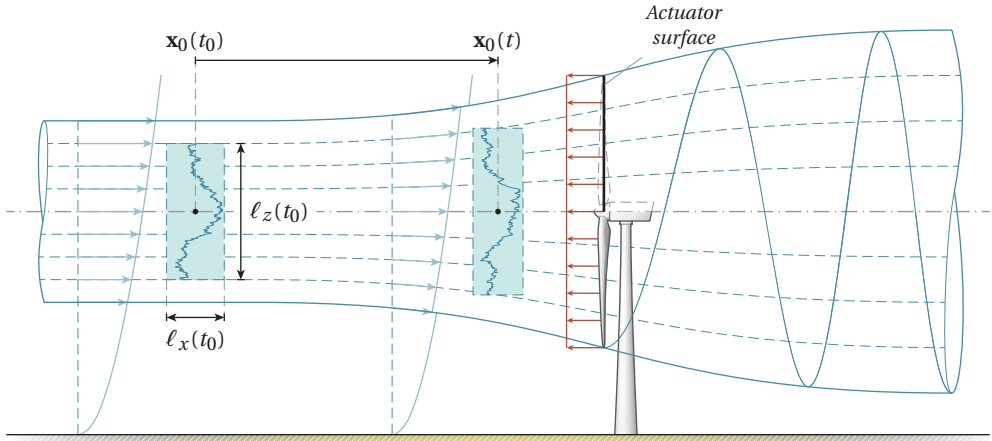
Figure 3.27: Sketch of a gust evolving from a time t_0 to a time t as it travels towards a rotor, here represented as an actuator disk applying a uniform pressure on the flow.

Fourier modes only, but it can easily be extended by writing $\Delta \mathbf{Z} = \mathbf{C}\mathbf{n}$ (see Equation (3.45)) and having it affect the entire white noise vector:

$$\mathbf{n}(t) = e^{-\frac{t-t_0}{\tau(\kappa)}} \mathbf{n}_1 + \left(1 - e^{-\frac{t-t_0}{\tau(\kappa)}}\right)\mathbf{n}_2, \tag{3.132}$$

where the initial state $\mathbf{n}_1$ evolves into another random vector $\mathbf{n}_2$.

3.5.3 A turbulent gust approaching an actuator disk

The special case treated here is that of an actuator disk, which is an imaginary surface normal to the flow that applies a uniform pressure. As a consequence, the mean wind speed drops and the streamlines expand (see Figure 3.27). By conservation of mass, an air parcel with dimensions $\ell_x \times \ell_y \times \ell_z$, traveling at a speed $\dot{\mathbf{x}}_0 = \bar{\mathbf{u}}(\mathbf{x}_0)$, would therefore be distorted according to

$$\ell_x(t) = \alpha \ell_x(t_0), \tag{3.133a}$$

$$\ell_y(t) = \alpha^{-1/2} \ell_y(t_0), \tag{3.133b}$$

$$\ell_z(t) = \alpha^{-1/2} \ell_z(t_0), \tag{3.133c}$$

where α is used to denote the streamwise deceleration of the mean flow:

$$\alpha = \frac{\bar{u}(\mathbf{x}_0(t))}{\bar{u}(\mathbf{x}_0(t_0))}. \tag{3.134}$$

This means the wave numbers are distorted according to

$$\boldsymbol{\kappa} = \begin{bmatrix} \alpha^{-1} & 0 & 0 \\ 0 & \alpha^{1/2} & 0 \\ 0 & 0 & \alpha^{1/2} \end{bmatrix} \boldsymbol{\kappa}_0. \tag{3.135}$$
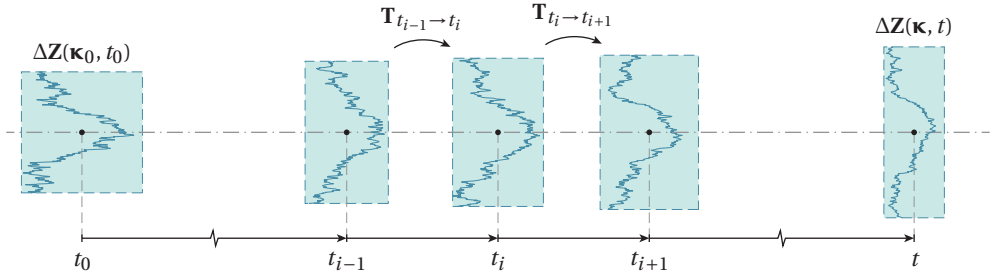
Following Townsend (1980), the transformation matrix from rapid distortion theory is:

$$
\mathbf{T}_{t_0 \to t} = \frac{1}{\|\boldsymbol{\kappa}\|^2}
\begin{bmatrix}
\|\boldsymbol{\kappa}_0\|^2 & 0 \\
\left(\alpha^{-3/2} - 1\right)\kappa_{x,0}\kappa_{y,0} & \|\boldsymbol{\kappa}_0\|^2 + \left(1 - \alpha^{-3/2}\right)\kappa_{x,0}^2 + \left(1 - \alpha^{3/2}\right)\kappa_{z,0}^2 \\
\left(\alpha^{-3/2} - 1\right)\kappa_{x,0}\kappa_{z,0} & \left(\alpha^{3/2} - 1\right)\kappa_{y,0}\kappa_{z,0}
\end{bmatrix}
$$

$$
\begin{matrix}
\cdots & 0 \\
\cdots & \left(\alpha^{3/2} - 1\right)\kappa_{y,0}\kappa_{z,0} \\
\cdots & \|\boldsymbol{\kappa}_0\|^2 + \left(1 - \alpha^{-3/2}\right)\kappa_{x,0}^2 + \left(1 - \alpha^{3/2}\right)\kappa_{y,0}^2
\end{matrix} \Bigg] . \tag{3.136}
$$

Expanding or contracting the flow has an effect on the turbulence kinetic energy (see Figure 3.28). Generally, the streamwise variance increases when the flow is expanded, and vice versa when contracted. A similar plot can be found in Batchelor (1953, p. 74), but only for large contraction ratios relevant for wind tunnels.

However, the contraction ratios in Figure 3.28 are not nearly as large enough for rapid distortion theory to hold on its own. Therefore, since the nonlinear term cannot be neglected entirely, Equation (3.132) is used to account for the transfer between the wave numbers inside the air parcel. After some rearranging, this leads to the following expression:

$$
\Delta \mathbf{Z}(\boldsymbol{\kappa}, t) = \underbrace{\mathbf{T}_{t_0 \to t}\mathbf{C}(\boldsymbol{\kappa}_0)}_{\substack{\text{Expansion/} \\ \text{contraction}}} \underbrace{\left\{ \exp\left[-\frac{t - t_0}{\tau(\boldsymbol{\kappa})}\right] (\mathbf{n}_0 - \mathbf{n}') + \mathbf{n}' \right\}}_{\text{Diffusion}}, \tag{3.137}
$$

where $\mathbf{n}' \sim \mathcal{CN}(0, \mathbf{I})$ is an arbitrary white noise vector that represents some later state. It models a diffusion process where the wave numbers in $\mathbf{n}_0$ lose energy at a rate determined by the eddy lifetime, τ, while at the same time, it is replenished by $\mathbf{n}'$ in order to keep the total kinetic energy constant during the transfer process.[15]

Figure 3.28: Change in variance due to a sudden contraction or expansion of isotropic turbulence.

---

[15] In other works, the second white noise vector is often included as a body force to sustain the turbulence process.

Figure 3.29: A complex distortion can be represented as a combination of moderate transformations.

The downside of using the above expression is that it only works for sharp, uniform distortions. However, Townsend (1980) argues that gradual distortions can be applied in steps to deal with more complex situations (see Figure 3.29):

$$\mathbf{T}_{t_0 \to t} = \prod_{t_i=t_0}^{t_i < t} \mathbf{T}_{t_i \to t_{i+1}}, \tag{3.138}$$

where the individual transformation matrices $\mathbf{T}_{t_i \to t_{i+1}}$ are determined as in Equation (3.136):

$$\mathbf{T}_{t_i \to t_{i+1}} = \frac{1}{\|\boldsymbol{\kappa}_{i+1}\|^2} \begin{bmatrix} \|\boldsymbol{\kappa}_i\|^2 & 0 \\ (\alpha^{-3/2}-1)\kappa_{x,i}\kappa_{y,i} & \|\boldsymbol{\kappa}(t_i)\|^2 + (1-\alpha^{-3/2})\kappa_{x,i}^2 + (1-\alpha^{3/2})\kappa_{z,i}^2 \\ (\alpha^{-3/2}-1)\kappa_{x,i}\kappa_{z,i} & (\alpha^{3/2}-1)\kappa_{y,i}\kappa_{z,i} \end{bmatrix}$$

$$\begin{matrix} \dots & 0 \\ \dots & (\alpha^{3/2}-1)\kappa_{y,i}\kappa_{z,i} \\ \dots & \|\boldsymbol{\kappa}_i\|^2 + (1-\alpha^{-3/2})\kappa_{x,i}^2 + (1-\alpha^{3/2})\kappa_{y,i}^2 \end{matrix} \Bigg], \tag{3.139}$$

with

$$\alpha = \frac{\bar{u}(\mathbf{x}_0(t_{i+1}))}{\bar{u}(\mathbf{x}_0(t_i))}. \tag{3.140}$$

Doing the transformation in steps also helps to better account for how the wave number distortion affects the transfer process (e.g., Fourier modes would decay faster after being compressed):

$$\exp\left[-\frac{t-t_0}{\tau(\boldsymbol{\kappa})}\right] = \exp\left[-\sum_{t_i=t_0}^{t_i<t}\frac{t_{i+1}-t_i}{\tau(\boldsymbol{\kappa}_i)}\right]. \tag{3.141}$$

Combining the above then leads to

$$\Delta\mathbf{Z}(\boldsymbol{\kappa},t) = \left(\prod_{t_i=t_0}^{t_i<t}\mathbf{T}_{t_i \to t_{i+1}}\right)\mathbf{C}(\boldsymbol{\kappa}_0)\left\{\exp\left[-\sum_{t_i=t_0}^{t_i<t}\frac{t_{i+1}-t_i}{\tau(\boldsymbol{\kappa}_i)}\right](\mathbf{n}_0-\mathbf{n}')+\mathbf{n}'\right\}. \tag{3.142}$$
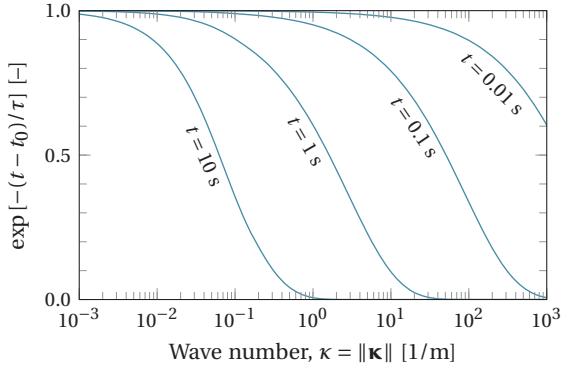
Figure 3.30: Plot of $\exp\left[-(t-t_0)/\tau\right]$ for $L=25$ m. For a value of 1, it holds that $\mathbf{n}(t)=\mathbf{n}_0$. For a value between 0 and 1, the white noise vector is a mixture of its initial state, $\mathbf{n}_0$, and a later state, $\mathbf{n}'$.

Concerning the eddy lifetime, Mann (1994) uses the expression given by Equation (3.35). However, since it is used only to limit the shear distortion, it is a function of the Γ parameter and the local wind shear. In isotropic turbulence, there is no need for an eddy lifetime and it reduces to zero. In the case of evolving turbulence, it is therefore more appropriate to use

$$\tau(\boldsymbol{\kappa}) = \gamma \|\boldsymbol{\kappa}\|^{-2/3} \left[{}_2F_1\left(\tfrac{1}{3}, \tfrac{17}{6}, \tfrac{4}{3}, -(\|\boldsymbol{\kappa}\| L)^{-2}\right) \right]^{-1/2}, \tag{3.143}$$

where γ is a scale parameter, which will have to be found experimentally or through large eddy simulation (LES), for example.[16] A plot of the factor $\exp\left[-(t-t_0)/\tau\right]$ is added in Figure 3.30.

The evolution model is demonstrated in Figure 3.31 for arbitrary values of α and γ. Figure 3.31a highlights the effects of diffusion only—for what is probably an exaggerated value of γ—causing the gust to die out over the course of ten seconds. The gust could, in theory, also grow in strength under pure diffusion. However, this would imply that the state $\mathbf{n}'$ contains an even higher magnitude event, which is very unlikely. Second, Figure 3.31b shows the effects of expansion only. This distorts the gust, but also results in new regions of high velocities, in accordance with the increase in variance in Figure 3.28. Finally, 3.31c shows both effects combined. How this would play out in reality is yet to be seen once proper values of α and γ are found.

---

[16]　Unfortunately, this was not feasible anymore within this thesis work.

$$\sqrt{u'^2 + v'^2 + w'^2}/A \ [-]$$

(a): Evolution of a wind gust by diffusion only ($\gamma = 1$).

(b): Evolution of a wind gust by expansion only ($\alpha = 0.5$).

(c): Evolution of a wind gust by diffusion and expansion ($\gamma = 1$, $\alpha = 0.5$).
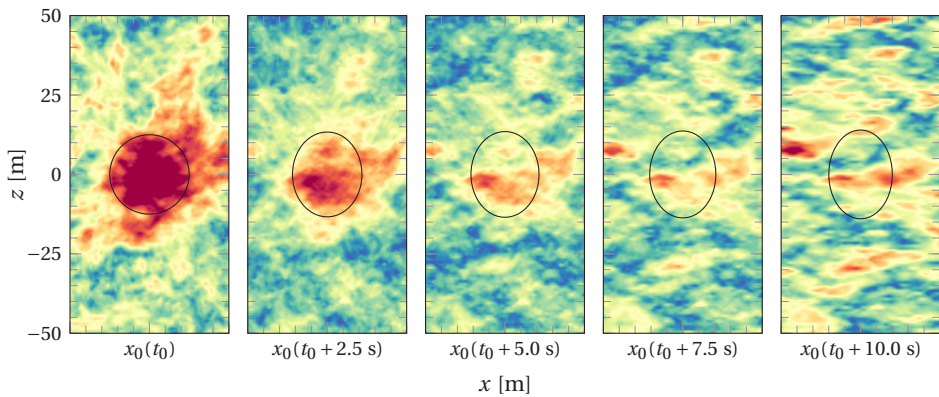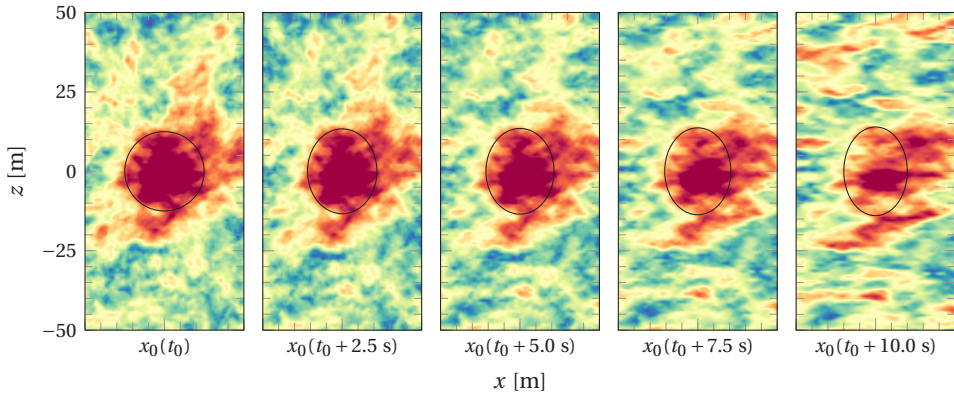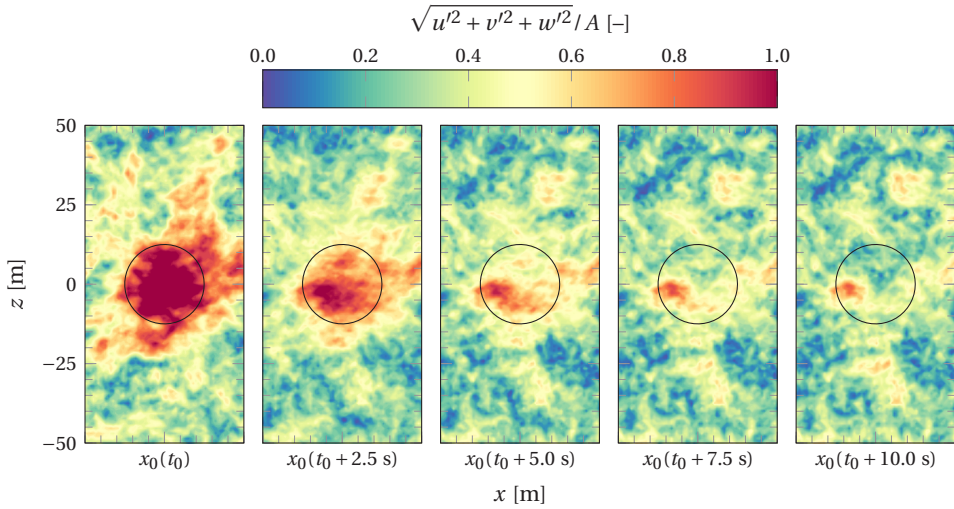
Figure 3.31: Evolution of a velocity field around a spherical concentration of momentum ($\ell_x = \ell_y = \ell_z = 25$ m) in isotropic turbulence by diffusion and expansion over a period of ten seconds.

Chapter 4

Gust loads on rotor blades

This chapter features work from the following publications:

Bos, R., W. A. A. M. Bierbooms, and G. J. W. van Bussel (2014). "Towards spatially constrained gust models." *Journal of Physics: Conference Series* 524, p. 12107.

Bos, R., A. Giyanani, and W. A. A. M. Bierbooms (2016). "Assessing the severity of wind gusts with lidar." *Remote Sensing* 8(9), 758.

"With a large enough sample, any outrageous thing is likely to happen."

— PERSI DIACONIS & FREDERICK MOSTELLER, *1989*

E XTREME GUSTS play an important role in the design of wind turbines as they are bound to occur sooner or later. The aim of this chapter is to study what happens during these rare events on a basic level. A simplified rotor model, together with the velocity fields derived in the previous chapter, shall offer a first look into the consequences of gusts being bounded in space.

Section 4.1 starts off by introducing a rotor model of a 10 MW wind turbine. This will be used in Section 4.2 to identify the parts on the blades and, overall, on the disk that are most vulnerable. Subsequently, Section 4.3 will reflect back on these results to see how relevant a single extreme event is in the grand scheme of things. To conclude, Section 4.4 will apply the theory from Chapter 3 to a measurements from a nacelle-mounted lidar in order to see whether gusts can be identified before they strike the rotor.

4.1 Definition of a 10 MW wind turbine

The DTU 10 MW reference wind turbine is a hypothetical machine designed to serve as a benchmark for large rotors.

4.1.1 Properties

The machine has a rotor diameter of 178.3 m at a hub height of 119 m. Figure 4.1 shows a drawing of the geometry. Other relevant properties are listed in Table 4.1.

4.1.2 Coordinate systems

Loads and deflections are described in several coordinate systems, drawn in Figure 4.2. First, the *ground coordinate system* is attached to the foundation interface and contains the tower base side-side, M_{x_G}, and fore-aft (or overturning) moments, M_{y_G}, respectively around the x_G- and y_G-axes. Second, the *hub coordinate system* houses the in-plane blade moment, M_{x_H}, and the out-of-plane blade moment, M_{y_H}. When rotated by a pitch angle, these translate into the blade edgewise and flapwise moments, $M_{x_{B,0}}$ and $M_{y_{B,0}}$.

For load analyses, the interest is often in the tower base overturning moment, $M_{y_{G,0}}$, and the blade root flapwise moment, $M_{y_{B,0}}$. These are usually the highest moments acting
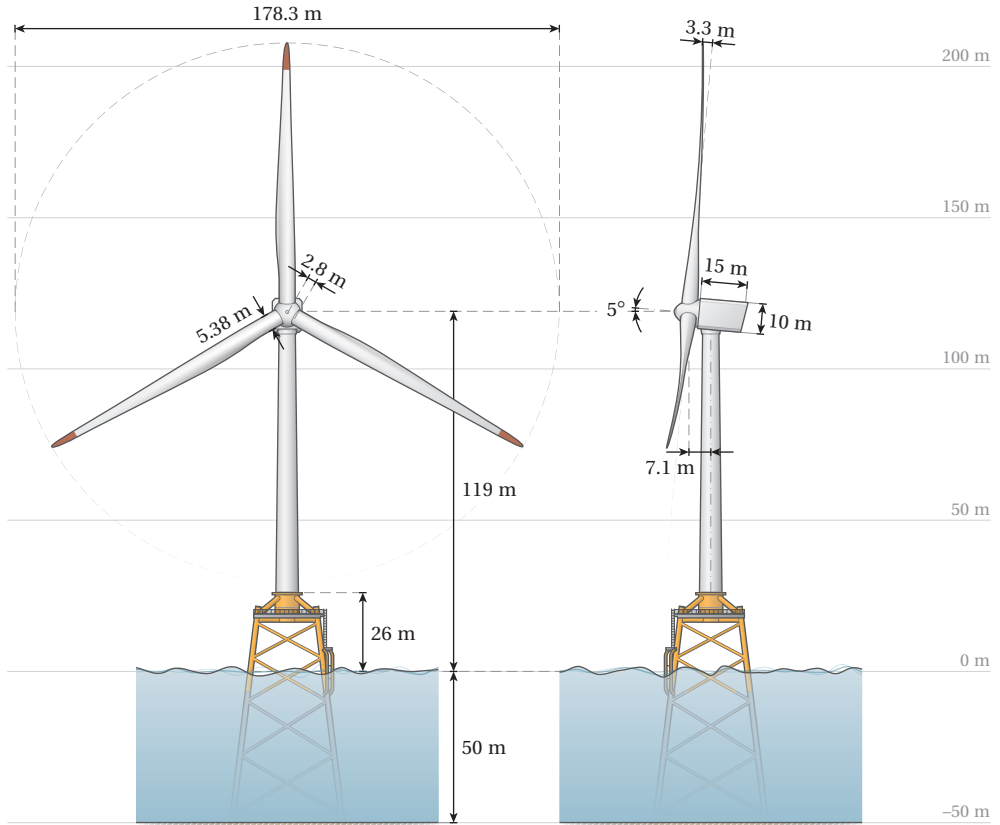
Figure 4.1: Drawing of the DTU 10 MW reference wind turbine with the relevant dimensions.

Table 4.1: Properties of the DTU 10 MW reference wind turbine (Bak et al., 2013).

IEC wind regime	Class 1A
Rated power	10 MW
Rotor orientation	Upwind
Control	Variable speed, collective pitch
Drivetrain	Medium speed, multiple-stage gearbox
Cut-in, rated, cut-out wind speed	4 m/s, 11.4 m/s, 25 m/s
Cut-in, rated rotor speed	6 rpm, 9.6 rpm
Rotor mass	228 t
Nacelle mass	446 t
Tower mass	628 t
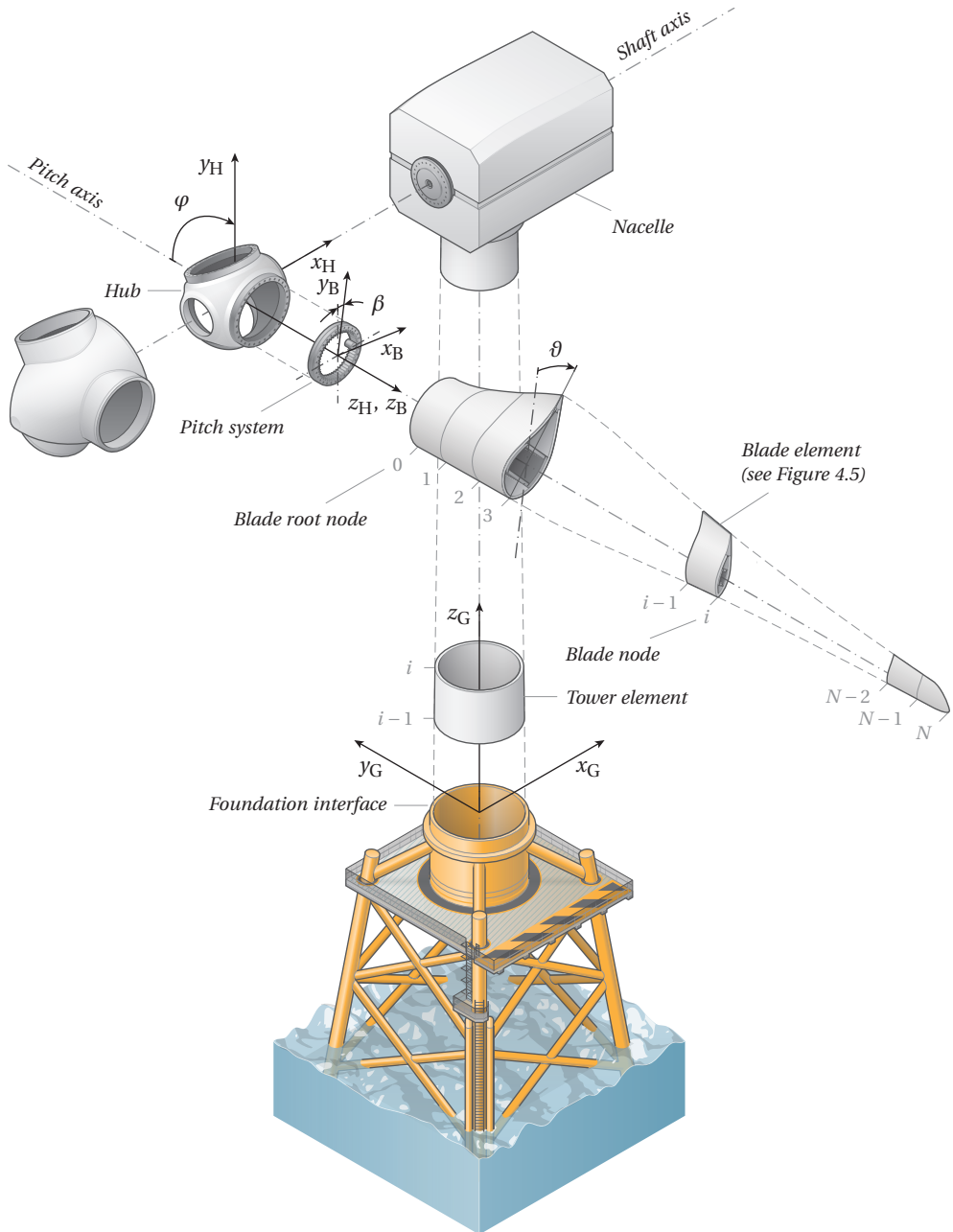
Figure 4.2: Exploded view of the DTU 10 MW wind turbine (not to scale), showing three coordinate systems: the *ground coordinate system* (G), attached to the foundation interface with its x-axis aligned with the mean wind and its z-axis pointing towards the zenith; the *hub coordinate system* (H), with its x-axis aligned with the shaft axis and its z-axis pointing upwards at zero azimuth angle ($\varphi = 0°$); and the *blade coordinate system* (B), which is equal to the hub coordinate system but rotated by the pitch angle, β.

on the tower and blades that, to a large extent, determine the required strength of the material and connections.

4.1.3 Complete aeroelastic BEM model

The loads and deflections of the DTU 10 MW reference turbine can be calculated with the Bladed v4.4 aeroelastic code. This is a blade element momentum (*BEM*)-based model that runs both steady and time-marching simulations with controller input. Figure 4.3 shows the steady operating curves of the DTU 10 MW. Clearly, the maximum thrust is found at the rated wind speed of 11.4 m/s. This is where maximum power is extracted from the wind, while the turbine is still operating at its optimum.[1]

In general, the highest loads can be expected at the point of maximum thrust. To illustrate, Figure 4.4 shows the moments along the tower and blades at rated wind speed. The moment curves follow from

$$\frac{\mathrm{d}M_x}{\mathrm{d}z} = F_y(z), \tag{4.1}$$

$$\frac{\mathrm{d}M_y}{\mathrm{d}z} = F_x(z), \tag{4.2}$$

where $F_x(z)$ and $F_y(z)$ are the forces over the z-axis pointing in the direction of the x- and y-axes, respectively. As a result, the maxima are clearly found at the tower base and the

(a): Steady electrical power curve.

(b): Steady thrust curve.

(c): Steady rotor speed curve.

(d): Steady pitch curve.
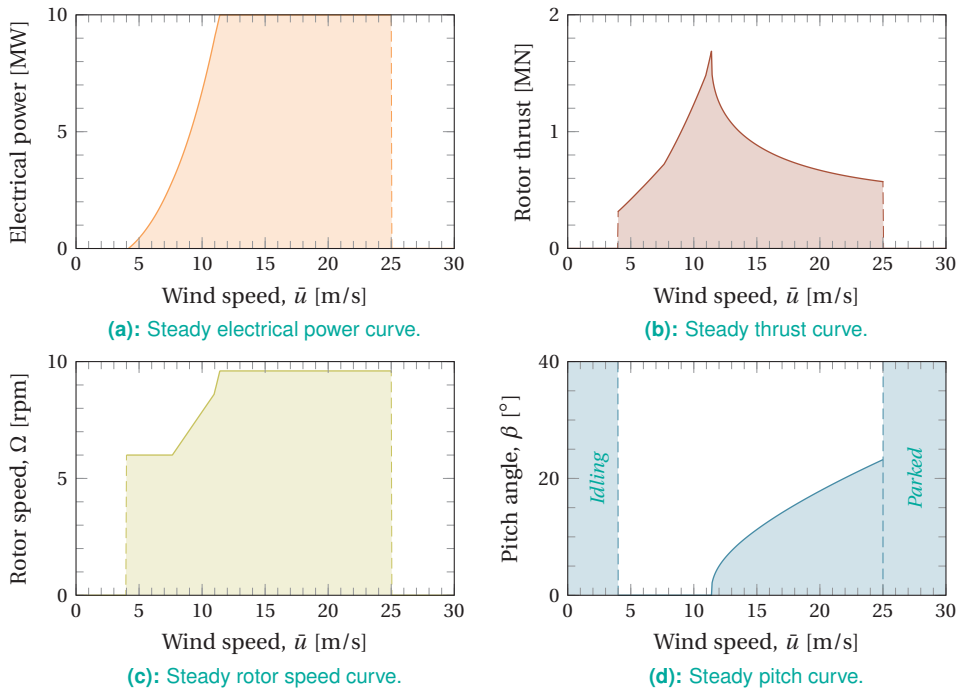
Figure 4.3: Steady operating curves for the DTU 10 MW.

---

[1] Note that peak shaving is not applied here. If it was, the controller would steer the wind turbine away from its optimum at the rated wind speed in order to reduce the loads.
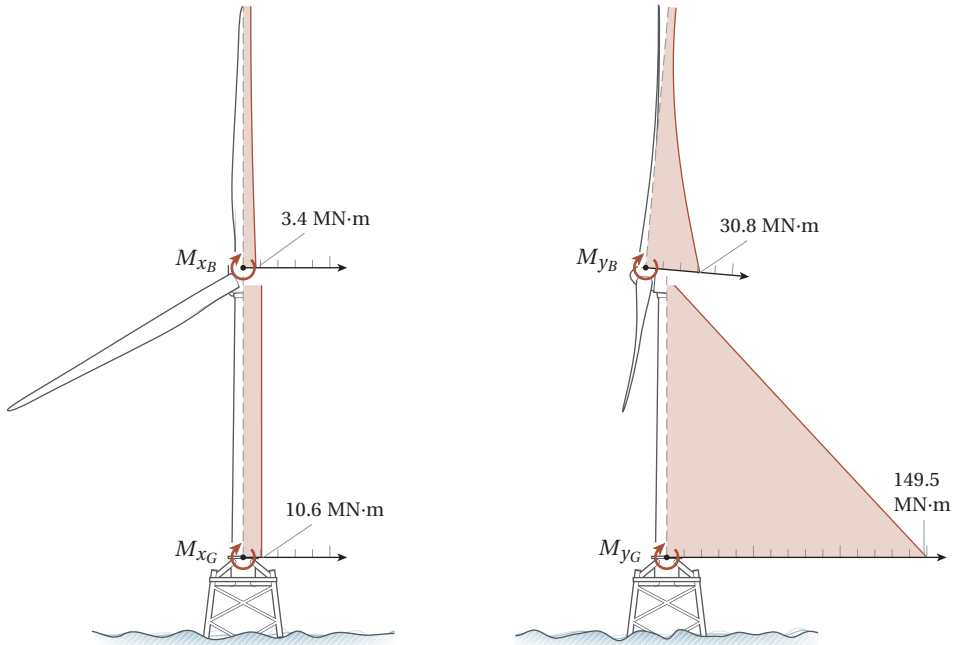
Figure 4.4: Moment curves for the tower and blades of the DTU 10 MW, calculated for steady operation at the rated wind speed of 11.4 m/s.

blade root (i.e., the points of clamping). The tower side-side moment distribution (M_{x_G}) is roughly constant; there are no forces acting on the tower in the y-direction and only the moments from the three blades are carried down to the foundation. The tower fore-aft moments (M_{y_G}) vary approximately linearly, since the rotor thrust can be replaced by a point force acting on the top of the tower.[2] Moreover, the moment distributions over the blades are roughly parabolic in shape, since a distributed load (i.e., pressure) is integrated over the length.

4.1.4 Simplified rotor model
The disadvantage of running a complete aeroelastic code is that the output depends strongly on the control strategy, which makes it difficult to generalize the results. Therefore, a simplified model is proposed that focuses solely on the blade root flapwise bending moment ($M_{y_{B,0}}$). It still relies on the steady operating curves and induction factors calculated by the full aeroelastic code, but contains no control actions within a ten-minute period. Furthermore, structural deflections are ignored when calculating the aerodynamic forces.

The advantage of having a fully rigid rotor operating under a constant speed and pitch is that the positions of the blade elements are known beforehand. For a zero shaft

---

[2]   The drag forces acting on the tower are very small compared to the rotor thrust.
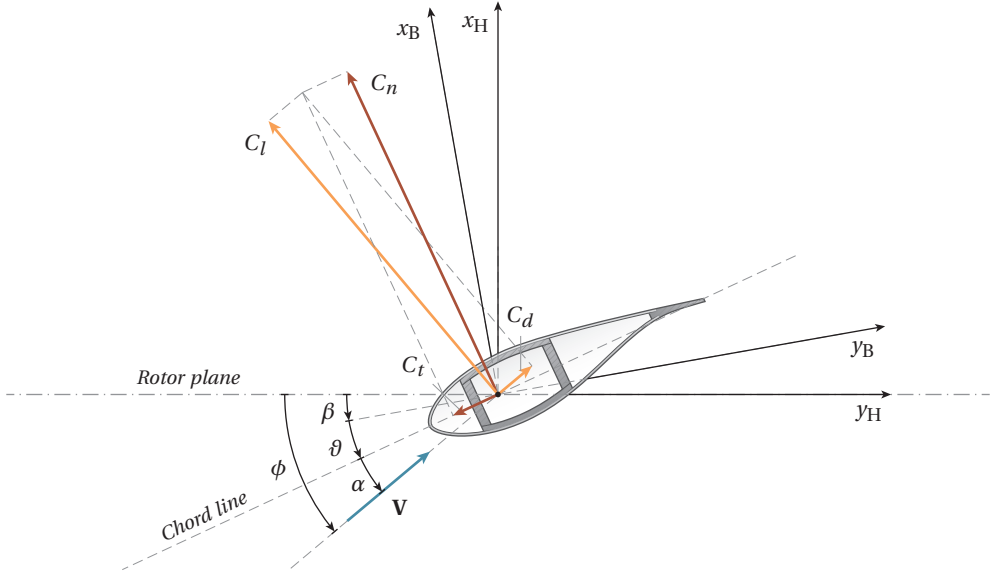
Figure 4.5: Cross-section of an arbitrary blade element with the angles and aerodynamic force coefficients.

tilt, the position of the ith blade element in the ground coordinate system is given by

$$x_{G,i} = 0, \tag{4.3a}$$

$$y_{G,i} = -z_{B,i} \sin(\varphi_0 + \Omega t), \tag{4.3b}$$

$$z_{G,i} = z_{G,hub} + z_{B,i} \cos(\varphi_0 + \Omega t), \tag{4.3c}$$

where $z_{G,hub}$ is the hub height, φ_0 is the initial blade azimuth angle, and Ω is the rotor speed. After interpolating the wind vector, the velocities can be derived for the hub coordinate system (see Figure 4.5):

$$V_{x_H,i} = u_i(1 - a_i), \tag{4.4a}$$

$$V_{y_H,i} = \left(\Omega z_{H,i} + v_i \cos\varphi + w_i \sin\varphi\right)(1 + a_i'), \tag{4.4b}$$

where a and a' are the axial and tangential induction factors, respectively. Then, the apparent velocity and angle of attack for each blade element are given by:

$$V_i = \sqrt{V_{x_H,i}^2 + V_{y_H,i}^2}, \tag{4.5}$$

$$\phi_i = \arctan\left(\frac{V_{x_H,i}}{V_{y_H,i}}\right), \tag{4.6}$$

after which the angle of attack follows from

$$\alpha_i = \phi_i - \vartheta_i - \beta. \tag{4.7}$$

The angle of attack is used to find the steady lift and drag coefficients per airfoil in a look-up table. With those, the steady tangential[3] and normal force coefficients are:

$$C_{t,i}^{(s)} = C_{d,i}^{(s)} \cos\alpha - C_{l,i}^{(s)} \sin\alpha, \tag{4.8a}$$

$$C_{n,i}^{(s)} = C_{d,i}^{(s)} \sin\alpha + C_{l,i}^{(s)} \cos\alpha. \tag{4.8b}$$

The Beddoes-Leishman dynamic stall model is used to translate the steady force coefficients into dynamic force coefficients. This is a semi-empirical model that accounts for unsteady effects on the attached and separated flow regimes, as well as on the vortex-induced lift after leading-edge separation. The code itself was authored and kindly supplied by Ricardo Santos Pereira, tuned according to his 2013 paper for it to be appropriate for a horizontal-axis wind turbine. The details of the model can be found in literature (Leishman and Beddoes, 1989); but, in short, it returns the dynamic tangential and normal force coefficients from:

$$C_{t,i}^{(dyn)}, C_{n,i}^{(dyn)} = f\left(\alpha_i, \frac{d\alpha_i}{dt}, \frac{d^2\alpha_i}{dt^2}, dt, c_i, V_i, C_{d,i}^{(s)}, C_{d,i}^{(s)}, \frac{dC_{n,i}^{(s)}}{d\alpha}\right), \tag{4.9}$$

where c is the (local) chord length.

With the aerodynamic force coefficients known, the forces along the blade can be calculated from

$$F_{t,i} = \tfrac{1}{2} C_{t,i}^{(dyn)}(c_i \Delta z_{B,i})\rho V_i^2, \tag{4.10a}$$

$$F_{n,i} = \tfrac{1}{2} C_{n,i}^{(dyn)}(c_i \Delta z_{B,i})\rho V_i^2, \tag{4.10b}$$

with ρ being the air density and $\Delta z_{B,i}$ the spanwise length of the blade element. Then, the forces along the axes of the blade coordinate system are

$$F_{x_{B,i}} = F_{n,i} \cos\vartheta - F_{t,i} \sin\vartheta + m_i g \sin\varphi \sin\beta, \tag{4.11a}$$

$$F_{y_{B,i}} = F_{n,i} \sin\vartheta + F_{t,i} \cos\vartheta + m_i g \sin\varphi \cos\beta, \tag{4.11b}$$

where m_i is the mass of the blade element and g the acceleration due to gravity. Finally, the edgewise and flapwise blade root moments are respectively

$$M_{x_{B,0}} = \sum_{i=1}^{N} F_{y_{B,i}}\left(z_{B,i} - z_{B,0}\right), \tag{4.12a}$$

$$M_{y_{B,0}} = \sum_{i=1}^{N} F_{x_{B,i}}\left(z_{B,i} - z_{B,0}\right), \tag{4.12b}$$

For a large part, these calculations can be vectorized, which speeds up the calculation by a factor 150 when compared to the full aeroelastic code. Figure 4.6 shows that the simplified model performs reasonably well in a statistical sense. As can be expected, the largest differences are found around the rated wind speed where the pitch controller is the most active (e.g., see Figure 4.3d). Moreover, the overall maximum loads in the simplified model are found closer to the cut-out wind speed, where the turbulence levels are highest.

---

[3]   By convention, the tangential force coefficient is defined positive pointing towards the airfoil trailing edge.
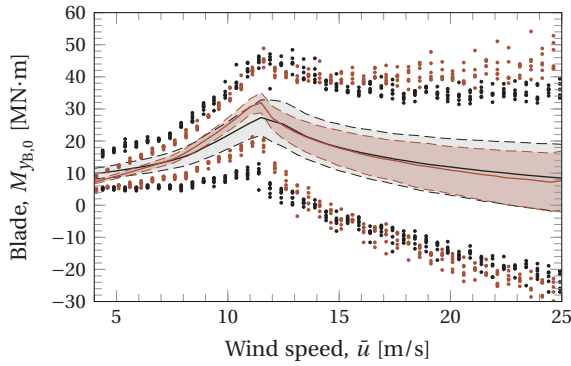
Figure 4.6: Comparison of the blade root flapwise moments of the DTU 10 MW reference turbine calculated by Bladed v4.4 (black) and the simplified rotor model (red) for an IEC class 1A site (see IEC, 2005b). Shown are the means, standard deviations, and minimum and maximum loads based on operation in six ten-minute turbulent wind fields per wind speed step.
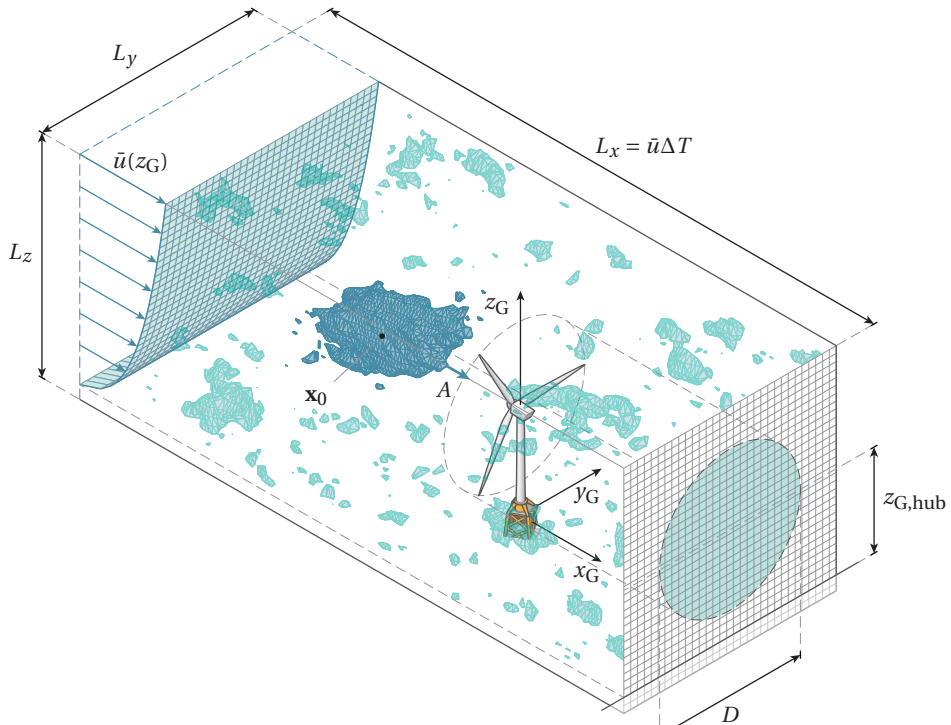

Figure 4.7: Sketch of a rectangular wind field, embedded with a gust at a position, $\mathbf{x}_0$, which is being advected with a steady mean wind speed, $\bar{u} = \bar{u}(z_{G,hub})$, over a time period, ΔT.

4.1.5 The wind field

The simulations are set up as sketched in Figure 4.7. The velocities experienced by the rotor originate from a rectangular box of frozen turbulence that is pushed through the

rotor disk with a steady hub-height mean wind speed, $\bar{u}$.[4] Each wind field is embedded with a gust at a position, $\mathbf{x}_0$, based on the theory of Section 3.3.

4.2 Response to spatial gusts

With wind turbines the size of the DTU 10 MW, extreme gusts cover but a small part of the rotor plane. Compared to a fully coherent gust, this considerably complicates the load analysis, since spatial gusts can take on various length scales and can land at any position. The purpose of this section is to take a closer look at these effects, starting from the basic mean gust shape and expanding the scope step by step to include anisotropy, wind shear, and stochastic turbulence.

4.2.1 Wind climate and definition of a 50-year gust event

Among other things, wind turbines are designed to withstand an extreme load with a 50-year return period in what is regarded "normal" turbulence. This requirement is set by the IEC 61400-1 standards (2005). It prescribes that the hub-height wind speed follows a Rayleigh distribution according to

$$f(\bar{u}_{\text{hub}}) = \frac{\pi \bar{u}}{2 \bar{u}_{\text{ave}}^2} \exp\left(-\frac{\pi \bar{u}^2}{4 \bar{u}_{\text{avg}}^2}\right), \tag{4.13}$$

where $\bar{u}_{\text{ave}}$ is a class-specific average wind speed. The rest of the wind profile is assumed to follow a simple power law:

$$\bar{u}(z_{\text{G}}) = \bar{u}(z_{\text{G,hub}}) \left(\frac{z_{\text{G}}}{z_{\text{G,hub}}}\right)^{\alpha}, \tag{4.14}$$

where $\alpha = 0.2$ is the shear exponent. Moreover, for a *normal turbulence model* (NTM), the standard deviation of the streamwise velocity component varies linearly with wind speed:

$$\sigma_u = I_{\text{ref}} (0.75 \bar{u} + 5.6), \tag{4.15}$$

where I_{ref} is a reference turbulence intensity. The DTU 10 MW machine is designed for a class 1A regime, which implies that $\bar{u}_{\text{avg}} = 10$ m/s and $I_{\text{ref}} = 0.16$.

The same set of standards also requires the designer to evaluate a gust with a 50-year return period. This *50-year gust* is an interesting study topic, since it should represent one of the worst-case scenarios. However, instead of trying to define a single 50-year event, the focus is instead on an amplitude that corresponds to a once-in-50-years probability that can manifest itself over the entire range of operating conditions. In particular, the focus is on the rated wind speed of 11.4 m/s. This is when the rotor is set for maximum momentum transfer (i.e., maximum thrust) and is the most vulnerable to gusts.

Throughout this section, gusts are generated from Mann's spectral model (Mann, 1994). They are defined as spheroidal momentum concentrations with a Lagrangian time scale of 2 s (i.e., $\tau = \ell_x/\bar{u} = 2$ s)[5] and a lateral length scale of 25 m (i.e., $\ell_y = \ell_z = 25$ m), chosen such to reflect the scale of the problem.[6] The gusts are generated in a rectangular

---

[4] Unless stated otherwise, $\bar{u}$ is used to denote the mean wind speed at hub height.

[5] This should favor events with a high $d\mathbf{p}\,dt$, as discussed in Subsection 2.2.5.

[6] The choice of size may look somewhat arbitrary at this point. Apart from its role to act as a yardstick in order to compute the probability, a well-chosen size will reduce the influence of the stochastic gust component and provide a better correlation with the loads. This will be discussed in Subsection 4.2.4.
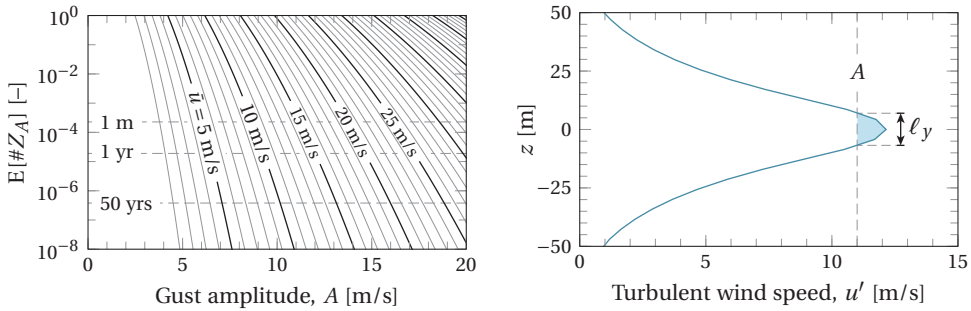
(a): Mean number of gusts in a 10 min × 270 m × 270 m domain.

(b): Mean velocity profile with a 50-year amplitude ($A \approx 11.0$ m/s) at $\bar{u} = 11.4$ m/s.

Figure 4.8: Properties of gusts where a velocity amplitude, A, is averaged over a spheroidal volume with a Lagrangian time scale of $\tau = 2$ s and a lateral length scale $\ell_y = \ell_z = 25$ m.

box with a size of 1 min × 8L × 8L ($\approx 720 \times 270 \times 270$ m), where $L = 33.6$ m is the turbulence length scale prescribed by the IEC for a rotor with a hub height higher than 60 m. The simulation time step was taken as $\Delta t = 0.25$ s and the yz-plane comprised of 64×64 grid points.

Equation (3.104) is then used to find the range of amplitudes that fit the description of a 50-year gust (see Figure 4.8a). A 50-year gust in these conditions has an amplitude of 11.0 m/s and has a streamwise velocity profile along the z-axis as plotted in Figure 4.8b.

4.2.2 Local gust loading

Following Subsection 4.1.4, the blade root moments are largely determined by

- the mean wind speed and the corresponding control mode of the turbine;

- the amplitude of the velocity excursion;

- the local angle of attack changes;

- the affected blade surface area;

- the distance from the blade root to the affected area.

Gust loading is triggered locally by *rotational sampling*. Although the wind turbine in its entirety is a stationary object, the blades are, in fact, moving observers that slice through the wind field with the rotor speed (see Figures 4.9 and 4.10). A gust's longitudinal length scale is therefore not fully appreciated by the blade, but instead sampled at an interval of $T_{1P} = 2\pi/\Omega$ (where 1P stands for once per revolution). As a result, the actual velocity peaks as seen by the blades are much narrower than the actual Lagrangian time scale of the gust. This is shown by Figure 4.11, in which a blade element crosses the mean gust shape[7] at radial positions $r/R = 0.25$ and $r/R = 0.85$ when the blade is at zero azimuth (i.e., at twelve o'clock). At this point, the mean wind speed profile is neglected to keep the maximum velocity at both blade elements the same. However, there are still some

---

7   The mean gust shape is the deterministic part (i.e., the mean velocity field) around a momentum concentration, given by Equation (3.85).
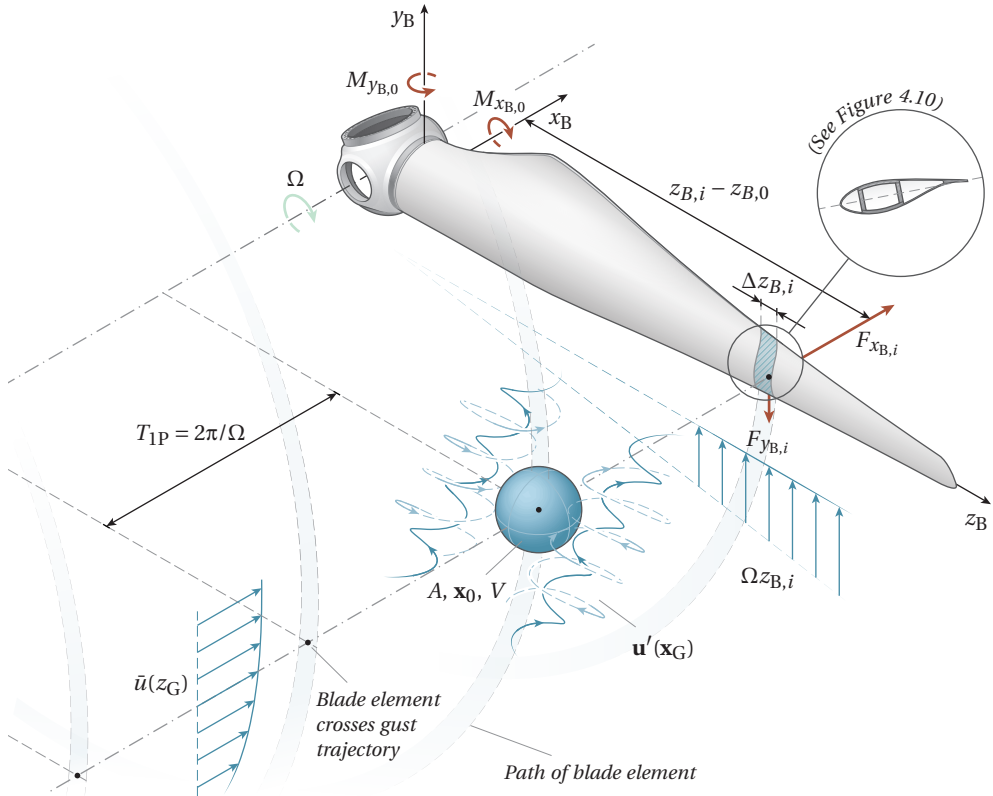
Figure 4.9: Rotational sampling of a velocity field surrounding a spherical concentration of momentum. The forces acting on the ith blade element contribute to the root moments, $M_{x_{B,0}}$, and $M_{y_{B,0}}$.
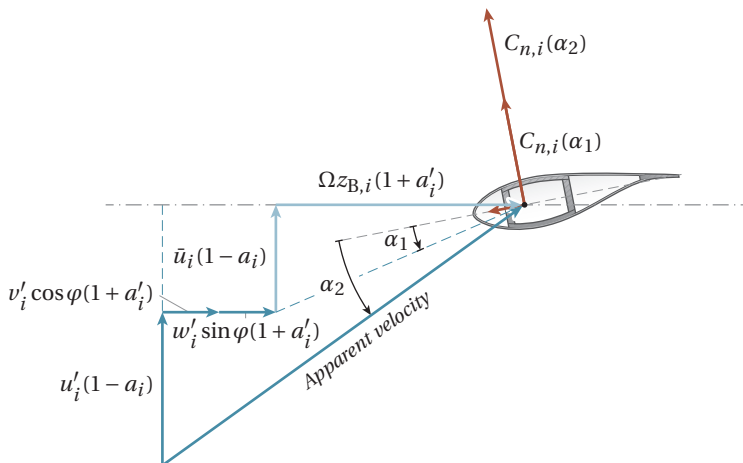

Figure 4.10: Velocities sampled by the ith blade element. Adding the turbulent velocities (u', v', and w') leads to an angle of attack change from α_1 to α_2.
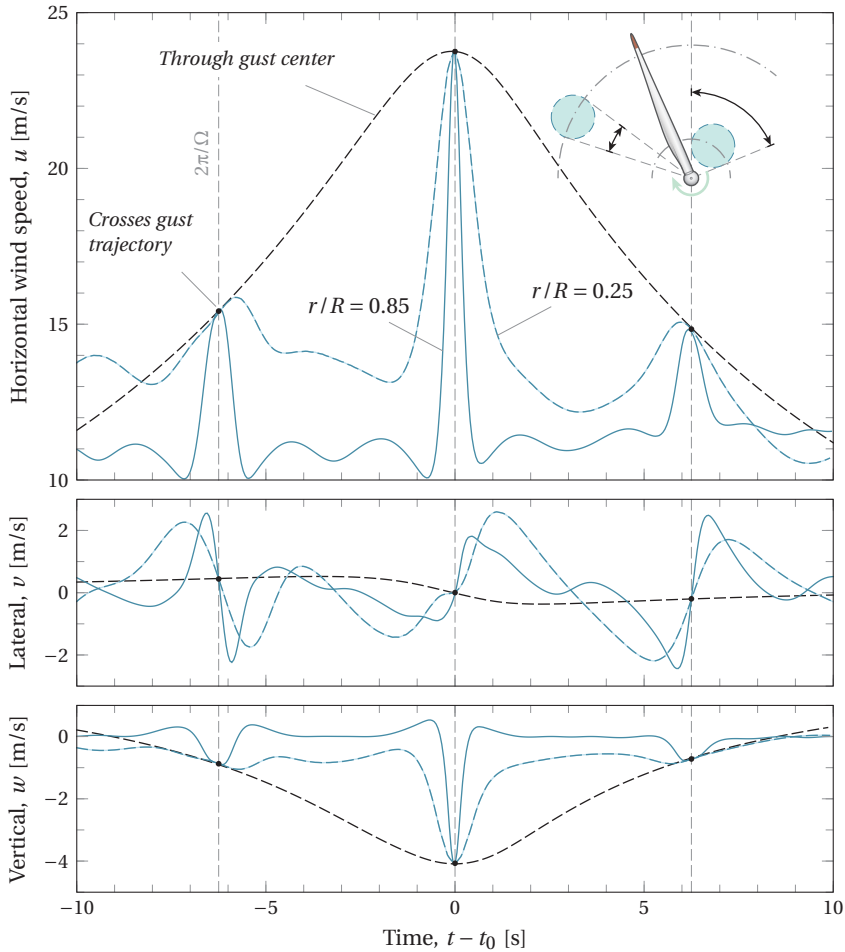
Figure 4.11: Rotational sampling of the mean gust shape ($\tau = 2$ s, $\ell_y = \ell_z = 25$ m, $A = 11.0$ m/s) at $\bar{u} = 11.4$ m/s by a blade element at $\varphi = 0°$ (neglecting induction and the mean wind speed profile), where the blade element collides with the gust center at $t = t_0$. The further a gust is located along the blade, the shorter the sampled velocity peak is.

asymmetries that can be traced back to the anisotropy of sheared turbulence. This causes the positive amplitude to be accompanied by variations of the v- and w-components as well.

When a gust with a positive (streamwise) amplitude hits a blade section, it locally increases the angle of attack for the duration (see Figure 4.10). The normal force coefficient then rises in a linear fashion according to the dynamic stall behavior of the airfoil (sketched in Figure 4.12). In fact, a strong angle of attack change may even push the airfoil beyond the maximum normal force found in the a static case. This is due to a vortex detaching from the leading edge, which briefly provides some suction until it leaves the trailing edge.

(a): The airfoil operates at a steady wind speed on the static normal force curve.

(b): As the airfoil encounters a gust, the boundary layer begins to adapt to the changing angle of attack.

(c): The boundary layer starts to separate at the trailing edge and a leading-edge vortex begins to form.

(d): The leading-edge vortex travels over the chord, providing additional suction. The airfoil is fully stalled.

(e): The vortex detaches from the trailing edge and the extra lift is lost. The airfoil is in deep stall.

(f): When the angle of attack decreases again, the boundary layer starts to reattach from front to back.

Figure 4.12: Step-by-step visualization of dynamic stall triggered locally on a blade section.
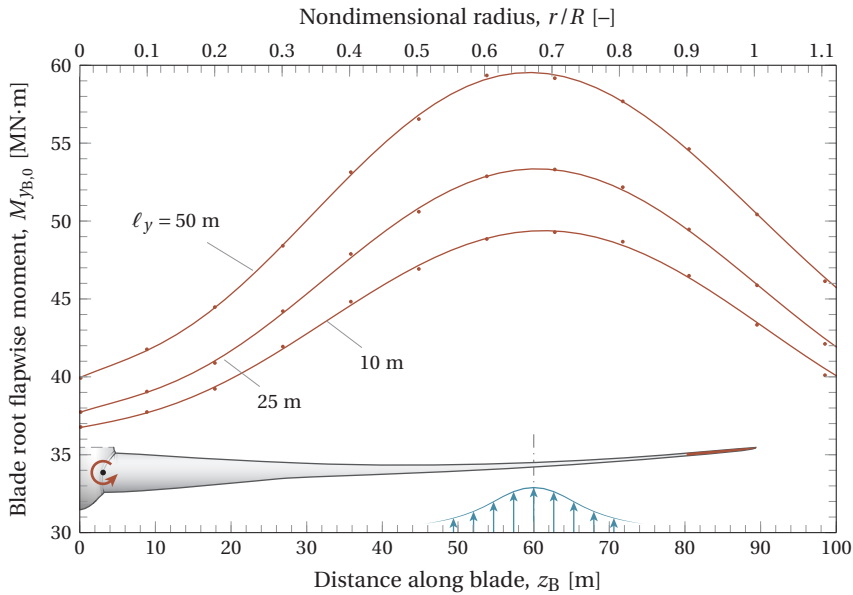
Figure 4.13: Flapwise bending moments triggered at the blade root by gusts located somewhere along the blade (neglecting the mean wind speed profile), taken as the maximum over all azimuthal positions. The lines indicate gusts with a lateral length scale of $\ell_y = 10$, 25, and 50 m, but with the same amplitude of $A = 11.0$ m/s.

Essentially, what a gust does is locally change the pressure distribution. This means that the larger the affected blade area, the higher the total force. Moreover, the further this area is located along the blade, the longer the arm and the higher the root moment. This is shown in Figure 4.13, where the gusts of Figure 4.11 hit the blade of the DTU 10 MW at different radial positions. Increasing the size of the gust, while keeping the amplitude constant, simply increases its momentum content and leads to higher moments. However, regardless of size, the most vulnerable position on the blade seems to be around $\frac{2}{3}$ span. For the rotor model used here, there could be several reasons for this. The most obvious is that wind turbine blades are normally tapered, meaning that the chord length (and thus the blade area) decreases towards the tip. Another reason is that the tip region is dominated by the high induction of the tip vortex (e.g., see Figure 4.14), which would weaken the gust.[8] All this while the high azimuthal velocities found at the tip make it harder for a gust to push the blade section into stall.

4.2.3 Vulnerable parts of the rotor disk

When expanding the scope from the blade level to the rotor level, it becomes possible to highlight the parts of the rotor disk that are most vulnerable to high blade root moments.

---

[8]   Admittedly, this is based purely on steady-state induction factors. How a tip vortex would react to a gust in reality is merely guesswork at this point.
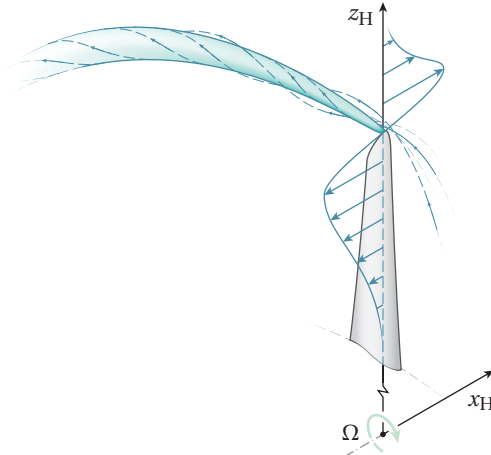
Figure 4.14: Sketch of the induced velocities around a tip vortex.

As illustrated by Figure 4.15d, this is approximately at $\frac{2}{3}$ blade span and at a 30° azimuth angle.[9] Two dominant sources of asymmetry are the cause of this.

First, there is the effect of anisotropic turbulence. This causes positive amplitudes to be correlated with negative vertical velocities (see Figures 3.14 and 4.11). When a gust hits a blade during its downstroke, it also reduces the azimuthal velocity component, increasing the angle of attack and thereby the normal force coefficient. The lateral velocity component also adds to this, which is the reason why the most vulnerable parts in Figure 4.15b are found near 30 and 150° azimuth. During a blade's upstroke, the exact opposite happens: the azimuthal velocity increases and the angle of attack is kept small.

Second, a sheared mean wind speed profile means that the longitudinal velocities increase with height. Apart from leading to higher apparent wind speeds, it also means that the angles of attack are generally larger when the blade nears zero azimuth. This leaves the upper half of the rotor disk relatively vulnerable to high gust loads.

4.2.4 Effect of size and the stochastic gust component

The only thing that is still missing from the complete picture is the addition of the gust's stochastic component. Next to the expected, deterministic gust shape, there are still countless possible velocity fields that match the same 50-year amplitude. In a spectral model, where gusts are generated through conditional sampling as in Equation (3.66), this variation originates from the unconditioned white noise vector, **n**. In principle, getting the right response to a 50-year gust involves evaluating an infinite number of realizations of the same shape (i.e., an infinite number of random seeds):

$$\mathrm{E}\left[M_{y_{\mathrm{B},0}}(\mathbf{n})\right] = \lim_{N \to \infty} \frac{1}{N} \sum_{i=1}^{N} M_{y_{\mathrm{B},0}}(\mathbf{n}_i). \tag{4.16}$$

---

9 Translating these results to another critical load, the tower base overturning moment, is relatively straightforward. In that case, the moment arm is measured from the foundation interface, which further aggravates the damage of gusts landing on the upper half of the disk.

Blade root flapwise moment, $M_{y_{B,0}}$ [MN·m]

(a): Uniform mean wind speed profile, isotropic turbulence ($\Gamma = 0$).

(b): Uniform mean wind speed profile, sheared turbulence ($\Gamma = 3.9$).

(c): Sheared mean wind speed profile, isotropic turbulence ($\Gamma = 0$).

(d): Sheared mean wind speed profile, sheared turbulence ($\Gamma = 3.9$).
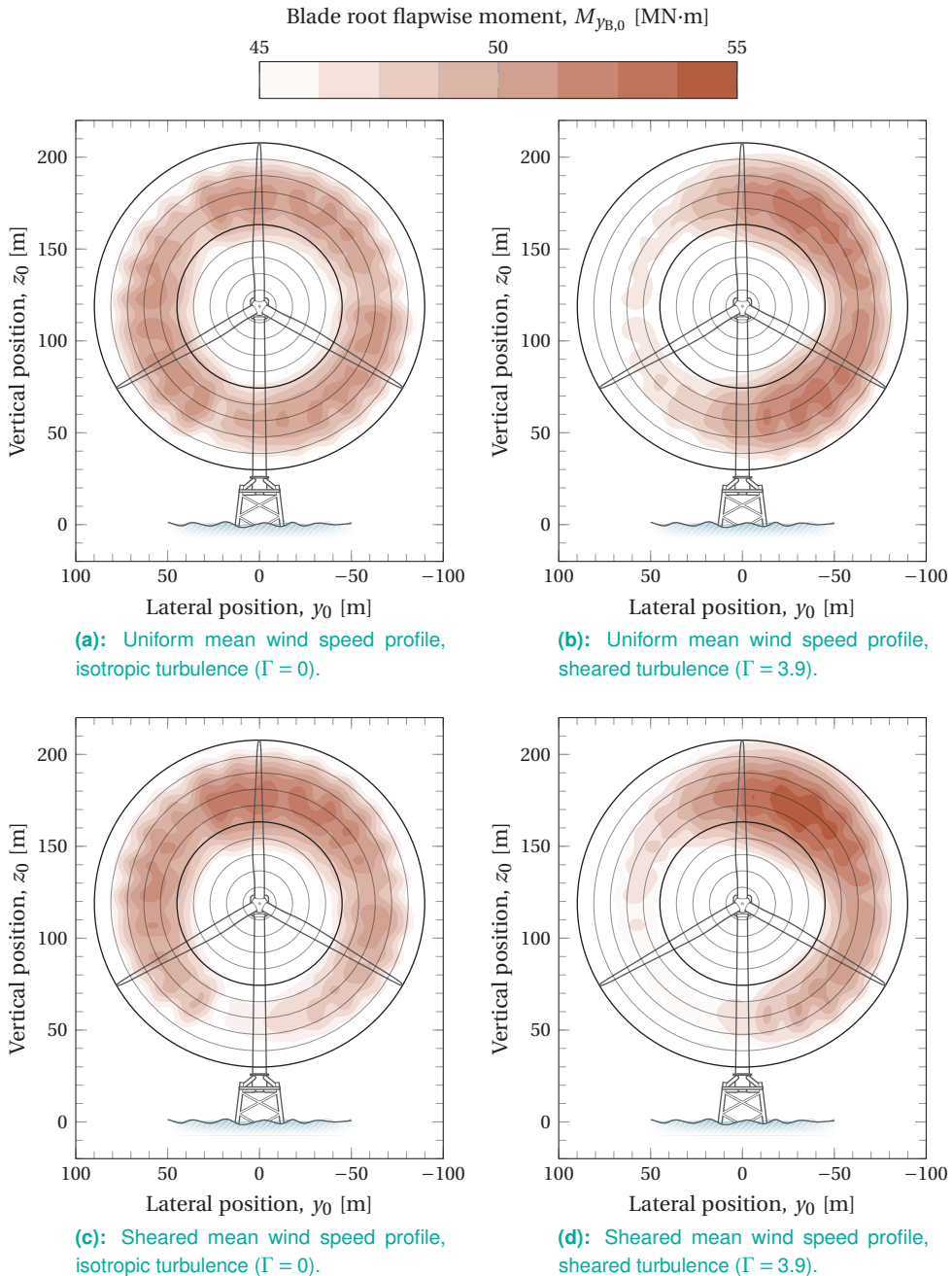
Figure 4.15: Flapwise bending moments triggered at the blade root by gusts located at a position $\mathbf{x}_0 = \begin{bmatrix} x_0, y_0, z_0 \end{bmatrix}^{\mathsf{T}}$ in the rotor disk. The longitudinal position is chosen such that it triggers the maximum load.

Of course, in practice, one has to settle for a finite number of seeds, where an acceptable number is determined by how well the gust amplitude and the load are correlated.

Following Subsection 2.2.5, a maximum correlation should be expected when all the momentum carried by the gust can be transferred to the structure. This is where the gust's volume, V, comes in. Effectively, it causes all the momentum in V to be stored in wave numbers lower than what is cut off by the low-pass filter, $G(\boldsymbol{\kappa})$ (see Subsection 3.3.1). The more relevant V is to the design problem, the more the velocity fields are correlated to the loads and the fewer realizations are needed to get a good estimate of $\mathrm{E}\left[M_{y_{\mathrm{B},0}}(\mathbf{n})\right]$.

The choice of an appropriate volume is, to some extent, set by the size of the problem. The reason for this is that the interaction between gusts and objects shows filter-like behavior too by being susceptible to certain wave numbers. For example, imagine a flat traffic sign facing the oncoming wind as sketched in Figure 4.16. The loads acting on the pole are determined by the pressure difference integrated over the sign's surface. Any fluctuations much smaller than the length scale of the sign, ℓ, are cancelled out and do not contribute to the total force. In the wave number domain, the sign therefore acts as another low-pass filter that cuts off wave numbers higher than $2\pi/\ell$.

A wind turbine rotor, although being much more complex, shows similar behavior. In the streamwise direction, low-pass behavior exists due to the controller response time and lag effects in the wake, for example. In the radial direction, small fluctuations will cancel out over the length of the blade, making them irrelevant for the root moment. One way to illustrate the impact of the smaller scales is by redrawing Figure 4.15d with fully turbulent velocity fields. Figure 4.17a shows that, over ten random seeds, the picture hardly changes and the highest loads are still found in the same areas. This can be explained by the fact that, despite the presence of the small scales, both the deterministic and the stochastic gusts have exactly the same momentum content and therefore the same *damaging potential*. Averaged over ten turbulence seeds, the highest load is about 55.9 MN·m, against 55.5 MN·m in response to the deterministic gusts. The most vulnerable part of the rotor disk is still at around $\frac{2}{3}$ span and at 30°azimuth.

Only when the 50-year gust arrives outside of vulnerable areas do the stochastic fields trigger higher loads, because neighboring velocity peaks take over the role of strongest gust. This is shown in Figure 4.17b, where the root-mean-squared difference between the two fields are plotted. It shows that, indeed, the stochastic gust component adds relatively little to the damaging potential of the 50-year gust. The root-mean-squared difference around the highest load is 1.7 MN·m ($\approx 3\%$) and comparable values can be found over the entire range of azimuths.
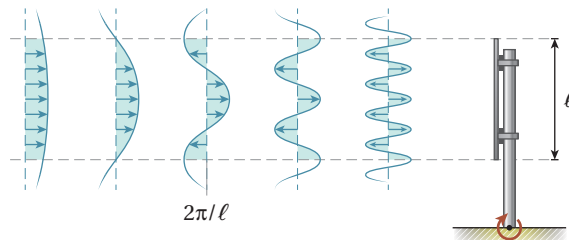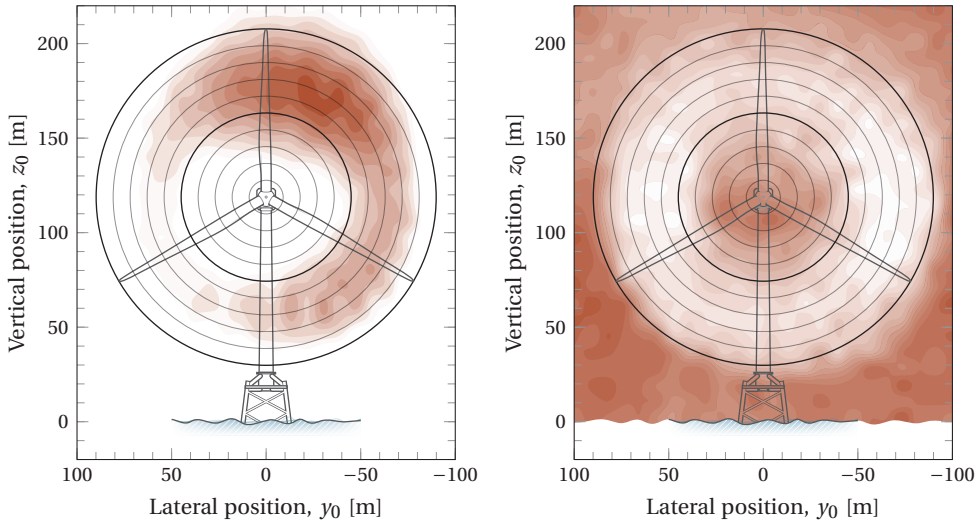

$2\pi/\ell$

Figure 4.16: A traffic sign operates similar to a low-pass filter by canceling out fluctuations that are much smaller than ℓ.

(a): Flapwise bending moments triggered by fully turbulent gusts.

(b): Root-mean-squared difference between Figure 4.17a and 4.15d.

Figure 4.17: Effect of the stochastic gust component on the flapwise bending moments.

4.3 How relevant is the 50-year gust?

Evidently, the instantaneous gust loading depends on where exactly a blade is hit and, to some extent, how the surrounding velocity field looks. On the one hand, a relatively weak gust might hit the rotor disk at a very vulnerable spot. On the other hand, a very severe gust entering the domain can trigger an insignicant load or may even go unnoticed by completely missing the rotor. In the end, it is all a matter of probability or, more specifically, risk.

Following the definition employed in Subsection 4.2.1, a 50-year deviation from the mean can manifest itself over a range of wind speeds and at any location in the domain. In homogeneous turbulence, for example, a gust has an equal chance of landing anywhere on the yz-plane. If an event is spawned in a rectangular domain, B, with sides $L_x \times L_y \times L_z$, the position of its center is uniformly distributed:

$$
f(\mathbf{x}_0) = \begin{cases} \dfrac{1}{\text{vol}(B)}, & \text{for } \mathbf{x}_0 \in B, \\[2mm] 0, & \text{for } \mathbf{x}_0 \notin B, \end{cases} \tag{4.17}
$$

The probability of it landing on the rotor annulus bounded by the $(i-1)$th and ith blade nodes is then

$$
P\left(r_0 \in \left[z_{\text{B},i-1}, z_{\text{B},i}\right]\right) = \frac{\pi z_{\text{B},i}^2 - \pi z_{\text{B},i-1}^2}{L_y L_z}, \tag{4.18}
$$

where r_0 is the gust's radial position. In addition, the blades rotate, which means the gust has a chance to partially or completely miss the target (i.e., not sampling the whole amplitude as in Figure 4.11). For a three-bladed rotor, the probability of encountering any

of the blades within a time period Δt is given by

$$P(t_0 \in [t, t + \Delta t]) = \frac{3\Omega}{2\pi} \Delta t, \tag{4.19}$$

where $3\Omega/(2\pi)$ is the blade passing frequency.

This brings up an important point with respect to spatial gusts. Even if the wind field would spawn an extreme 50-year gust event, the chances of it hitting a blade exactly at the right spot are very slim. When a gust is described by a combination of variables, $\boldsymbol{\theta} = [\bar{u}, \mathbf{x}_0, \ldots]^\mathsf{T}$, the risk associated with it is given by

$$\mathrm{E}\left[M_{y_{\mathrm{B},0}}\right] = \int M_{y_{\mathrm{B},0}}(\boldsymbol{\theta}) f(\boldsymbol{\theta}) \, \mathrm{d}\boldsymbol{\theta}. \tag{4.20}$$

To put matters into perspective: the expected flapwise moment triggered in the situation depicted in Figure 4.13d is a mere 40.1 MN·m, which is way lower than the 50-year load and even lower than the ten-minute extreme. Just exactly how insigificant the 50-year gust seems to be, is perhaps even better illustrated with a cumulative distribution function, conditional on the mean wind speed of 11.4 m/s and the amplitude of 11.0 m/s (see Figure 4.18). It shows that there is just a one-in-five probability of triggering a blade root moment higher than the ten-minute extreme, owing to all the ways the gust can miss the rotor. Surely, this means that the 50-year *gust* cannot solely be responsible for the 50-year *load*.

But even though the deterministic and the stochastic gusts have the same damaging potential, clearly the *risk* associated with the latter is much higher (42.6 MN·m). This is because, if the 50-year gust is not hitting anything, one of the neighboring gusts will. And considering that a turbine is continuously being bombarded with gusts, it is not hard to imagine that the highest load over a 50-year period is ultimately triggered by one of these weaker amplitudes.[10]
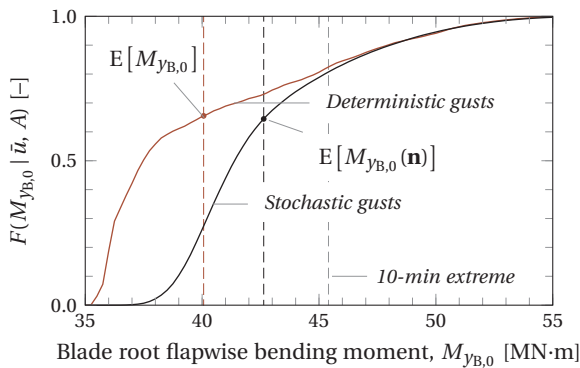
Figure 4.18: Probability of non-exceedance for 50-year gust events at $\bar{u} = 11.4$ m/s ($A = 11.0$ m/s), where the distribution of the stochastic gusts is constructed from ten turbulence seeds. The ten-minute extreme load is obtained from Figure 4.6.

---

[10] The gust ultimately responsible for this might as well just be a monthly event. Due to how rapidly the probability for high amplitudes decreases, the monthly extreme at $\bar{u} = 11.4$ m/s is still $A = 9.4$ m/s (see Figure 4.8a), but is exceeded 600 times more frequent than the 50-year extreme.

Therefore, instead of focusing on the 50-year gust, finding the design loads is a matter of going through all the possible gust events:

$$F\left(M_{y_{B,0}}\right) = \int F\left(M_{y_{B,0}} \,|\, \boldsymbol{\theta}\right) f\left(\boldsymbol{\theta}\right) \mathrm{d}\boldsymbol{\theta}, \tag{4.21}$$

and finding the case where the probability of exceedance, $1 - F\left(M_{y_{B,0}}\right)$, matches the 50-year level. By doing so, every gust event is put into perspective by weighting it with its probability of occurrence. However, the problem is that the above integral is computationally very expensive—if not impossible—to determine for even a handful of parameters. In order to get around this, one should rather rely on stochastic simulation methods, which is the subject of the next chapter.

4.4 Tracking severe gusts with lidar

High gust loads are not completely unavoidable. Proper control schemes with the aid of lidar systems can anticipate oncoming gusts and help to alleviate loads.

4.4.1 Lidar basics

Lidar, short for *LIght Detection And Ranging*,[11] is a remote sensing technique that uses a laser to measure distances and velocities. Particularly in wind energy, it is used to replace expensive met masts for resource assessment, but can also be coupled to controllers for load alleviation.

The two main types used for wind speed measurements are the *continuous wave* and *pulsed lidars*. Continuous wave lidars operate by sending out an uninterrupted laser beam, focused on a certain upstream distance. When the light is scattered back from natural aerosols, the Doppler shift can be used to calculate the velocity at which the particle is traveling with respect to the direction of the beam. Following a certain scanning pattern then allows the system to gather information of the oncoming yz-plane. A pulsed lidar works in a similar fashion, but—as the name might suggest—sends out pulses instead of a continuous beam (see Figure 4.19). The time it takes for a pulse to arrive back at the detector is then used to determine the distance to the particle. This can be done for several *range gates*, providing a set of point measurements over several upwind distances.

What the lidar receives are *line-of-sight velocities* along the beam angle, ψ, which can be used to get an estimate of the longitudinal wind speed. However, there is no way of telling how the line-of-sight velocity is influenced by the lateral and vertical velocity components. This is often referred to as the *cyclops dilemma*. The error (or directional bias) worsens as the beam angle increases (Simley et al., 2014):

$$\varepsilon_{\hat{u}} = \tan\psi \left(v\sin\varphi - w\cos\varphi\right), \tag{4.22}$$

where φ is the lidar azimuth angle. This makes it hard to get a good and accurate coverage of a larger plane, especially during unstable and low-wind-speed conditions. In addition, the pulse that is sent out has a duration in the order of 10^{-7} s that, after multiplying with the speed of light, means that the velocity is integrated over several tens of meters. When assuming that the streamwise component is large enough (i.e., $u \gg v, w$), the line-of-sight

---

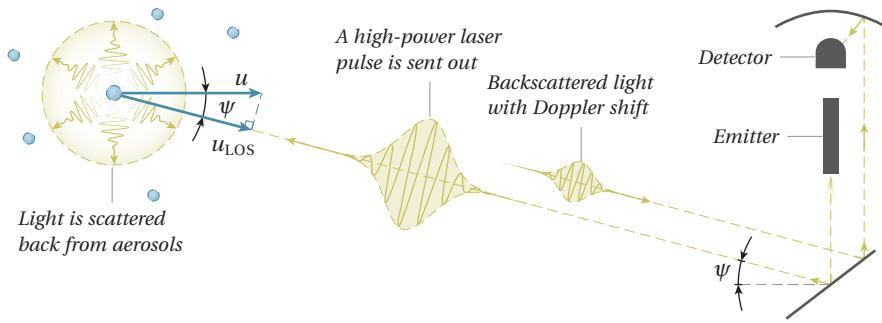[11] Like radar, the word "lidar" is often written lower case.

Figure 4.19: Working principle of a pulsed lidar system.

velocity follows from

$$u_{\mathrm{LOS}}(\mathbf{x}, t) \approx \cos \psi \int u(x + r, y, z, t) g(r) \, \mathrm{d}r, \tag{4.23}$$

which essentially implies low-pass filtering with a weighting function, $g(r)$. For a pulsed lidar, this is usually represented as a Gaussian pulse shape (Frehlich et al., 2006):

$$g(r) = \frac{1}{2\Delta R} \left[\mathrm{erf}\left(\frac{R - r + \frac{1}{2}\Delta R}{\Delta Z} \right) - \mathrm{erf}\left(\frac{R - r - \frac{1}{2}\Delta R}{\Delta Z} \right) \right], \tag{4.24}$$

where R is the distance to a range gate, ΔR is the spacing between range gates, r_{p} is the e^{-1} radius of the pulse, and $\mathrm{erf}(\square)$ is the error function. The e^{-1} radius of the pulse is derived from the full-width-at-half-maximum pulse width (FWHM):

$$r_{\mathrm{p}} = \frac{\mathrm{FWHM}}{2\sqrt{\ln 2}}. \tag{4.25}$$

4.4.2 Velocity field reconstruction

To study the integration of lidar technology in wind energy, an Avent-Lidar five-beam prototype pulsed lidar system was installed on top of the nacelle of a Darwind XD115-5MW wind turbine. This machine, with a rotor diameter of 115 m and a hub height of 100 m, is located at the test field of the Energy Research Centre of the Netherlands (ECN) in the Wieringermeer polder.

The lidar is pointed upwind and measures the incoming velocity at ten range gates simultaneously, from 50 to 185 m in steps of 15 m (see Figure 4.20). The laser beam cycles over five positions in a 1.25-s period by changing its azimuth every 0.25 s. A center position (0) is aligned with the incoming wind speed and four positions (1–4) make an angle of 15°.

By doing so, the lidar collects a series of scattered measurement points that are each advected downstream by a local mean velocity, $\bar{u}(\mathbf{x}_j)$. After a certain time, the velocity is
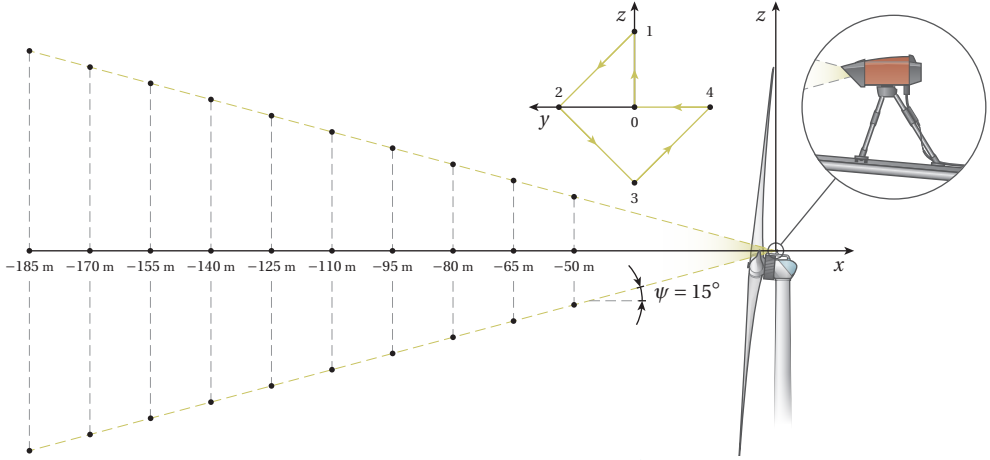
Figure 4.20: A pulsed lidar system mounted on the nacelle of a Darwind XD115-5MW wind turbine.
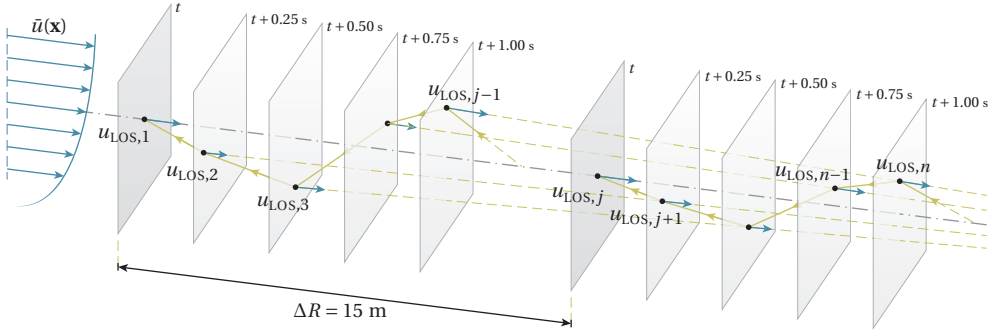
Figure 4.21: Line-of-sight velocities measured within a certain time period at range gates spaced by $\Delta R = 15$ m. Every time step, the points are expected to advect downstream with a mean velocity $\bar{u}(\mathbf{x}_j)$.

known at n points in space, making the surrounding field a conditional field given by

$$\hat{\mathbf{u}}(\mathbf{x}, t) = \left\{ \mathbf{u}(\mathbf{x}, t) \mid \int u(x_1 + r, y_1, z_1, t)g(r)\,\mathrm{d}r = \frac{u_{\mathrm{LOS},1}}{\cos\psi_1}, \dots, \right.$$

$$\left. \int u(x_n + r, y_n, z_n, t)g(r)\,\mathrm{d}r = \frac{u_{\mathrm{LOS},n}}{\cos\psi_n} \right\}. \quad (4.26)$$

Based on the theory of Section 3.3, the set of all homogeneous Gaussian velocity fields matching those measurements is described by

$$\mathrm{E}\left[\hat{\mathbf{u}}(\mathbf{x}, t)\right] = \mathrm{E}\left[\bar{\mathbf{u}}(\mathbf{x})\right] + \boldsymbol{\Psi}\mathrm{E}\left[\mathbf{n} \mid \mathbf{Yn} = \mathbf{b}\right],$$

$$= \bar{\mathbf{u}}(\mathbf{x}) + \boldsymbol{\Psi}\mathbf{Y}^*\left(\mathbf{YY}^*\right)^{-1}\mathbf{b}; \quad (4.27a)$$

$$\mathrm{var}\left[\hat{\mathbf{u}}(\mathbf{x}, t)\right] = \mathrm{var}\left[\bar{\mathbf{u}}(\mathbf{x})\right] + \boldsymbol{\Psi}\mathrm{var}\left[\mathbf{n} \mid \mathbf{Yn} = \mathbf{b}\right]\boldsymbol{\Psi}^*,$$

$$= \boldsymbol{\Psi}\boldsymbol{\Psi}^* - \boldsymbol{\Psi}\mathbf{Y}^*\left(\mathbf{YY}^*\right)^{-1}\mathbf{Y}\boldsymbol{\Psi}^*; \quad (4.27b)$$

where $\mathbf{n}\,|\,\mathbf{Yn} = \mathbf{b}$ is a conditional white noise vector and $\mathbf{\Psi}$ follows from Equation (3.52). Moreover, the matrix $\mathbf{Y}$ is given by

$$\mathbf{Y} = \begin{bmatrix} \dots, G(\kappa_{x,j}) \left[C_{uu}(\mathbf{\kappa}_j), C_{uv}(\mathbf{\kappa}_j), C_{uw}(\mathbf{\kappa}_j) \right] e^{i\mathbf{\kappa}_j \cdot \mathbf{x}_1}, \dots \\ \dots, G(\kappa_{x,j}) \left[C_{uu}(\mathbf{\kappa}_j), C_{uv}(\mathbf{\kappa}_j), C_{uw}(\mathbf{\kappa}_j) \right] e^{i\mathbf{\kappa}_j \cdot \mathbf{x}_2}, \dots \\ \vdots \\ \dots, G(\kappa_{x,j}) \left[C_{uu}(\mathbf{\kappa}_j), C_{uv}(\mathbf{\kappa}_j), C_{uw}(\mathbf{\kappa}_j) \right] e^{i\mathbf{\kappa}_j \cdot \mathbf{x}_n}, \dots \end{bmatrix}, \tag{4.28}$$

where $G(\kappa_x)$ is the Fourier transform of the range-weighting function, $g(r)$, with FWHM = 30 m for the experimental set-up. The constraint vector, $\mathbf{b}$, now contains the set of all velocity measurements of the positions $\mathbf{x}_1, \mathbf{x}_2, \dots, \mathbf{x}_n$:

$$\mathbf{b} = \begin{bmatrix} u_{\text{LOS},1}/\cos\psi_1 - \bar{u}(\mathbf{x}_1) \\ u_{\text{LOS},2}/\cos\psi_2 - \bar{u}(\mathbf{x}_2) \\ \vdots \\ u_{\text{LOS},n}/\cos\psi_n - \bar{u}(\mathbf{x}_n) \end{bmatrix}. \tag{4.29}$$

Equations (4.27a) and (4.27b) can be used to compute the most probable velocity fields matching the lidar measurements, together with the analytical uncertainty.

To illustrate, consider a severe gust picked up by the experimental set-up on 22 December 2013. During this time, the XD115-5MW machine was operating in a ten-minute mean wind speed of 13.3 m/s and a longitudinal turbulence intensity of 5.9%,[12] outside of the wakes of neighboring turbines or met masts. Based on time-averaged data from the beam positions 0, 1, and 3, a neutral wind shear profile was fitted to the measurements:

$$\bar{u}(z) = \bar{u}(z_{\text{ref}}) \frac{\ln(z/z_0)}{\ln(z_{\text{ref}}/z_0)}, \tag{4.30}$$

corresponding to a roughness length of $z_0 \approx 0.55$ m that is representative of the site (e.g., see de Jong, de Vries and Klaasen, 1999).

Measurements of the unsteady velocity component were then used to estimate the parameters for the spectral model of Mann (1994), $\mathbf{\Phi}(\kappa; L, \alpha\epsilon^{2/3}, \Gamma)$. The two hours preceding the gust were used to construct the longitudinal velocity spectrum, yielding $L \approx 25$ m. The dissipation rate was found by matching the longitudinal component of the spectral tensor by the variance measured by the center beam; i.e.,

$$\int G^2(\kappa_x) \Phi_{uu}(\mathbf{\kappa})\,d\mathbf{\kappa} = \sigma_{u,\text{LOS}}^2, \tag{4.31}$$

where G takes the effect of range-weighting into account. This led to a value of $\alpha\epsilon^{2/3} \approx 0.16$ m$^{4/3}$/s^2. Furthermore, the shear parameter was set to $\Gamma = 3$, which should be appropriate for conditions that are approximately neutral (following Sathe et al., 2013).

---

[12] This value was taken directly from the lidar measurements (i.e., $\sigma_{u,\text{LOS}}/u_{\text{LOS}}$), which underestimates the true value since part of the variance stored in the high frequencies is missing.
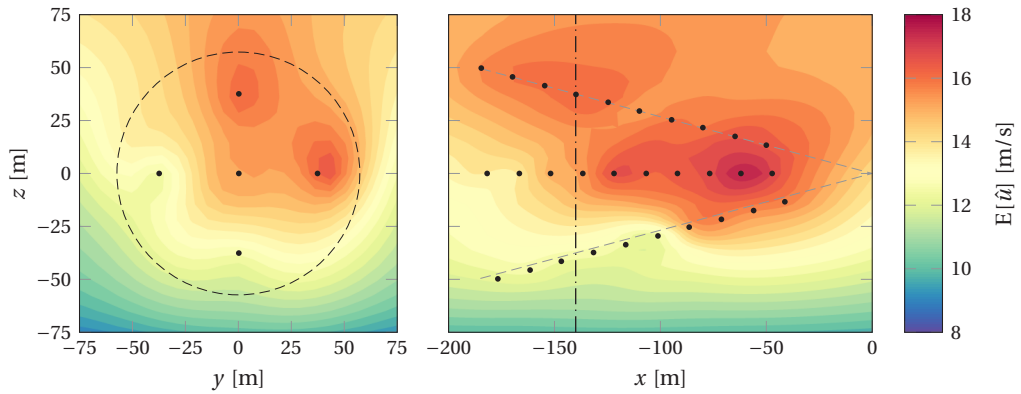
(a): Expected streamwise velocities (u-component) in the yz-plane at $r = -140$ m and in the xz-plane at $y = 0$ m.
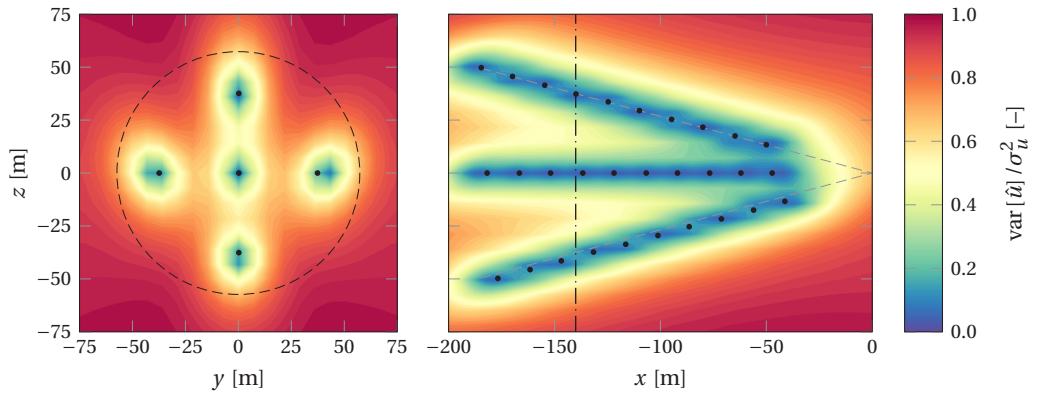
(b): Variances, normalized by the longitudinal variance, in the yz-plane at $r = -140$ m and in the xz-plane at $y = 0$ m.

Figure 4.22: Streamwise velocity fields around a severe gust, reconstructed from one full cycle of lidar measurements ($n = 50$) that was recorded on 22 December 2013. Dots mark the locations $\mathbf{x}_1, \mathbf{x}_2, \dots, \mathbf{x}_n$, including the distance they are expected to have advected during the 1.25 s cycle (see Figure 4.21).

The reconstructed velocity field then looks like Figure 4.22a, showing that the large-scale features of the gust are well-captured by the lidar. In addition, Figure 4.22b indicates how much variation is present between all the possible fields that contain the velocities $u_{\mathrm{LOS},1}, u_{\mathrm{LOS},2}, \dots, u_{\mathrm{LOS},n}$ at positions $\mathbf{x}_1, \mathbf{x}_2, \dots, \mathbf{x}_n$. Essentially, this is the uncertainty present in the lidar forecast. The variance in the reconstructed field ranges from zero, meaning the velocity is known for certain, to σ_u^2, meaning that there is no knowledge but the ten-minute statistics. Of course, the uncertainty grows as one moves further away from the beam locations, depending on the turbulent length scale (the larger the scales present in the flow, the more the measurements are correlated to their surroundings). Still, the uncertainty never reaches absolute zero due to range-weighting.

4.4.3 **Turning lidar measurements into useful control input**

Yet, a big set of measurement points or even a full three-dimensional field is far too much information for a controller to make an easy decision. Therefore, a lidar-assisted control scheme requires a procedure to interpret these velocities and assess the severity of an oncoming threat. One way is to rely on the rate at which momentum is transferred through the yz-plane. This is represented by an along-wind force, F, pushing on a surface, S, perpendicular to the flow at a location r upwind.

For a gust that is carried by the mean wind speed, following Taylor's hypothesis,[13] a momentum balance in streamwise direction dictates that

$$\rho \bar{u} \frac{\partial u}{\partial x} = -\frac{\partial P}{\partial x}, \tag{4.32}$$

where $\partial P / \partial x$ is the streamwise pressure gradient. This can be written as

$$\frac{\partial}{\partial x} \left(\rho \bar{u} u + P \right) = 0, \tag{4.33}$$

leading to Bernoulli's principle:

$$P + \rho \bar{u} u = \text{const}, \tag{4.34}$$

with the constant being the total (stagnation) pressure. Integrating this dynamic pressure term, $\rho \bar{u} u$, then gives

$$F(t; r) = \rho \iint_S \bar{u}(r, y, z) u(r, y, z, t) \, \mathrm{d}y \, \mathrm{d}z. \tag{4.35}$$

The along-wind force represents the *potential* of triggering damaging loads (see Subsection 2.2.5) and can be used to issue a gust warning. Owing to the Gaussian nature of $\hat{u}(\mathbf{x})$, the statistics of $\hat{F}$ are also Gaussian and can be computed analytically:

$$\mathrm{E}\left[\hat{F}(t; r)\right] = \rho \iint_S \bar{u}(r, y, z) \mathrm{E}\left[\hat{u}(r, y, z, t)\right] \mathrm{d}y \, \mathrm{d}z, \tag{4.36}$$

$$\mathrm{var}\left[\hat{F}(t; r)\right] = \rho^2 S \iint_S \bar{u}^2(r, y, z) \mathrm{var}\left[\hat{u}(r, y, z, t)\right] \mathrm{d}y \, \mathrm{d}z. \tag{4.37}$$

A designer can use this to set up a control logic based on avoiding risk. For the situation depicted in Figure 4.22, this results in the time series shown in Figure 4.23. That $\hat{F}$ is Gaussian means that, for example, $\mathrm{E}\left[\hat{F}\right] + 3\sigma_{\hat{F}}$ (i.e., the expectation plus three standard deviations) can be used as a signal to tell the controller that a threat will stay under a certain level with 99.9% certainty. Including the uncertainty in the forecast in this way is very convenient, because it will adjust to the amount of available data points. This gives an indication of what the prediction is worth during periods of low technical availability (or simply when the rotor blades are passing in front of the lidar's eye).

---

[13] This appears to hold for at least the low wave numbers, which contain most of the momentum (Schlipf et al., 2010).
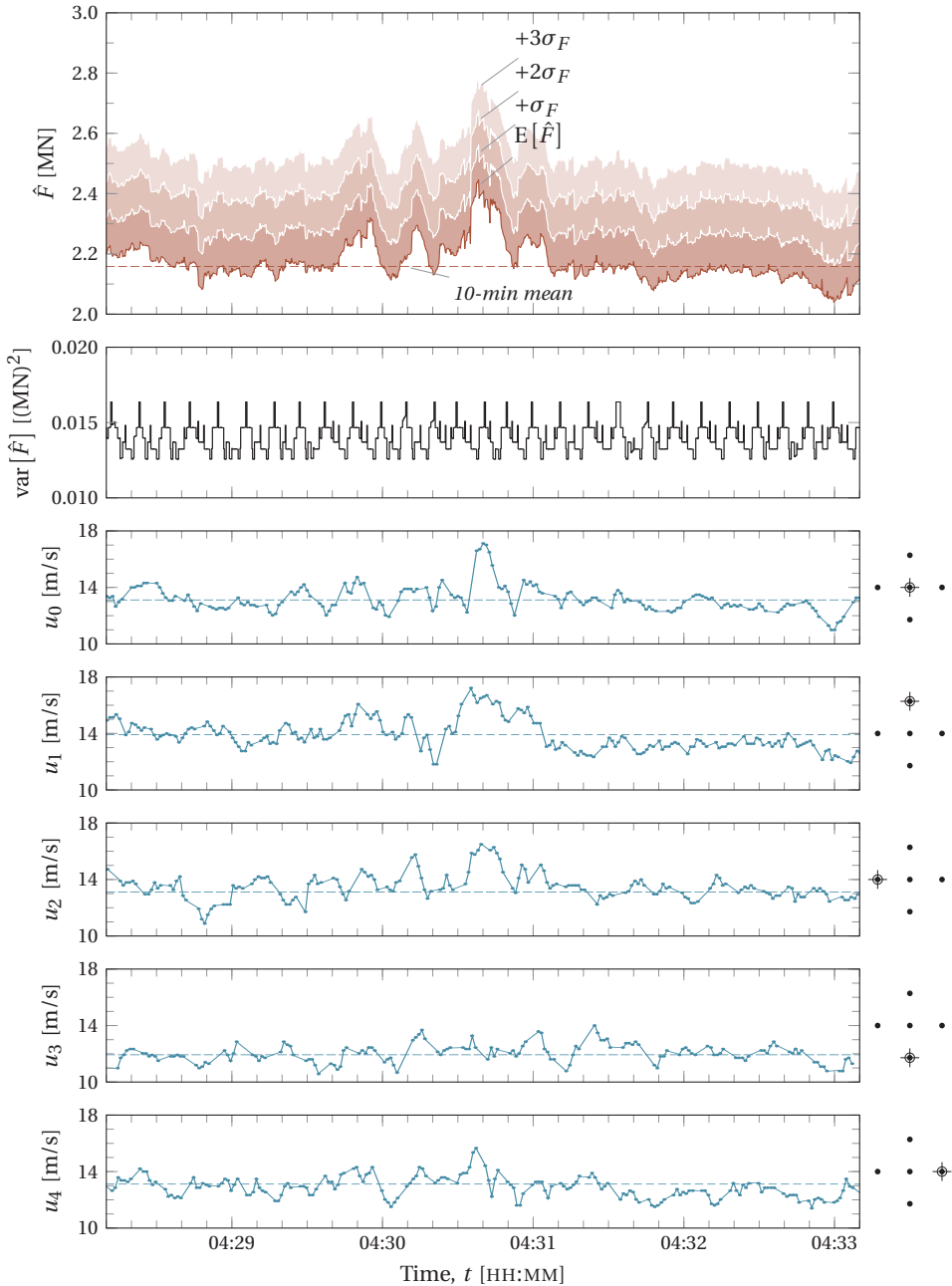
Figure 4.23: Along-wind force and its variance, constructed from five individual velocity signals, $u_0, \dots, u_4$, recorded at 22 December 2014 at the $r = -140$ m range gate (where 0–4 are the beam positions). The time series are centered around a gust event.
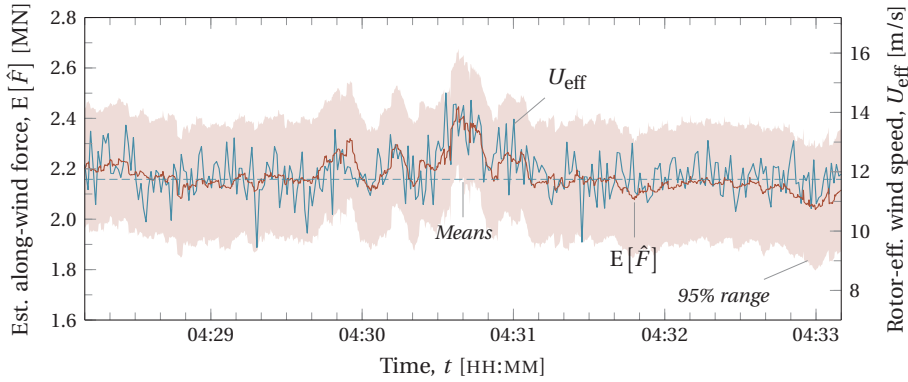
Figure 4.24: The along-wind force forecasted with lidar (in red, including a 10.5-s delay to account for the advection from $r = -140$ m to $r = 0$ m with $\bar{u} = 13.3$ m/s), compared to the rotor-effective wind speed (blue) derived directly from the turbine shaft torque (downsampled to 1 Hz for clarity).

For conventional feedback controllers, similar input signals exist. One in particular is the *rotor-effective wind speed*, which is a pseudo signal derived directly from the shaft torque, Q, and has been demonstrated to improve turbine behavior under gust loading (see Van der Hooft, 2003, 2004). The rotor-effective wind speed, U_{eff}, follows from

$$Q = \tfrac{1}{16}\rho C_Q(\beta,\lambda)\pi D^3 U_{\text{eff}}^2, \tag{4.38}$$

where D is the rotor diameter and C_Q is a (precalculated) dimensionless torque coefficient that depends on the blade pitch angle, β, and tip speed ratio, λ. ECN has supplied this signal from the XD115-5MW machine for the time period of Figure 4.23. Compared to the along-wind force (see Figure 4.24), it clearly shows similar behavior—at least the important low-frequency up- and downcrossings—despite it being disturbed by control actions and noise coming from structural vibrations.

Chapter 5

Predicting extreme gust loads

This chapter features work from the following publications:

Bos R., W. A. A. M. Bierbooms, and G. J. W. van Bussel (2015). "Importance sampling of severe wind gusts." *11th EAWE PhD Seminar on Wind Energy in Europe.* 23–25 September. Stuttgart, Germany.

Bos, R. and H. F. Veldkamp (2016). "A method to find the 50-year extreme load during production." *Journal of Physics: Conference Series* 753, p 42021.

van Eijk, S. F., R. Bos, and W. A. A. M. Bierbooms. "The risks of extreme load extrapolation." *Manuscript submitted for publication.*

*"(...) if the difference between N and N − 1 ever matters
to you, then you are probably up to no good anyway."*

— WILLIAM PRESS et al., *2007*

WIND TURBINES are designed to withstand a load with a 50-year return period, plus safety factors (IEC, 2005b). Yet, determining this load is a challenging task, as it requires the designer to evaluate models with tens of thousands—and preferably millions—of wind fields. This is especially difficult during a conceptual design phase, when the computational resources are scarce and load predictions are often clouded by uncertainty. However, this chapter will show that knowledge of the extreme events present in turbulent wind fields can be used to a designer's advantage.

Section 5.1 discusses some of the fundamentals behind extreme value predictions. Then, Section 5.2 presents two simulation cases that will be used to validate several prediction methods. These methods, the crude Monte Carlo method, importance sampling, and a genetic algorithm, will be explained in Sections 5.3, 5.4, and 5.5, respectively. Section 5.6 compares their accuracy and precision, taking the computational burden into account. Finally, Section 5.7 treats a simple design exercise to show what these results mean in practice.

5.1 Extreme value theory

Extreme value theory focuses on the statistical behaviour of extremes. An extreme value may be defined as the maximum value of a sequence or time series:

$$X_n = \max\{\Xi_1, \Xi_2, \ldots, \Xi_n\},$$

where $\Xi_1, \Xi_2, \ldots, \Xi_n$ is a set of n independent random variables having a common distribution function $F(x)$. The distribution of the maximum, X_n, can be estimated by finding the parent distribution:

$$
\begin{aligned}
\mathrm{P}(X_n \leq x) &= \mathrm{P}(\Xi_1 \leq x \cap \Xi_2 \leq x \cap \ldots \cap \Xi_n \leq x), \\
&= \mathrm{P}(\Xi_1 \leq x)\mathrm{P}(\Xi_2 \leq x) \cdots \mathrm{P}(\Xi_n \leq x), \\
&= [F(x)]^n.
\end{aligned}
\tag{5.1}
$$

However, this has the disadvantage that the distribution fit is sensitive to small variations in the data, which can quickly lead to large errors in F^n.

5.1.1 **Extreme value distributions**

Instead of using the bulk of the data, the preferred approach is to focus on the extremes and directly look for families of F^n. This makes use of the centered normalized maximum, $(X_n - b_n)/a_n$, with the constants $a_n > 0$ and b_n. The possible limit distributions then follow the *extremal types theorem*, *Fisher-Tippett theorem* or *Fisher-Tippett-Gnedenko theorem* (after Fisher and Tippett, 1928; Gnedenko, 1943):

> If a sequence of constants $a_n > 0$, b_n exists such that
> $$\mathrm{P}\left(\frac{X_n - b_n}{a_n} \leq x\right) \to F(x) \text{ as } n \to \infty,$$
> for some non-degenerate distribution function F, then F is a member of one of the following families of *extreme value distributions*:
>
> I: $F(x) = \exp\left[-\exp\left(-\frac{x - b_n}{a_n}\right)\right]$, for $x \in \mathbb{R}$;
>
> II: $F(x) = \begin{cases} 0, & \text{for } x \leq b_n, \\ \exp\left[-\left(\frac{x - b_n}{a_n}\right)^{-\alpha}\right], & \text{for } x > b_n; \end{cases}$
>
> III: $F(x) = \begin{cases} \exp\left[-\left(-\frac{x - b_n}{a_n}\right)^{\alpha}\right], & \text{for } x \leq b_n, \\ 1, & \text{for } x > b_n. \end{cases}$

The three types of distributions—I, II, and III—are the *Gumbel*, *Fréchet* and (reversed)[1] *Weibull* families, respectively. It was shown by Von Mises (1936) and Jenkinson (1955) that these families can be derived from one single distribution function, dubbed the *generalized extreme value distribution* (GEV):

$$F(x) = \exp\left[-\left(1 + \xi\frac{x - \mu}{\sigma}\right)^{-1/\xi}\right], \tag{5.2}$$

with a density function of

$$f(x) = \frac{1}{\sigma}\left(1 + \xi\frac{x - \mu}{\sigma}\right)^{-1/\xi - 1}\exp\left[-\left(1 + \xi\frac{x - \mu}{\sigma}\right)^{-1/\xi}\right], \tag{5.3}$$

for $1 + \xi(x - \mu)/\sigma > 0$. This model relies on three parameters: a location parameter, μ, a scale parameter, σ, and a shape parameter, ξ. The three families of extreme value

---

[1]   The type III distribution is actually a mirror image of the ordinary Weibull family, which can be obtained by substituting $x' = \mu - x$.
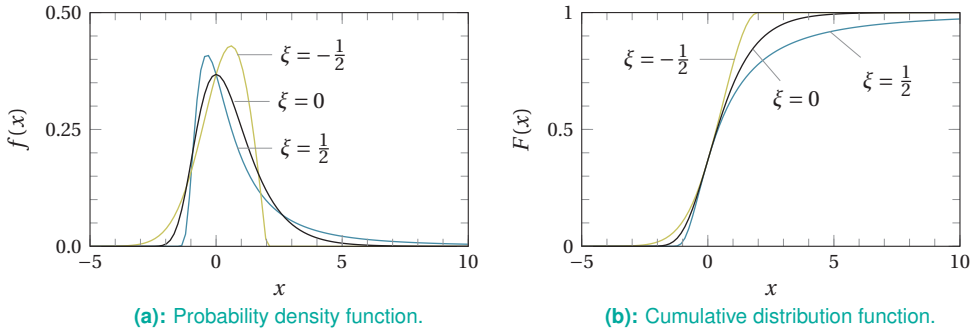
(a): Probability density function.   **(b):** Cumulative distribution function.
Figure 5.1: Families of extreme value distributions ($\mu = 0$, $\sigma = 1$).

distributions can then be derived according to

$$\text{Gumbel } (\xi \to 0): \quad F(x) = \exp\left[-\exp\left(-\frac{x-\mu}{\sigma}\right)\right], \qquad \text{for } x \in \mathbb{R}; \tag{5.4a}$$

$$\text{Fréchet } (\xi > 0): \quad F(x) = \begin{cases} 0, & \text{for } x \leq \mu, \\ \exp\left[-\left(\frac{x-\mu}{\sigma}\right)^{-1/\xi}\right], & \text{for } x > \mu; \end{cases} \tag{5.4b}$$

$$\text{Weibull } (\xi < 0): \quad F(x) = \begin{cases} \exp\left[-\left(-\frac{x-\mu}{\sigma}\right)^{1/\xi}\right], & \text{for } x \leq \mu, \\ 1, & \text{for } x > \mu. \end{cases} \tag{5.4c}$$

Figures 5.1a and b show the differences in shape between the three families. The Gumbel (type I) family is unlimited and is generally used to model the extremes of distributions that have exponentially decreasing tails (e.g., the normal distribution). The Fréchet (type II) family has a lower limit and corresponds to (heavy-tailed) distributions whose tails decrease according to a polynomial (e.g., the t distribution). The reversed Weibull (type III) family has an upper limit and can be used to represent data of a bounded distribution (e.g., the beta distribution).

A way to squeeze more information out of the same data set is to select more than one maximum per block. Say that $X_n^{(k)}$ is the kth largest value of a sequence $\Xi_1,\ldots,\Xi_n$. Then, the above theorem can be extended as follows:

If a sequence of constants $a_n > 0$, b_n exists such that

$$P\left(\frac{X_n - b_n}{a_n} \leq x\right) \to F(x) \text{ as } n \to \infty,$$

for some non-degenerate distribution function F; then, for some k, the limiting distribution of

$$\mathbf{X}_n^{(k)} = \left[\frac{X_n^{(1)} - b_n}{a_n}, \ldots, \frac{X_n^{(k)} - b_n}{a_n}\right]^{\mathsf{T}},$$

has the shape of the joint density function

$$f\left(x^{(1)},\ldots,x^{(k)}\right) = \begin{cases} \exp\left[-\left(1+\xi\dfrac{x^{(k)}-\mu}{\sigma}\right)^{-1/\xi}\right]\cdots \\ \quad\cdots\displaystyle\prod_{i=1}^{k}\dfrac{1}{\sigma}\left(1+\xi\dfrac{x^{(i)}-\mu}{\sigma}\right)^{-1/\xi-1}, \quad\text{for }\xi\neq 0, \\ \exp\left[-\exp\left(-\dfrac{x^{(k)}-\mu}{\sigma}\right)\right]\cdots \\ \quad\cdots\displaystyle\prod_{i=1}^{k}\dfrac{1}{\sigma}\exp\left(-\dfrac{x^{(i)}-\mu}{\sigma}\right), \quad\text{for }\xi = 0, \end{cases} \tag{5.5}$$

for $\mu \in \mathbb{R}$; $\sigma > 0$; $\xi \in \mathbb{R}$; $x^{(k)} \leq x^{(k-1)} \leq \cdots \leq x^{(1)}$ and $1 + \xi\left(x^{(i)} - \mu\right)/\sigma > 0$ for $i = 1,\ldots,k$.

Taking $k = 1$ will then, of course, cause Equation (5.5) to revert back the ordinary generalized extreme value distribution, given by Equation (5.3).

The difficulty with this method is the trade-off between bias and variance. In principle, selecting multiple maxima from a block of data should provide more information to establish the right distribution (i.e., decreasing the uncertainty or variance). However, extremes have the tendency to cluster around a certain event (e.g., a storm), which violates the independence requirement. Therefore, each extreme has to be checked for independence, which is a process that is hard to automate (Lott and Cheng, 2016).

5.1.2 Peak-over-threshold method

Another way of selecting more than one maximum is to only consider values that exceed a certain threshold, A. If $\Xi_1,\ldots,\Xi_n$ is a series of n independent random variables with an underlying distribution function $F(x)$, then there exists a conditional distribution function $F_A(x)$ of the excess value over the threshold A:

$$\begin{aligned} F_A(x') &= P\left(x \leq x' + A \,|\, x > A\right), \\ &= \frac{1 - F(A + x')}{1 - F(A)}, \text{ for } x' > 0. \end{aligned} \tag{5.6}$$

When dealing with extremes, one is of course interested in finding situations where a high threshold value is exceeded. As A increases, the above converges to a limiting distribution according to the *Pickands-Balkema-de Haan theorem* (after Balkema and de Haan, 1974; Pickands, 1975).

Let $\Xi_1,\ldots,\Xi_n$ be a set of n independent random variables having a common distribution function $F(x)$. Then, for some large threshold value, A, the distribution function of $x' = x - A$, conditional on $x > A$, can be approximated according to

$$F_A(x') \to H(x'), \text{ as } A \to \infty,$$

where H is the *generalized Pareto family*:

$$H(x') = \begin{cases} 1 - \left(1 + \dfrac{\xi x'}{\tilde{\sigma}}\right)^{-1/\xi}, & \text{for } \xi \neq 0, \\[2ex] 1 - \exp\left(-\dfrac{x'}{\tilde{\sigma}}\right), & \text{for } \xi = 0, \end{cases} \tag{5.7}$$

provided that $x' \geq 0$ and $\tilde{\sigma} > 0$ when $\xi \geq 0$, and $0 \leq x' \leq -\tilde{\sigma}/\xi$ when $\xi < 0$.[a]

---
[a] The parameter ξ is shared by both the generalized extreme value distribution and the generalized Pareto families.

The peak-over-threshold method is naturally dependent on the threshold value. Low values of A will result in many exceedences—which have to be checked for independence—but will also invalidate the limit of $A \to \infty$ on which the theorem is based. On the other hand, high values of A have the drawback of leaving only few extremes to fit a model to.

5.1.3 Return levels

When studying extremes, one often is interested in finding an extreme with a certain *return period*, T. This value, called the *return level*, z_T, is *expected* to be exceeded once in a period of T and can be found by solving equation (5.2) for the variable x:

$$z_T = \begin{cases} \mu - \dfrac{\sigma}{\xi}\left\{1 - \left[-\ln\left(1 - \dfrac{1}{T}\right)\right]^{-\xi}\right\}, & \text{for } \xi \neq 0, \\[3ex] \mu - \sigma \ln\left[-\ln\left(1 - \dfrac{1}{T}\right)\right], & \text{for } \xi = 0, \end{cases} \tag{5.8}$$

with

$$F(z_T) = 1 - \frac{1}{T}. \tag{5.9}$$

For example, if annual extremes are recorded, the value that is exceeded once every 100 years (on average)[2] is called the *100-year return level* and corresponds to a yearly probability of non-exceedance of $F = 0.99$.

Traditionally, extreme value distributions are plotted on a double logarithmic scale where the probability level is expressed as a *reduced variate*; i.e.,

$$y = -\ln[-\ln(F)]. \tag{5.10}$$

The reason for this is that it reduces the Gumbel distribution to a linear function, which can be drawn by hand on graph paper. However, plotting on a logarithmic or double-logarithmic scale still has other advantages, even with the availability of modern plotting tools. It is a natural way of aggregating the abundant events at the base of the plot and magnifying the tail of the distribution where the high return periods reside (e.g., see Figure 5.2).

---
[2] It does not guarantee that this value is exceeded every 100 years. Such exceedance probabilities can be calculated with the Poisson distribution, given by Equation (2.6).
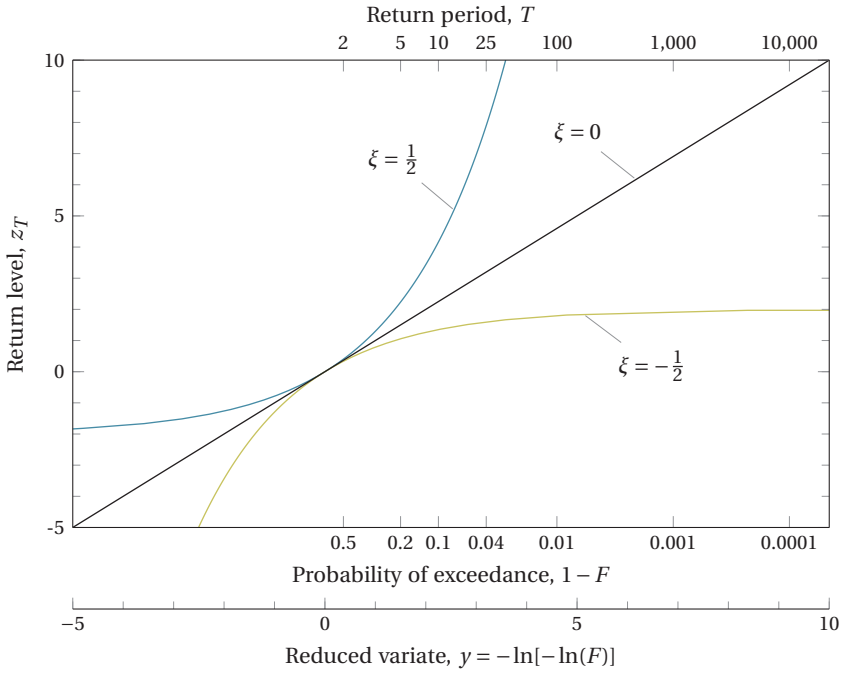
Figure 5.2: Return level plots for families of extreme value distributions ($\mu = 0$, $\sigma = 1$).

Similar to Equation (5.8), the return level for the generalized Pareto families can be expressed as

$$
z_T = \begin{cases} A + \dfrac{\tilde{\sigma}}{\xi}\left[(\lambda_A T)^{\xi} - 1\right], & \text{for } \xi \neq 0, \\[2mm] A + \tilde{\sigma}\ln(\lambda_A T), & \text{for } \xi = 0, \end{cases}
\tag{5.11}
$$

where λ_A is the expected number of threshold exceedances per unit of time.

5.1.4 The empirical distribution

In practice, extremes are extracted from N time series of a fixed length, leading to a set of *block maxima*: $X_1, X_2, \ldots, X_N$. An *empirical distribution function* can then be constructed by ranking its members from low to high (see Figure 5.3):

$$
Z_1 \leq Z_2 \leq \ldots \leq Z_i \ldots \leq Z_N,
$$

and assigning a sample estimate for the non-exceedance probability, $\hat{F}$, to each value: the *plotting position*.

Perhaps the most straightforward non-exceedance probability would be to use the *natural estimator*:

$$
\hat{F}(Z_i) = \frac{i}{N}.
\tag{5.12}
$$

However, this makes it impossible to extrapolate, since $\hat{F} = 1$ is already reserved for the highest value. The alternative is to correct the probability values, and there are several
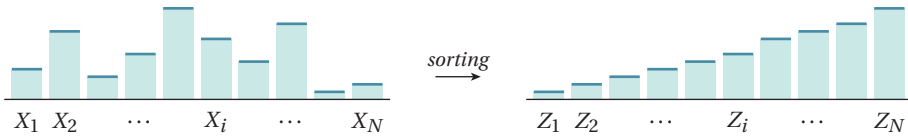
Figure 5.3: A sequence of values $X_1, X_2, \ldots, X_N$ is sorted as $Z_1, Z_2, \ldots, Z_N$.

ways of doing that. One of the most accepted plotting positions (and the one that will be used throughout this chapter) is the one proposed by Weibull (1939):

$$\hat{F}(Z_i) = \frac{i}{N+1}. \tag{5.13}$$

Although it has the appearance of being a primitive solution, it does have a theoretical basis (see Appendix A).

5.1.5 Extrapolation

When the data span a time shorter than the return period, the target return level has to be obtained from extrapolation. The empirical distribution is then matched to an extreme value distribution (e.g., by a least-squares fit) and extended to low probabilities.

The problem with extrapolating is that it magnifies the *sampling error* inherently present in the data; there is always variation between random samples that lead to different predictions. A way to show this is by repeatedly sampling sets of N values from a standard Gumbel distribution ($\mu = 0$, $\sigma = 1$, $\xi = 0$). The distribution of the predicted return levels then follows from the extrapolated values of k sets:

$$
\begin{array}{c}
\textit{rank} \rightarrow \\
\begin{array}{ccccccccc}
Z_{1,1} & \leq & Z_{2,1} & \leq & \ldots & \leq & Z_{N,1} & \rightarrow & \hat{z}_{T,1} \\
Z_{1,2} & \leq & Z_{2,2} & \leq & \ldots & \leq & Z_{N,2} & \rightarrow & \hat{z}_{T,2} \\
\vdots & & \vdots & & & & & & \vdots \\
Z_{1,j} & \leq & Z_{2,j} & \leq & \ldots & \leq & Z_{N,j} & \rightarrow & \hat{z}_{T,j} \\
\vdots & & \vdots & & & & & & \vdots \\
Z_{1,k} & \leq & Z_{2,k} & \leq & \ldots & \leq & Z_{N,k} & \rightarrow & \hat{z}_{T,k} \\
& & & & & & & & \downarrow \\
& & & & & & & & f(\hat{z}_T)
\end{array}
\end{array}
$$

($\downarrow$ set)

The normalized error with respect to the true return level is then

$$\varepsilon = \frac{\hat{z}_T - z_T}{z_T}, \tag{5.14}$$

and its expectation, $\mathrm{E}[\varepsilon]$, describes the bias.

(a): The prediction error decreases as the sample size increases.

(b): The distribution of prediction errors for various sample sizes.
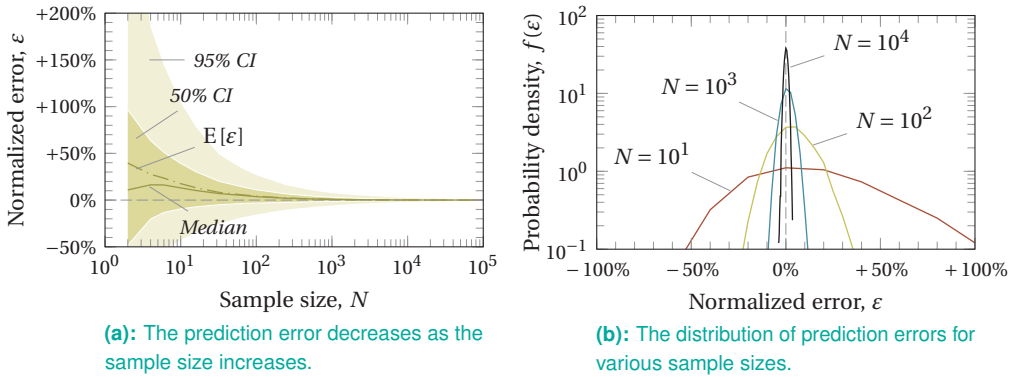
Figure 5.4: Uncertainty surrounding the prediction of the $T = 10,000$ return level—here shown by the bias, median, and confidence intervals (CI)—found by sampling from the standard Gumbel distribution ($\mu = 0$, $\sigma = 1$, $\xi = 0$).

To illustrate, Figure 5.4 shows the $T = 10,000$, which were extrapolated by fitting a straight line with a least-squares method. The uncertainty is considerable for small N and is still considerable when the full return period is covered, owing to the sampling error. In addition, there is an upward bias for small sample sizes that is caused by the fitting method.[3] Also, there are other plotting positions that yield better results for the specific case of Gumbel-distributed extremes.[4] A more extensive discussion of the uncertainty surrounding extrapolation can be found in Van Eijk (2016).

5.2 Wind turbine extremes

Although extreme value theory is a useful tool to predict rare events, it is formally only valid for an isolated process with a single parent distribution. Extreme load distributions of practical applications are, more often than not, mixtures that originate from many different processes. Wind turbines are no exception, as they are subjected to a wide range of atmospheric conditions and adapt their control strategy to the mean wind speed.

5.2.1 Two simulation cases

Extreme loads or extreme deflections of wind turbine components are often obtained by repeatedly simulating time series of a length, ΔT, which is usually ten minutes (see Figure 5.5). The output signals yield a set of N independent maxima that can be sorted and fitted to an extreme value distribution.

Because of the difficulty of finding the 50-year load, Barone et al. (2012) conducted an extensive simulation campaign of which the full dataset was published. This study

---

[3] A least-squares method has a tendency to overpredict, whereas a maximum likelihood method has a tendency to underpredict. That is why engineers are more in favor of using least-squares fitting (Van Gelder, 2000, pp. 82–84).

[4] This does not necessarily mean that Weibull's plotting position is inappropriate. In the past, linearity was often used as a measure for the goodness of fit (Makkonen, 2008), because that made it easier to draw Gumbel diagrams by hand on graph paper. Attempts to improve linearity have lead to the use of modified expressions for $\hat{F}$ that produce better fits under the specific assumption that the data is Gumbel-distributed.
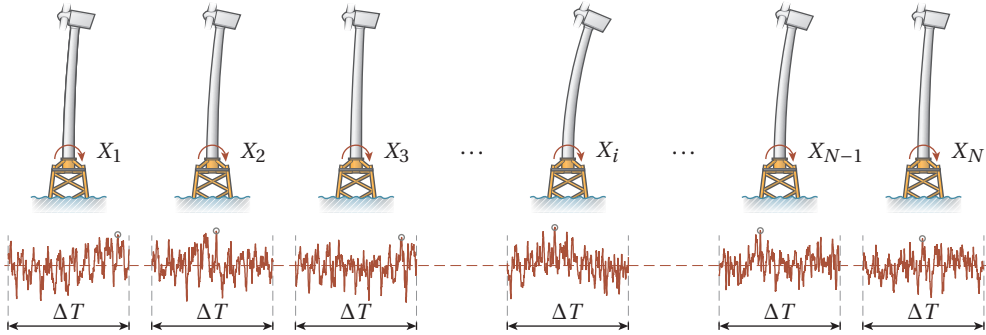
Figure 5.5: A series of extremes, $X_1, X_2, \ldots, X_N$, extracted from time series with length ΔT.

Table 5.1: Most important differences between two sets of extreme load simulations, generated with the NREL 5 MW (Jonkman, Butterfield et al., 2009) and DTU 10 MW reference turbines (Bak et al., 2013).

	NREL 5 MW	DTU 10 MW
IEC wind regime	1B ($\bar{u}_{ave} = 10$ m/s, $I_{ref} = 0.14$)	1A ($\bar{u}_{ave} = 10$ m/s, $I_{ref} = 0.16$)
Rated power	5 MW	10 MW
Rotor diameter	126 m	178 m
Controller	Baseline NREL	Steady speed and pitch
Software used	FAST v7	As described in 4.1.4
Total simulated time	103 years	7.5 years
Number of extremes	$5.4 \cdot 10^6$	$3.9 \cdot 10^5$
Operating wind speeds	$3 \leq \bar{u} \leq 25$ m/s	$4 \leq \bar{u} \leq 25$ m/s
Turbulence spectrum	Kaimal et al. (1972)	Mann (1994)
Frontal grid size	137×137 m (20×20)	269×269 m (64×64)
Time step	0.05 s (20 Hz)	0.25 s (4 Hz)

used the onshore version of the NREL 5 MW reference turbine as a study object, simulated in the FAST v7 aeroelastic code (Jonkman and Buhl, Jr., 2005). The data set contains over 5 million extremes extracted from ten-minute time series for wind speeds between 3 and 25 m/s, totalling about 96 years. For this study, the data set was completed with zero loads to represent idling ($\bar{u} < 3$ m/s) and parked conditions ($\bar{u} > 25$ m/s), increasing the length to 103 years.

As a complementary test case, another 7.5 years of extreme loads were generated for the DTU 10 MW machine using the simplified model explained in Subsection 4.1.4 and the wind climate discussed in Subsection 4.2.1. Compared to the test case of Barone et al. (2012), this simulation set uses a larger rotor with a finer turbulence grid that can incorporate severe wind gusts with more detail. No control action is taken within a ten-minute period to make the results independent of particular controller settings. The two test cases are listed side by side in Table 5.1.

5.2.2 Distribution of the extreme blade root flapwise moment

As in Chapter 4, the remainder of this chapter will focus on the blade root flapwise bending moment, which is characteristic for the loads acting on the rotor blades. The simulated extremes, taken as the maximum over three blades,[5] are shown in Figure 5.6e and f. The clear difference between the two sets is that the extremes of the NREL 5 MW show more scatter. This has partly to do with the number of data points ($5.4 \cdot 10^6$ vs $3.9 \cdot 10^5$), but also with how they are distributed over the mean wind speed.

The extremes of the DTU 10 MW are more tightly packed around the mean, while showing a clear peak at the rated wind speed that can be linked to the point of maximum thrust (see Figure 4.3b). This is because the simplified model of the DTU 10 MW does not allow any control actions within the ten minute period. Therefore, the extremes belonging to wind speeds below the rated wind speed ($\bar{u} < 11.4$ m/s) all correspond to the partial load, variable speed regime, while extremes belonging to $\bar{u} > 11.4$ m/s correspond to the full load, pitch-regulated regime (see Figure 4.3d).

The NREL 5 MW does not show such a clear distinction between control regions, because the controller can react to changing wind speeds within the ten-minute period. For example, when the turbine is operating in a ten-minute mean wind speed of 10 m/s, gusts may push the machine into the pitch-operated control regime, but any extreme load that occurs during a pitch action will still be indexed $\bar{u} = 10$ m/s. Another difference between the two sets is that the active controller of the NREL 5 MW is able to reduce the loads at higher wind speeds, whereas the DTU 10 MW with a steady control experiences increasingly higher loads beyond 16 m/s (also visible in Figure 4.6).

The extreme load distributions in Figures 5.6a and b show a clear bend at a probability level of approximately $\hat{F} = 0.5$. This is different from what is shown in Figure 5.2 and indicates that they are, in fact, mixtures of several distributions. Somewhere in the operating regime, certain processes reside that dominate the extreme load behavior and shape the tail of the distribution. The origin of these processes can be made visible by dividing the extremes into three categories (zero loads, $\hat{F} \leq 0.5$, and $\hat{F} > 0.5$) and tracing

---

[5]   Using the maximum over three blades yields the probability of any of the three blades failing. Alternatively, one can decide to do the analysis per blade, but then a different target failure probability would have to be chosen. If each of the blades is designed to fail once every 50 years, then a three-bladed rotor would, on average, fail every $\frac{1}{1-(1-1/50)^3} = 17$ years.
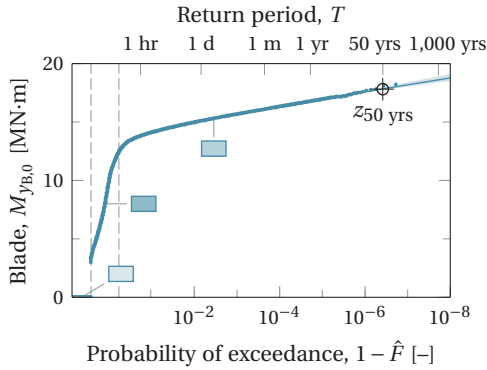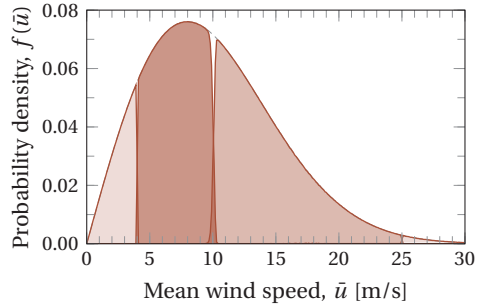
(a): Return level plot of the blade root flapwise bending moment (NREL 5 MW), yielding a 50-year extreme of 17.8 MN·m.
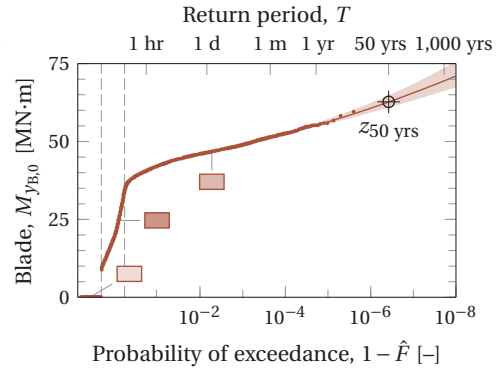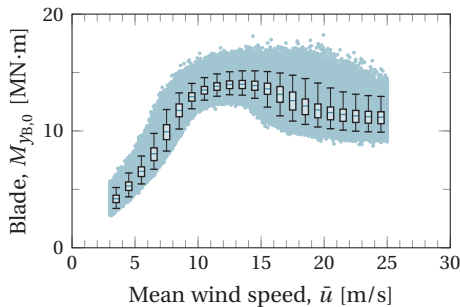
(b): Return level plot of the blade root flapwise bending moment (DTU 10 MW), yielding a 50-year extreme of ≈ 63 MN·m.
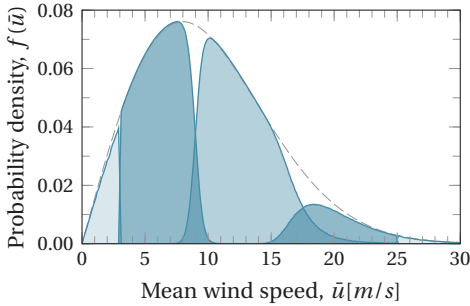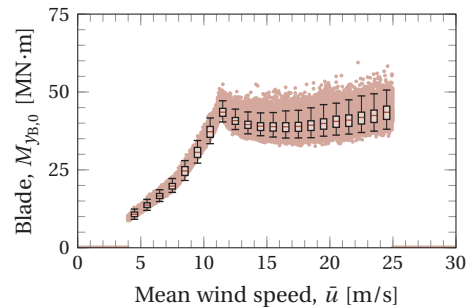
(c): Wind speeds belonging to different parts of the return level plot (NREL 5 MW).

(d): Wind speeds belonging to different parts of the return level plot (DTU 10 MW).

(e): Simulated extremes (NREL 5 MW).

(f): Simulated extremes (DTU 10 MW).

Figure 5.6: Extreme loads and return levels for the blade root flapwise bending moment of the NREL 5 MW and DTU 10 MW reference turbines. The 50-year extreme loads are chosen as the median return level obtained by resampling the data set and fitting an extreme value distribution to the tail, as explained in Subsection 5.3.2. For the box plots, the boxes mark the 25th and 75th percentiles, the whiskers mark the 2.5th and 97.5th percentiles, and the bar is the median.

back the wind speeds, which results in Figures 5.6c and d. In both cases, this reveals that the high return levels originate from certain events occurring in the pitch-regulated control regime.

Fitting an extreme load distribution to the total data set is called "aggregation-before-fitting". The alternative is to fit a separate distribution to a number of wind speed bins, called "fitting-before-aggregation", which is briefly treated in Appendix B.

5.3 Monte Carlo simulation of extreme loads

The return levels in the previous section were obtained by a Monte Carlo method, where the extreme load behavior is found by repeatedly sampling ten-minute time series.

5.3.1 Basics

One approach is to directly sample the parameters from their parent distribution, $f(\boldsymbol{\theta})$. The crude Monte Carlo method relies on brute force and the load distribution follows naturally from ranking the extremes and assigning an appropriate plotting position (see Subsection 5.1.4):

$$\hat{F}(x) = \frac{1}{N+1} \sum_{i=1}^{N} \mathbf{1}(X_i \le x), \tag{5.15}$$

where

$$\mathbf{1}(x \in S) = \begin{cases} 1, & \text{if } x \in S, \\ 0, & \text{if } x \notin S, \end{cases} \tag{5.16}$$

is the indicator function. In essence, the crude Monte Carlo method directly mimics real life. In order to obtain a set of N ten-minute extreme loads, N randomized ten-minute wind fields have to be generated and fed to an aeroelastic code. The general workflow is sketched in Figure 5.7.
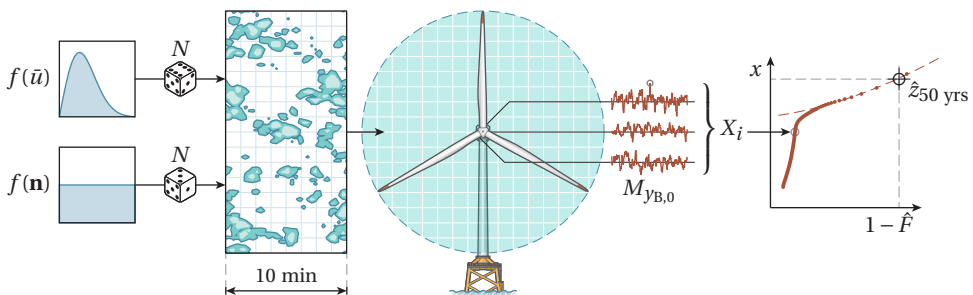
Figure 5.7: Workflow of a crude Monte Carlo method, where N ten-minute extreme loads are calculated by brute force. Randomized turbulent wind fields are generated from the parent mean wind speed distribution, $f(\bar{u})$, and fed to an aeroelastic code to yield the bending moments. The resulting loads are sorted and translated to an extreme load distribution, from where the 50-year return level can be derived.
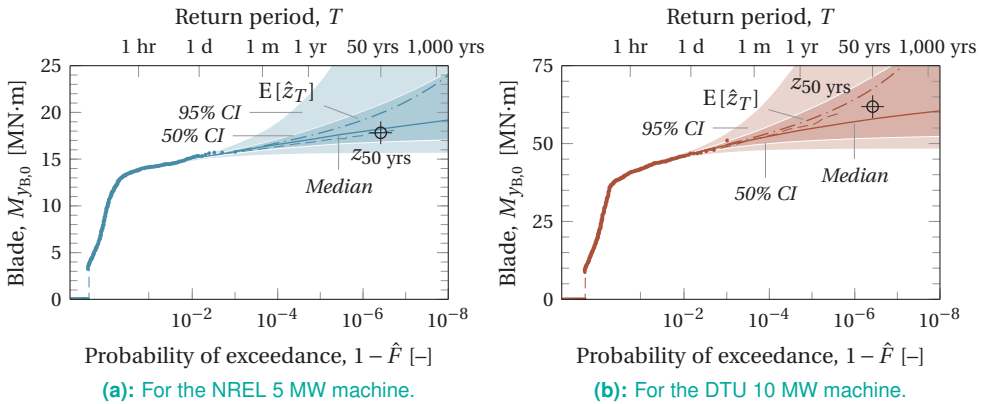
(a): For the NREL 5 MW machine.   **(b):** For the DTU 10 MW machine.

Figure 5.8: Examples of distribution fits to the tails of the empirical extreme load distribution, resulting from a sample size of $N = 1{,}000$ ten-minute wind fields ($\sim$ 1 week). The means, medians, and confidence intervals (CI) were obtained as explained in Subsection 5.1.5. The dashed lines indicate the complete, 103- and 7.5-year data sets. The dot markers belong to an abitrary sample.

5.3.2 Uncertainty induced by extrapolation

Perhaps not surprising when judging by its name, the crude Monte Carlo method is not very efficient; about $2.6 \cdot 10^6$ maxima have to be extracted from ten-minute time series to reach the 50-year return level (i.e., $1 - F = 3.8 \cdot 10^{-7}$). That is why, more often than not, a designer has to resort to extrapolation.

Following the shape of the extreme load distribution (see Figures 5.6a and b), extrapolation is best done by fitting an extreme value distribution to the relevant upper percentiles of the data. This produces a model of the dominant process that is responsible for the high return levels. However, fitting the tail of the extreme load distribution is not completely straightforward. Because of the plotting position formula, the start of the tail depends on the sample size. Moreover, the bend in the distribution can be very gradual for large sample sizes, which makes it difficult to completely separate the different extreme load processes.

The quality of the fit can be improved by varying the assumed starting position of the tail with sample size or by using a weighted fitting method; however, both solutions add a degree of subjectivity. A simple empirical solution that seems to work for most sample sizes is to assume that the tail covers the second half of the distribution when drawn on Gumbel paper:

$$ -\ln[-\ln(\hat{F})] > -\tfrac{1}{2} \ln\left[-\ln\left(\frac{1}{N+1}\right)\right] - \tfrac{1}{2} \ln\left[-\ln\left(\frac{N}{N+1}\right)\right]. \tag{5.17} $$

Some examples of fits applied to the NREL 5 MW and DTU 10 MW data sets are shown in Figures 5.8a and b.

Extrapolating crude Monte Carlo results produces unreliable predictions, mainly because of the sampling error associated with the ten-minute extremes (see Figures 5.6e and f). In addition, the extrapolation process itself produces more uncertainty than straightforward sampling from a Gumbel distribution would (comparing Figure 5.9 to Figure 5.4). This is due to the sheer distance to the 50-year probability level, but also
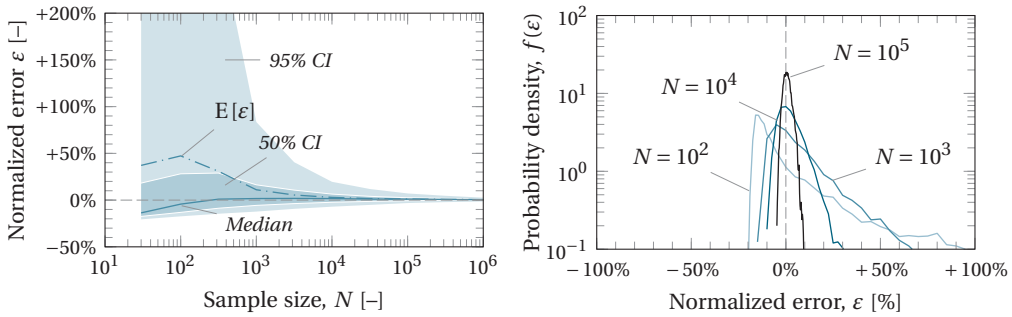
(a): The decrease of uncertainty with increasing sample size.

(b): The distribution of prediction errors for various sample sizes.

Figure 5.9: Uncertainty surrounding the 50-year blade root flapwise bending moment of the NREL 5 MW reference turbine, found by resampling.

due to the additional shape parameter, ξ, which turns the GEV distribution function to either a Gumbel, Fréchet, or a reversed Weibull distribution. For the case of the NREL 5 MW, the tail has a downward slope that fits a GEV distribution with a slightly negative ξ. However, this parameter is often overestimated for small sample sizes and large positive values of ξ can sometimes lead to severe overpredictions. This is also why the median is a much better measure of the accuracy of a method than the mean. For very small sample sizes ($N < 100$), something peculiar happens: the tail has so few data points that it often matches best with a straight line ($\xi \approx 0$), which is a safer estimate that results in a lower bias and a lower overall uncertainty.

5.3.3 The curse of dimensionality

The wind turbine design problem may be kept relatively confined by assuming that the extreme loads are influenced by only a few variables. This is definitely the case with the IEC (2005b) design standard, which only prescribes a conservative wind climate with little variation in operational conditions.[6] In a real-life situation, however, more factors affect the 50-year load; for example, variations in wind direction, turbulence intensity, and atmospheric stability (not to mention the sea state when designing offshore foundations).

Neglecting atmospheric stability has already been shown to have an impact on fatigue loads. In a study by Holtslag (2016, pp. 96–97), following the IEC standards led to a 27.6% overestimation of the equivalent tower base fore-aft moment compared to actual offshore conditions. With the introduction of only one new stability parameter, however, the problem gained a dimension in complexity, which increased the computational burden by a factor 34.

This effect is referred to as the *curse of dimensionality*. If a design problem requires 10 function evaluations for one variable, then adding a second variable will require 10^2 points, a third variable 10^3 points, a fourth variable 10^4 points, etc. Although Monte Carlo methods are often regarded as the solution to this, they cannot fully escape it. The search for extreme loads is already very expensive in one dimension because of the sampling

---

[6]   Some would say being conservative is the purpose of a design standard. However, the question is when this starts to harm the economic viability of wind energy.

error associated with ten-minute extremes. Increasing the number of variables inevitably means that the computational resources will have to be divided over an exponentially growing parameter space, causing high uncertainty. The only way to cope with this is to devise a way to limit the sampling space or by using a smart way to search for extreme loads. For the latter, two methods will be presented in the following sections.

5.4 Importance sampling

When simply drawing from the parent distribution, there is a danger that much computational effort is wasted in evaluating uninteresting events. A simulation budget can be used more efficiently by putting weight on situations where extreme loads of a certain return period are more likely to occur. Such an approach is called *importance sampling*.

(a): Role of the likelihood ratio.

(b): Fraction of the load distribution that has to be corrected when the support of the sampling distribution does not match that of the parent distribution.
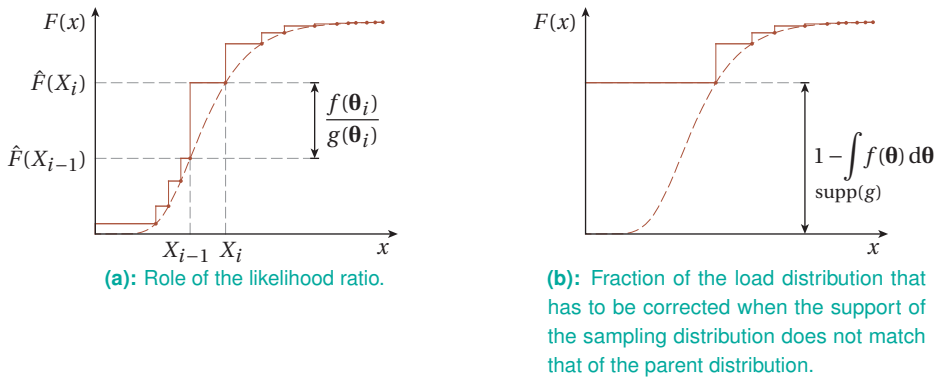
Figure 5.10: Construction of an empirical load distribution, $\hat{F}(x)$, by importance sampling.
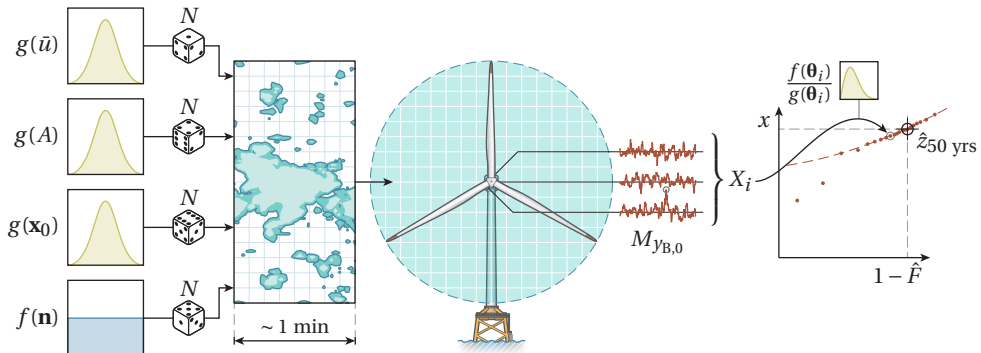
Figure 5.11: Workflow of an importance sampling method. Instead of being completely random, each wind field contains a severe gust, following the method explained in Section 3.3. These gusts are defined by a set of k parameters (e.g., amplitude, A, position, $\mathbf{x}_0$, etc.), drawn from sampling distributions that are set up in such a way that they have a high probability of triggering high loads. The 50-year load can be derived from a weighted distribution, where each extreme load is weighted by the *likelihood ratio*, $f(\boldsymbol{\theta})/g(\boldsymbol{\theta})$.

5.4.1 **Basics**

With some prior knowledge, a designer can sample the parameters from a sampling distribution, $g(\boldsymbol{\theta})$, such that a load distribution follows from

$$\hat{F}(x) = \frac{\sum\limits_{i=1}^{N} \mathbf{1}(X_i \le x) \dfrac{f(\boldsymbol{\theta}_i)}{g(\boldsymbol{\theta}_i)}}{\sum\limits_{i=1}^{N} \dfrac{f(\boldsymbol{\theta}_i)}{g(\boldsymbol{\theta}_i)}}, \tag{5.18}$$

where each point is weighted by a *likelihood ratio*, $f(\boldsymbol{\theta})/g(\boldsymbol{\theta})$. The likelihood ratio represents the contribution that each point has to the load distribution. When a sampling distribution is focused on rare events, the common events are weighted relatively more to make up for the part of $\hat{F}(x)$ that they are supposed to cover (see Figure 5.10a).

In principle, the sampling distribution, $g(\boldsymbol{\theta})$, can be any function, but it needs to have at least the same support as $f(\boldsymbol{\theta})$. If this is not the case, part of the parameter space is missing and the results will be biased. In some cases, however, a designer may already know for certain that some parts of the parameter space are of no interest (e.g., below the cut-in wind speed). The bias can then be avoided by correcting the load distribution:

$$\hat{F}(x) = 1 - \left[1 - \frac{\sum\limits_{i=1}^{N} \mathbf{1}(X_i \le x) \dfrac{f(\boldsymbol{\theta}_i)}{g(\boldsymbol{\theta}_i)}}{\sum\limits_{i=1}^{N} \dfrac{f(\boldsymbol{\theta}_i)}{g(\boldsymbol{\theta}_i)}} \right] \int\limits_{\mathrm{supp}(g)} f(\boldsymbol{\theta}) \, \mathrm{d}\boldsymbol{\theta}, \tag{5.19}$$

where $\mathrm{supp}(g)$ denotes the support of $g(\boldsymbol{\theta})$. The effect is sketched in Figure 5.10b.

Importance sampling can be very effective if a designer has some information on what conditions are associated with the 50-year load. One can imagine that, apart from high wind speeds, extreme loads often follow from unusual events within the wind field (i.e., severe gusts). With the method set up in Section 3.3, it is possible for a designer to generate such events within very short time series (e.g., ~ 1 min). Since the sampling distributions represent the effort that go into running certain load cases, a good setup means that computational resources can be spent more efficiently. This significantly reduces the uncertainty in the 50-year load, or equivalently means that far fewer simulations are required for the same quality result. The workflow of importance sampling is sketched in Figure 5.11.

5.4.2 **Sampling operating wind speeds**

A simple example that demonstrates the power of importance sampling is to resample the data from the NREL 5 MW machine with four different sampling distributions:

1. A uniform distribution, $g_1(\bar{u})$, which assigns equal probability to every wind speed between $\bar{u} = 3$ and 25 m/s (i.e., the cut-in and cut-out wind speeds).

2. A cut-off version of the parent distribution, $g_2(\bar{u})$, with the idea that wind speeds under $\bar{u} = 8$ and above 25 m/s are irrelevant (see Figure 5.6c).

3. A normal distribution, $g_3(\bar{u})$, centered on $\bar{u} = 20$ m/s and with a standard deviation of 2 m/s.

4. A distribution, $g_4(\bar{u})$, obtained from exactly tracing back the wind speeds belonging to return periods higher than 1 year. This was done by using the full data set and finding the data points associated with $1 - F \leq 1.9 \cdot 10^{-5}$.

The first three distributions have analytical expressions given by

$$g_1(\bar{u}) = \begin{cases} \frac{1}{22}, & \text{for } \bar{u} \in [3, 25] \text{ m/s, ,} \\ 0, & \text{otherwise;} \end{cases} \tag{5.20a}$$

$$g_2(\bar{u}) = \begin{cases} \dfrac{\dfrac{\pi \bar{u}}{2\bar{u}_{\text{ave}}^2} \exp\left(-\dfrac{\pi \bar{u}^2}{4\bar{u}_{\text{ave}}^2}\right)}{\exp\left(-\dfrac{\pi \cdot 8^2}{4\bar{u}_{\text{ave}}^2}\right) - \exp\left(-\dfrac{\pi \cdot 25^2}{4\bar{u}_{\text{ave}}^2}\right)}, & \text{for } \bar{u} \in [8, 25] \text{ m/s, ,} \\ 0, & \text{otherwise;} \end{cases} \tag{5.20b}$$

$$g_3(\bar{u}) = \frac{1}{2\sqrt{2\pi}} \exp\left[-\frac{(\bar{u} - 20)^2}{2 \cdot 2^2}\right]. \tag{5.20c}$$

The resulting extreme load distributions are shown in Figure 5.12. Return levels that lie in between the samples are obtained by interpolation. The ones beyond are extrapolated with a least-squares-fit extreme value distribution.

In most cases, importance sampling offers an improvement over the crude Monte Carlo method with less uncertainty around the 50-year load. Although the sampling distributions g_3 and g_4 are the most sophisticated ones, they perform worse than g_1 and g_2, because they do not fit the lower tail region well enough. The most extreme loads are clearly found at these wind speeds, when judging from Figure 5.9e, but a sample size of $N = 1,000$ is not enough to capture the right extreme load behavior. This can be remedied by increasing the sample size (and the computational burden), or by finding another way to sample loads more effectively.

5.4.3 Sampling point gusts

When looking at the large spread in Figures 5.6e and f, it becomes clear that the extreme loads cannot be solely dependent on the mean wind speed. In most cases, peak loads can be traced to certain events happening inside the wind field. For the case of the NREL 5 MW turbine, the extreme loads can be connected to instances where the wind speed takes a suddden drop and then quickly recovers, tricking the pitch controller into increasing the thrust (see Figure 5.13).[7]

Similar events can be recreated by generating conditionally random wind fields, containing a strong local velocity minimum (or maximum), as explained in Section 3.3. The probability associated with such events can be approximated with the Euler characteristic heuristic (see Subsection 3.4.2):

$$P\left(p'(\mathbf{x}; t_0, V) = \rho \operatorname{vol}(V) A\right) \approx -\frac{d}{dA} E\left[\chi\left(\mathbf{x} \in B : p'(\mathbf{x}; t_0, V) \geq \rho \operatorname{vol}(V) A\right)\right], \tag{5.21}$$

where the expected Euler characteristic, $E[\chi]$, is given by Equation (3.95).

---

[7] This type of behavior is normally prevented by a nonlinear gust controller, but this was missing in the baseline NREL controller used by Barone et al. (2012).
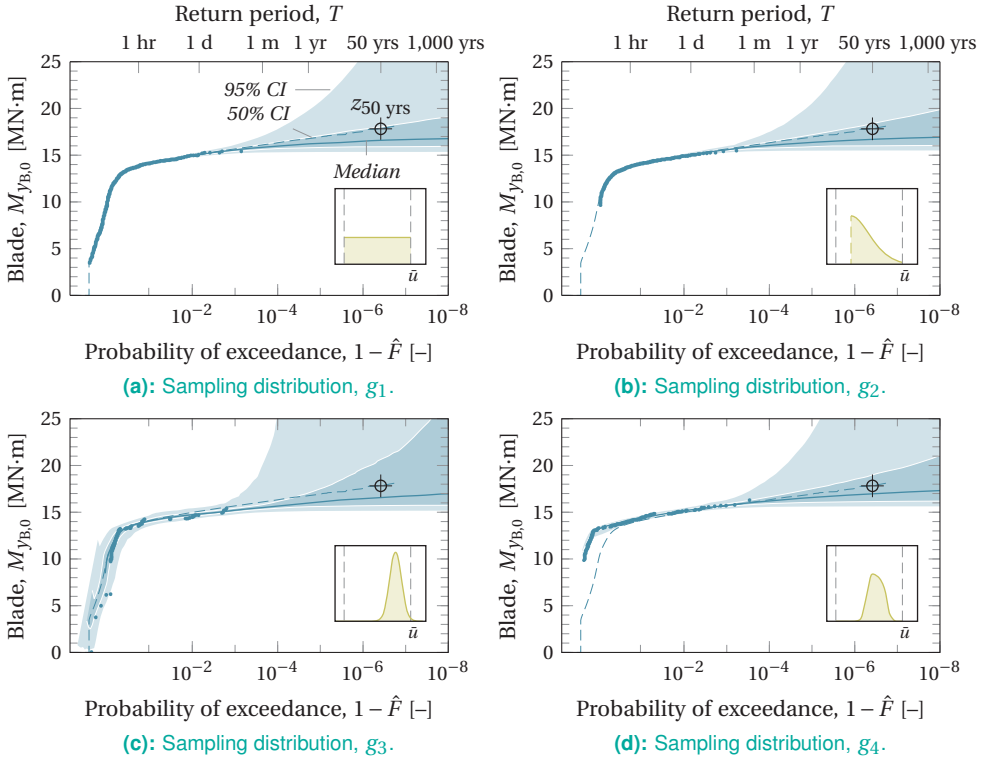
Figure 5.12: Extreme load predictions for the NREL 5 MW turbine, constructed by importance sampling of mean wind speeds, based on $N = 1,000$ ten-minute wind fields ($\sim$ 1 week). The dashed line indicates the complete, 103-year data set. The dot markers belong to an abitrary sample.

In this first example, the events are limited to point gusts (i.e., $\text{vol}(V) = 0$, which excite a single grid point) that are placed randomly in the yz-plane.[8] Figure 5.14 shows the extreme flapwise bending moments above a 14 MN·m threshold, obtained from uniformly sampling $N = 50,000$ events from the two-dimensional parameter space bounded by $\bar{u} \in [0, 30]$ m/s, $A/\sqrt{\Lambda_0} \in [-10, 10]$. The results confirm that the highest loads are found well above the rated wind speed and for strongly negative gust amplitudes. This also explains the shape of the scatter plot in Figure 5.6e.

With the location of the highest loads inside the parameter space, a sampling distribution is set up: a bivariate normal distribution, centered on a normalized amplitude of $A/\sqrt{\Lambda_0} = -7$ and a mean wind speed of 20 m/s. In addition, a uniform distribution is

---

[8] With the grid spacing used for the NREL 5 MW, the gusts are actually generated based on a size of $\ell_y = \ell_z = \Delta y \approx 7$ m, $\tau = \Delta t = 0.05$ s.

Streamwise (turbulent) wind speed, u' [m/s]

(a): The streamwise component of the fluctuating wind speed in the plane through $y = 0$ m.

(b): The blade root flapwise bending moments of all three blades.

(c): The collective blade pitch angle.

(d): The rotor speed.
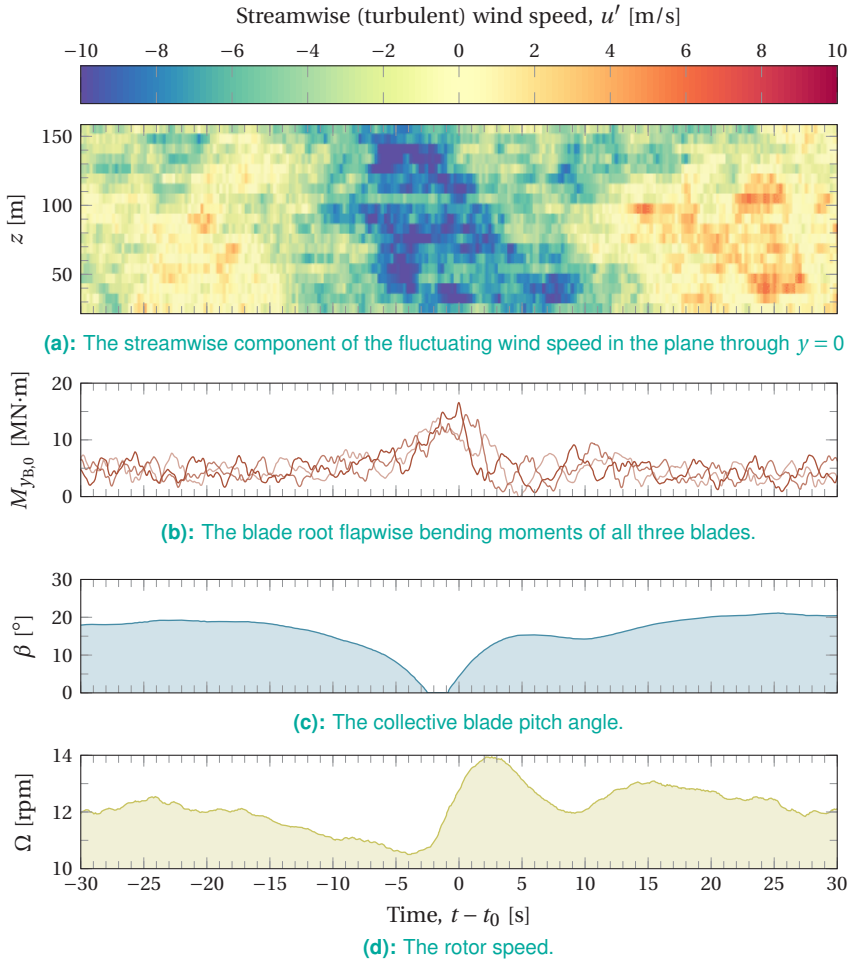
Figure 5.13: Example of a sudden drop in wind speed that triggers an extreme blade root flapwise bending moment for the NREL 5 MW turbine (operating at $\bar{u} = 19$ m/s).

added for reference:

$$g_5(\bar{u}, A) = \begin{cases} \frac{1}{440}, & \text{for } \bar{u} \in [3, 25] \text{ m/s}, \; A/\sqrt{\Lambda_0} \in [-10, 10], \\ 0, & \text{otherwise;} \end{cases} \tag{5.22a}$$

$$g_6(\bar{u}, A) = \frac{1}{2\pi \cdot 2 \cdot 0.5} \exp\left[-\frac{(\bar{u} - 20)^2}{2 \cdot 2^2} - \frac{(A/\sqrt{\Lambda_0} + 7)^2}{2 \cdot 0.5^2} \right]. \tag{5.22b}$$

The resulting distributions are shown in Figures 5.15a and b. As in the previous exercise, wind fields sampled from the uniform distribution do not trigger the relevant loads. Moreover, the 50-year load is now also underpredicted. This is because each gust is embedded into a short, one-minute wind field. Therefore, if a gust is not able to trigger a relevant load, all the wind field can produce is a one-minute extreme load.
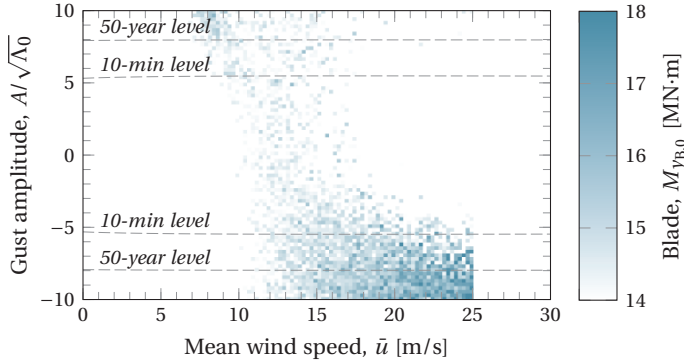
Figure 5.14: Extreme blade root flapwise bending moments triggered by 50,000 point gusts for the NREL 5 MW (where, for zero volume, $\Lambda_0 = \sigma_u^2$).
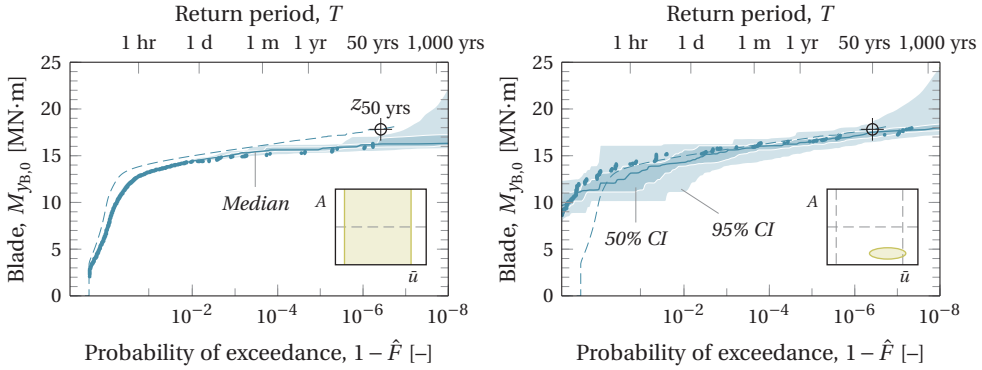
(a): Sampling distribution, g_5.

(b): Sampling distribution, g_6.

Figure 5.15: Extreme load predictions for the NREL 5 MW turbine constructed by importance sampling of point gusts, embedded in $N = 10,000$ one-minute wind fields ($\sim$ 1 week). The dashed line indicates the complete, 103-year data set. The dot markers belong to an abitrary sample.
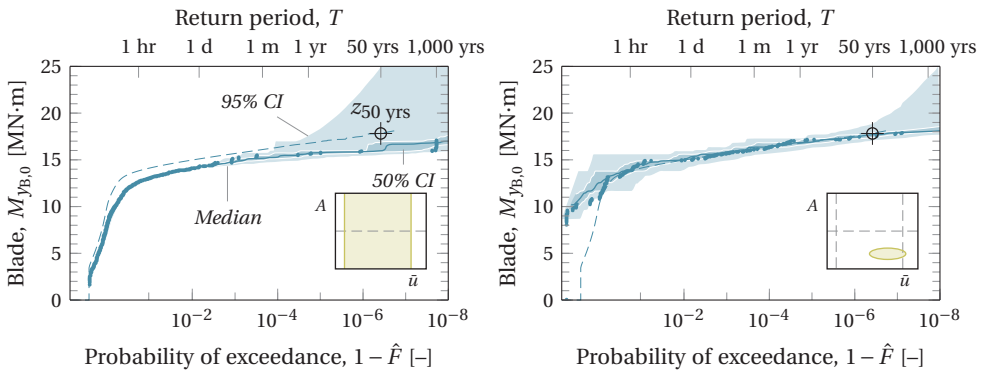
(a): Sampling distribution, g_7.

(b): Sampling distribution, g_8.

Figure 5.16: Extreme load predictions for the NREL 5 MW turbine constructed by importance sampling of spheroidal gusts, embedded in $N = 10,000$ one-minute wind fields ($\sim$ 1 week). The dashed line indicates the complete, 103-year data set. The dot markers belong to an abitrary sample.
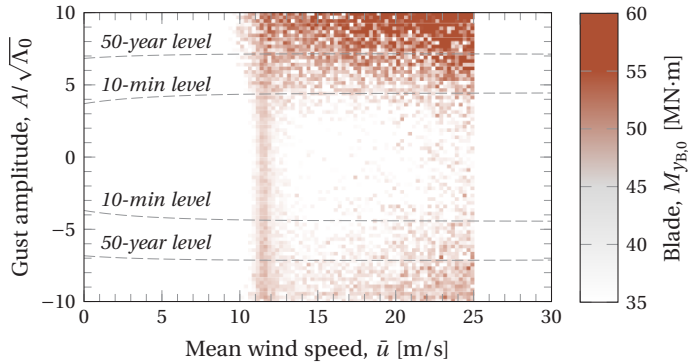
Figure 5.17: Extreme blade root flapwise bending moments triggered by 50,000 spheroidal gusts for the DTU 10 MW ($\ell_y = \ell_z = 25$ m, $\tau = 2$ s).

The sampling distribution g_6 yields more accurate results. Compared to the uniform distribution, the data points are placed further towards low probabilities, which is also visible by the way the uncertainty decreases halfway the tail of the distribution. The distribution g_6 is able to reduce the 95% confidence interval around the 50-year load considerably—from [15.6, 35.4] to [16.4, 18.6] MN·m—when compared to the crude Monte Carlo method.

5.4.4 Sampling of volumetric gusts

One way of improving the results of the importance sampling method is to increase the volume of the generated gusts. This increases their momentum content, which should make it easier to trigger higher loads. In this subsection, the same gusts are used as in Chapter 4, having a spheroidal volume with lateral length scales of $\ell_y = \ell_z = 25$ m and a Lagrangian time scale of $\tau = 2$ s.

Figures 5.16a and b show the return level plots constructed with a uniform and a normal sampling distribution:

$$g_7(\bar{u}, A) = \begin{cases} \frac{1}{440}, & \text{for } \bar{u} \in [3, 25] \text{ m/s}, \, A/\sqrt{\Lambda_0} \in [-10, 10], \\ 0, & \text{otherwise;} \end{cases} \tag{5.23a}$$

$$g_8(\bar{u}, A) = \frac{1}{2\pi \cdot 2 \cdot 0.5} \exp\left[-\frac{(\bar{u} - 20)^2}{2 \cdot 2^2} - \frac{(A/\sqrt{\Lambda_0} + 6)^2}{2 \cdot 0.5^2} \right]; \tag{5.23b}$$

where the normal distribution is now centered on $A/\sqrt{\Lambda_0} = -6$ to account for the smaller spectral moments caused by filtering. Compared to Figures 5.15a and b, the loads from each gust now end up slightly higher in the tail of the extreme load distribution. As a result, the uncertainty reduces closer to the 50-year probability. For the sampling distribution g_8, the 95% confidence interval around the 50-year load is now [17.0, 18.8] MN·m, which is a significant reduction compared to when point gusts are used.

With the DTU 10 MW data set, which was generated with wind fields on a 64×64 grid, it is possible to look into gusts in more detail. Figure 5.17 shows the extreme blade root flapwise bending moments for this turbine above a 35-MN·m threshold. Clearly, the absence of a controller leads to a totally different response than found in Figure 5.14.

Local maxima are found all along the rated wind speed. However, the highest loads are found at higher wind speeds, due to the prescribed increase in turbulence intensity (see Equation (4.15)) and because the simplified turbine model does not have a controller.

The previous exercise can be repeated with similar sampling distributions. In Figure 5.18, the following six distributions are used:

$$g9(\bar{u}) = \begin{cases} \frac{1}{21}, & \text{for } \bar{u} \in [4, 25] \text{ m/s}, \\ 0, & \text{otherwise}; \end{cases} \tag{5.24a}$$

$$g_{10}(\bar{u}) = \frac{1}{2\sqrt{2\pi}} \exp\left[-\frac{(\bar{u}-20)^2}{2 \cdot 2^2}\right]; \tag{5.24b}$$

$$g_{11}(\bar{u}, A) = \begin{cases} \frac{1}{420}, & \text{for } \bar{u} \in [4, 25] \text{ m/s}, A/\sqrt{\Lambda_0} \in [-10, 10], \\ 0, & \text{otherwise}; \end{cases} \tag{5.24c}$$

$$g_{12}(\bar{u}, A) = \frac{1}{2\pi \cdot 2 \cdot 0.5} \exp\left[-\frac{(\bar{u}-20)^2}{2 \cdot 2^2} - \frac{(A/\sqrt{\Lambda_0}+6)^2}{2 \cdot 0.5^2}\right]; \tag{5.24d}$$

$$g_{13}(\bar{u}, A, y_0, z_0) = \begin{cases} \dfrac{g_8(\bar{u}, A)}{8L \cdot 4L}, & \text{for } z_0 > H, \\ 0, & \text{otherwise}; \end{cases} \tag{5.24e}$$

$$g_{14}(\bar{u}, A, y_0, z_0) = \begin{cases} \dfrac{g_8(\bar{u}, A)}{\frac{1}{2}\pi\left[R^2 - (0.4R)^2\right]}, & \text{for } 0.4R \le r_0 \le R, z_0 > H, \\ 0, & \text{otherwise}; \end{cases} \tag{5.24f}$$

where $r_0 = \sqrt{y_0^2 + (z_0 - H)^2}$ is the gust's radial position with respect to the rotor. The first sampling distribution, g_9, is a simple uniform distribution where the mean wind speed is confined to the operating range of the DTU 10 MW machine. This is further refined with g_{10}, which is a normal distribution centered on the high-load region in Figure 5.6f. The sampling distribution g_{11} is a copy of g_9, but includes gusts with amplitudes up to $|A|/\sqrt{\Lambda_0} = 10$. Then, g_{12} is a joint normal distribution that focuses the computational effort on the area around $\bar{u} = 20$ m/s and gusts that have a return period of approximately 1 year. Another distribution, g_{13}, introduces a constraint on the gust position. It follows the same shape as g_{12}, but limits the vertical gust position to above the hub. The distribution g_{14} refines this further and positions the gusts between 40 and 100% blade span, the area that according to Figure 4.17a should be where the highest loads are found.

The results are shown in Figure 5.18. Overall, the quality of the predictions improves as more variables are involved and as the sampling distributions narrow down to the region of interest. Compared to the volumetric gusts that were used with the NREL 5 MW machine, the uncertainty levels are comparable when the gust position is left unconstrained (i.e., comparing Figures 5.16b and 5.18d). In that case, the 95% confidence interval around the 50-year extreme load is reduced from [48.2, 125.8] to [57.8, 62.4] MN·m when compared to the crude Monte Carlo. The best results are obtained when the gust

position is narrowed to the arc of g_{14}, producing a narrow 95% confidence interval of [60.8, 63.7] MN·m.

Evidently, importance sampling is able to achieve significant improvements in accuracy. The further the sampling distribution is narrowed down to the region of interest, the lower the uncertainty. Though, this is assuming that the designer knows where this region of interest lies.

(a): Sampling distribution, g_9.

(b): Sampling distribution, g_{10}.

(c): Sampling distribution, g_{11}.

(d): Sampling distribution, g_{12}.

(e): Sampling distribution, g_{13}.

(f): Sampling distribution, g_{14}.
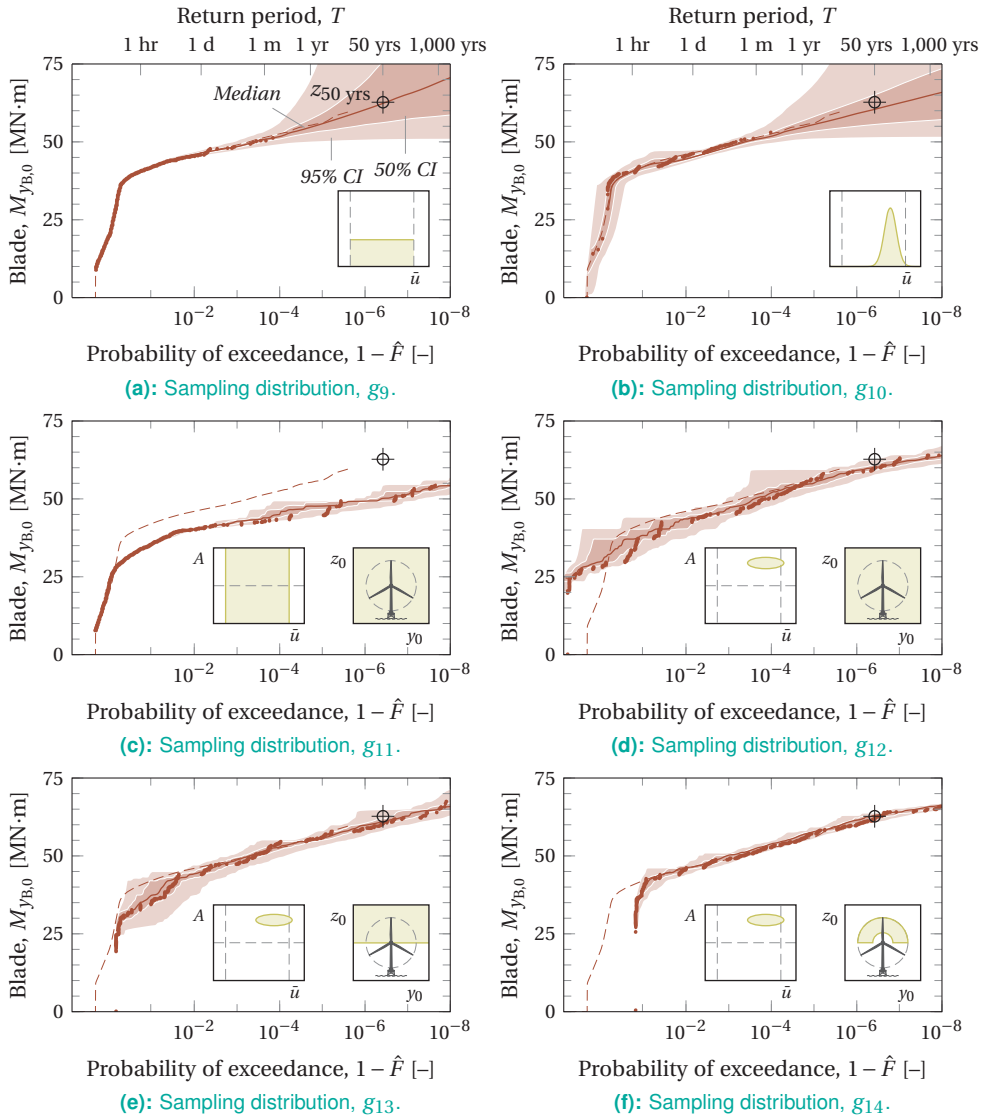
Figure 5.18: Extreme load predictions for the DTU 10 MW turbine, constructed by importance sampling of mean wind speeds **(a, b)** and spheroidal gusts **(c–f)**, based on $N = 1{,}000$ ten-minute and $N = 10{,}000$ one-minute wind fields, respectively (~ 1 week). The dashed line indicates the complete, 7.5-year data set. The dot markers belong to an abitrary sample.

5.5 Genetic algorithm

The disadvantage of importance sampling is that a designer needs to know beforehand what kind of events trigger extreme loads. Setting up proper sampling distributions can be a tedious process—especially if a controller shows unexpected behavior—and sometimes requires an expensive survey over all the operating conditions. In order to work around this, a *genetic algorithm* may be used to automate the search inside the parameter space.

5.5.1 Basics

The idea is to turn the search for a good sampling distribution into an optimization problem and to have a genetic algorithm search for the best solution. First, an initial population is seeded with m gusts, each defined by a genotype (i.e., $\boldsymbol{\theta}_1, \boldsymbol{\theta}_2, \ldots, \boldsymbol{\theta}_m$). These gusts are fed to an aeroelastic model to determine the loads, after which an extreme load distribution can be set up. Based on a certain *fitness function*, the most successful genotypes are selected and used to spawn a new generation with mutations and crossovers. This process, sketched in Figure 5.19, is repeated for n generations or until the 50-year load is found with sufficient accuracy.

The likelihood ratio, used to construct a weighted extreme load distribution with Equation (5.18), is somewhat harder to set up since no clear sampling distributions are defined. A *Delaunay tessellation* to divide a k-dimensional sample space up into k-simplices (i.e., triangles in 2D, tetrahedra in 3D, etc.). The probability mass assigned to a point $\boldsymbol{\theta}_i$ is then given by the integrated probability density of all neighboring simplices (see Figure 5.20):

$$\frac{f(\boldsymbol{\theta}_i)}{g(\boldsymbol{\theta}_i)} \approx \frac{1}{k+1} \sum_{S \in \boldsymbol{\theta}_i} \int_S f(\boldsymbol{\theta}) \, \mathrm{d}\boldsymbol{\theta}, \tag{5.25}$$
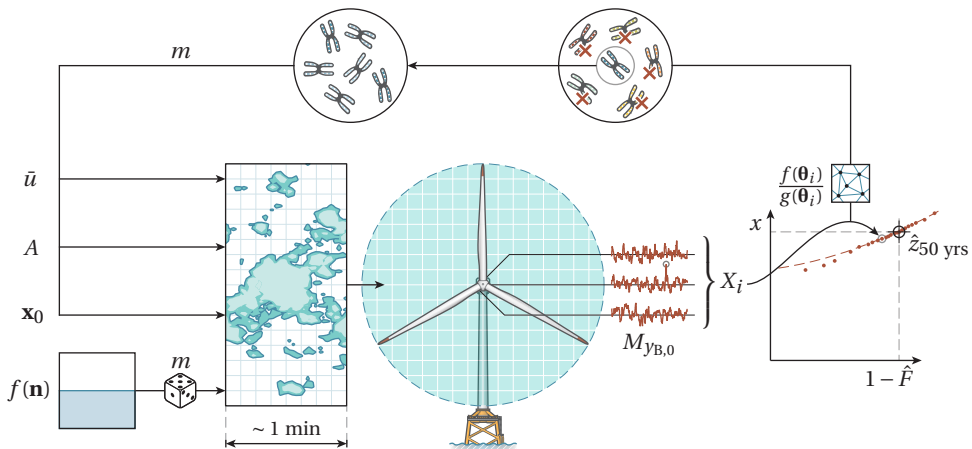
Figure 5.19: Workflow of a genetic algorithm. Combinations of k parameters are stored in a gene pool with a certain population size, m. Each generation, wind fields are generated and fed to an aeroelastic model to determine the loads. Successful genotypes are selected based on a fitness functions (e.g., the distance to the 50-year probability) and are used to spawn a new generation with slight mutations. This is repeated for n generations until the target return level is found.
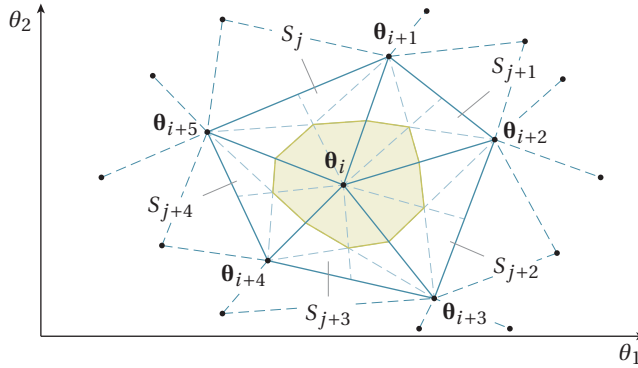
Figure 5.20: Delaunay tessellation of a two-dimensional sample space with scattered points. The sampling probability mass assigned to the point $\boldsymbol{\theta}_i$ is made up from the contributions of the neighboring simplices, $S_j, S_{j+1}, \ldots, S_{j+4}$ (i.e., the contiguous Voronoi cell).

where $S \in \boldsymbol{\theta}_i$ denotes the collection of the simplices that share $\boldsymbol{\theta}_i$ as a vertex. Summed together, they form a *contiguous Voronoi cell*, which provides a better estimate of density than a regular Voronoi tessellation (Schaap, 2007, pp. 64–71). The integral over the k-simplex can be computed with the method of Stoyanova (2006), for example.

The factor $1/(k+1)$ is a normalization constant to take into account that every vertex is counted $k+1$ times in a k-dimensional space. To visualize, Figure 5.20 shows a two-dimensional case where the summation adds up the areas enclosed by the medians of $S_j, S_{j+1}, \ldots, S_{j+4}$. It can be shown with simple geometry that this is exactly one-third of the combined area of the triangles. For higher dimensions, the integral has to be divided by $k+1$, since each k-simplex can be divided by $k+1$ medians. In the case where the parent distribution, $f(\boldsymbol{\theta})$, is uniform, Equation (5.25) simply returns the space surrounding the point $\boldsymbol{\theta}_i$. What in Equation (5.18) was defined as the sampling probability, $g(\boldsymbol{\theta}_i)$, can now be related to the density of the points:

$$g(\boldsymbol{\theta}_i) \propto \left(\frac{1}{k+1} \sum_{S \in \boldsymbol{\theta}_i} \int_S \mathrm{d}\boldsymbol{\theta} \right)^{-1}. \tag{5.26}$$

Therefore, the closer the points lie together, the higher the density assigned to them.

5.5.2 Set-up

The genetic algorithm is applied to the NREL 5 MW and the DTU 10 MW machines, using volumetric gusts with $\ell = 25$ m. For both cases, the genotypes describe gusts with four parameters: mean wind speed, $\bar{u}$, normalized amplitude, $A/\sqrt{\Lambda_0}$, lateral position, y_0, and vertical position, z_0. The time stamp of the gust is randomized. At the start of every run, an initial population with a size of $m = 50$ is seeded from a uniform distribution,[9] limited to $\bar{u} \in [0, 30]$ m/s, $A/\sqrt{\Lambda_0} \in [-10, 10]$, $y0 \in \left[-\frac{1}{2}L_y, \frac{1}{2}L_y \right]$, and $z_0 \in \left[H - \frac{1}{2}L_z, H + \frac{1}{2}L_z \right]$, where L_y and L_z are the lateral and vertical dimensions of the domain, respectively.

---

[9] Alternatively, one can choose to seed the first population with successful genotypes of a previous run or by drawing a sample from a good sampling distribution. This is not done in this section, however, since the goal is to avoid needing any prior knowledge of the extreme load behavior.

Since the goal is to determine a certain return level, perhaps the most straightforward fitness function is the distance to that probability on Gumbel graph paper:

$$C(\boldsymbol{\theta}_i) = \left| \ln \left[-\ln \left(\hat{F}(X_i) \right) \right] - \ln \left[-\ln \left(1 - \frac{1}{T} \right) \right] \right|, \tag{5.27}$$

where the empirical distribution, $\hat{F}(X_i)$, is obtained from the entire gene pool together with the past generations. Based on this, the five best performing genotypes from every generation are selected as the elite and are guaranteed to produce offspring. The algorithm halts when a fixed number of generations, n, is exceeded, or when the average change in fitness over the last ten generations is smaller than 0.0001%.

5.5.3 **Performance**

The genetic algorithm yields some interesting results, shown in Figures 5.21 and 5.22. As seen already in Section 5.4, the NREL 5 MW and DTU 10 MW machines have very different extreme load behaviors, caused by the pitch control and the lack of one. For the NREL 5 MW case, the genetic algorithm starts to converge to negative amplitudes after a couple of generations to trigger the behavior shown in Figure 5.13. High bending moments are the result of briefly decreasing the generator torque, which tricks the controller into pitching to full thrust in above-rated wind speeds. Therefore, they are not generated locally by the gusts' amplitudes, but by the recovering wind speed. Although this makes the gust position somewhat less relevant, it does seem to favor the blades' upstroke and the lower half of the rotor disk—exactly the opposite of what is found in Figure 4.17.

For the DTU 10 MW case, the gusts' positions are clearly more important and the algorithm converges nicely to the vulnerable areas of the rotor disk (see Figure 4.17). Furthermore, positive amplitudes are favored as they directly affect the blade loads. However, with considerably larger confidence intervals around the 50-year load, the overall performance is worse than in the previous case. This is probably because the algorithm needs more time to search in a four-dimensional parameter space. Even after 40 generations, optimal values for y_0 and z_0 are still not found, whereas with the NREL 5 MW it was already sufficient to be approximately in the right rotor quadrant.

After about 10 generations, the genotypes start to develop extreme amplitudes, often in excess of 7 to $8\sqrt{\Lambda_0}$. The most obvious reason for this is that it is much easier to construct damaging gusts with optimal values of $\bar{u}$ and A and non-optimal values of y_0 and z_0 than it is the other way around. Therefore, the genotypes are favored to develop strong gusts before the start to narrow down on a position. In future work, several other cost functions will have to be tried to see if they can produce better results.

5.6 **A comparison between methods**

A way to compare the three methods is by checking how accurate and precise they are in predicting the 50-year load, where the normalized error is calculated by Equation (5.14). The uncertainty for the methods that rely on ten-minute time series (i.e., g_1, g_3, g_9, and g_{10}) is estimated by resampling the crude Monte Carlo sets ($N = 5.4 \cdot 10^6$ and $N = 3.9 \cdot 10^5$). For the methods that rely on embedded gusts (i.e., g_6, g_8, g_{12}, and g_{14}), this is done by resampling from sets of $N = 5 \cdot 10^4$ one-minute time series. The uncertainty for the genetic algorithm is estimated by comparing 50 different runs, each halted after 40 generations.
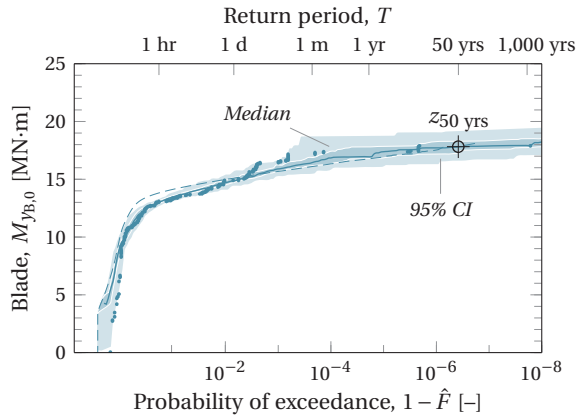
(a): Extreme load predictions after 40 generations (i.e., $N = 2{,}050$ one-minute wind fields). The dashed line indicates the complete 103-year data set. The dot markers belong to an abitrary sample.
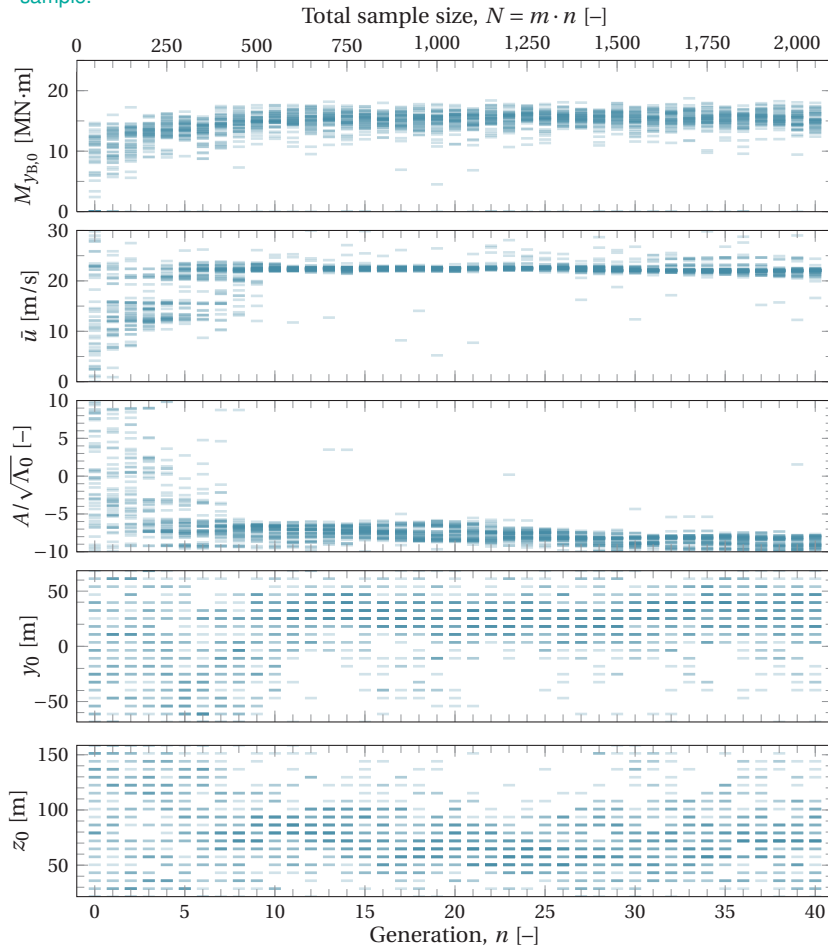
(b): Evolution of the genotypes over n generations.

Figure 5.21: Performance of the genetic algorithm when predicting the 50-year blade flapwise bending moment of the NREL 5 MW machine.
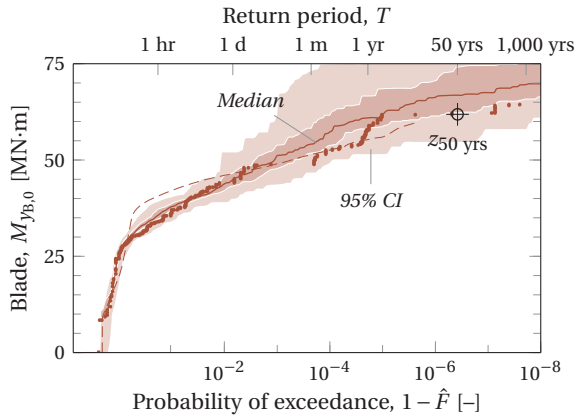
(a): Extreme load predictions after 40 generations (i.e., $N = 2{,}050$ one-minute wind fields). The dashed line indicates the complete 7.5-year data set. The dot markers belong to an abitrary sample.
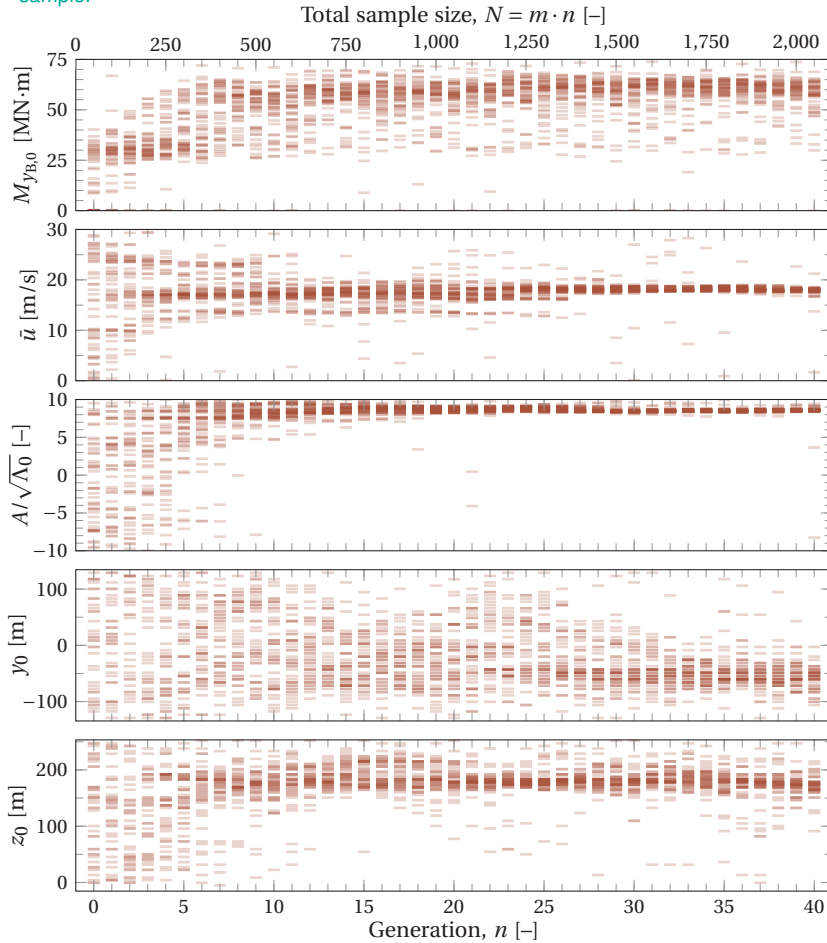
(b): Evolution of the genotypes over n generations.

Figure 5.22: Performance of the genetic algorithm when predicting the 50-year blade flapwise bending moment of the DTU 10 MW machine.

By following the process explained in Subsection 5.1.5, the confidence intervals are then compared for various sample sizes. These sample sizes are multiplied with the length of the time series to give a total simulated time period, which acts as a direct measure of the computational burden.

Apart from the confidence intervals, the prediction quality can be expressed in terms of the *median absolute deviation* (MAD) from the true 50-year level:

$$\text{MAD} = \text{median}\left(|\hat{z}_T - z_T|\right). \tag{5.28}$$

In this case, the MAD is preferred over the root-mean-squared error, which may be distorted by a single bad distribution fit. Nevertheless, it should be noted that the true 50-year level for the DTU 10 MW was established on the basis of 7.5 years of data (see Figure 5.6b) and therefore still contains some uncertainty itself.[10]

Figures 5.23 and 5.24 show a direct comparison of the best performing methods of this chapter with the crude Monte Carlo method as the benchmark. An additional error bar is added in Figure 5.23 for $N = 1,000$ ten-minute wind fields (~ 1 week), which was the sample size used for most of the return level plots in this chapter.

Probably the most commonly used alternative is to uniformly sample wind speeds between the cut-in and cut-out points, as done with the sampling distributions g_1 and g_9. Assigning equal weight to every wind speed means that more load cases are run in the pitch-regulated control regime, which is where the 50-year extreme loads are expected to be. Compared to the crude Monte Carlo method, the prediction quality is better, although it suffers from the occasional bad distribution fit (which ends up above the 75th percentile). Narrowing the sampling distributions with a normal distribution, as done with g_3 and g_{10}, is a strategy that seems to work out better for the DTU 10 MW machine. Together with the uniform g_1, the MAD for g_3 is always smaller than that of the crude Monte Carlo. For the NREL 5 MW, a much larger sample size is required to trigger the right kind of pitching behavior (i.e., ending up in the upper percentiles of Figure 5.6e). The MAD of the sampling distributions g_1 and g_3 becomes smaller than that of the crude Monte Carlo method after $N = 10^4$ and $N = 10^5$, respectively.

The results from the gust methods are notably better, and not only because the sample size can be ten times larger for the same computational burden. Compared to the crude Monte Carlo method, the bias is significantly reduced and also the confidence intervals are narrower around the true 50-year level. Moving towards larger gust volumes was definitely successful for the NREL 5 MW, since it increased the chance of finding high loads in a time series. Therefore, the predictions made by g_8 ($\ell_y = \ell_z = 25$ m, $\tau = 2$ s) have a smaller negative bias than those by g_6 ($\ell_y = \ell_z = \Delta y \approx 7$ m, $\tau = \Delta t = 0.05$ s). Again, compared to the crude Monte Carlo method, the distribution g_8 reduces the median absolute deviation to the 50-year level by a factor 3 to 8, which is roughly a factor 100 increase in computational efficiency.

For the DTU 10 MW, limiting the gust positions to the area between 40 and 100% (g_{14}) blade span also yields more consistent high loads than when they are left unconstrained (g_{12}). This is especially noticeable at small sample sizes, which is where the sampling distribution g_{12} has problems triggering the right loads. The distribution g_{14} is able to

---

[10] Still, considering that all the methods are converging to roughly the same 50-year level gives some confidence in the results.
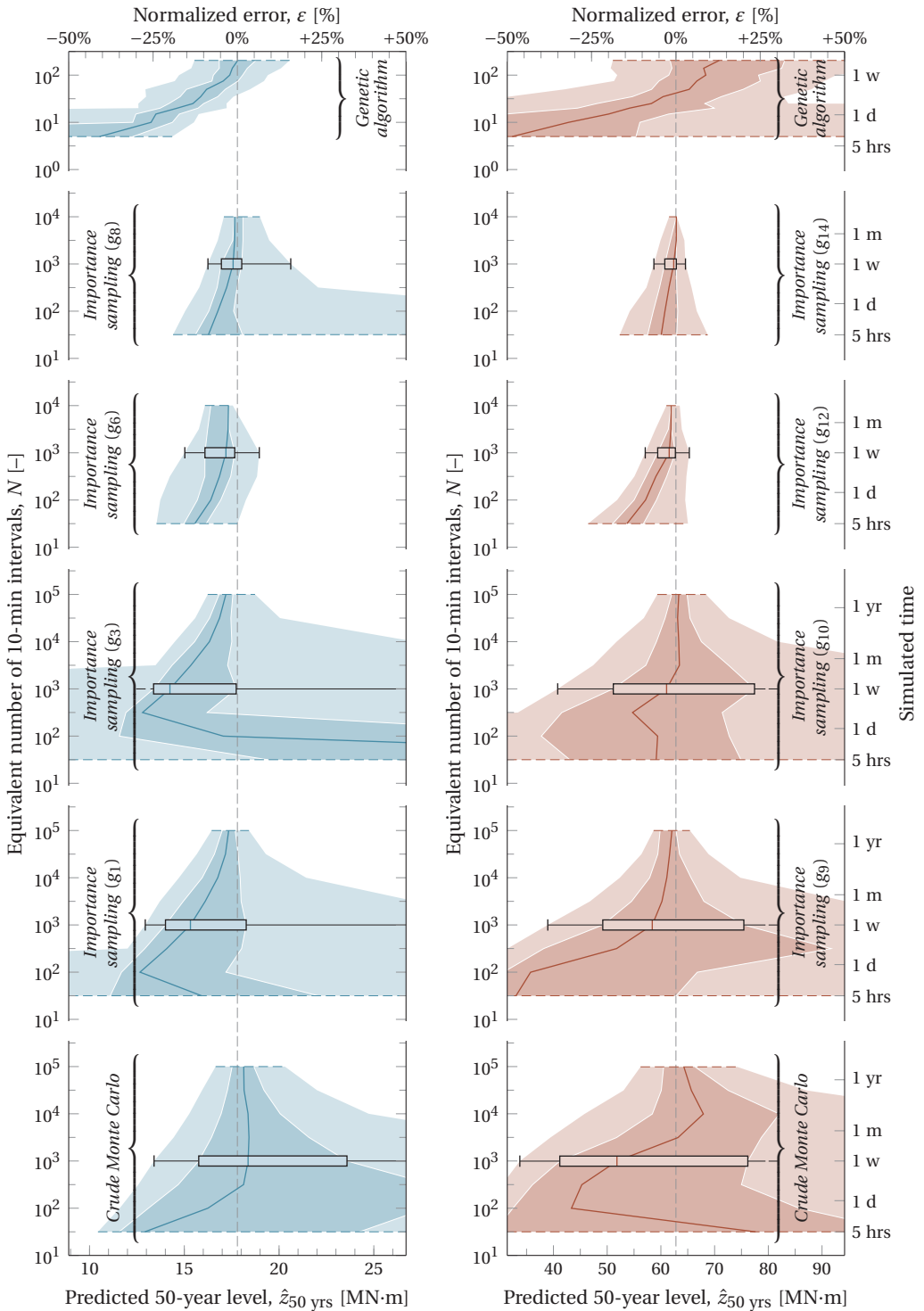
(a): For the NREL 5 MW.   **(b):** For the DTU 10 MW.

Figure 5.23: Performance of various methods to predict the 50-year blade root flapwise bending moment. For the box plots, the boxes mark the 25th and 75th percentiles, the whiskers mark the 2.5th and 97.5th percentiles, and the bar is the median.
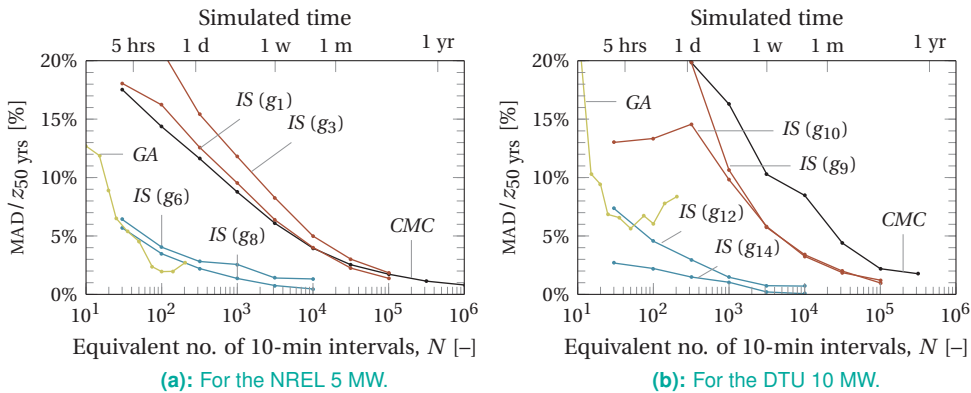
(a): For the NREL 5 MW.　　　　　　**(b):** For the DTU 10 MW.

Figure 5.24: Median absolute deviation (MAD) from the true 50-year blade root flapwise bending moment, resulting from a crude Monte Carlo method (CMC), importance sampling (IS), and a genetic algorithm (GA).

reduce the deviation to the 50-year level by a factor 10 to 100, the equivalent of roughly a factor 1,000 in computational efficiency.

The performance of the genetic algorithm is not very clear from Figure 5.23, since 40 generations were not enough to converge.[11] Judging from Figure 5.24, however, it does seem to outperform some of the manual methods in terms of the MAD. Nonetheless, the genetic algorithm has a distinct advantage when controllers are involved. In retrospect, settling on a sampling distribution with negative gust amplitudes for the NREL 5 MW machine took some effort when done manually. Much unnecessary work would have been avoided when a genetic algorithm had immediately pointed to the right area of the parameter space.

5.7 Implications for design

So far, the results of this chapter have been presented as return level plots and narrowing confidence intervals, which is somewhat abstract. In order to make the results more tangible, this chapter is concluded with a fictive redesign of the blade root section of the DTU 10 MW machine, based on a similar exercise performed by Van Eijk (2016).

5.7.1 A simple redesign

The goal is to find a new shell thickness to reduce the 50-year extreme stress caused by the flapwise bending moment:

$$\sigma_z = \frac{M_{y_{\mathrm{B},0}} \cdot \frac{1}{2}c}{I_{yy}}, \tag{5.29}$$

where σ_z is the normal stress in the material, c the chord length (or diameter) of the root section, and I_{yy} the second moment of area. When the blade root is approximated by a

---

[11] More generations were not attempted because every run had to be redone 50 times at minimum to establish the 95% confidence interval.

thin-walled cylinder, the latter is given by

$$I_{yy} \approx \tfrac{1}{8}\pi c^3 t_s,$$ (5.30)

with t_s as the shell thickness. A new design is then considered better than the old one if

$$\sigma_{z,\text{new}} < \sigma_{z,\text{old}},$$ (5.31)

or

$$\frac{\hat{M}_{y_{B,0},\text{new}}}{t_{s,\text{new}}} < \frac{M_{y_{B,0},\text{old}}}{t_{s,\text{old}}}.$$ (5.32)

At first glance, this seems straightforward; simply increasing the shell thickness would already achieve lower stresses. However, the difficulty lies in estimating the extreme flapwise bending moment for the new design.[12] Whereas the original design already has been through a full detailed structural analysis, the computational budget for a freshly new concept is limited. This means that the old stress levels are known, but the new ones are going to be clouded by uncertainty.

Figure 5.25a shows how often a new design is favored over the old one when a crude Monte Carlo method is used. In the ideal case, every design that is more than a 100% thick, compared to the old design, should be favored in 100% of the cases. Clearly, this is not the case. On the basis of 100 ten-minute wind fields, even a design that is 50% thicker will be discarded in 17% of the cases due to higher stress levels. It is even worse when considering that, in reality, the changes are usually not in the order of 50%, but much smaller. In fact, for changes in the order of ±5%, the gains in strength by a new design are outweighed by the uncertainty. The new design is favored in 60% of the cases—almost irrespective of positive or negative changes to thickness—due to the biased extrapolation method (see

(a): With a crude Monte Carlo method.

(b): With an importance sampling method, using the sampling distribution g_{14}.
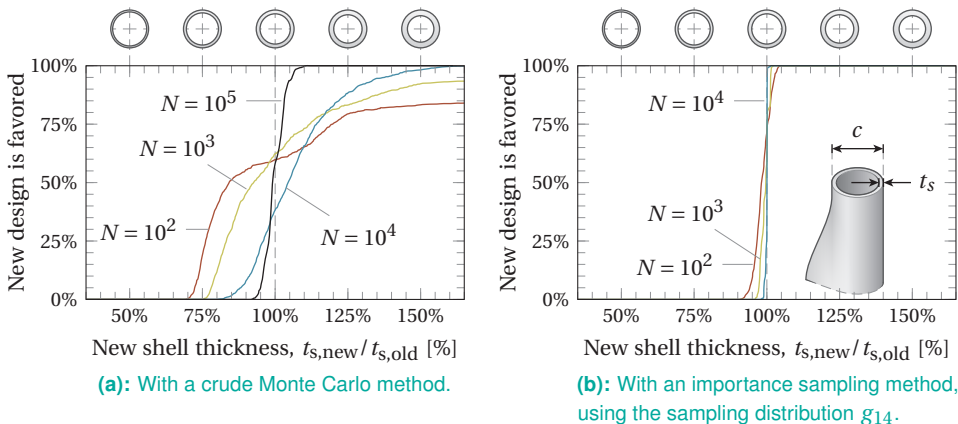
Figure 5.25: Relative number of times a root section with a new shell thickness, $t_{s,\text{new}}$, is favored over the old design, $t_{s,\text{old}}$. The sample size, N, denotes the equivalent number of ten-minute intervals.

---

[12] This is, of course, assuming that the root section is part of a whole new blade design for which a full aeroelastic analysis has to be carried out.

Figure 5.8). The same problem could arise in the design of a new gust controller, which could, purely by chance, be wrongly accepted or wrongly rejected.

With a crude Monte Carlo method, it is almost impossible to prove that a new design is able to reduce the long-term extreme loads when computational resources are limited. This is where importance sampling methods come in. Figure 5.25b shows that, on the basis of the sampling distribution g_{14}, the probability for a false acception or false rejection is much smaller.

5.7.2 Comparing several concepts

Conceptual design studies often look at more than one configuration. For example, say that there are five concepts that are copies of the DTU 10 MW but with a different blade root design. Based on their 50-year stress levels, they are then ranked according to

$$\sigma_{z,1} \leq \sigma_{z,2} \leq \sigma_{z,3} \leq \sigma_{z,4} \leq \sigma_{z,5}. \tag{5.33}$$

Again, in the ideal case, the thickest design should always end up on rank 1 and the thinnest design in rank 5. However, as shown in Figures 5.26a and c, this is certainly not always the case when a crude Monte Carlo method is used. With $N = 100$ ten-minute wind fields, the thickest design is ranked the best only 55% of the time. Investing more computational resources does improve the quality of the predictions, but even when the sample size is increased to $N = 10,000$, the order is often wrong.

On the other hand, with the importance sampling method and an equally expensive simulation campaign, the concepts are always ranked in the right order. Such a method, together with the others presented in Section 5.6, removes much of the uncertainty from a design process. This allows designers to investigate new solutions for extreme load reductions more effectively.

(a): With a crude Monte Carlo method ($N = 100$).

(b): With an importance sampling method, using g_{14} ($N = 100$).

(c): With a crude Monte Carlo method ($N = 10{,}000$).

(d): With an importance sampling method, using g_{14} ($N = 10{,}000$).

Figure 5.26: Average rank in a series of 5 concepts, with 1 being the best performing and 5 the worst. The sample size, N, denotes the equivalent number of ten-minute intervals.

Chapter 6

Conclusions

"Remember kids, the only difference between screwing around and science is writing it down"

— Adam Savage, *2012*

T HIS RESEARCH was motivated by three main objectives; namely, (1) to gain a better overall understanding of wind gusts, (2) to study the effects of finite gust volumes on large rotor blades, and (3) to obtain a better picture of the extreme load behavior of the major structural components of wind turbines. To conclude, this sixth and final chapter serves as a reflection on these objectives. Moreover, some recommendations for future research are given.

6.1 Summary of the most important findings

Most of the results of this thesis are based on the mathematical description of wind gusts in three-dimensional space, derived in Chapter 3. It covers the mean and stochastic velocity fields around concentrations of momentum and subsequently connects them to a probability of occurrence. The numerical results of Chapters 4 and 5 were based largely on this, but it also led to some insights into the nature of gusts, which formed the groundwork of Chapter 2.

6.1.1 On the overall understanding of gusts

- Wind gusts are symptoms of turbulent momentum transport (Section 2.2). As such, their intensity scales with that of the forcing term (e.g., mechanical shear, heat flux, the movement of the observer, etc.).

- Volume is an essential parameter in the treatment of gusts (Sections 2.2 and 3.4). From a mathematical standpoint, single-point gusts contain zero momentum and zero energy, and—while infinitely abundant by their fractal nature—are imperceptible by any observer.

- As dictated by the principle of continuity, the fluid displaced in a wind gust has to recirculate in order to conserve the amount of mass in the domain (Section 3.3). Therefore, unless when dealing with a compressible flow, uniform velocity fronts cannot exist in reality. This renders many deterministic gust models unrealistic.

- The Euler characteristic heuristic, attributed to Adler and Hasofer (1976), is successful in modelling the statistics of gusts in three-dimensional homogeneous Gaussian

velocity fields (Section 3.4). Based on conventional one-dimensional measurements, there is some evidence that this can be extended to real-life turbulence as well, since gusts are found to lean towards Gaussian behavior when their velocity is averaged over increasingly larger volumes (Section 2.4).

6.1.2 On the effect of finite gust volumes on rotor blades

- For the DTU 10 MW reference wind turbine, the rotor blades appear to be most vulnerable to high gust loads when hit around two-thirds of the blade span (Section 4.2). A positive wind shear profile (i.e., the mean wind speed increases with height) amplifies the impact of gusts landing on the top half of the rotor plane. Furthermore, the anisotropy induced by shear tends to make the blades more vulnerable during their downstroke.

- With all of the gust's momentum stored in its deterministic part (as defined by Equation (3.85)), its stochastic component adds little to the damaging potential (Section 4.2).

- The contribution of a single 50-year gust to the 50-year load is close to insignificant (Section 4.3). The probability of such an event occurring, combined with the probability of it actually hitting something, is very low. Moreover, the 50-year gust loses its meaning in a three-dimensional space, since its definition relies on the domain size, which can be arbitrarily chosen.

- Since the majority of a gust's momentum is stored in the large scales of motion, a lidar-assisted control system would be able to track damaging events and take preventive action (Section 4.4).

6.1.3 On the prediction of extreme loads

- The extreme loads that follow from long periods of operation in homogeneous Gaussian velocity fields can be predicted by weighting the response to a set of extreme gusts (Sections 5.4 and 5.6). This can greatly reduce the computational burden or, equivalently, decrease the uncertainty surrounding these loads.

- A genetic algorithm can take over the role of choosing a proper sampling distribution for importance sampling methods (Section 5.5).

- A simple exercise on designing with high uncertainty has shown that importance sampling methods are invaluable for early conceptual design (Section 5.7). The uncertainty that surrounds crude Monte Carlo predictions will often far outweigh any potential benefits of a new design.

6.2 Recommendations

Like any other research, there are still many open issues and topics that this work was not able to cover. The most pressing ones are listed below:

- With the further growth in rotor diameters, it becomes increasingly difficult to defend the assumption of vertical homogeneity. Extending this work to inhomogeneous fields of turbulence would therefore be a logical next step.

- The majority of a gust's momentum is carried by the low wave numbers that, unfortunately, are notoriously difficult to capture by experiments. Now that more advanced measurement techniques such as lidar are becoming available, it would be interesting to see how the low-wave-number behavior of commonly used turbulence spectra compares to real life.

- The work on the time evolution of gusts (Section 3.5) is, so far, purely theoretical and still relies on two unknown parameters to account for diffusion and expansion. There was the intention of finding values for these parameters by doing large eddy simulations (LES) of velocity fields embedded with gusts. However, this had to be put off as this research started to focus more on extreme load prediction.

- How well the along-wind force performs as control input (Section 4.4), will have to be evaluated more thoroughly. This can be done through aeroelastic simulations (i.e., in FAST, Bladed, etc.), preferably with inhomogenous wind fields (such as those obtained from LES) to test the assumptions of the method.

- For the genetic algorithm, various other fitness functions can be investigated to find out whether the performance can be improved.

- Lastly, it would not hurt to test the accuracy and robustness of the importance sampling schemes with a cluster. Larger sample sizes can then be tested that are more representative for later design phases.

6.3 Some final thoughts

This research has resulted in some very effective methods to reduce the uncertainty of extreme load predictions in conceptual design phases. The emphasis here is on conceptual design phases, since most designers will anyway resort to clusters for a full detailed analysis, if possible. Nevertheless, the computational resources that are spared by an importance sampling method can also be spent on increasing the parameter space. Although not included in current wind turbine design standards, some obvious variables that ought to be included in an exteme load analysis are the variation in turbulence kinetic energy and the atmospheric stability.

In any case, this work has hopefully led to some useful insights into extreme gusts and extreme loads. A better understanding of these things will help to get rid of some of the conservatism in wind turbine design. Especially the commonly used gust models that assume uniform inflow (e.g., the IEC extreme operating gust) are in dire need of replacement. Relying instead on stochastic gusts will help designers to tailor structures for the actual operating environments. This means less overdimensioning; therefore lighter structures, and, ultimately, cheaper wind energy.

References

Adcock, T. A. A. and P. H. Taylor (2014). "The physics of anomalous ('rogue') ocean waves". *Reports on Progress in Physics* 77 (10), p. 105901. DOI: `10.1088/0034-4885/77/10/105901`.

Adler, R. J. (1976). "On generalising the notion of upcrossings to random fields". *Advances in Applied Probability* 8 (4), p. 789. DOI: `10.2307/1425934`.

Adler, R. J. and A. M. Hasofer (1976). "Level crossings for random fields". *The Annals of Probability* 4 (1), pp. 1–12. DOI: `10.1214/aop/1176996176`.

Adler, R. J. and J. E. Taylor (2007). *Random fields and geometry*. Springer Monographs in Mathematics. New York, NY, United States: Springer. DOI: `10.1007/978-0-387-48116-6`.

ARC Centre of Excellence for Coral Reef Studies (2016). *Life and death after Great Barrier Reef bleaching*. URL: `http://www.coralcoe.org.au/media-releases/life-and-death-after-great-barrier-reef-bleaching` (accessed on 2 December 2016).

Bak, C., F. Zahle, R. Bitsche, T. Kim, A. Yde, L. C. Henriksen, A. Natarajan and M. Hansen (2013). *Description of the DTU 10 MW reference wind turbine*. Technical report Report-I-0092. Roskilde, Denmark: DTU Wind Energy.

Balkema, A. A. and L. de Haan (1974). "Residual life time at great age". *The Annals of Probability* 2 (5), pp. 792–804. DOI: `10.1214/aop/1176996548`.

Barone, M., J. Paquette, B. Resor and L. Manuel (2012). "Decades of wind turbine load simulation". *50th AIAA Aerospace Sciences Meeting including the New Horizons Forum and Aerospace Exposition*. 9–12 January. Nashville, TN, United States: American Institute of Aeronautics and Astronautics. DOI: `10.2514/6.2012-1288`.

Batchelor, G. K. (1953). *The theory of homogeneous turbulence*. Cambridge, United Kingdom and New York, NY, United States: Cambridge University Press.

Batchelor, G. K. and I. Proudman (1954). "The effect of rapid distortion of a fluid in turbulent motion". *The Quarterly Journal of Mechanics and Applied Mathematics* 7 (1), pp. 83–103. DOI: `10.1093/qjmam/7.1.83`.

BEARD, L. R. (1943). "Statistical analysis in hydrology". *Transactions of the American Society of Civil Engineers* 108 (1), pp. 1110–1121.

BELJAARS, A. C. M. (1987a). "The influence of sampling and filtering on measured wind gusts". *Journal of Atmospheric and Oceanic Technology* 4 (4), pp. 613–626. DOI: `10.1175/1520-0426(1987)004<0613:TIOSAF>2.0.CO;2`.

BELJAARS, A. C. M. (1987b). *The measurement of gustiness at routine wind stations.* Technical report WR 87-11. De Bilt, The Netherlands: Koninklijk Nederlands Meteorologisch Instituut.

BENARD, A. and E. C. BOS-LEVENBACH (1953). "Het uitzetten van waarnemingen op waarschijnlijkheids-papier". *Statistica Neerlandica* 7 (3), pp. 163–173. DOI: `10.1111/j.1467-9574.1953.tb00821.x`.

BERG, J., A. NATARAJAN, J. MANN and E. G. PATTON (2016). "Gaussian vs non-Gaussian turbulence: impact on wind turbine loads". *Wind Energy* 19 (11), pp. 1975–1989. DOI: `10.1002/we.1963`.

BIERBOOMS, W. A. A. M. (2009). "Application of constrained stochastic simulation to determine the extreme loads of wind turbines". *Journal of Solar Energy Engineering* 131 (3), p. 031010. DOI: `10.1115/1.3142726`.

BIERBOOMS, W. A. A. M., P.-W. CHENG, G. C. LARSEN and B. J. PEDERSEN (2001). *Modelling of extreme gusts for design calculations.* Technical report JOR3-CT98-0239. Delft, The Netherlands: Delft University of Technology.

BIERBOOMS, W. A. A. M., J. B. DRAGT and H. CLEIJNE (1999). "Verification of the mean shape of extreme gusts". *Wind Energy* 2 (3), pp. 137–150. DOI: `10.1002/(SICI)1099-1824(199907/09)2:3<137::AID-WE24>3.0.CO;2-W`.

BLOM, G. (1958). *Statistical estimates and transformed beta variables.* New York, NY, United States: Wiley.

BORTKEWITSCH, L. VON (1898). *Das Gesetz der Kleinen Zahlen.* Leipzig, Germany: Teubner.

BOS, R. (2012). "Self-starting of a small urban Darrieus rotor". Master's thesis. Delft University of Technology.

BOSSANYI, E. (2012). "Un-freezing the turbulence: improved wind field modelling for investigating Lidar-Assisted wind turbine control". *EWEA Annual Event.* Copenhagen, Denmark.

BRASSEUR, O. (2001). "Development and application of a physical approach to estimating wind gusts". *Monthly Weather Review* 129 (1), pp. 5–25. DOI: `10.1175/1520-0493(2001)129<0005:DAAOAP>2.0.CO;2`.

CALIFORNIA ENERGY COMMISSION (2016). *Overview of wind energy in California.* URL: `http://www.energy.ca.gov/wind/overview.html` (accessed on 4 December 2016).

CASTAING, B., Y. GAGNE and E. HOPFINGER (1990). "Velocity probability density functions of high Reynolds number turbulence". *Physica D: Nonlinear Phenomena* 46 (2), pp. 177–200. DOI: 10.1016/0167-2789(90)90035-N.

CROWL, T. A., T. O. CRIST, R. R. PARMENTER, G. BELOVSKY and A. E. LUGO (2008). "The spread of invasive species and infectious disease as drivers of ecosystem change". *Frontiers in Ecology and the Environment* 6 (5), pp. 238–246. DOI: 10.1890/070151.

CUNNANE, C. (1978). "Unbiased plotting positions – A review". *Journal of Hydrology* 37 (3-4), pp. 205–222. DOI: 10.1016/0022-1694(78)90017-3.

DIACONIS, P. and F. MOSTELLER (1989). "Methods for studying coincidences". *Journal of the American Statistical Association* 84 (408), pp. 853–861. DOI: 10.1080/01621459.1989.10478847.

DIEZ, J. M., C. M. D'ANTONIO, J. S. DUKES, E. D. GROSHOLZ, J. D. OLDEN, C. J. SORTE, D. M. BLUMENTHAL, B. A. BRADLEY, R. EARLY, I. IBÁÑEZ, S. J. JONES, J. J. LAWLER and L. P. MILLER (2012). "Will extreme climatic events facilitate biological invasions?" *Frontiers in Ecology and the Environment* 10 (5), pp. 249–257. DOI: 10.1890/110137.

DOTI (2015). *Fact-sheet Alpha Ventus.* Oldenburg, Germany: Deutsche Offshore-Testfeld und Infrastruktur.

ECB (2016). *Annual report 2015.* Technical report QB-AA-16-001-EN-E. Frankfurt am Main, Germany: European Central Bank.

EEA (2009). *Europe's onshore and offshore wind energy potential.* Technical report 6/2009. Copenhagen, Denmark: European Environment Agency.

EECEN, P. J. (2008). *Meteorological measurements OWEZ.* Technical report ECN-E–08-061. Petten, The Netherlands: Energy Research Centre of the Netherlands.

EECEN, P. J. and E. BRANLARD (2008). *The OWEZ meteorological mast.* Technical report ECN-E–08-067. Petten, The Netherlands: Energy Research Centre of the Netherlands.

EIJK, S. F. VAN (2016). "Wind turbine load extrapolation". Master's thesis. Delft University of Technology.

EMEIS, S. (2011). *Surface-based remote sensing of the atmospheric boundary layer.* Dordrecht, The Netherlands: Springer.

EPSTEIN, P. R. (2001). "Climate change and emerging infectious diseases". *Microbes and Infection* 3 (9), pp. 747–754. DOI: 10.1016/S1286-4579(01)01429-0.

EWEA (2007). "Focus on supply chain". *Wind Directions* 30 (1), pp. 27–34.

EWEA (2015). *Wind energy scenarios for 2030.* Brussels, Belgium: European Wind Energy Association.

FILLIBEN, J. J. (1975). "The probability plot correlation coefficient test for normality". *Technometrics* 17 (1), p. 111. DOI: 10.2307/1268008.

FISHER, R. A. and L. H. C. TIPPETT (1928). "Limiting forms of the frequency distribution of the largest or smallest member of a sample". *Mathematical Proceedings of the*

Cambridge Philosophical Society 24 (2), pp. 180–190. DOI: 10.1017/S0305004100015
681.

FOLLAND, C. and C. ANDERSON (2002). "Estimating changing extremes using empirical
ranking methods". *Journal of Climate* 15 (20), pp. 2954–2960. DOI: 10.1175/1520-04
42(2002)015<2954:ECEUER>2.0.CO;2.

FREHLICH, R., Y. MEILLIER, M. L. JENSEN, B. BALSLEY and R. SHARMAN (2006). "Mea-
surements of boundary layer profiles in an urban environment". *Journal of Applied
Meteorology and Climatology* 45 (6), pp. 821–837. DOI: 10.1175/JAM2368.1.

GELDER, P. H. A. J. M. VAN (2000). "Statistical methods for the risk-based design of civil
structures". PhD thesis. Delft University of Technology.

GNEDENKO, B. V. (1943). "Sur la distribution limite du terme maximum d'une série aléa-
toire". *Annals of Mathematics* 44, pp. 423–453.

GRACHEV, A. A. and C. W. FAIRALL (1997). "Dependence of the Monin-Obukhov stability
parameter on the bulk Richardson number over the ocean". *Journal of Applied Meteo-
rology* 36 (4), pp. 406–414. DOI: 10.1175/1520-0450(1997)036<0406:DOTMOS>2.0
.CO;2.

GRINGORTEN, I. I. (1963). "A plotting rule for extreme probability paper". *Journal of Geo-
physical Research* 68 (3), pp. 813–814. DOI: 10.1029/JZ068i003p00813.

GRYNING, S.-E., E. BATCHVAROVA, B. BRÜMMER, H. JØRGENSEN and S. LARSEN (2007).
"On the extension of the wind profile over homogeneous terrain beyond the surface
boundary layer". *Boundary-Layer Meteorology* 124 (2), pp. 251–268. DOI: 10.1007/s10
546-007-9166-9.

GUMBEL, E. J. (1958). *Statistics of Extremes*. Mineola, NY, United States: Dover.

GWEC (2016). *Global wind report – Annual market update 2015*. Brussels, Belgium: Global
Wind Energy Council.

HARTER, H. L. (1984). "Another look at plotting positions". *Communications in Statistics -
Theory and Methods* 13 (13), pp. 1613–1633. DOI: 10.1080/03610928408828781.

HAVER, S. (2004). "A possible freak wave event measured at the Draupner jacket January 1
1995". *Rogue Waves workshop at the Brest Sea Tech Week*. 20–22 October. Brest, France.

HAZEN, A. (1914). "Storage to be provided in impounding reservoirs for municipal water
supply". *Transactions of the American Association of Civil Engineers* 77, pp. 1539–1669.

HELMHOLTZ, H. L. F. VON (1847). *Über die Erhaltung der Kraft*. Berlin, Germany: Reimer.

HIGGINS, C. W., M. FROIDEVAUX, V. SIMEONOV, N. VERCAUTEREN, C. BARRY and M. B.
PARLANGE (2012). "The effect of scale on the applicability of Taylor's frozen turbulence
hypothesis in the atmospheric boundary layer". *Boundary-Layer Meteorology* 143 (2),
pp. 379–391. DOI: 10.1007/s10546-012-9701-1.

HOLTON, J. R. (2004). *An introduction to dynamic meteorology*. 4th edn. New York, NY,
United States: Elsevier.

HOLTSLAG, M. C. (2016). "Far offshore wind conditions in scope of wind energy". PhD thesis. Delft University of Technology.

HOOFT, E. L. VAN DER and T. G. VAN ENGELEN (2004). "Estimated wind speed feed forward control". *European Wind Energy Conference*. 22–25 November. London, United Kingdom.

HOOFT, E. L. VAN DER, P. SCHAAK and T. G. VAN ENGELEN (2003). *Wind turbine control algorithms*. Technical report DOWEC-F1W1-EH-03-094/0, ECN-C–03-111. Petten, The Netherlands: Energy Research Centre of the Netherlands.

HUCHO, W.-H. and H. J. EMMELMANN (1973). "Theoretical prediction of the aerodynamic derivatives of a vehicle in cross wind gusts". *SAE Technical Paper* 730232. DOI: 10.427 1/730232.

HUTSCHEMAEKERS, J. J. W. (2014). "Comparison of classification systems to define atmospheric Stability". Master's thesis. Delft University of Technology.

IEA (2016a). *Key world energy statistics*. Paris, France: International Energy Agency.

IEA (2016b). "Key world energy trends". *World energy balances*. Paris, France: International Energy Agency.

IEC (2005a). *IEC 61400-1 Wind turbines - Part 1: Design requirements*. 3rd edn. Geneva, Switzerland: International Electrotechnical Commission.

IEC (2005b). *IEC 61400-12-1 Wind turbines - Part 12-1: Power performance measurements of electricity producing wind turbines*. 1st edn. Geneva, Switzerland: International Electrotechnical Commission.

IPCC (2013). "Summary for policymakers". *Climate change 2013: the physical science basis. Contribution of Working Group I to the Fifth Assessment Report of the Intergovernmental Panel on Climate Change*. Ed. by T. Stocker, D. Qin, G.-K. Plattner, M. Tignor, S. Allen, J. Boschung, A. Nauels, Y. Xia, V. Bex and P. Midgley. Cambridge, United Kingdom and New York, NY, United States: Cambridge University Press.

ISO (2001). *ISO/NP 19902 Petroleum and natural gas industries – fixed steel offshore structures*. Geneva, Switzerland: International Organization for Standardization.

ISYUMOV, N. (2012). "Alan G. Davenport's mark on wind engineering". *Journal of Wind Engineering and Industrial Aerodynamics* 104-106, pp. 12–24. DOI: 10.1016/j.jweia. 2012.02.007.

JANSSEN, T. T. and T. H. C. HERBERS (2009). "Nonlinear wave statistics in a focal zone". *Journal of Physical Oceanography* 39 (8), pp. 1948–1964. DOI: 10.1175/2009JPO4124 .1.

JENKINSON, A. F. (1955). "The frequency distribution of the annual maximum (or minimum) values of meteorological elements". *Quarterly Journal of the Royal Meteorological Society* 81 (348), pp. 158–171. DOI: 10.1002/qj.49708134804.

JONG, J. J. M. DE, A. C. DE VRIES and W. KLAASEN (1999). "Influence of obstacles on the aerodynamic roughness of the Netherlands". *Boundary-Layer Meteorology* 91 (1), pp. 51–64. DOI: `10.1023/A:1001888629613`.

JONKMAN, J. M. and M. BUHL, JR. (2005). *FAST user's guide*. Technical report NREL/EL-500-38230. Golden, CO, United States: National Renewable Energy Laboratory.

JONKMAN, J. M., S. BUTTERFIELD, W. MUSIAL and G. SCOTT (2009). *Definition of a 5-MW reference wind turbine for offshore system development*. Technical report NREL/TP-500-38060. Golden, CO, United States: National Renewable Energy Laboratory.

KAIMAL, J. C., J. C. WYNGAARD, Y. IZUMI and O. R. COTÉ (1972). "Spectral characteristics of surface-layer turbulence". *Quarterly Journal of the Royal Meteorological Society* 98 (417), pp. 563–589. DOI: `10.1002/qj.49709841707`.

KÁRMÁN, T. VON (1938). "Airfoil theory for non-uniform motion". *Journal of the Aeronautical Sciences* 5 (10), pp. 379–390. DOI: `10.2514/8.674`.

KÁRMÁN, T. VON (1948). "Progress in the statistical theory of turbulence". *Proceedings of the National Academy of Sciences of the United States of America* 34 (11), pp. 530–539.

KNMI (2009). *Climate change in the Netherlands – Supplements to the KNMI'06 scenarios*. Ed. by A. M. G. Klein Tank and G. Lenderink. De Bilt, The Netherlands: Koninklijk Nederlands Meteorologisch Instituut.

KNMI (2015). *KNMI'14-klimaatscenario's voor Nederland; Leidraad voor professionals in klimaatadaptatie*. De Bilt, The Netherlands: Koninklijk Nederlands Meteorologisch Instituut.

KOAY, C. G., J. E. SARLLS and E. ÖZARSLAN (2007). "Three-dimensional analytical magnetic resonance imaging phantom in the Fourier domain". *Magnetic Resonance in Medicine* 58 (2), pp. 430–436. DOI: `10.1002/mrm.21292`.

KOLMOGOROV, A. N. (1941a). "Dissipation of energy in the locally isotropic turbulence". *Doklady Akademiia Nauk SSSR* 32, pp. 16–18.

KOLMOGOROV, A. N. (1941b). "The local structure of turbulence in incompressible viscous fluid for very large Reynolds numbers". *Doklady Akademiia Nauk SSSR* 30, pp. 299–303.

KOST, C., J. N. MAYER, J. THOMSEN, N. HARTMANN, C. SENKPIEL, S. PHILIPPS, S. NOLD, S. LUDE, N. SAAD and T. SCHLEGL (2013). *Levelized cost of electricity – renewable energy technologies*. Freiburg, Germany: Fraunhofer Institute for Solar Energy Systems ISE.

KOUWENHOVEN, H. J. (2007). *Manual data files meteo mast NoordzeeWind*. Technical report NZW-16-S-4-R03. IJmuiden, The Netherlands: NoordzeeWind.

KRISTENSEN, L. (1979). "On longitudinal spectral coherence". *Boundary-Layer Meteorology* 16 (2), pp. 145–153. DOI: `10.1007/BF02350508`.

KRISTENSEN, L., M. CASANOVA, M. S. COURTNEY and I. TROEN (1991). "In search of a gust definition". *Boundary-Layer Meteorology* 55 (1-2), pp. 91–107. DOI: `10.1007/BF00119328`.

KUIK, G. A. M. VAN, J. PEINKE, R. NIJSSEN, D. LEKOU, J. MANN, J. N. SØRENSEN, C. FER-REIRA, J. W. VAN WINGERDEN, D. SCHLIPF, P. GEBRAAD, H. POLINDER, A. ABRAHAMSEN, G. J. W. VAN BUSSEL, J. D. SØRENSEN, P. TAVNER, C. L. BOTTASSO, M. MUSKULUS, D. MATHA, H. J. LINDEBOOM, S. DEGRAER, O. KRAMER, S. LEHNHOFF, M. SONNENSCHEIN, P. E. SØRENSEN, R. W. KÜNNEKE, P. E. MORTHORST and K. SKYTTE (2016). "Long-term research challenges in wind energy – a research agenda by the European Academy of Wind Energy". *Wind Energy Science* 1 (1), pp. 1–39. DOI: 10.5194/wes-1-1-2016.

KUIK, G. A. M. VAN (2007). "The Lanchester-Betz-Joukowsky limit". *Wind Energy* 10 (3), pp. 289–291. DOI: 10.1002/we.218.

KÜSSNER, H. G. (1936). "Zusammenfassender Bericht über den instationären Auftrieb von Flügeln". *Luftfahrtforschung* 13 (12), pp. 410–424.

LANDWEHR, J. M., N. C. MATALAS and J. R. WALLIS (1979). "Probability weighted moments compared with some traditional techniques in estimating Gumbel parameters and quantiles". *Water Resources Research* 15 (5), pp. 1055–1064. DOI: 10.1029/WR015i005 p01055.

LEISHMAN, J. G. and T. S. BEDDOES (1989). "A semi-empirical model for dynamic stall". *Journal of the American Helicopter Society* 34 (3), pp. 3–17.

LINDGREN, G. (1970). "Some properties of a normal process near a local maximum". *The Annals of Mathematical Statistics* 41 (6), pp. 1870–1883. DOI: 10.1214/aoms/1177696 688.

LOTT, S. and P. W. CHENG (2016). "Load extrapolations based on measurements from an offshore wind turbine at alpha ventus". *Journal of Physics: Conference Series* 753, p. 072004. DOI: 10.1088/1742-6596/753/7/072004.

MAKKONEN, L. (2008). "Problems in the extreme value analysis". *Structural Safety* 30 (5), pp. 405–419. DOI: 10.1016/j.strusafe.2006.12.001.

MAKKONEN, L., M. PAJARI and M. TIKANMÄKI (2013). "Closure to "Problems in the extreme value analysis" (Struct. Safety 2008:30:405-419)". *Structural Safety* 40, pp. 65–67. DOI: 10.1016/j.strusafe.2012.09.007.

MANDELBROT, B. B. (1967). "How long is the coast of britain? Statistical self-similarity and fractional dimension." *Science* 156 (3775), pp. 636–8. DOI: 10.1126/science.156.37 75.636.

MANDELBROT, B. B. (1975). "On the geometry of homogeneous turbulence, with stress on the fractal dimension of the iso-surfaces of scalars". *Journal of Fluid Mechanics* 72 (3), pp. 401–416. DOI: 10.1017/S0022112075003047.

MANN, J. (1994). "The spatial structure of neutral atmospheric surface-layer turbulence". *Journal of Fluid Mechanics* 273, pp. 141–168. DOI: 10.1017/S0022112094001886.

MANN, J. (1998). "Wind field simulation". *Probabilistic Engineering Mechanics* 13 (4), pp. 269–282. DOI: 10.1016/S0266-8920(97)00036-2.

McClung, D. and A. Mears (1991). "Extreme value prediction of snow avalanche runout". *Cold Regions Science and Technology* 19 (2), pp. 163–175. DOI: `10.1016/0165-232X(91)90006-3`.

Merriam-Webster Online (2016). *Gust [Def. 2]*. URL: `http://www.merriam-webster.com/dictionary/gust` (accessed on 27 September 2016).

Mises, R. von (1936). "La distribution da la plus grande de n valeurs". *Revue de l'Union Interbalkanique* 1, pp. 1–20.

NASA (2000). *Terrestrial environment and (climatic) criteria handbook for use in aerospace vehicle development*. Technical report NASA-HDBK-1001. Huntsville, AL, United States: National Aeronautics and Space Administration.

National Weather Service (2016). *Element definitions*. URL: `http://www.nws.noaa.gov/ndfd/definitions.htm` (accessed on 20 October 2016).

NUON (2016). *Windpark Lely uit IJsselmeer verwijderd*. URL: `http://www.nuon.com/nieuws/nieuws/2016/windpark-lely-uit-ijsselmeer-verwijderd/` (accessed on 4 December 2016).

Onorato, M. and D. Proment (2012). "Approximate rogue wave solutions of the forced and damped nonlinear Schrödinger equation for water waves". *Physics Letters A* 376 (45), pp. 3057–3059. DOI: `10.1016/j.physleta.2012.05.063`.

Orlanski, I. (1975). "A rational subdivision of scales for atmospheric processes". *Bulletin of the American Meteorological Society* 56 (5), pp. 527–530.

Paulsen, U. S., M. Borg, H. A. Madsen, T. F. Pedersen, J. Hattel, E. Ritchie, C. S. Ferreira, H. Svendsen, P. A. Berthelsen and C. Smadja (2015). "Outcomes of the DeepWind conceptual design". *Energy Procedia* 80, pp. 329–341. DOI: `10.1016/j.egypro.2015.11.437`.

Pearson, J. R. A. (1959). "The effect of uniform distortion on weak homogeneous turbulence". *Journal of Fluid Mechanics* 5 (2), p. 274. DOI: `10.1017/S0022112059000192`.

Pereira, R., G. Schepers and M. D. Pavel (2013). "Validation of the Beddoes-Leishman dynamic stall model for horizontal axis wind turbines using MEXICO data". *Wind Energy* 16 (2), pp. 207–219. DOI: `10.1002/we.541`.

Pickands, J. I. (1975). "Statistical inference using extreme order statistics". *The Annals of Statistics* 3 (1), pp. 119–131. DOI: `10.1214/aos/1176343003`.

Press, W. H., S. A. Teukolsky, W. T. Vetterling and B. P. Flannery (2007). *Numerical recipes: the art of scientific computing*. 3rd edn. Cambridge, United Kingdom and New York, NY, United States: Cambridge University Press.

Rashkin, S. D. and P. Goetze van Steyn (1986). *Results from the Wind Performance Reporting System – 1985 annual report*. Technical report P500-86-013. Sacramento, CA, United States: California Energy Commission.

REUTERS (2009). *China starts building first 10-GW mega wind farm.* URL: `http://www.reuters.com/article/us-china-wind-power-idUSTRE5771IP20090808` (accessed on 4 December 2016).

RICE, S. O. (1944). "Mathematical analysis of random noise". *Bell System Technology Journal* 23 (3), pp. 282–332.

RICHARDSON, L. F. (1926). "Atmospheric diffusion shown on a distance-neighbour graph". *Proceedings of the Royal Society A: Mathematical, Physical and Engineering Sciences* 110 (756), pp. 709–737. DOI: `10.1098/rspa.1926.0043`.

RICHARDSON, L. F. (1922). *Weather prediction by numerical process.* Cambridge, United Kingdom and New York, NY, United States: Cambridge University Press.

RICHARDSON, L. F. (1961). "The problem of contiguity: An appendix to Statistics of Deadly Quarrels". *Yearbook of the Society for General Systems Research* 6, pp. 140–187.

ROPELEWSKI, C. F., H. TENNEKES and H. A. PANOFSKY (1973). "Horizontal coherence of wind fluctuations". *Boundary-Layer Meteorology* 5 (3), pp. 353–363. DOI: `10.1007/BF00155243`.

RUBAN, V. P. (2010). "Giant waves in weakly crossing sea states". *Journal of Experimental and Theoretical Physics* 110 (3), pp. 529–536. DOI: `10.1134/S1063776110030155`.

SATHE, A. R., J. MANN, T. BARLAS, W. A. A. M. BIERBOOMS and G. J. W. VAN BUSSEL (2013). "Influence of atmospheric stability on wind turbine loads". *Wind Energy* 16 (7), pp. 1013–1032. DOI: `10.1002/we.1528`.

SCHAAP, W. E. (2007). "DTFE: the Delaunay Tessellation Field Estimator". PhD thesis. Rijksuniversiteit Groningen.

SCHLIPF, D., D. TRABUCCHI, O. BISCHOFF, M. HOFSÄSS, J. MANN, T. MIKKELSEN, A. RETTENMEIER, J. J. TRUJILLO and M. KÜHN (2010). "Testing of frozen turbulence hypothesis for wind turbine applications with a scanning LIDAR system". *15th International Symposium for the Advancement of Boundary Layer Remote Sensing.* 28–30 June. Paris, France.

SEIDEL, M. (2007). "Jacket substructures for the REpower 5M wind turbine". *European Offshore Wind Conference & Exhibition.* 4–6 December. Berlin, Germany.

SHUKLA, S. and S. SAWYER (2012). *30 years of policies for wind energy.* Abu Dhabi, United Arab Emirates: International Renewable Energy Agency.

SIEBENSOHN SMALL, C. (1997). *Wind Performance Reporting System – 1995 summary.* Technical report P500-97-003. Sacramento, CA, United States: California Energy Commission.

SIMLEY, E., L. Y. PAO, R. FREHLICH, B. JONKMAN and N. KELLEY (2014). "Analysis of light detection and ranging wind speed measurements for wind turbine control". *Wind Energy* 17 (3), pp. 413–433. DOI: `10.1002/we.1584`.

SMITH, C. B. (2007). "Extreme waves and ship design". *10th International Symposium on Practical Design of Ships and Other Floating Structures*. 4 October. Houston, TX, United States.

STEYN, D. G., T. R. OKE, J. E. HAY and J. L. KNOX (1981). "On scales in meteorology and climatology". *McGill Climatological Bulletin* 30, pp. 1–8.

STOCKER, T., D. QIN, G.-K. PLATTNER, L. ALEXANDER, S. ALLEN, N. BINDOFF, F.-M. BRÉON, J. CHURCH, U. CUBASCH, S. EMORI, P. FORSTER, P. FRIEDLINGSTEIN, N. GILLETT, J. GREGORY, D. HARTMANN, E. JANSEN, B. KIRTMAN, R. KNUTTI, K. K. KUMAR, P. LEMKE, J. MAROTZKE, V. MASSON-DELMOTTE, G. MEEHL, I. MOKHOV, S. PIAO, V. RAMASWAMY, D. RANDALL, M. RHEIN, M. ROJAS, C. SABINE, D. SHINDELL, L. TALLEY, D. VAUGHAN and S.-P. XIE (2013). "Technical summary". *Climate change 2013: the physical science basis. Contribution of Working Group I to the Fifth Assessment Report of the Intergovernmental Panel on Climate Change*. Ed. by T. Stocker, D. Qin, G.-K. Plattner, M. Tignor, S. Allen, J. Boschung, A. Nauels, Y. Xia, V. Bex and P. Midgley. Cambridge, United Kingdom and New York, NY, United States: Cambridge University Press.

STOYANOVA, S. B. (2006). "Invariant cubature formulae of degree 6 for the n-simplex". *Journal of Computational and Applied Mathematics* 193 (2), pp. 446–459. DOI: `10.101 6/j.cam.2005.06.027`.

STULL, R. B. (1988). *An introduction to boundary layer meteorology*. Dordrecht, The Netherlands: Kluwer.

STULL, R. B. (2011). *Meteorology for scientists and engineers*. 3rd edn. Vancouver, Canada: University of British Columbia.

SUOMI, I., S.-E. GRYNING, R. FLOORS, T. VIHMA and C. FORTELIUS (2015a). "On the vertical structure of wind gusts". *Quarterly Journal of the Royal Meteorological Society* 141 (690), pp. 1658–1670. DOI: `10.1002/qj.2468`.

SUOMI, I., S.-E. GRYNING, R. FLOORS, T. VIHMA and C. FORTELIUS (2015b). "On the vertical structure of wind gusts". *Quarterly Journal of the Royal Meteorological Society* 141 (690), pp. 1658–1670. DOI: `10.1002/qj.2468`.

SUTHERLAND, H. J., D. E. BERG and T. D. ASHWILL (2012). *A retrospective of VAWT technology*. Technical report SAND2012-0304. Albuquerque, NM, United States: Sandia National Laboratories.

TAYLOR, G. I. (1938). "The spectrum of turbulence". *Proceedings of the Royal Society A: Mathematical, Physical and Engineering Sciences* 164 (919), pp. 476–490. DOI: `10.1098 /rspa.1938.0032`.

TAYLOR, M., K. DANIEL, A. ILAS and E. Y. SO (2015). *Renewable power generation costs in 2014*. Abu Dhabi, United Arab Emirates: International Renewable Energy Agency.

TENNEKES, H. and J. L. LUMLEY (1972). *A first course in turbulence*. Cambridge, MA, United States: MIT Press.

THEISSEN, P. (2012). "Unsteady vehicle aerodynamics in gusty crosswind". PhD thesis. Technical University of Munich.

THEODORSEN, T. (1935). *General theory of aerodynamic instability and the mechanism of flutter.* Technical report 496. Langley Field, VA, United States: National Advisory Committee for Aeronautics.

TOWNSEND, A. A. (1970). "Entrainment and the structure of turbulent flow". *Journal of Fluid Mechanics* 41 (1), p. 13. DOI: 10.1017/S0022112070000514.

TOWNSEND, A. A. (1980). "The response of sheared turbulence to additional distortion". *Journal of Fluid Mechanics* 98 (01), p. 171. DOI: 10.1017/S0022112080000092.

TROMANS, P. S., A. R. ANATURK and P. HAGEMEIJER (1991). "A new model for the kinematics of large ocean waves-application as a design wave". *First International Offshore and Polar Engineering Conference.* 11–16 August. Edinburgh, United Kingdom.

TUKEY, J. W. (1962). "The future of data analysis". *The Annals of Mathematical Statistics* 33 (1), pp. 1–67. DOI: 10.1214/aoms/1177704711.

UPWIND (2011). *Design limits and solutions for very large wind turbines.* Technical report. Brussels, Belgium: EWEA.

US ENERGY INFORMATION ADMINISTRATION (2016). *U.S. crude oil first purchase price.* URL: www.eia.gov/dnav/pet/hist/LeafHandler.ashx?n=pet&s=f000000__3&f=m (accessed on 25 November 2016).

U.S. NATIONAL ARCHIVES AND RECORDS ADMINISTRATION (2006). *Code of federal regulations. Title 14 - Aeronautics and Space.*

VAN DER HOVEN, I. (1957). "Power spectrum of horizontal wind speed in the frequency range from 0.0007 to 900 cycles per hour". *Journal of Meteorology* 14.

VERGOUWE, R. (2014). *De veiligheid van Nederland in kaart.* Technical report HB 2540621. Rijkswaterstaat Projectbureau VNK.

WAGENAAR, J. W. and P. J. EECEN (2010). *3D turbulence at the Offshore Wind Farm Egmond aan Zee.* Technical report ECN-E–10-075. Petten, The Netherlands: Energy Research Centre of the Netherlands.

WAGNER, H. (1925). "Über die Entstehung des dynamischen Auftriebes von Tragflügeln". *Zeitschrift für Angewandte Mathematik und Mechanik* 5 (1), pp. 17–35. DOI: 10.1002/zamm.19250050103.

WEIBULL, W. (1939). "A statistical theory of strength of materials". *Ingeniörsvetenskapsakademiens Handlinger* 151, pp. 1–45.

WMO (1995). *Manual on codes.* Technical report WMO-No. 306. Geneva, Switzerland: World Meteorological Organization.

YU, G.-H. and C.-C. HUANG (2001). "A distribution free plotting position". *Stochastic Environmental Research and Risk Assessment* 15 (6), pp. 462–476. DOI: 10.1007/s004770100083.

Appendices
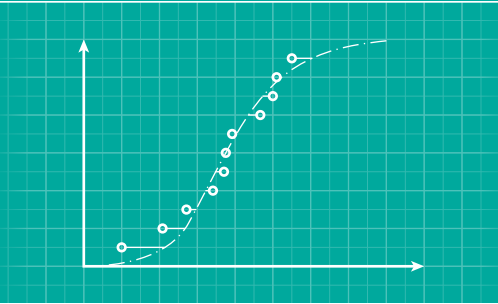
Plotting positions

The problem of using the natural estimator (i.e., $\hat{F}(z_i) = i/N$ as a plotting position is that it does not allow for extrapolation. A simple fix is to move the position to the center of the element (Hazen, 1914):

$$\hat{F}(z_i) = \frac{i - \frac{1}{2}}{N}. \tag{A.1}$$

Many similar expressions have been formulated throughout the years (e.g., see Harter, 1984). In an attempt to clarify on the subject, Gumbel (1958) posed five requirements that a good plotting formula should fulfill:

"1. The plotting position should be such that all observations can be plotted.

2. The plotting position should lie between the observed frequencies $(i-1)/N$ and i/N and should be universally applicable, i.e., it should be distribution-free. This excludes the probabilities of the mean, median, and modal ith value which differ for different distributions.

3. The return period of a value equal to or larger than the largest observation, and the return period of a value smaller than the smallest observation, should approach N, the number of observations. This condition need not be fulfilled by the choice of the mean and median ith value.

4. The observations should be equally spaced on the frequency scale, i.e., the difference between the plotting positions of the $(i+1)$th and the ith observation should be a function of n only, and independent of i. This condition need not be fulfilled for the probabilities at the mean, median, or modal ith values.

5. The plotting position should have an intuitive meaning, and ought to be analytically simple. The probabilities at the mean, modal, or median mth value have an intuitive meaning. However, the numerical work involved is prohibitive."

(Gumbel, 1958, pp. 32–35)

One such candidate is the function proposed by Weibull (1939) in his work on predicting the strength of materials:

$$\hat{F}(z_i) = \frac{i}{N+1}. \tag{A.2}$$

The derivation of Equation (A.2) starts from *order statistics* (e.g., see Folland and Anderson, 2002). Suppose there is a collection of independent random variables $X_1, X_2, \ldots, X_N$ with a common density $f(x)$ and distribution function $F(x)$. Then, ordering the entries from low to high yields a sequence

$$Z_1 \leq Z_2 \leq \ldots \leq Z_i \ldots \leq Z_N.$$

Instead of a single ordered sequence, say there are k sets of data with a size N. In that case, k individual ith-ranked values will exist that will make up the density of the ith order statistic:

$$
\begin{array}{c}
rank \rightarrow \\[6pt]
\begin{array}{ccccccccccc}
Z_{1,1} & \leq & Z_{2,1} & \leq & \ldots & \leq & Z_{i,1} & \leq & \ldots & \leq & Z_{N,1} \\
Z_{1,2} & \leq & Z_{2,2} & \leq & \ldots & \leq & Z_{i,2} & \leq & \ldots & \leq & Z_{N,2} \\
\vdots & & \vdots & & & & \vdots & & & & \vdots \\
Z_{1,j} & \leq & Z_{2,j} & \leq & \ldots & \leq & Z_{i,j} & \leq & \ldots & \leq & Z_{N,j} \\
\vdots & & \vdots & & & & \vdots & & & & \vdots \\
Z_{1,k} & \leq & Z_{2,k} & \leq & \ldots & \leq & Z_{i,k} & \leq & \ldots & \leq & Z_{N,k}
\end{array}
\end{array}
$$

$$\downarrow$$

$$f_i(z_i)$$

This density function will describe how z_i can vary among repeated samples. An expression for $f_i(z_i)$ can be found by finding and grouping all the ith order statistics for all sets of data. For any particular value $Z_{i,j}$ to be the ith order statistic, $i - 1$ elements need to have a value lower than $Z_{i,j}$ and $N - i$ elements need to have a value higher than $Z_{i,j}$. Basically, any member of a set $Z_{1,j}, Z_{2,j}, \ldots, Z_{N,j}$ would fall into one of three categories:

$$
\underbrace{Z_{1,j}, \ldots, Z_{i-1,j}}_{i-1} \quad Z_{i,j} \quad \underbrace{Z_{i+1,j}, \ldots, Z_{N,j}}_{N-i}
$$

A situation like this is described by a multinomial distribution, of which the probability mass function[1] is given by

$$f\left(n_1, \ldots, n_q; N, p_1, \ldots, p_q\right) = \frac{N!}{n_1! \cdots n_q!} p_1^{n_1} \cdots p_q^{n_q}, \tag{A.3}$$

---

[1] A probability *mass* function is different from a probability *density* function in the sense that it deals with discrete variables, rather than continuous variables.

where n_q is the size of a subset of $Z_{1,j}, Z_{2,j}, \ldots, Z_{N,j}$ belonging to an event with a probability of $p_q^{n_q}$. Then, for this example, Equation (A.3) can be written as

$$f_i(z_i) = \frac{N!}{(i-1)!\,(1)!\,(N-i)!} \mathrm{P}\left(Z_{1,j} \le z_i \cap \cdots \cap Z_{i-1,j} \le z_i\right)$$

$$\cdots \mathrm{P}\left(Z_{i,j} = z_i\right) \mathrm{P}\left(Z_{i+1,j} \ge z_i \cap \cdots \cap Z_{N,j} \ge z_i\right),$$

$$= i \binom{N}{i} F(z_i)^{i-1} \left[1 - F(z_i)\right]^{N-i} f(z_i). \tag{A.4}$$

This is where the derivation of Makkonen, Pajari and Tikanmäki (2013) takes off. The probability assigned to the ith order statistic is the probability of a variable x not to exceed z_i:

$$\hat{F}(z_i) = P(x \le z_i),$$

$$= \int_{-\infty}^{\infty} \int_{-\infty}^{z_i} f_i(z_i) f(x)\, \mathrm{d}x\, \mathrm{d}z_i,$$

$$= \int_{-\infty}^{\infty} \left[\int_{-\infty}^{z_i} f(x)\, \mathrm{d}x \right] f_i(z_i)\, \mathrm{d}z_i,$$

$$= \int_{-\infty}^{\infty} F(z_i) f_i(z_i)\, \mathrm{d}z_i,$$

$$= \int_{-\infty}^{\infty} F(z_i)\, i \binom{N}{i} F(z_i)^{i-1} \left[1 - F(z_i)\right]^{N-i} f(z_i)\, \mathrm{d}z_i,$$

$$= i \binom{N}{i} \int_{-\infty}^{\infty} F(z_i)^{i} \left[1 - F(z_i)\right]^{N-i} f(z_i)\, \mathrm{d}z_i.$$

When making the substitution $v = F(z_i)$, $\mathrm{d}v = f(z_i)\, \mathrm{d}z_i$, one arrives at a beta function $\mathrm{B}(i+1, N-i+1)$:[2]

$$\hat{F}(z_i) = i \binom{N}{i} \int_{0}^{1} v^{i} (1-v)^{n-i}\, \mathrm{d}v,$$

$$= i \binom{N}{i} \frac{i!\,(N-i)!}{(N+1)!},$$

$$= i \frac{N!}{i!\,(N-i)!} \frac{i!\,(N-i)!}{N!\,(N+1)},$$

$$= \frac{i}{N+1},$$

which should hold for any parent distribution function, $f(x)$.

---

2    $\mathrm{B}(x,y) = \int_{0}^{1} t^{x-1} (1-t)^{y-1}\, \mathrm{d}t.$
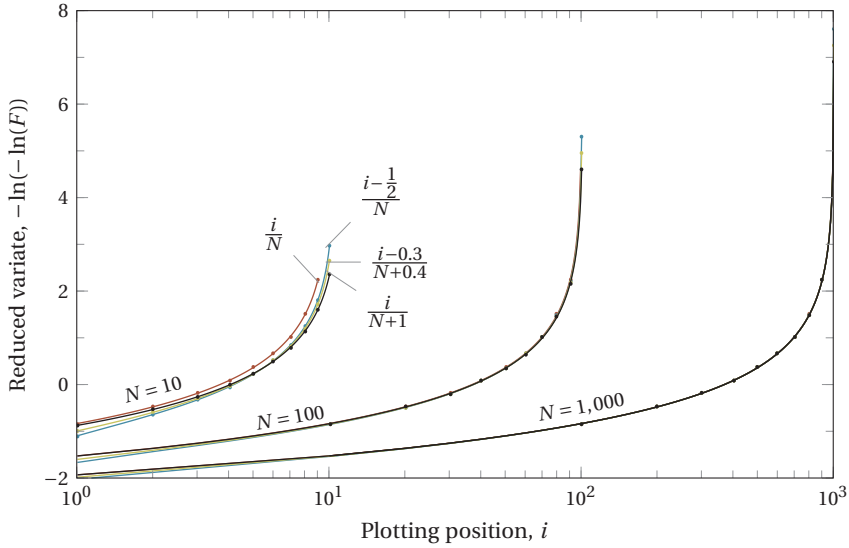
Figure A.1: Assigned probabilities according to the natural estimator and the plotting positions of Hazen (1914), Benard and Bos-Levenbach (1953), and Weibull (1939).

The above derivation clings to the idea that the expected value, $E[F(z_i)]$, provides an unbiased estimate for the plotting position $\hat{F}(z_i)$. However, another approach would be to use the median or mode instead, resulting in a different expression. In fact, many formulas have been proposed in the past, most of which are in the form of

$$\hat{F}(z_i) = \frac{i - a}{N + 1 - 2a},\tag{A.5}$$

where a is some constant. When $a = 0$, Equation (A.5) yields the mean position $i/(N+1)$, whereas for $a = 1$ it reduces to the modal position $(i-1)/(N-1)$. Moreover, $a \approx 0.3$ is a good representation of the median (Harter, 1984). Disagreement about which position to use has led to a variety of different functions, of which some examples are listed in Table 6.1. As shown in Figure A.1, the differences in plotting positions are most pronounced when the sample size, N, is small or at the tail of the distribution ($\hat{F} \to 0$ or $\hat{F} \to 1$).

Table 6.1: Examples of plotting positions from literature.

Author(s)	$\hat{F}$	a
Beard (1943)	$(i-0.31)/(N+0.38)$	0.31
Benard and Bos-Levenbach (1953)	$(i-0.3)/(N+0.4)$	0.3
Blom (1958)	$(i-\frac{3}{8})/(N+\frac{1}{4})$	$\frac{3}{8}$
Cunnane (1978)	$(i-0.4)/(N+0.2)$	0.4
Filliben (1975)	$(i-1)/(N-1)$	1
Gringorten (1963)	$(i-0.44)/(N+0.12)$	0.44
Hazen (1914)	$\left(i-\frac{1}{2}\right)/N$	$\frac{1}{2}$
Landwehr, Matalas and Wallis (1979)	$(i-0.35)/N$	n/a
McClung and Mears (1991)	$(i-0.4)/N$	n/a
Tukey (1962)	$(3i-1)/(3N+1)$	$\frac{1}{3}$
Weibull (1939)	$i/(N+1)$	0
Yu and Huang (2001)	$(i-0.326)/(N+0.348)$	n/a

IEC 61400-1 extrapolation procedure

The IEC 61400-1 design standards (IEC, 2005a) also contain guidelines for obtaining the 50-year extreme loads. The goal of this appendix is to compare the performance of this extrapolation method against the crude Monte Carlo method used in Chapter 5, based on the blade root flapwise bending moment of the NREL 5 MW machine.

The method demonstrated in Appendix F of the IEC (2005a) guidelines is a peak-over-threshold method (see Subsection 5.1.2). It specifies a threshold level that is 1.4 times the standard deviation of the load process above the mean. In this work, the extremes are selected through an automated procedure in which they are required to be at least 30 seconds apart from neighboring peaks in order to ensure independence. In addition to the peak-over-threshold method, block maxima are also collected for comparison.

Instead of the approach used in Chapter 5, where all the data is collected in one big pile (i.e., "aggregation before fitting"), the IEC guidelines promote the use of discrete bins (i.e., "fitting before aggregation"). Extreme load distributions are constructed per wind speed bin and are weighted according to

$$\hat{F}(x) = 1 - \int_{\bar{u}_1 - \frac{1}{2}\Delta\bar{u}}^{\bar{u}_m + \frac{1}{2}\Delta\bar{u}} f(\bar{u})\,\mathrm{d}\bar{u} + \sum_{i=1}^{m} F(x|\bar{u}_i) \int_{\bar{u}_i - \frac{1}{2}\Delta\bar{u}}^{\bar{u}_i + \frac{1}{2}\Delta\bar{u}} f(\bar{u})\,\mathrm{d}\bar{u}, \tag{B.1}$$

where the integrals are taken from the cut-in wind speed of $\bar{u}_1 = 3$ m/s to the cut-out wind speed of $\bar{u}_m = 25$ m/s. The IEC guidelines do not specify the required bin width nor a recommended sample size per bin, only a bare minimum of 300 minutes. Therefore, several values are used:

- $\Delta\bar{u} = 2$ m/s ($m = 11$): $\bar{u} = 4, 6, \ldots, 24$ m/s;

- $\Delta\bar{u} = 1$ m/s ($m = 22$): $\bar{u} = 3.5, 4.5, \ldots, 24.5$ m/s;

- $\Delta\bar{u} = 0.5$ m/s ($m = 44$): $\bar{u} = 3.25, 3.75, \ldots, 24.75$ m/s.

Every bin contains a sample size, n, leading to a total number of $N = m \cdot n$ time series. For each case, a total of 4,400 ten-minute wind fields were evaluated and resampled to establish the confidence intervals.

Figure B.1 shows the return level plots with several distribution fits, based on a combined sample size of 1 week. In a fitting-before-aggregation extrapolation scheme, the computational budget has to be shared over several bins. Because of the difficulty to
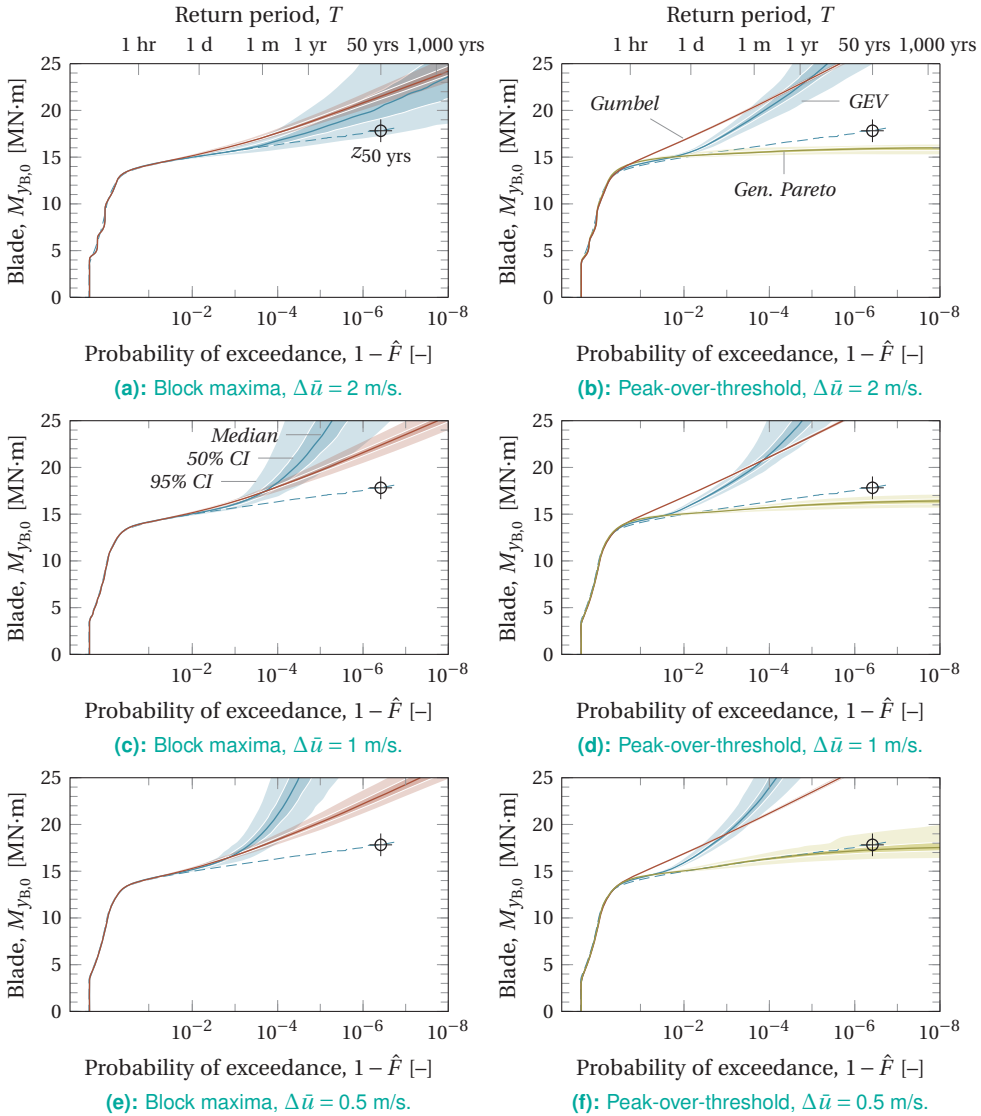
Figure B.1: Extreme load predictions for the NREL 5 MW turbine, following the guidelines in Appendix F of the IEC 61400-1 standards (IEC, 2005a), based on $N \sim 1{,}000$ ten-minute wind fields (~ 1 week). The dashed line indicates the complete, 106-year data set.

estimate the shape factor, ξ, the generalized extreme value distribution (GEV) tends to produce a positive bias (as seen throughout Chapter 5). A straight[3] Gumbel distribution ($\xi = 0$), however, cannot solve this and also produces a positive bias. The generalized Pareto distribution tends to have negative values of ξ and a negative bias, which is an advantage in this case. It results in an upper bound and therefore the predictions stay

---

[3]   Straight in the sense that every wind speed bin has a linear fit on a double logarithmic scale.

(a): Block maxima, $\Delta\bar{u} = 2$ m/s.

(b): Peak-over-threshold, $\Delta\bar{u} = 2$ m/s.

(c): Block maxima, $\Delta\bar{u} = 1$ m/s.

(d): Peak-over-threshold, $\Delta\bar{u} = 1$ m/s.

(e): Block maxima, $\Delta\bar{u} = 0.5$ m/s.

(f): Peak-over-threshold, $\Delta\bar{u} = 0.5$ m/s.

Figure B.2: The decrease of uncertainty with increasing sample size.
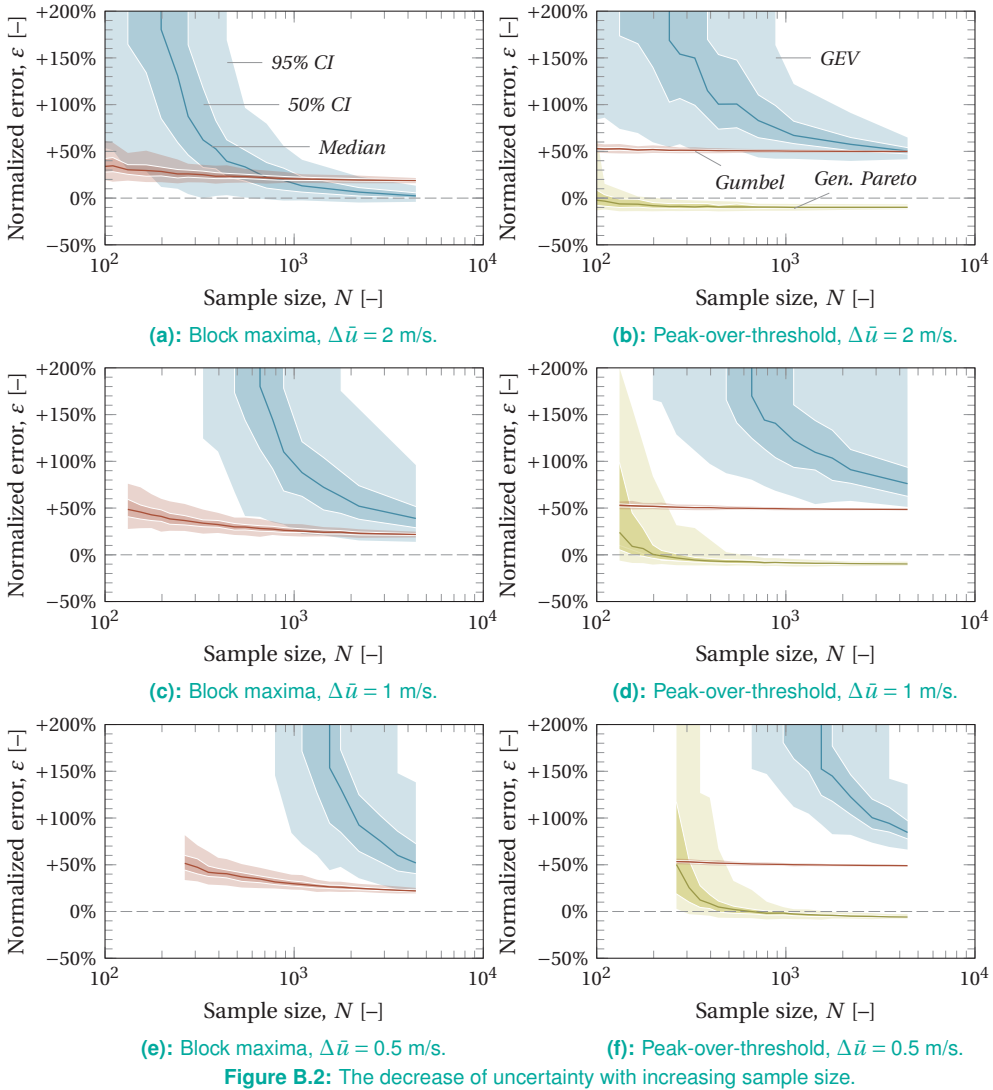
closer to the true 50-year load. For $\Delta\bar{u} = 0.5$ m/s, the 95% confidence interval around the 50-year load is estimated to be [16.3, 19.3] MN·m.

As a result of fitting-before-aggregation, the final load distribution is often a weighted average of many bad fits and much of the error ends up in the tail. Wide bins—having more data points per bin—are more likely to produce better estimates at small N. It also explains why the peak-over-threshold method gives consistently better results than when block maxima are used, since it collects multiple peaks per ten-minute time series.

Figure B.2 shows the 50% and 95% confidence intervals for several sample sizes, starting at $N = 6m$ (i.e., 6 ten-minute wind fields per bin). Because of the large bias in every bin, the GEV distribution performs better with aggregation-before-fitting (see

Figure 5.9a) instead of fitting-before-aggregation. At the same time, whereas a Gumbel is usually a good estimate with aggregation-before-fitting at small N, here it does not seem to converge to the right level at all. The peak-over-threshold method, extrapolated with the generalized Pareto distribution, clearly performs the best. It converges to a 50-year load that is several percent below the true value, depending on the bin width.

Acknowledgements

They say that doing a PhD is one of the most stressful periods in your life. I could not disagree more. The last four years were, without a doubt, the best years of my life so far. I got married, traveled to many wonderful places, and had all the freedom to develop myself and to flourish. But most of all, I have had the privilege of being surrounded by a lot of great people.

First of all, I have to express my deepest gratitude to Wim, my supervisor for the last four years. I had the fortune of being guided by someone who already laid much of the groundwork for this research. Yet, you provided me all the freedom to give my own twist to it. I thoroughly enjoyed working with you. Thank you for your patience and motivation.

Furthermore, my promotor, Gerard: thanks so much for your time and wisdom. I doubt whether there are many research groups where the professor is so open and sociable. I am happy to have been part of this unique family-like group that you and Gijs have created.

Of course, Sylvia, our section's secretary. Even though Gerard is officially the head of the group, we all know who actually runs things around there. Thank you for keeping an eye out for all of us and stepping in when needed.

Michiel, Carlos, Henk, Jan-Willem: I had the pleasure of being taught by you as a student and to end up at the other side of the classroom myself. Thanks for all the help and the valuable lessons. Also, Jan-Paul, Danika, Rody, and Nils: thanks for all the good times while making the MOOC. Working with you to develop new teaching material has been a unique learning experience for me. Even though the workload was peaking at times and deadlines were tight, it was always a pleasure.

Dick: thanks for the pleasant collaboration, the many interesting discussions, and the helpful comments on the last part of this thesis. Working with you has certainly improved my understanding of certain subjects; plus, it is always nice to get help from someone who is a much more patient and precise programmer than I am.

Daniel, Ashim, Wei, Tom, and Delphine: thanks for being wonderful office mates. It was impossible to have a bad day at work with you guys around. I will miss our discussions and all our office shenanigans, without which this thesis would surely have been finished much earlier. I am sure we will stay in touch. Sebastian, Bruce, Ricardo, Lars, Jaco, Vinit, Sachin, and all the other PhDs at Wind Energy: thanks for all the memorable times and the laughs. Stay awesome and I look forward to sharing many more beers with you in the future. Maarten: thanks so much for being a great companion and sparring partner. I enjoyed our many discussions about the challenges of combining meteorology

and engineering, and of course our vrijmibo discussions about everything else. I doubt whether this thesis would have the same quality if it were not for your input.

Stefan, the master student I had the privilege of supervising: thanks for your hard work and dedication. The work that you did during your graduation period certainly sparked many new ideas and helped shape my final chapter. I wish you a great future with great coffee!

Hans, Robin, Stefan: I believe I haven't seen Spiñal Tap in a while...

Arjen, André, Thomas, Jasper: thanks for being great friends and helping to keep my mind off work in the weekends. I realize I haven't been able to visit Utrecht as much as I'd like, but I hope that will solve itself now the PhD is finished.

My in-laws, Jack and Wilma: thanks for always being so supportive and showing a keen interest in what I was doing. Moreover, Mike and Lisette, Niels and Saskia, and the kids: thanks for all the support and for being a much-needed distraction at times. I hope this book will help you to understand at least a little of what I have been doing.

My brother Ronald, and (practically my sister) Esmé: thanks for being awesome and supplying me with a steady stream of cat videos to get through the week. It is always a joy seeing you guys. Ronald: thanks for all the input and help with the math, the writing, the figures, and everything else. You have a tough time ahead of you with finishing your own PhD, but I am sure you are more than capable to succeed.

My parents, Jozef and Thérèse: thanks for providing me with the love and support I needed to get where I am today. I am sure you are very interested in seeing the outcome of all the tuition fees you spent on me. I hope that, by browsing through the pages, you are able to recognize the result of the lego kits you bought for me as a child, the influence of the Das brothers' books, and the many hours spent with me preparing for my high school exams.

To my wife, Esther: thanks for enduring the long relationship test called a PhD. It must not always have been easy to live with someone who regularly spent his evenings and weekends working. Yet, you have shown me nothing but unconditional love and support (and coffee) over the years, even though you often had to work much harder than I did. Thank you for being there for me during the ups and downs, and sitting through all the nerdy talks. I apologize in advance for all the lame doctor jokes you will have to hear from now on.

Finally, I would like to thank the community of whisky brewers for catalyzing many of the ideas in this thesis.

I dedicate this work to Jack. He would have loved to read it.

Curriculum vitæ

René Bos was born on 19 October 1987 in Nieuwegein, The Netherlands. He attended College de Heemlanden in Houten and graduated with a double degree in 2006. After high school, he enrolled for the BSc Aerospace Engineering at Delft University of Technology with a minor in Aerospace for Sustainable Earth. In 2009, he started with the MSc Sustainable Energy Technology, which is an interfaculty program covering many engineering disciplines. He decided to return to the Faculty of Aerospace Engineering for his MSc thesis work on small vertical-axis wind turbines, on which he graduated in 2012.

In 2013, he began his PhD research at the Wind Energy group at Delft University of Technology as part of the European Innwind project. Under the supervision of Wim Bierbooms, he studied the spatial structure of extreme wind gusts and the effect on large rotors. In 2017, René started working at Eneco where he helps realizing offshore wind farms in the North Sea.

Publications

BOS, R., W. A. A. M. BIERBOOMS, and G. J. W. VAN BUSSEL (2013). "Extreme gust loads for novel wind turbines." *9th EAWE PhD Seminar on Wind Energy in Europe.* 22–25 September. Visby, Sweden.

BOS, R., W. A. A. M. BIERBOOMS, and G. J. W. VAN BUSSEL (2014). "Towards spatially constrained gust models." *Journal of Physics: Conference Series* 524, p. 12107. DOI: 10.1088/1742-6596/524/1/012107.

BOS, R., W. A. A. M. BIERBOOMS, and G. J. W. VAN BUSSEL (2014). "3D stochastic gusts as an alternative to the Mexican hat wavelet." *10th EAWE PhD Seminar on Wind Energy in Europe.* 28–31 October. Orléans, France.

BOS, R., W. A. A. M. BIERBOOMS, and G. J. W. VAN BUSSEL (2015). "Importance sampling of severe wind gusts." *11th EAWE PhD Seminar on Wind Energy in Europe.* 23–25 September. Stuttgart, Germany.

BOS, R., A. GIYANANI, and W. A. A. M. BIERBOOMS (2016). "Assessing the severity of wind gusts with lidar." *Remote Sensing* 8(9), 758. DOI: 10.3390/rs8090758.

BOS, R. and H. F. VELDKAMP (2016). "A method to find the 50-year extreme load during production." *Journal of Physics: Conference Series* 753, p 42021. DOI: 10.1088/1742-6596/753/4/042021.

BOS, R., W. A. A. M. BIERBOOMS, and G. J. W. VAN BUSSEL. "The spatial structure of severe wind gusts." *Manuscript submitted for publication.*

VAN EIJK, S. F., R. BOS, and W. A. A. M. BIERBOOMS. "The risks of extreme load extrapolation." *Manuscript submitted for publication.*

Nomenclature

Notations

Abbreviations

Index